

LOW SURFACE BRIGHTNESS GALAXIES AND
THE GALAXY STELLAR MASS FUNCTION

Richard Williams

A thesis submitted in partial fulfilment of the requirements of
Liverpool John Moores University
for the degree of
Doctor of Philosophy.
May 30, 2017

Declaration

The work presented in this thesis was carried out at the Astrophysics Research Institute, Liverpool John Moores University. Unless otherwise stated, it is the original work of the author with the exception of:

All IOTA magnitudes in both Chapters 2 and 3 were created by Dr. Lee Kelvin whilst working at the Astrophysics Research Institute.

All mask_ic values in Chapter 3 which were created by Dr. Peder Norberg.

While registered as a candidate for the degree of Doctor of Philosophy, for which submission is made, the author has not been registered as a candidate for any other award.

This thesis has not been submitted in whole, or in part, for any other degree.

Richard Williams
Astrophysics Research Institute
Liverpool John Moores University
IC2, Liverpool Science Park
146 Brownlow Hill
Liverpool
L3 5RF
UK

MAY 2016

Abstract

The galaxy stellar mass function (GSMF) has been well measured by the Galaxy And Mass Assembly (GAMA) survey down to a mass of $M_* = 10^8 M_\odot$. Below this mass the values produced so far can only be taken as lower limits on the distribution. One source of this incompleteness is failing to account for undetected low-surface-brightness galaxies (LSBGs) within the fields observed. These galaxies have been known about for some time, however, taking a true census of their population is difficult because of the biases associated with their detection in large surveys. The focus of this thesis is to improve the census of these objects and to try and apply those results to the low-mass end of the GSMF.

First the SDSS data used to create the original GAMA catalogues is re-examined for low-surface brightness galaxies (LSBGs). To accomplish this SDSS DR7 imaging was used and a specialised detection algorithm created. This was based on masking sources detected with SDSS PHOTO, combining the *gri* images with a weighting that maximises the signal-to-noise (SNR), and smoothing the images. These were then run through a detection algorithm which finds all pixels above a set threshold and groups them based on their proximity to one another. The list of detections is cleaned of contaminants such as diffraction spikes and the faint wings of masked objects. This produces a final list of 343 newly discovered LSBGs. Measuring their $g - i$ and $J - K$ colours shows that most are likely to be at redshifts less than 0.15. The photometry is carried out using a flexible auto aperture for each detection giving surface brightness measurements of $\mu_r > 23.7 \text{ mag arcsec}^{-2}$ and r -band magnitudes of $r_{AUTO} \gtrsim 20 \text{ mag}$. Through this method we show there are at least 343 new LSBGs within the GAMA

fields, however none of these galaxies are bright enough to be within the GAMA main survey limit.

It was noticed during the previous work that the detected LSBGs were all visible in VIKING Z -band data, and so it was decided to run a more traditional detection algorithm over these data to increase the number of LSBGs detected. This could then be used to create a new GSMF based on the deeper Z -band imaging. By using this imaging it will be possible to detect many more faint galaxies than previously and also increase the depth to which surface brightness can be effectively probed. The three GAMA equatorial regions have had mosaics created from the Z -band imaging which are searched using SOURCE EXTRACTOR (SEXTRACTOR) and catalogues of detections are made. These are then compared to the original GAMA catalogues to remove duplicate detections and identify any possible new ones. Criteria are then applied to the source lists to remove any stars or objects which are either not galaxies or artefacts. This then leaves only likely galaxies in the catalogue to be used. The next stage is to create the GSMF based on the data collected, through applying corrections for the volume searched, and the spectroscopic completeness of the objects after they have been binned in $g - i$, $J - K$, and apparent magnitude. The GSMF created is compared to previous versions, namely that from Baldry et al. (2012), and a rise in the number density at masses of $M_* \leq 10^8 M_\odot$ is shown. These can still only be thought of as lower limits however as improvement to the imaging can still be made in future surveys.

With a full catalogue obtained using the VIKING Z -band it was decided to revisit the detection algorithm developed in Chapter 2. A pilot study was undertaken to both test the validity of the method, and the suitability of the VIKING images for further study. Whilst applying the detection algorithm to the data improved the ability to detect low surface brightness features within the images, no new galaxies were discovered over the pilot study area of 0.75 deg^2 . This method applied to the Z -band data, even over the full area, is unlikely to lead to large numbers of new LSBGs.

This work has shown that there are still LSBGs in the field to be discovered. The result of finding new LSBGs has been to raise the measurement of the GSMF at low masses, further constraining the number of low mass galaxies in the Universe.

Acknowledgements

I would like to firstly thank my supervisory team, Prof. Ivan Baldry and Prof. Phil James for all of the help and guidance they have given throughout this work, especially when it came to wading through the terrible english. That was just difficult for everyone involved. So much so I will be expecting corrections to this section as well. I would also like to thank those who have had a direct impact on these studies, namely Dr. Lee Kelvin, for dealing very well with a blond, floating head appearing over his divider on day one, and always being happy to help. The wider GAMA team, for all the comments and much needed feedback on my work, which improved it immeasurably, must also be thanked. I would like to thank my examiners for the comments which vastly improved the science and conclusions contained within the thesis and the extra work which has helped to show the validity of the work done.

It wouldn't be an acknowledgements section without thanking all of the poor soles who have had to directly deal with me on a day to day basis for the last three and a half years. Andy, Helen, Caroline, Rob, Katie, and Chris I am going to miss all the tea time chats we had, not so much the insults, but definitely the chats. It's going to be difficult to not have a cohort to take over the kitchen with on a regular basis. I must also thank all of the lecturers, post docs and other PhD students who where always up for a trip to the pub, or just a chat in the hallway, there are truly too many to name, so i'll just say a collective thank you for the memories.

I wouldn't be here if weren't for the constant push from my parents, and family to always follow what you want in life. You always found a way to make me keep improving whether through a kind word, piece of advice, or a shattered ruler (I told you

you wouldn't live it down mum). But seriously I wouldn't have made it this far in life if it weren't for you, and for that I will be eternally grateful.

And finally, I would like to give a special thanks to my loving partner Pippa. You were always able to make me see the crazy side of my stress, and kept me going whilst I tried to slog through the boring bits of the last three years, there were a few of them. I honestly don't know how you put up with it. Thanks for letting me me just talk to you about my work when I needed it and understanding when to change the subject when I didn't. Thank you for the all of the help and support. And finally thanks for all of the red.

"Mr Fletcher looked around the little room. It was currently occupied only by Adrian 'Nozzer' Miller, who'd wanted to be an astronomer because he thought it was all to do with staying up late looking through telescopes, and hadn't bargained on it being basically about adding columns of figures in a little shed in the middle of a windy field."

-Johnny and the Dead by Terry Pratchett

Contents

Contents	viii
List of Tables	xii
List of Figures	xiii
1 Introduction	1
1.1 Galaxy Classification	2
1.2 Dwarf Galaxies	4
1.3 Hierarchical Formation	5
1.4 Galaxy Stellar Mass Function	7
1.4.1 Schechter Function	7
1.4.2 Creating the GSMF	8
1.4.3 Low mass GSMF	11
1.5 Sub-structure Problem	13
1.5.1 Reionization	14
1.5.2 Supernova Feedback	16
1.5.3 Warm Dark Matter	16
1.6 Low Surface Brightness Galaxies	17

1.6.1	Detection Methods	19
2	Searching for LSBGs in SDSS data	25
2.1	Surveys	27
2.1.1	GAMA	27
2.1.2	Sloan Digital Sky Survey (SDSS)	27
2.1.3	VISTA VIKING	28
2.2	Image Processing	29
2.3	Detection Algorithm	36
2.4	Results	41
2.4.1	Spatial Distribution	41
2.4.2	Magnitudes	45
2.4.3	Colour Distribution	46
2.4.4	Catalogue	48
2.5	Summary & Conclusions	50
3	Determining the GLF and GSMF using a VIKING-Z band catalogue	55
3.1	Detecting Objects	56
3.1.1	Source Extraction	56
3.1.2	Removing Artefacts and Stars	58
3.1.3	Ghosts in the Images	62
3.1.4	Creating a Z selected catalogue	65
3.2	Galaxy Luminosity Function	75

3.2.1	Calculating the K-correction	76
3.2.2	Density Correction	78
3.2.3	Calculating Completeness	82
3.2.4	Determining the GLF	84
3.3	Galaxy Stellar Mass Function	91
3.3.1	Mass Estimation	93
3.3.2	Plotting the GSMF	96
3.4	Discussion	99
3.4.1	Defining the completeness correction	99
3.4.2	LSBGs within the study	106
3.4.3	Surface brightness, limits and challenges	108
3.5	Summary & Conclusions	110
4	Detecting VIKING LSBGs	113
4.1	Images	114
4.1.1	Image Reduction	114
4.2	Object Detection	118
4.3	Conclusions	122
5	Future Work	125
5.1	LSBG Follow Up	125
5.2	Future measurements of the GLF and GSMF	126
5.3	Future Surveys	128

A Table of LSBG sources from SDSS	130
B LSBG images from SDSS search algorithm	141
Bibliography	153

List of Tables

2.1	fpM file extensions from SDSS	31
2.2	The ranges of weights and other pertinent information about the images being processed	36
3.1	Binned values for the Z -band created GSMF	97
4.1	Defining the cut out regions used in the pilot study	114
4.2	The ranges of weights and other pertinent information about the images being processed	115

List of Figures

1.1	SB limits for SDSS photometric sample	18
2.1	Image panles showing the effects on the images as they are processed ready for searching	30
2.2	difference between the central coordinates of the different SDSS bands when viewing the same sky area.	33
2.3	$g - r$ and $r - i$ colour distributions for GAMA dwarf populations. . .	35
2.4	The number of masked pixels witin a fixed radius of a detection and comparison to a random sample.	39
2.5	Examples of imageproblems when searching for LSBGs.	40
2.6	Examples of what a detection could look like in the processed SDSS fields.	42
2.7	Comparisons between r -band and Z -band magnitudes for 343 LSBG's	43
2.8	Sky positions of all 343 objects dscovered in the search, relative to a volume limited sample of all GAMA galaxies.	44
2.9	Comparison of Auto magnitudes with Aperture magnitudes for the SDSS LSBG catalogue	47
2.10	Colour distribution loosley describing the possible redshift distribution of the 343 LSBGs	49

2.11	Surface brightness vs apparent magnitude of the newly discovered LSBGs compared to the GAMA main sample.	51
2.12	Distribution describing the effective radii of the 343 confirmed LSBG sources	53
3.1	Galactic extinction map outlining the 3 main GAMA equatorial regions.	58
3.2	VIKING Z -band magnitudes vs SDSS r -band magnitudes, to determine the cutoff magnitude for the VIKING survey.	60
3.3	Distribution of class_star for all objects in the VIKING survey.	61
3.4	Examples of objects missing from the VIKING catalogue	62
3.5	Examples of a common ghosting error found in the VIKING imaging	63
3.6	Examples of false detections from the VIKING data	64
3.7	Example of moving unidentified imaging error within VIKING data	65
3.8	$g - i$ vs $J - K$ colour plot of all sources detected in VIKING and not in the original TilingCat	69
3.9	Corrected $J - K$ to show the stellar locus and the cut used for removing stars from the data.	70
3.10	Uncorrected $g - i$ vs $J - K$ with criteria applied to remove the stellar locus.	72
3.11	Difference between SExtractor magnitudes and IOTA magnitudes.	73
3.12	Number of galaxies per apparent magnitude bin.	74
3.13	Spectroscop completeness of the survey showing larger than expected incompleteness at bright magnitudes.	75
3.14	Showing another method of separating stars from galaxies in the survey.	76

3.15	The final corrected spectroscopic completeness as a function of apparent magnitude.	77
3.16	K-correction vs. redshift for VIKING Z -band objects	79
3.17	Absolute magnitude versus redshift for the full population of galaxies with a redshift	80
3.18	Number density per volume bin for two volume limited samples	81
3.19	Cumulative DDP for the Z -defined catalogue	82
3.20	Comparison between V_{max} and V'_{max} against absolute Z -band magnitude	83
3.21	Spectroscopic completeness of all VIKING sources within three magnitude defined bins	85
3.22	Average value of C_i values against absolute Z -band magnitude	87
3.23	Comparison of before and after applying corrections to the Z -band GLF	88
3.24	Z -band GLF compared to past measurements.	90
3.25	Galaxy cluster GLF measured in the SDSS z -band by Popesso et al. (2006)	92
3.26	Plot to show the differences in mass estimates from two methods	95
3.27	VIKING GSMF compared to past measurements.	98
3.28	Schechter fit of the VIKING GSMF	99
3.29	Surface brightness vs Z -band apparent magnitude for the two combined populations from VIKING data	101
3.30	2 dimensional histogram of surface brightness vs apparent magnitude for calculation of C_i values.	102
3.31	Comparison between the output GSMFs given different C_i values. . . .	103
3.32	Distribution of Z -band apparent magnitude against mass	104

3.33	Example LSBGs from VIKING	107
3.34	Surface brightness versus mass for the VIKING survey	108
3.35	GAMA objects with known redshifts which have been affected by bright sources	109
4.1	$i - Z$ and $Z - Y$ colour distributions for GAMA dwarf populations. .	116
4.2	Image panles showing the effects on the Z -band images as they are processed ready for searching	117
4.3	Distribution of the percentage of NaN values, within 50 and 100 pixel radius apertures, placed around detections and random points in the images	120
4.4	Detections from the VIKING imaging showing some of the issues which may have caused an increase in spurious results	121
4.5	Image showing some of the problems in the VIKING imaging brought out through the masking and smoothing	124
5.1	This plot was created by Ivan Baldry. The limiting magnitudes for the GAMA swarps from the four main optical and NIR survey mosaics . .	127

Chapter 1

Introduction

Most galaxy surveys to date have been limited by a combination of apparent magnitude and surface brightness (SB) constraints. This has led to an over-representation of bright, high-SB galaxies compared to a true, volume-limited sample. Such limited samples have been used to construct our picture of galaxy types, e.g. the Hubble Tuning Fork (Hubble, 1926). However the majority of galaxies are, in fact, low mass dwarfs ($M_* \leq 10^{8.5} M_\odot$) (Karachentsev et al., 2004; Driver et al., 2005; Baldry et al., 2012), which often do not fit neatly into the ‘tuning fork’: irregulars (Hubble, 1926; de Vaucouleurs, 1959), little blue spheroids (Kelvin et al., 2014a), blue compact dwarfs (Zwicky & Zwicky, 1971) and dwarf spheroidals (Shapley, 1938) are some examples.

Λ CDM dark matter simulations have been used to try to determine how many low mass galaxies there could be compared to the overall population of galaxies. These simulations when compared to observations showed a discrepancy. This is known as the substructure problem (Moore et al., 1999) which can be characterised in two distinct ways. The first is by the observed deficiency of the number of observed satellites, around the Milky Way in particular, compared to the number of sub-halos predicted by models (Klypin et al., 1999; Moore et al., 1999). The second deals with the discrepancy between the predicted number of halos and observed galaxies on a cosmological scale (e.g., Peebles, 2001). There has been work towards solving this problem in the Local Group with the discovery of dwarf galaxies around the Milky Way (Gilmore

et al., 2007; Irwin et al., 2007; Walsh, Jerjen & Willman, 2007; Belokurov et al., 2010) and M31 (Ibata et al., 2007; Martin et al., 2009; Richardson et al., 2011; Martin et al., 2013b). They have not, however, been discovered in the numbers expected from simulation.

Most dwarf systems have intrinsically lower surface brightnesses than their higher mass counterparts (Kormendy, 1985; Baldry, Glazebrook & Driver, 2008). A loose definition has been placed in the literature for central surface brightness of low-surface-brightness galaxies (LSBGs) of $\mu_{\text{central,B}} \geq 23 \text{ mag arcsec}^{-2}$ (Impey & Bothun, 1997). This surface brightness makes them difficult to detect against the sky and leads to detection biases (Disney, 1976). There is also the problem of the environment the galaxies populate, often requiring a different detection method based on the environment the galaxy exists in. The following sections will detail the different techniques and some of the current efforts to search for these LSBGs across all environments.

Historically many studies have used the central surface brightness, denoted here as $\mu_{\text{central,filter}}$. In this study we will be using the mean surface brightness within a half light aperture also known as the effective surface brightness, denoted as μ_{filter} . As a comparison to the limit from Impey & Bothun (1997), converting between $\mu_{\text{central,B}}$ and μ_B assuming an exponential profile a conversion factor of 1.1 is applied meaning the limit is $\mu_B > 24.1 \text{ mag arcsec}^{-2}$. The filters used in this thesis are the r and Z bands from SDSS and VIKING respectively. Given typical colours of $B - r = 0.5$ & $B - Z = 1.0$ means that one would expect that, approximately, LSBGs would have $\mu_r \sim 23.5$ and $\mu_Z \sim 23$.

1.1 Galaxy Classification

The most well used and well known galaxy classification system was developed by Hubble (1926). His system was to create a simple “tuning fork” type diagram to classify galaxies, starting at early type (Elliptical galaxies) and moving to late type (Spiral and Irregular galaxies). The tuning fork structure comes from the separation in the

system between barred and unbarred spirals. The system ranks from late type to early type galaxies. It ranks the differences between systems using letters, to denote elliptical (E), spiral (S) and spiral barred (SB). Hubble then assigned ranks to the different types, such that E galaxies were given a number of 0 - 7 representing circular to highly elliptical respectively. For the S and SB types he gave a ranking of a - c representing a decreasing bulge-to-disk ratio and also tightly wound spirals to loosely wound spiral arms. A fourth class of objects was included to cover the Irregular (Irr) systems which had shapes that could not be easily sorted into one of the common classes listed above. An intermediate galaxy was added by Hubble known as a lenticular or S0 galaxy to be able to more fluidly move from E to S/SB galaxies. This galaxy had a large bright central bulge like an E type but also had a disk-like structure around it like an S type. At the time this was a theoretical idea to join the two ends of the tuning fork however through photometric surveys the S0 type was confirmed to exist (Sandage, 1975).

A further category was added by Shapley & Paraskevopoulos (1940) to include an Sd and SBd type galaxy which included irregular structures in the original diagram. This label was used and further extended by de Vaucouleurs (1959) in his version of the Hubble sequence which also contains transition stages between barred and unbarred spirals. The main aim of this system was to effectively reduce the bin size of the classifications by combining the labels to create extra transitional states between the different classifications, so for instance instead of moving straight from Sa to Sb you would have a transitional state of Sab. The extension of the Sd class was to include Magellanic type galaxies before the Irr types within the system, after spiral structure had been found in the Large Magellanic Cloud (de Vaucouleurs, 1955).

A further addition to this system was made by van den Bergh (1960) who added a luminosity classification from $I - V$ at each type to separate high luminosity systems from low luminosity systems with the same morphological structure. It has been found that there are no Sa or Sb low luminosity systems. This is due to low luminosity galaxies almost exclusively having morphologies which are categorised as S0 or Sc - Irr (Kormendy, 1982).

The classification of these systems in this way is important as it can give an idea of the

formation histories of galaxies, for instance a bright central bulge is likely evidence of a history of large mergers in the system (Roberts & Haynes, 1994). Dwarf field galaxies generally fall into the category of Irregular galaxies in these systems, due to their undefined morphology compared to their higher mass counterparts.

1.2 Dwarf Galaxies

A galaxy is considered a dwarf in the literature when it meets a certain set of criteria. These are mainly based on the luminosity or mass. The first of these parameters, that of luminosity, has been historically defined as a galaxy with an absolute magnitude fainter than -16 (Hodge, 1971), however some now consider the limit to be fainter than $M_B = -18$ (van Zee, 2000). Dwarf galaxies are also defined using stellar masses; this definition is more physically motivated than for the luminosity limits with a maximum of $M_* \leq 10^8 M_\odot$ (Kirby et al., 2013). It is also observed that dwarf galaxies have an intrinsically low surface brightness compared to their higher luminosity or higher mass counterparts (Binggeli, 1994).

In the original Hubble (1926) classification system, dwarf galaxies fall under the S0, Sc and Irr classifications, but by applying de Vaucouleurs (1959) extensions to the system many will then fall into the Sd, Sm, and Im classes where they can be further separated. This is due in part to the low luminosities of these systems as any intermediate galaxy classifications have large, bright central bulges with spiral structure, which the dwarf population does not have.

The most common types of dwarf galaxy are known as dwarf elliptical (dE), dwarf spheroidal (dSph) and dwarf irregular (dIrr). Dwarf elliptical galaxies are generally found in clusters and dwarf spheroidals are generally found in close proximity to larger galaxies. Because of this they have both been through, generally, the same evolutionary history and therefore have similar structure. Because of this these two populations are usually put together in the same category, in which case they are known as dwarf spheroidals (Kormendy, 1982).

dSph and dIrr galaxy types are generally found in different environments in the Universe. dSph galaxies are found gravitationally bound to larger systems, dIrr are found more in the field away from other systems (Grebel, 2001; Blanton et al., 2005a). These differing environments mean that the galaxies will experience different formation and evolutionary histories. dSph galaxies, will have been affected by tidal effects and ram pressure stripping, stripping the satellite galaxy of its gas and dust through interaction with a host galaxy or intra cluster medium, due to their proximity to a larger host galaxy. This means they will have little to no gas contained within the system and will therefore have old stellar populations with no star formation taking place within the galaxy (Grebel, 2001). dIrr galaxies have not been exposed to these environments as they form in isolation, so their formation will have been shaped by processes such as supernova feedback (Ferrara & Tolstoy, 2000) or reionization (Hoeft et al., 2006). Because of the lack of gas stripping they will have more gas and so host some star formation (Gallagher & Hunter, 1986).

1.3 Hierarchical Formation

White & Rees (1978), noted that the dominant method of galaxy formation in the universe was through a hierarchical process, where small systems merge together over cosmological time scales to form the large galaxies we see today. The first part of this galaxy formation is the collapse of dark matter into low mass halos. This is where the first galaxies were able to form as baryonic matter falls into the potential wells created by these dark matter halos, and cools to a point where star formation can occur. It has been shown with the use of cold dark matter (CDM) models of the universe that these structures formed together to create complex webs and filaments which interconnect. This has formed the large scale structure which is seen today (Benson, 2010).

The cold dark matter theory of structure formation is a prescription for what the Universe as a whole is made of, commonly known as Λ CDM. Λ is used to show that dark energy is the dominant part of the Universe making up some 70% of it. The rest of the matter content of the Universe is split between cold dark matter (25%) and baryons

(5%) (Planck Collaboration et al., 2016). This has been established for over a decade using both observation and simulation.

The observational evidence in support of a Λ CDM universe, and in turn a hierarchical formation mechanism for galaxies comes from the observation of the cosmic microwave background (CMB) and of large scale structure. The CMB provides precise constraints on the Λ CDM model with observations from COBE (Smoot et al., 1992), WMAP (Bennett et al., 2013), and now *Planck* (Planck Collaboration et al., 2014). This shows that the power spectrum of fluctuations is consistent with a spatially flat Λ CDM universe which implies hierarchical formation. Observations of the galaxy power spectrum using 2dF data (Cole et al., 2005) and SDSS (Tegmark et al., 2004) show stronger clustering on smaller scales, which is consistent with cold dark matter being the dominant mass component in the Universe. It has also been shown that galaxy clustering within a hot dark matter (HDM) simulation compared to a CDM model is incompatible with observations from galaxy redshift surveys (Davis et al., 1985). Further confirmation has also been found through the comparison of the observed merger rates of galaxy haloes and merger rates within CDM simulations matching to a high degree (Frenk et al., 1985; Lotz et al., 2011).

Whilst it is hard in most cases to measure the total mass of typical systems, it is more straightforward to measure stellar mass. The light emitted from the system reflects the total stellar content rather than the total mass of the system. Stellar masses are typically estimated by fitting a model to a spectral energy distribution, and applying the mass to light ratio from the model to the observed luminosity. This means that one of the key diagnostics is the galaxy stellar mass function (GSMF), which is a measure of the number of galaxies as a function of stellar mass. The form of the GSMF can give a good indication of how galaxies have evolved and formed together over time (Baldry et al., 2012).

1.4 Galaxy Stellar Mass Function

The first step in measuring the GSMF is to measure the Galaxy Luminosity Function (GLF) which measures the number of galaxies per luminosity bin per unit volume. Until the development of CCDs the GLF had been measured mostly in the B -band (Felten, 1977; Binggeli, Sandage & Tammann, 1988; Loveday et al., 1992). However since their invention and continued use in astronomy, it has been possible to measure the low redshift GLF in great detail in all visible bands (Brown et al., 2001; Blanton et al., 2003). Extensions of CCD technology have pushed these measurements into further areas of the electromagnetic spectrum such as IR detectors for measuring near-IR bands (Cole et al., 2001; Kochanek et al., 2001) which follow the shape of the GSMF more closely.

The GSMF is an important diagnostic when it comes to understanding the formation of the universe. It is one of the key tools used in checking the consistency of simulations with observations. In order to ensure that they are representative of the observed universe, simulations must be ‘tuned’ to reflect the currently accepted number densities of galaxies as a function of stellar mass within the simulated volume. **Tuning will often take the form of varying the efficiency of feedback mechanisms within the simulation as this is not a parameter which can naturally be derived from first principles.** While simulations are tuned to match the global GSMF, they can be tested using other distribution measurements such as the GSMF for different morphological types of galaxy (Kelvin et al., 2014b).

1.4.1 Schechter Function

The GSMF has been shown to be well fitted with a double Schechter function (Schechter, 1976), which can be described with a single value for the break mass (\mathcal{M}^*) (Baldry, Glazebrook & Driver, 2008; Pozzetti et al., 2010) and takes the form:

$$\phi_{\mathcal{M}}d\mathcal{M} = e^{-\mathcal{M}/\mathcal{M}^*} \left[\phi_1^* \left(\frac{\mathcal{M}}{\mathcal{M}^*} \right)^{\alpha_1} + \phi_2^* \left(\frac{\mathcal{M}}{\mathcal{M}^*} \right)^{\alpha_2} \right] \frac{d\mathcal{M}}{\mathcal{M}^*} \quad (1.1)$$

where $\phi_{\mathcal{M}}d\mathcal{M}$ is the number density of galaxies with mass between \mathcal{M} and $\mathcal{M} + d\mathcal{M}$, where α_1 and α_2 determine the shape of the curve, and ϕ_1^* and ϕ_2^* are normalisation constants to be applied to the fit. For low redshift populations of galaxies observations show that \mathcal{M}^* has a value between $10^{10.6}$ and $10^{11} M_{\odot}$.

The double Schechter Function is an expansion of the original Schechter Function with an extra additional term to account for a change in slope at low masses. Originally the form of the function was based on observations of only higher mass/luminosity systems and were not sensitive to the change in slope at low masses. The original Schechter function is a single power law with an exponential cutoff above L_* . The double Schechter function allows for the sum of two power laws with an exponential cutoff as before. A more negative α value in the second addition term, as in equation 1.1, means that the second power law will dominate over the first function at low masses.

There have been suggestions for why this is the form this distribution should take. The most revealing was that proposed by Peng et al. (2010). In their model, all star-forming (SF) galaxies have a near constant specific star-formation rate (SFR) which is modelled as a function of epoch. SF galaxies are then turned into passive galaxies through either mass quenching or environmental quenching where the probability of a galaxy becoming passive through mass quenching is proportional to its SFR. This means that high mass galaxies more naturally transition into passive galaxies than low mass galaxies. This process gives a double Schechter fit for passive galaxies, and a single Schechter fit for SF galaxies. The two functions have different power law slopes at the high mass end so that passive galaxies dominate here. It was shown by Baldry et al. (2012), using the GAMA data, that this model fits with the observations and leads to a double Schechter fit for the overall population.

1.4.2 Creating the GSMF

The GLF is binned and the value of each bin is determined as the sum of the values in the bin, these are defined as $1/V_{max}$ (Schmidt, 1968; Felten, 1977). V_{max} describes

the comoving volume slice over which the galaxy could be observed within the survey limits. Calculating $1/V_{max}$ then gives the fractional contribution of the galaxy to the overall number density over the survey area within the defined bin. To calculate the V_{max} value a well determined redshift is required, as the redshift is a good determination for the radial distance of an object from the observer and so this value can be used to determine a ‘luminosity distance’ (D_L , Hogg, 1999), in parsecs to the target. From this the distance modulus (DM) of the target object can be calculated using:

$$m - M = 5 \log_{10} \left(\frac{D_L}{10pc} \right) \quad (1.2)$$

where $m - M$ is the DM. With this calculated it is then possible to determine what the maximum DM would be for an individual object given the magnitude limit on the survey being used:

$$DM_{limit} = DM + m_s - m \quad (1.3)$$

where DM_{limit} is the maximum DM, DM is the distance modulus calculated from equation 1.2, m_s is the magnitude limit applied to the survey, and m is the apparent magnitude of the target object. With this calculated it is a simple task to reverse the processes above to find the maximum redshift (z_{max}) at which the target object could be observed within the survey’s magnitude limits. Where necessary equation 1.3 must be modified to account for the differential k -correction of the object, that is the difference between the actual k -correction applied to the galaxy and the k -correction which would be applied at the maximum detectable redshift for the system. This can then be used to calculate V_{max} for the target object:

$$V_{max} = \left(\frac{D_{L,limit}}{1 + z_{max}} \right)^3 \times \frac{1}{3} \times \Omega \quad (1.4)$$

where $D_{L,limit}$ is the calculated limit of the luminosity distance at the limit of the survey measurements, z_{max} is the maximum redshift clipped at the maximum survey redshift limit, and Ω is the solid angle of the survey being used.

However this method can lead to distortions of the GLF if there are large variations in the number density of galaxies versus redshift (Efstathiou, Ellis & Peterson, 1988; Cole, 2011). For instance if there is an overdensity in the lower redshift region of the survey where it will be more sensitive to low mass galaxies, then the contribution to the respective bin will be larger due to the higher number of galaxies. It is important, therefore, to be able to correct for these effects. The density corrected V_{max} , V'_{max} accounts for this change of density by correcting the amount each galaxy contributes to its respective bin. The importance of using this correction is shown well in Baldry et al. (2012). Using the GAMA data in the three equatorial regions of the sky it was shown how not taking into account the density change in these different environments creates three different GSMFs. Once a density correction is applied to the different regions it was shown how the GSMFs become more consistent with each other.

To calculate V'_{max} one must use:

$$V'_{max,i} = \frac{\rho_{ddp}(z_1; z_{max,i})}{\rho_{ddp}(z_1; z_2)} V_{max,i} \quad (1.5)$$

where $\rho_{ddp}(z_1; z_2)$ is the number density of a density defining population between z_1 and z_2 , the minimum and maximum redshifts of the survey region respectively. $z_{max,i}$ is the maximum redshift at which the object could be observed, and $V_{max,i}$ is the current V_{max} of the object before density correction. It is also necessary to compute correction values (C_i) which are based on a measure of completeness within the survey. This will have the effect of correcting for bins where the number of objects without measured redshifts is high.

This can then be used in place of the standard V_{max} to compute the number density per luminosity (or mass) bin in computing the GLF (or GSMF) using:

$$\phi_{\log L} = \frac{1}{\Delta \log L} \sum_i \frac{1}{V'_{max,i} C_i} \quad (1.6)$$

where C_i is the completeness correction factor applied to V'_{max} . The C_i values are

equal to the number of sources with measured redshifts divided by the total number of sources within a bin. Note the bins used to calculate the C_i are not the bins of the GSMF but are rather observed magnitude and/or colour, typically.

As mentioned above the GLF as measured in near-IR and visible bands follows the form of the GSMF closely, yet it is still necessary to estimate the stellar masses for the systems to measure an accurate GSMF. The estimate of the stellar masses can be done using a mass-to-light ratio from a calibrated relation (Bell & de Jong, 2001) or by using spectral fitting (Taylor et al., 2011), and either of these are known to be good methods to allow for the GSMF to be computed.

Users of stellar masses should bear in mind that there are a number of systematic uncertainties. It is necessary to assume a stellar initial mass function (IMF) and thus any error in that will result in an over or under estimate of the stellar masses. For the colour calibrated relation method, there will be scatter associated with assuming that the mass-to-light ratio can be unambiguously determined using one colour. Due to the high number of flux measurements needed to generate the best fit to template spectra to measure the masses of systems, spectral fitting will usually be more accurate. However the advantage of the colour method is transparency: its derivation from the photometry can be written down simply. In both cases one is relying on the accuracy of stellar population synthesis modelling which is especially challenging given galaxies are complex systems of different stellar populations, gas, and dust.

In Chapter 3 of this thesis the masses are generated through spectral fitting, these have been used unless there were serious errors within the output, as measured by the chi squared value of the fit. In these instances the fall back was to use the linear approximation as calculated by Taylor et al. (2011).

1.4.3 Low mass GSMF

The local GSMF has been measured accurately down to a mass of $M_* \approx 10^8 M_\odot$ by the Galaxy and Mass Assembly (GAMA) survey collaboration (Baldry et al., 2012).

Whilst the GLF has been measured down to lower luminosities, these have been in ‘focused’ environments such as the local group (Koposov et al., 2008) and clusters (Rines & Geller, 2008). It is more difficult to measure the GSMF down to these same luminosities, and so masses, in the field. It is however, crucial to fit to the low mass GSMF as at these masses, processes such as SNe feedback (Ferrara & Tolstoy, 2000) and photoionisation (Benson et al., 2002b) will have an effect on the formation of these galaxies. Using simulations it is possible to understand how prevalent these processes are in the early universe through tuning the processes and then fitting to the low mass GSMF.

There are estimates of the low mass GSMF currently given through simulations such as those of Guo (2011) who applied semi analytical models to dark matter only simulations from Springel et al. (2005), and Boylan-Kolchin et al. (2009) who simulated the GSMF to a limit of $10^6 M_{\odot}$, which shows the mass function continuing to rise to low masses. They do, however, caution that they see a higher fraction of passive galaxies in their simulations than is seen in observations. Although, currently, it is inferred the most common galaxies in the universe are low mass star forming galaxies, the difficulty in detecting passive dwarf galaxies in the field may be biasing those results. On the other hand studies have suggested that in fact passive dwarf galaxies do not form at all in the field (Geha et al., 2012), which would be inconsistent with the simulations

More recently high resolution hydrodynamical simulations such as the EAGLE project (Schaye et al., 2015), have been employed to better simulate how the currently accepted GSMF might have formed using a consistent treatment of baryons and dark matter. This has produced several interesting results, but most importantly for this work the team used the simulation to match the GSMF created within the simulation to the observed GSMF down to $10^8 M_{\odot}$, which is the current level at which GAMA has constrained the GSMF. EAGLE has also been used to look at the H I contents of some of the simulated galaxies to compare to observations (Crain et al., 2016). They found that most of the H I contained in galaxies had most likely gotten there through steady accretion of intergalactic, ionized gas and had very little provided through feedback

mechanisms within the galaxies themselves.

The problem of the missing fraction of dwarfs, as highlighted by the difference between the observed and simulated low mass GSMFs is known as the Sub-structure problem. There are several reasons postulated as to why there could be missing galaxies, such as reionization or supernova feedback, these are explored further in the next section.

1.5 Sub-structure Problem

There is an observed discrepancy between the number of low mass halos predicted by the CDM simulations and the number of observed low mass galaxies. This sub-structure problem can be characterised in two ways. The first is by the observed deficiency of the number of observed satellites, around the Milky Way in particular, compared to the number of sub-halos predicted by models (Moore et al., 1999). The second deals with the discrepancy between the predicted number of halos and observed galaxies on a cosmological scale. There has been work towards solving the first of these problems in the Local Group with the discovery of dSph galaxies around the Milky Way (Gilmore et al., 2007) and M31 (Martin et al., 2009).

The sub-structure problem for the field population however is still unsolved with a large under-density detected through the comparisons of CDM models and observations. This population of field dwarfs will probably comprise mostly dIrr type galaxies, however due to their intrinsic low surface brightness they are difficult to find and measure (Cross & Driver, 2002).

The GSMF has been measured accurately down to $\sim 10^8 M_\odot$ and cosmological surveys have endeavoured to measure the number density of galaxies with a lower mass. For instance the GAMA survey found a number density of galaxies of $\sim 0.02 \text{Mpc}^{-3} \text{dex}^{-1}$ in the mass range of $10^{6.5} \leq M_\odot \leq 10^7$ (this corresponds approximately to an absolute magnitude range of $-12 \leq M_r \leq -15$). However through cosmological simulations it has been suggested that this number density should be as high as $\sim 0.1 \text{Mpc}^{-3} \text{dex}^{-1}$

(Guo, 2011). These number densities will be different due to the surface brightness limits on the surveys used as the majority of the dwarf population, having intrinsically low surface brightness, will not be detected by these surveys. This means that the GSMF at masses below $10^8 M_{\odot}$ should be taken as a lower limit.

There are a number of reasons why the field population may be incomplete as effects on their evolution will have affected the way they formed and could even result in the removal of all luminous matter from in the halo. The following sections shall outline the possible evolutionary mechanisms which may have had an effect on the growth of these low mass systems.

1.5.1 Reionization

Background

Two important processes occurred in the early universe: recombination and reionization. Recombination is a process whereby the free electrons and nuclei present in the very early Universe cool enough so that they can ‘recombine’ to form neutral atoms. This is known to have happened at $z \sim 1100$ (Zeldovich, Kurt & Syunyaev, 1968). At $z \sim 50$ the first dark matter halos began to form which were, as discussed earlier, low mass halos. As they formed they would attract baryonic matter to coalesce at their centres forming gas clouds. The gas in these halos cooled through radiative cooling and would have begun to collapse forming the first stars and so the first galaxies and quasars. These objects were the cause of the reionization of the universe, as they are strong emitters of UV photons (Couchman & Rees, 1986). Through this photoionization of the immediate area surrounding these first luminous objects, the remaining neutral hydrogen and helium would become reionized. It is believed that this process started at around $z \sim 10$ and finished by $z \sim 6$ (Robertson et al., 2015). These boundaries have been determined through several indirect measures such as; the lack of Gunn-Peterson troughs¹ in the spectra of quasars (e.g. Fan, Carilli & Keat-

¹Troughs which appear in spectra in the presence of neutral hydrogen, characterised by the suppression of the spectra below Ly α emission (Gunn & Peterson, 1965)

ing, 2006; McGreer, Mesinger & D’Odorico, 2015), observations of CMB polarisation (Planck Collaboration et al., 2015), and the measurement of the temperature of the IGM (Bolton et al., 2012). Direct observations of star forming galaxies have not been made at high enough redshifts to fully test these hypotheses, but there are efforts to extend the redshift range deeper (Bouwens et al., 2015).

Effects on early structure formation

Early galaxies formed in two stages. The first of these stages was the mutual collapse of dark matter halos and baryonic matter, and the second was the collapse of only the baryonic matter, through radiative cooling, into the central potential of the DM halo (Benson et al., 2002a,b). It is the second stage which is most important for galaxy formation as it is at this point where the gas must become self gravitating so as to be able to collapse further into stars. As the UV background imparts energy into the gas then the number of particles which will be available for energy transfer is reduced, which means that effective cooling of the galaxy cannot take place. It is believed that the threshold for this effect would be a system with a virial temperature of $T_{vir} \sim 10^4 K$ as this is the temperature the Inter Galactic Medium (IGM) is heated to by the UV ionizing background (Barkana & Loeb, 2001). This significantly raised the mass at which baryons could collapse into galaxies, therefore a system with a virial temperature below this threshold will not be able to condense into a stable system thereby suppressing the formation (Rees, 1986; Efstathiou, 1992; Miralda-Escudé & Rees, 1998). From this it is therefore believed that for a low mass galaxy to have formed it must have done so before reionization took effect (Benson et al., 2002b).

This may explain why there is a discrepancy between the theoretical CDM models and the observed number density of galaxies in the local universe. There may still be the predicted number of DM halos, however reionization will have suppressed the star formation in the system to such a degree that the galaxy will not have formed stars, or that the galaxy have only formed stars slowly since the end of reionization, meaning that the known number of low mass galaxies would still be incomplete.

1.5.2 Supernova Feedback

When energy is released from a supernova the resulting winds will push gas away to form an empty pocket around where the star used to be. In a high mass galaxy such as the Milky Way this would not have too much of an effect on the galaxy other than to kick start some star formation in the immediate area of the explosion. In a low mass system, such as a dwarf galaxy, supernovae can impart high enough energies into the surrounding gas that it will suppress star formation within the system until the gas is able to cool. Ferrara & Tolstoy (2000) ran simulations to test this and found that if a galaxy had a mass $M_* \leq 5 \times 10^6 M_\odot$ then all of the gas in the system could be lost through these outflows, and that outflows could occur in galaxies with gas masses up to $\sim 10^9 M_\odot$. This shows the suppressive effect supernova feedback may have on the dwarf population of galaxies.

1.5.3 Warm Dark Matter

The Cosmic Microwave Background (CMB), has been observed to be homogeneous in nature, with only very small fluctuations in its temperature. It is thought that these variations in the CMB describe the large scale structure of the early Universe and would have expanded as the early Universe expanded and then collapsed into small dark matter halos, which would have been where the first matter collected to form the first stars and galaxies. This is a correct assessment for standard Λ CDM cosmology. However if there was a warm dark matter component in the early universe then these fluctuations would have been suppressed below a certain mass, dependent on the mass of the DM particles. However as stated in Kang, Macciò & Dutton (2013), by using warm dark matter (WDM) to match the observed number of low mass halos the slope is changed for the luminosity-rotational velocity relation (Tully-Fisher relation) and so no longer matches these well defined observations. Due to this effect within the simulations, of distorting the shape of such a well defined relation it is unlikely that WDM had any great effect on early structure formation.

1.6 Low Surface Brightness Galaxies

Low surface brightness galaxies (LSBGs) are a type of galaxy which is not well observed within the Universe. As the name suggests they are difficult to detect because of a physical characteristic which means the light emitted from the galaxy is diffuse, making detection difficult. The point at which a galaxy is classified as low surface brightness can be defined as $\mu_{\text{central,B}} \geq 22.0 \text{ mag arcsec}^{-2}$ (Impey, Burkholder & Sprayberry, 2001). Past surveys have always had issues with detection of these systems as they did not go to faint enough magnitudes or they covered too small an area to be able to find these galaxies effectively (Dalcanton et al., 1997). They have plagued results for decades and have contributed largely to the issues of lower than expected number density at low masses, as low mass galaxies are more likely to be LSBGs.

Several pieces of work have been carried out to classify the effect of missing low surface brightness galaxies within surveys. Disney & Phillipps (1983) showed that a surface brightness selection effect should be considered when conducting a large scale survey, as the volume over which galaxies can be detected is a function of their central surface brightness and absolute magnitudes. Cross & Driver (2002) were able to show that there is a strong dependency in the construction of the GLF on surface brightness, which could account for the differences seen between published values of the curves. Figure 1.1 shows how the completeness of LSBGs is poor compared to galaxies with higher surface brightnesses within the photometric survey results of SDSS (Blanton et al., 2005b). This was done by adding fake sources to the data and rerunning the pipelines. It is noted that this does not describe the physical limit of the SDSS imaging only the limit of the pipeline. This does show, however, that it is often not a priority for a large-survey pipeline to worry about the detection of LSBGs.

Figure 1.1 also shows that at low surface brightness the completeness is almost independent of apparent magnitude.

It is however important to complete the census of these galaxies as they will help to complete the low mass end of the GSMF which is important for galaxy formation theory (Cross & Driver, 2002). To accomplish this, different strategies must be used

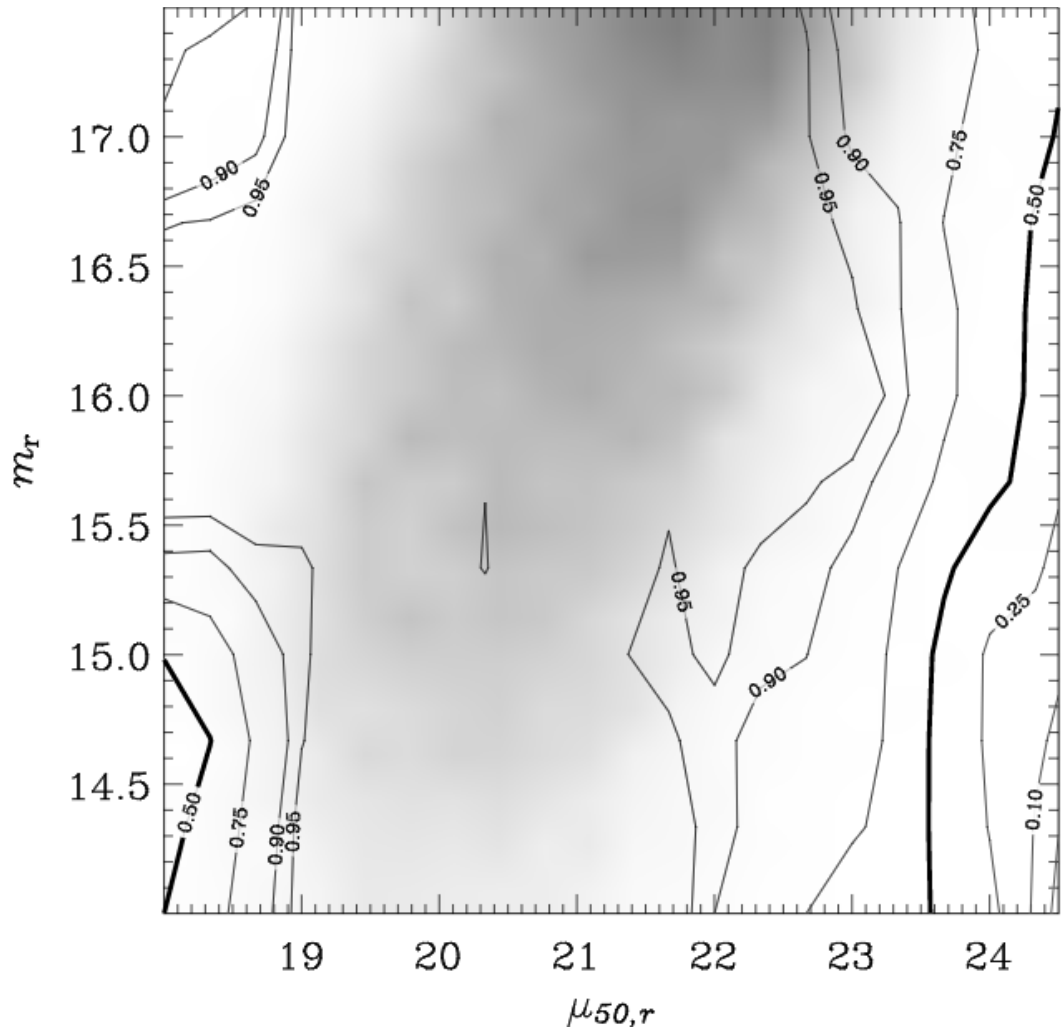


Figure 1.1: This plot is taken from Blanton et al. (2005b) Figure 2. It shows the completeness limits within the SDSS photometric sample. The right hand side of the plot shows, quite starkly, the difficulties in detecting low luminosity galaxies, as these are generally the ones with lowest surface brightness measurements.

for different environments.

1.6.1 Detection Methods

There are different environments to consider when searching for LSBGs and these environments can be broadly defined as: (i) nearby satellite galaxies within the Local Group; (ii) satellites in external groups and clusters; and (iii) field galaxies away from luminous galaxies and clusters, or within a random cosmological volume. The detection methods appropriate for each environment will be discussed in the following subsections.

Searches for galaxies in the Local Group

There are currently 100 known faint dwarf galaxies in the local group (McConnachie, 2012) and this number has been steadily increasing over the last decade (15 years ago only 11 were known). These galaxies became observable with the advent of such wide field surveys as the Sloan Digital Sky Survey, (SDSS, Gilmore et al., 2007; Irwin et al., 2007; Walsh, Jerjen & Willman, 2007; Belokurov et al., 2010; Balbinot et al., 2013), and the Pan-Andromeda Archaeological Survey, (PAndAS, Ibata et al., 2007; Martin et al., 2009; Richardson et al., 2011; Martin et al., 2013b).

The method utilised and described by Koposov et al. (2008) and Walsh, Willman & Jerjen (2009) to detect local LSBGs, is to identify stellar over-densities as compared to the Galactic foreground. To determine whether they are real dwarf spheroidal galaxies (dSph) or noise requires the fitting of theoretical stellar isochrones to the over-densities. These isochrones describe old, metal poor stellar populations and will be constructed to represent different distance moduli based on the colour-magnitude diagram (CMD) of the stars. With this knowledge it is then possible to determine the distance to the object. New surveys such as DES (Dark Energy Survey; Wester & Dark Energy Survey Collaboration, 2005) or PS1 3π survey (Pan-STARRS1; Chambers, 2005) are improving the census of local group galaxies further. Koposov et al. (2015) has recently utilised

the aforementioned method with data from DES, to discover 9 new LSBGs which can be considered part of the Local Group.

Searches for satellites and substructure in external groups and clusters

The satellite populations within clusters and around luminous galaxies have been hinted at in the data for many years (Shapley, 1938; Shapley & Paraskevopoulos, 1940). However, concerted efforts were not made to actively look for these satellites until the discovery of many more dwarf, low surface-brightness companions to the MW and M31 and further motivation came later with the identification of the substructure problem (Klypin et al., 1999; Moore et al., 1999). Searches for satellites in external systems cannot be based on star catalogues if the systems are too distant. Therefore, one is forced to search for flux from extended sources, which has the disadvantage that distances cannot be derived from CMD fitting. However, once candidate satellite galaxies are found there is a high probability that they do lie within the system, particularly for rich clusters (Ferguson & Binggeli, 1994, and references therein).

Arguably the most well-studied galaxy cluster is the Virgo cluster, mostly due to its proximity to our own galaxy. It has been the subject of numerous studies and surveys, in particular, the Virgo Cluster Catalogue (VCC) (Binggeli, Sandage & Tarenghi, 1984; Sandage & Binggeli, 1984; Binggeli, Sandage & Tammann, 1985; Sandage, Binggeli & Tammann, 1985a,b; Binggeli, Tammann & Sandage, 1987). This survey discovered ~ 1000 dwarf systems contained within the cluster characterised by their low mass, low surface brightness, and small size. The majority of these galaxies were classified as dwarf elliptical galaxies (Sandage & Binggeli, 1984). However, this survey had limitations as they could not probe below a central surface brightness of $\mu_B \sim 24 \text{ mag arcsec}^{-2}$ (Binggeli, Sandage & Tarenghi, 1984).

Here again, detection efficiency is limited by the depth of the survey being employed, necessitating surveys and instruments which can probe deeper magnitudes for detection. New surveys have been used to try and complete the survey of dwarf LSBGs within the Virgo cluster, such as the Next Generation Virgo Cluster Survey (NGVS;

Ferrarese et al., 2012). The data from this survey are deeper, and it thus has an effective surface brightness limit of $\mu_{\text{Re,g}} \sim 29 \text{ mag arcsec}^{-2}$ within one effective radius. Using these data Davies, Davies & Keenan (2015) were able to identify 303 new extended LSBGs associated with the cluster.

The Coma cluster is another cluster, like Virgo, which has been well studied and in recent years has seen deeper imaging than cluster surveys of the past. For instance, the HST/ACS Coma Cluster Survey (Carter et al., 2008) was able to probe a significant fraction of the cluster to a central surface brightness limit of $\mu_{\text{central,g}} \sim 25.8 \text{ mag arcsec}^{-2}$. The Coma cluster has also been explored to new depths; for instance, with the use of the Subaru telescope, Koda et al. (2015) were able to uncover ~ 1000 possible extended sources reaching effective surface brightnesses of $\mu_{\text{Re,R}} = 28 \text{ mag arcsec}^{-2}$.

We find a similar situation when considering satellites of luminous galaxies. Despite the predictions that substructure should exist around all galaxies of a certain size (Moore et al., 1999) most galaxies observed remain without detected satellites, despite deep imaging to try and uncover some of these systems (e.g., van Dokkum, 2005; Atkinson, Abraham & Ferguson, 2013). This problem is due in part to the effective surface brightness limits of these surveys which, despite advances in detector technology, are no better than $\sim 28 \text{ mag arcsec}^{-2}$ (e.g., van Dokkum, 2005; Tal et al., 2009; Martínez-Delgado et al., 2010; Atkinson, Abraham & Ferguson, 2013).

Whilst this highlights the current status of deep imaging it still may not be sufficient for the detection of the majority of low surface brightness objects around these systems. Simulations of tidal debris around both Milky Way type galaxies and elliptical galaxies have indicated that the majority of accreted stars in these systems may sit at levels $\mu_{\text{central,B}} \gtrsim 29 \text{ mag arcsec}^{-2}$ (Naab et al., 2007; Johnston et al., 2008a; Cooper et al., 2010). Therefore, to properly image these systems requires many hours of telescope time to probe the magnitude limits needed for detection, something which many large surveys do not offer.

To this end a new detector, the Dragonfly Array, has been constructed (Abraham &

van Dokkum, 2014) to look for LSBGs in both cluster and satellite environments. The first results of the Dragonfly telephoto array are impressive, imaging the structure of galaxy M101 down to a surface brightness of $\mu_{\text{central,g}} \sim 32 \text{ mag arcsec}^{-2}$ (van Dokkum, Abraham & Merritt, 2014). This search resulted in the discovery of 7 previously unknown LSBGs in the neighbourhood of the galaxy, with central surface brightness ranges of $\mu_{\text{central,g}} \sim 25.5 - 27.5 \text{ mag arcsec}^{-2}$ (Merritt, van Dokkum & Abraham, 2014). The Dragonfly Array (Abraham & van Dokkum, 2014) detector has also been deployed on observations of the Coma cluster, discovering a possible 47 new extended objects (van Dokkum et al., 2015).

Similarly a new survey has been commissioned, the dwarf galaxy survey with amateur telescopes (DGSAT; Javanmardi et al., 2016) which uses amateur telescopes in long exposures directed at large host galaxies. This has so far detected 11 previously unknown LSBGs ranging in effective surface brightness between $25 \lesssim \mu_{\text{R}_e} \lesssim 28.8$. With these and further advances in detector technology the number of known dwarfs around these systems is set to increase.

Searches for field galaxies

Field galaxies are considered to be central in the modern parlance of halo occupation theory. Unlike their satellite counterparts, which have a more complex and turbulent formation history, field galaxies form and evolve in a relatively isolated environment, and are expected to be the dominant galaxy type in a blind survey over a large cosmological volume. Despite processes such as supernova feedback (Ferrara & Tolstoy, 2000) and heating from the cosmic ionising background radiation (Hoeft et al., 2006), they will have a larger cool gas fraction and higher star formation rate than those dwarfs that are gravitationally bound to a larger system. Instead of being stripped away, most of their gas will have cooled back into the system (Rosenbaum et al., 2009). It is because of these factors that it is believed passive dwarf galaxies do not exist in the field (Geha et al., 2012).

Compared to the Local Group, where stars can be resolved, and around luminous

galaxies and in clusters, where deep imaging is more easily done and membership is more easily assigned, finding LSBGs in the field is more problematic. A large area of the sky needs to be covered for a statistically significant detection. This implies that a lower depth is obtained in the imaging compared with cluster surveys in order to obtain a cosmologically representative sample. In addition, redshifts need to be obtained for all candidate galaxies in order to assign distances.

There is currently a significant difference in the number density of low mass systems ($10^{6.5}M_{\odot} \leq M_{*} \leq 10^7M_{\odot}$) between observations and simulations. For instance Guo (2011), through the use of simulations, predicted a number density of $0.1 \text{ Mpc}^{-3} \text{ dex}^{-1}$. Currently the best observations put that number density lower, e.g. Baldry et al. (2012) with the galaxy and mass assembly (GAMA; Driver et al., 2009b) survey quoting a number of $\sim 0.02 \text{ Mpc}^{-3} \text{ dex}^{-1}$ within this mass range. Therefore, observations must push to deeper magnitudes, and lower masses, in order to test whether observational SB limits are the reason, or part of the reason, for the discrepancy.

One of the ways to detect these systems is to develop specialised algorithms to find low mass galaxies in processed images from deep wide angle surveys such as the Sloan Digital Sky Survey (SDSS, York et al., 2000). Work has been carried out on the SDSS data to check their suitability for finding LSBGs. It has been determined that due to its wide field and high fidelity imaging it is useful for searches in this area (Kniazev et al., 2004). Known galaxies can be masked out, meaning specialised algorithms can be applied to the images to search for the much fainter signals from the LSBGs which were not initially detected (Scaramella & Sabatini, 2009). James et al. (2015) used an archival search of the SDSS data to search for Leo P (Skillman et al., 2013) type morphologies² and were able to detect ~ 100 of these objects with embedded H II regions.

Another detection method is to use radio HI surveys, such as the Arecibo Legacy Fast ALFA survey (ALFALFA, Giovanelli et al., 2005). This survey has been used to look for HI which could be associated with undiscovered LSBGs. For instance

²Leo P is an extremely metal poor, diffuse galaxy discovered near to the Milky Way. James et al. (2015) used the morphology of this galaxy to detect others like it. Hence a Leo P galaxy morphology.

Trachternach et al. (2006) and Du et al. (2015) have found many hundreds of new low surface brightness galaxies based on their HI counterparts in these images, mostly in the field. Recently Sand et al. (2015) detected 5 new blue diffuse dwarf galaxies within 10 Mpc, associated with Ultra-compact High-Velocity Clouds, using a search of archival ALFALFA data. Another search by Tollerud et al. (2015), using a blind HI survey (GALFA-HI, Peek et al., 2011), was able to detect two more faint diffuse galaxies, again within 10 Mpc. These were identified from the survey data within a set of 22 possible detections.

With the release of further deep optical imaging from imagers such as OmegaCAM on the VST (Kuijken, 2011) and DeCAM on the 4m Blanco telescope, and with the advent of deeper all-sky surveys such as the Deep Investigation of Neutral Gas Origins (DINGO; Meyer, 2009) survey on the Square Kilometre Array (SKA, Carilli & Rawlings, 2004), and other surveys such as the Wide Area VISTA Extra-galactic Survey (WAVES, Driver et al., 2015), the numbers of these galaxies found in the field are set to increase.

Chapter 2

Searching for LSBGs in SDSS data

The galaxy stellar mass function (GSMF), is a fundamental tool used for describing the evolution of the universe and comparison with simulations. It describes the number density of galaxies as a function of their mass within a volume of the universe. The GAMA (Galaxy and Mass Assembly) survey team have accurately described the GSMF down to $M_* = 10^8 M_\odot$. The current incarnation, however, is incomplete at masses below this due to surface brightness limits (Baldry et al., 2012). It is therefore useful to carry out a search of the SDSS DR7 data within the GAMA fields. SDSS data have been chosen for this work as this survey has already demonstrated its suitability for finding low-SB systems (Kniazev et al., 2004).

The GAMA survey has made significant progress towards uncovering and classifying the dwarf population within its three main regions. For instance, work by Baldry et al. (2012) in plotting the GAMA GSMF, showed that the most common type of galaxy in the universe is star forming dwarf galaxies. Kelvin et al. (2014a,b) were able to characterise a new type of dwarf galaxy, the little blue spheroid. Mahajan et al. (2015) showed that classifying processes for dwarf galaxies currently only reflect observational differences rather than the physical differences between them such as the star formation rate (SFR) or specific star formation rate (sSFR). However, progress still needs to be made into the search for, and detection of, LSBGs within this survey to meaningfully work towards completing the census of galaxies within it.

There are, generally, several reasons for missing galaxies from surveys due to their LSB nature. Incorrect magnitudes could be measured for the object due to several causes such as too small an aperture being used or deblending of the galaxy. This can occur because the LSB nature of the system makes it difficult for a pipeline to properly discern where the galaxy truly ends as some of it may be disguised in the noise of the image. This is a particular problem for star forming (SF) LSBGs as small pockets of the galaxy can be ‘easily’ detected but the surrounding gas may not be resulting in possibly several ‘detections’ for one system. Of course another effect, linked to the previous, is that you could miss the system completely with no part of the system being above the threshold for detection. This can lead to significantly underestimating the true number of galaxies within the searched volume.

For a redshift survey, like GAMA for instance, a LSBG could be missed from the census because its spectra have too low a signal-to-noise (S/N) making getting a correct redshift measurement difficult for the system. This is likely to be less of an issue for SF LSBGs as the emission lines from the SF regions will likely have high S/N meaning an accurate redshift can be calculated. This all needs to be taken into account when accounting for the number density of LSBGs.

As described in §1.6.1, this search is complicated, and the method employed will depend on the type of data which is provided by the SDSS and the nature of the objects being searched for. The distance range desired for the detection of LSBGs in this work is between $\sim 10 - 100$ Mpc, which places them beyond the range of the local group and volume (McConnachie, 2012). Also due to the SDSS imaging being already extensively searched for objects, and containing only one ‘deep’ area located at stripe 82 (Adelman-McCarthy et al., 2006), outside the scope of the GAMA survey, a specialised detection algorithm was developed to detect LSBGs which have been made difficult to detect due to noise constraints.

This chapter will deal with the method for the creation and implementation of such a search algorithm for use on the SDSS imaging to search for LSBGs, with comparisons to other data from the VISTA Kilo-degree Infrared Galaxy Survey (VIKING, Edge et al., 2013). This is being used to confirm or deny a detection as the VIKING Z -band is ~ 1

magnitude deeper than SDSS r -band when compared to an average SED for a low redshift galaxy (Driver et al., 2012, Table 7).

2.1 Surveys

The work carried out in this chapter utilised SDSS gri imaging within the limits of the three GAMA equatorial regions, G09, G12, and G15. For confirmation that these detections are galaxies, further optical confirmation was required. As stated above this was carried out through the use of deep Z -band VIKING imaging data. The technical details of these surveys are described below.

2.1.1 GAMA

The GAMA survey is a wide field spectroscopic survey that was undertaken to study cosmology, galaxy structure and galaxy evolution at low redshift (Driver et al., 2009a,b, 2011). It is based mainly around redshifts of galaxies taken using the AAOmega spectrograph on the Anglo Australian Telescope (AAT; Sharp et al., 2006; Hopkins et al., 2013). The survey has covered 286 square degrees to a limiting magnitude of $r = 19.8$. AAOmega optical spectra have been obtained for 238 000 objects in five survey regions (G02, G09, G12, G15, and G23 which are fields centred at RA 2h, 9h, 12h, 14.5h, and 23h; Liske et al., 2015). Independent imaging has been compiled from several other surveys whose footprints fall on the GAMA regions, covering wavelengths from 1nm – 1m (?). This paper will primarily use data from the three equatorial regions G09, G12, and G15, due to coverage of these areas by SDSS and VIKING.

2.1.2 Sloan Digital Sky Survey (SDSS)

The Sloan Digital Sky Survey (SDSS) uses a 2.5 metre telescope, with a wide field of view, at the Apache Point Observatory in southern New Mexico (York et al., 2000). The survey started in 2000 with the goal of observing 10000 square degrees of high

latitude sky. The imaging was done using twenty-four 2048×2048 CCDs and five filters u , g , r , i and z (Fukugita et al., 1996). The survey completed its initial aims in 2009 and almost all of its imaging data were released in Data Release 7 (Abazajian et al., 2009).

The SDSS takes its images in ‘drift scan’ mode. An image is read out approximately every 54 seconds, as the sky moves across the detector. This creates long strips which line up in the scan direction and are subsequently processed through the SDSS PHOTO pipeline (Stoughton et al., 2002). These strips are then divided into fields along the scan direction for convenience of use.

The data used in this work are the corrected images stored under fpC extensions in the DR7 database. All information stored in the images is presented in counts, which can be converted into the AB magnitude system by applying equations supplied by SDSS. These images are supplemented by fpM files which contain the various masks for each filter. A code supplied by SDSS, READATLASIMAGES-V5_4_11, is used to extract the mask file desired by the user (Stoughton et al., 2002).

2.1.3 VISTA VIKING

The Visible and Infrared Survey Telescope for Astronomy (VISTA, Emerson & Sutherland 2010) is a 4.1 metre short focal length infrared optimised survey telescope. It is located on the NTT peak at Cerro Paranal in Chile. One of the surveys this telescope is carrying out is the VIKING survey. This survey covers 1500 deg^2 in the near infrared, specifically Z , Y , J , H and K bands.

We used the $J - K$ colour as a redshift check, and produced SEDs for the detected objects to check their suitability as LSBG candidates. The Z band was used as a check for the detections due to its improved depth of imaging over the SDSS bands.

2.2 Image Processing

The reduced SDSS images were processed in order to search for low-SB galaxies that had been missed by the initial SDSS reduction pipeline. The image processing can be separated into five distinct phases:

1. masking of image fields,
2. alignment of images,
3. weighting using expected SNR,
4. coadding of g , r , and i image fields,
5. smoothing of the final image products.

These processes are discussed in detail in the following paragraphs.

SDSS uses a drift scan mode to take images. This leads to long images spread across the sky with a width equivalent to the detector. For ease these images are split into ‘fields’ of 1489 pixels by 2048 pixels, equivalent to $\sim 590'' \times 810''$. The 6424 fields that were used for target selection were selected from the GAMA equatorial regions. An example of the image files taken from the SDSS is given in the top panel of Figure 4.2.

The images are first masked to remove high surface brightness objects which have been discovered within SDSS PHOTO (Stoughton et al., 2002). The mask files supplied by SDSS contain 10 different masks and are outlined in table 2.1. The 4th mask extension, which masks any pixel which is part of some object, was chosen for this project. This mask is used to remove all detected objects from the image files, including stars, galaxies, cosmic ray detections, and anomalous ‘objects’ within the image fields. Note this is a pixel-based mask rather than a mask based on polygons or ellipses around detected objects, as shown in the middle panel of Figure 4.2.

The data files taken from the SDSS for each field are not aligned with each other because the detectors from the different bands are not perfectly aligned in the cross-

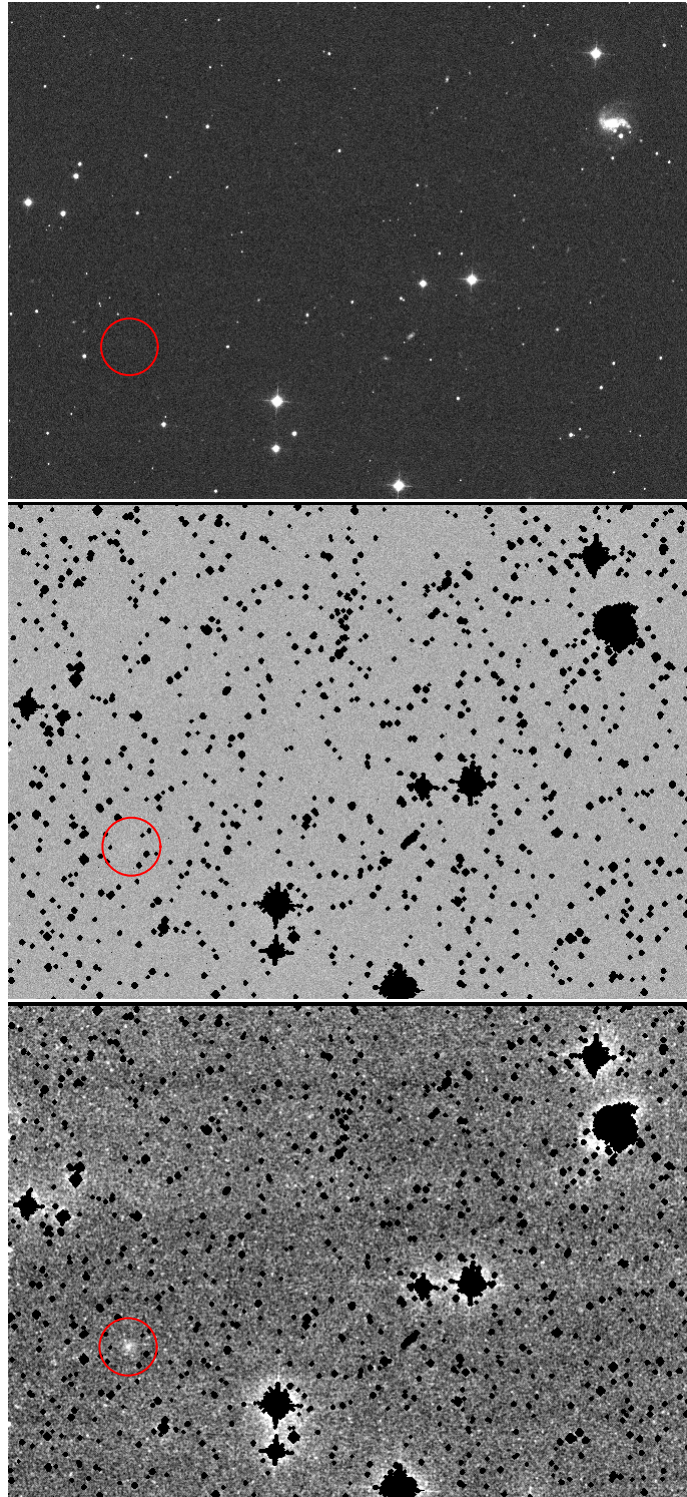


Figure 2.1: These image panels show how the image files are affected through the processes described in § 2.2. **The top panel** shows the initial image file of the field in question. This particular image is from run number 001458 filter g of camera column 5, field 0623. **The middle panel** is this same field after masking of known sources detected from the SDSS PHOTO pipeline. **The bottom panel** shows the field after smoothing and coadding has taken place. This brings out the low surface brightness features around the brighter detected objects within the field and gives a good representation of the challenges faced when trying to detect LSBGs in the field. The red circle highlights the point at which an undetected LSBG becomes clearly visible within this field after processing. The object is identified in the catalogue as LSB15283.

Table 2.1: fpM File extensions and descriptions supplied by SDSS PHOTO. Extension 4 was used in this work as it masks out all detected objects in the fields, whilst the other masks only cover selected objects such as cosmic rays or saturated pixels.

Extension Number	Extension Name	Description
1	S_MASK_INTERP = 0	pixel's value has been interpolated
2	S_MASK_SATUR	pixel is/was saturated
3	S_MASK_NOTCHECKED	pixel was NOT examined for an object
4	S_MASK_OBJECT	pixel is part of some object
5	S_MASK_BRIGHTOBJECT	pixel is part of bright object
6	S_MASK_BINOBJECT	pixel is part of binned object
7	S_MASK_CATOBJECT	pixel is part of a cataloged object
8	S_MASK_SUBTRACTED	model has been subtracted from pixel
9	S_MASK_GHOST	pixel is part of a ghost
10	S_MASK_CR	pixel is part of a cosmic ray

scan direction. The scan direction is in RA and the cross-scan direction is DEC. This means that the images can be misaligned, relative to the r -band, by up to 16 pixels difference ($\approx 6.4''$) in the g -band, and 5 pixels ($\approx 2''$) in the i band. Figure 2.2 shows these misalignments relative to the r -band.

The images were aligned using a geometrical translation with the r -band coordinates as a reference. The g and i band images are moved on to the central pixel coordinates of the r -band images. Once the alignment is complete all images are aligned to within one pixel ($< 0.4''$). This difference is not significant enough to be of concern because we are searching for significantly extended sources. Once aligned the images can be coadded prior to smoothing.

As mentioned in the above sections, LSBGs are diffuse in nature to the extent that their total integrated flux falls below the sky level for observations, so it is important to maximize the expected SNR in the images, through weighting the images and coadding the results. The following steps will describe this process for low mass, star forming (SF) dwarf galaxies. The images are to be weighted towards these objects as, for the limits probed, SF galaxies dominate in the field (Geha et al., 2012). In the long term it is a more realistic aim to determine if there is a turnover in the mass function of SF galaxies.

The weighting is applied using the typical $g-r$ and $r-i$ colour for the GAMA dwarf galaxies as shown in Figure 2.3. The galaxy masses used in determining the weights for each image field were calculated using the method outlined in Taylor et al. (2011). Only objects of $10^6 M_{\odot} \leq M_{*} \leq 10^{7.5} M_{\odot}$ and $z \geq 0.002$ are chosen from the catalogue. The redshift limit is applied to the data to remove any mis-classified stars; the remaining galaxies can then be used to calibrate the weights to be applied to the images. The ranges for the final weights are shown in Table 2.2, and are a result of the different extinction and sky-noise conditions on the nights on which the respective fields were observed.

To calculate these weights the equations supplied by SDSS can be rearranged to calculate the counts of the objects for each filter. This gives an expected signal value which

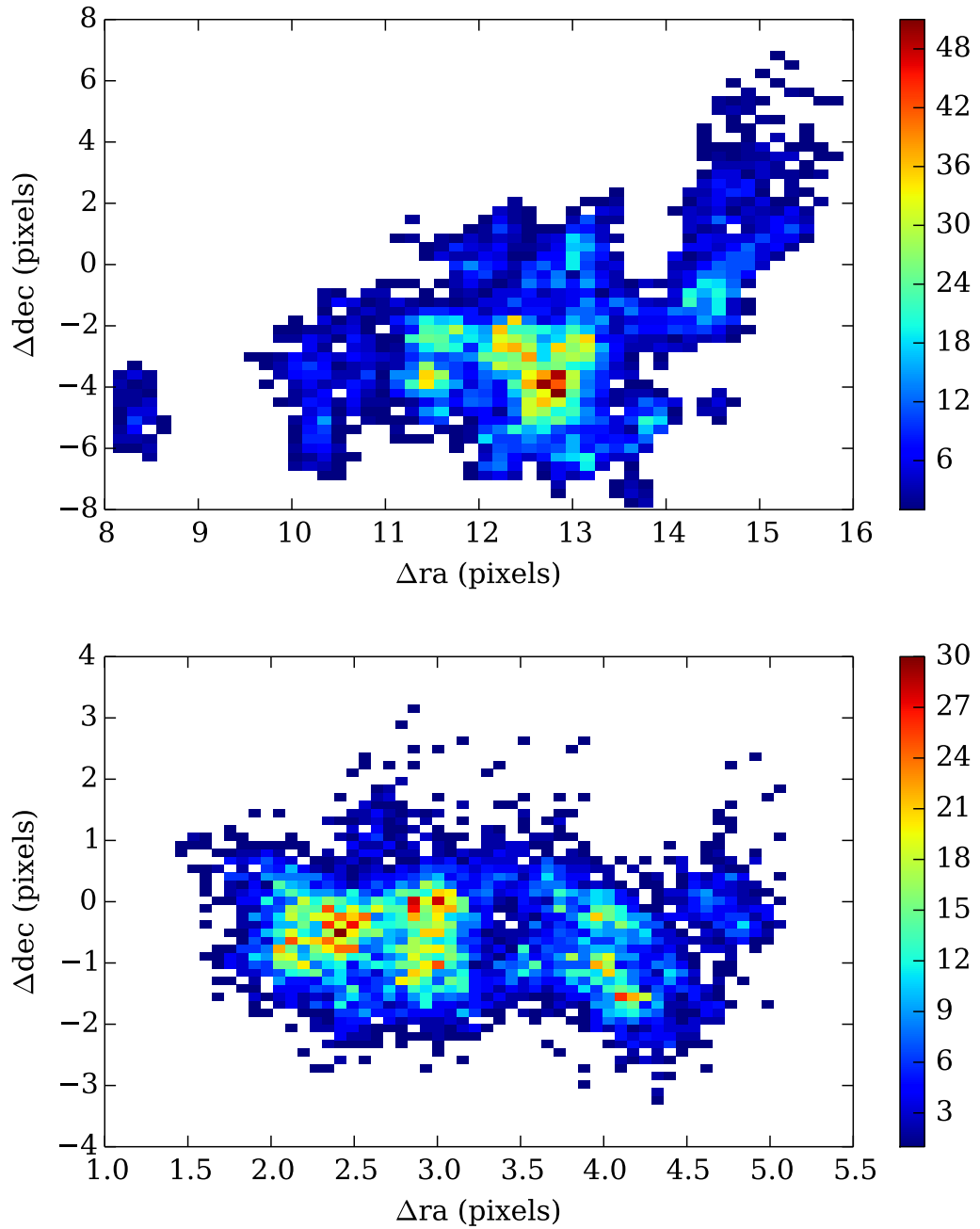


Figure 2.2: 2D histograms displaying the difference in locations between the central coordinates of the SDSS images. **The top panel** is the difference between g and r images. **The bottom panel** is the difference between r and i images. At all times r was used as the reference frame between the three images.

can be used to calculate the weighting for each filter in each field. The SNR weighting is calculated using the equation:

$$\omega_x = \frac{S_x \sigma_g^2}{S_g \sigma_x^2} \quad (2.1)$$

where ω_x is the weighting factor to be applied to image x , and S_x is the expected signal obtained from the image x expressed in counts for a typical star-forming dwarf galaxy. This is determined using Figure 2.3 to calculate the median values of the $g - r$ (0.233) and $r - i$ (0.154) colours for the population and an i -band magnitude of 19 mag (this is an arbitrary value), which gives the magnitudes stated in Table 2.2. σ_x refers to the standard deviation in image x , determined from the background of the image after masking. As the g -band fields have been used as the reference fields for calculating the weightings to be applied to the data, the g -band weighting value is always 1. Figure 4.2 shows how the image changes after the masking, weighting and coadding process.

The final step is to smooth the images, which will further improve the SNR. SDSS use a maximum 4×4 binning kernel for detection purposes, meaning 16 pixels worth of information are binned onto one pixel. Here, we use a circular kernel (a matrix of ones and zeros defining the region to be convolved) of diameter 7 pixels ($\approx 3''$). This value is chosen as at the larger distances of interest, ~ 100 Mpc, we expect objects of only a few arcseconds on the sky (Impey & Bothun, 1997).

The bottom panel of Figure 4.2 shows the effect the smoothing has on the image. Whilst the smoothing increases the SNR in the image it also reduces the spatial scales which can be detected. This is not such a large problem for this study as it is not necessary to discern small structure in detected LSBGs. The improvement in the detection limit, at a SNR = 5, can be estimated and compared with the original r -band limit. The SDSS r -band, with 4×4 binning, had a calculated limit of ~ 23.7 mag arcsec $^{-2}$, through coadding and smoothing a 1 mag arcsec $^{-2}$ improvement is achieved. There are two aspects to this: using a kernel of 37 pixels resulting in $\sqrt{\frac{37}{16}}$ improvement in flux limit, and coadding of $g - r - i$ resulting in $\sqrt{2.7}$ improvement in flux limit for fiducial SF galaxies. This will mean LSBGs will have been made visible which were

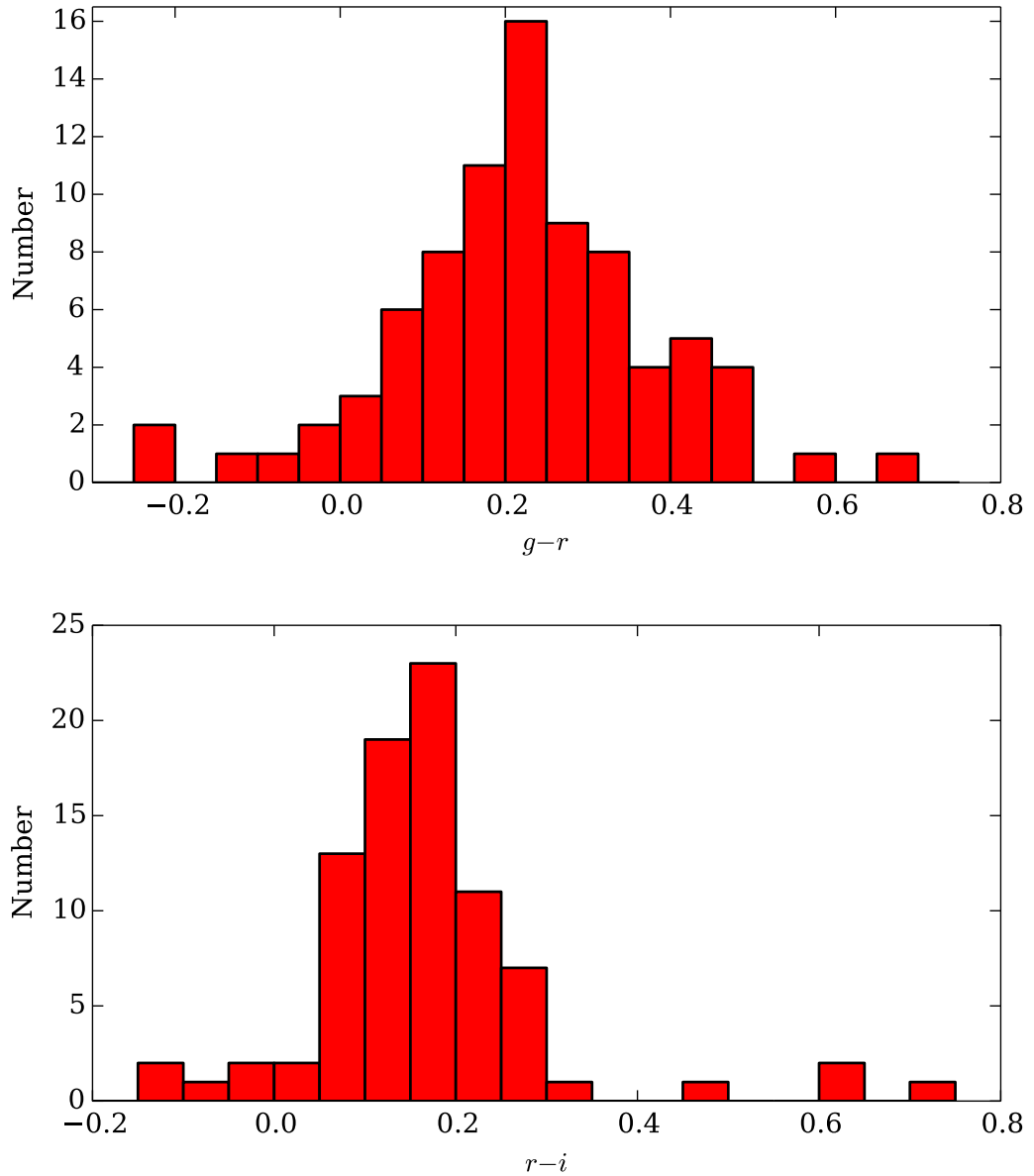


Figure 2.3: **Top panel:** GAMA dwarf galaxy numbers as a function of $g - r$ colour. This distribution gives a median value for the colour of 0.233. **Bottom panel:** The same population as a function of $r - i$ colour, the median of this distribution being 0.154. The galaxies used for these plots fall in the stellar mass range $10^6 M_{\odot} \leq M_* \leq 10^{7.5} M_{\odot}$ and $z \geq 0.002$. These median values are used to calculate the equivalent magnitude in each band.

Filter	m	Counts	σ	Weights (ω)
g	19.387	4283 - 5148	4.37 - 6.55	1
r	19.154	4169 - 4770	5.29 - 6.41	0.558 - 0.921
i	19	3245 - 4028	6.18 - 8.01	0.303 - 0.505

Table 2.2: The filter, apparent magnitude (m), the range of signals calculated for the different images (Counts), noise (σ), and the range of weightings (ω) to be applied to the images. The counts are calculated using an *i*-band magnitude of 19 mag, and are included to show the spread in counts across the images due to different conditions based on the night the image was taken.

not before.

Now that the *g*, *r*, and *i* bands for each field have been masked, weighted, coadded, and smoothed, using a larger kernel than was used by the PHOTO pipeline, there is increased sensitivity in the images for the discovery of field dwarf LSBGs than SDSS was able to achieve. The next step is to develop an algorithm which can be used to detect these hitherto undetected galaxies.

2.3 Detection Algorithm

To detect the galaxies it is important to understand their angular size on the sky within the range of distances that are being investigated, this range being $\sim 10 - 100$ Mpc. LSBGs have an expected scale length (R_e) of 1 - 2 kpc (Impey & Bothun, 1997). The equation;

$$\Theta_{50} = A \times \left(\frac{d_{50}}{D} \right) \quad (2.2)$$

where Θ_{50} is the radius in arcseconds that will be viewed on the sky, A is the constant 206265 used to convert between radians and arcseconds, d_{50} is the radius of the galaxy in Mpc and, D is the distance to the galaxy in Mpc. Assuming the scale and distance parameters given above a range of observed radii can be calculated of between $2'' \lesssim R_{e,obs} \lesssim 40''$ for any objects falling within the given distance range. With this in mind a detection algorithm can be developed and constraints can be applied to develop a

final list of detections to be searched through for LSBGs.

There are several distinct parts within the detection algorithm created to search the images. First is the detection of all pixels in the smoothed images whose value falls above a set SNR threshold. They are then grouped together based on their proximity to one another to form extended sources. This process however returns too many objects as many of the initial detections are emission from the edges of luminous objects, diffraction spikes, or noise. To remove these false detections, constraints, such as proximity to luminous objects, and image quality, are applied to the initial list of objects. Finally the remaining candidates are visually inspected.

For the analysis we adopt 5σ above the background of each smoothed image as the detection threshold for a pixel. Note that in the unsmoothed images SNR per pixel will be less than 5. In the smoothed image, pixels with an $\text{SNR} > 5$ are grouped into ‘candidate’ detections. For this, the COYOTES IDL library¹ is used. This library contains a programme for grouping pixels together within an image once a mask of these pixels is supplied to the code. Modifications were made to the code `BLOB_ANALYZER...DEFINE` to output the locations of the pixels contained within each candidate. The grouping of the pixels is based on adjacency to one another. For pixels to be grouped they must be touching in any direction, it is therefore possible to have a detected pixel which is not grouped with other detected pixels at this stage. A single isolated detected pixel is still likely to represent an $\sim 3''$ source because of the smoothing scale.

This returned $\sim 1\,000\,000$ potential detections. As can be seen from the bottom panel of Figure 4.2, most of the low-SB light detected is just the excess light around bright stars and galaxies. In some fields there are also other types of artefacts. The list of sources therefore needs to be cleaned to remove these artefacts and the light excess, by applying a set of constraints to the detections list. These constraints include:

1. proximity to more luminous objects.
2. anomalously high detection rates per field.

¹downloadable from <http://www.idlcoyote.com>

3. proximity to other low-SB detections.

The way these constraints are applied, and the reasons for applying them, will be discussed in the following paragraphs.

As can be seen from a comparison between the middle and bottom panels of Figure 4.2, the smoothing process pulls the low surface brightness emission out from around the edges of bright objects such as stars. The code identifies this emission as a source, therefore false detections must be tested for and removed. To carry out this test, two apertures of radius 50 and 100 pixels ($\sim 20''$ and $40''$ respectively) were placed over all candidate detections. The percentage of pixels found in the aperture which had been masked was recorded for each detection. The top panel of Figure 2.4 shows the percentage of masked pixels found within these apertures as a function of the number of candidates with that percentage, and the lower panel of Figure 2.4 is a histogram of the same information but produced from randomly placed apertures, 1000 apertures each of 50 (N_{50}) and 100 (N_{100}) pixel radius per field.

As can be seen by a comparison between the two plots there is a peak of detections occurring away from large objects. However the second peak within the top panel of Figure 2.4 shows the increase in detections as you approach larger objects, and the fact that there is a large amount of low-SB emission which is not masked out by the SDSS PHOTO pipeline. The parameters used for rejection based on the percentage of masked pixels are $N_{50} > 15\%$ AND $N_{100} > 15\%$. These cuts left the detection algorithm with 84% of searchable sky from the survey data.

Figure 2.5 gives some examples of objects which were not removed by the masked-pixel checks carried out above, and which need to be dealt with as separate cases. The first of these are fields containing very extended wings of ultra-bright objects, making the detection of LSBGs difficult as it produces a large number of erroneous LSBG detections within the images which need to be excluded. Therefore, the constraint decided on was to reject all fields with more than 100 detections within it, which affects only 22 fields out of 6424. As this was a small number of fields they were visually checked, to ensure nothing was rejected that should not have been.

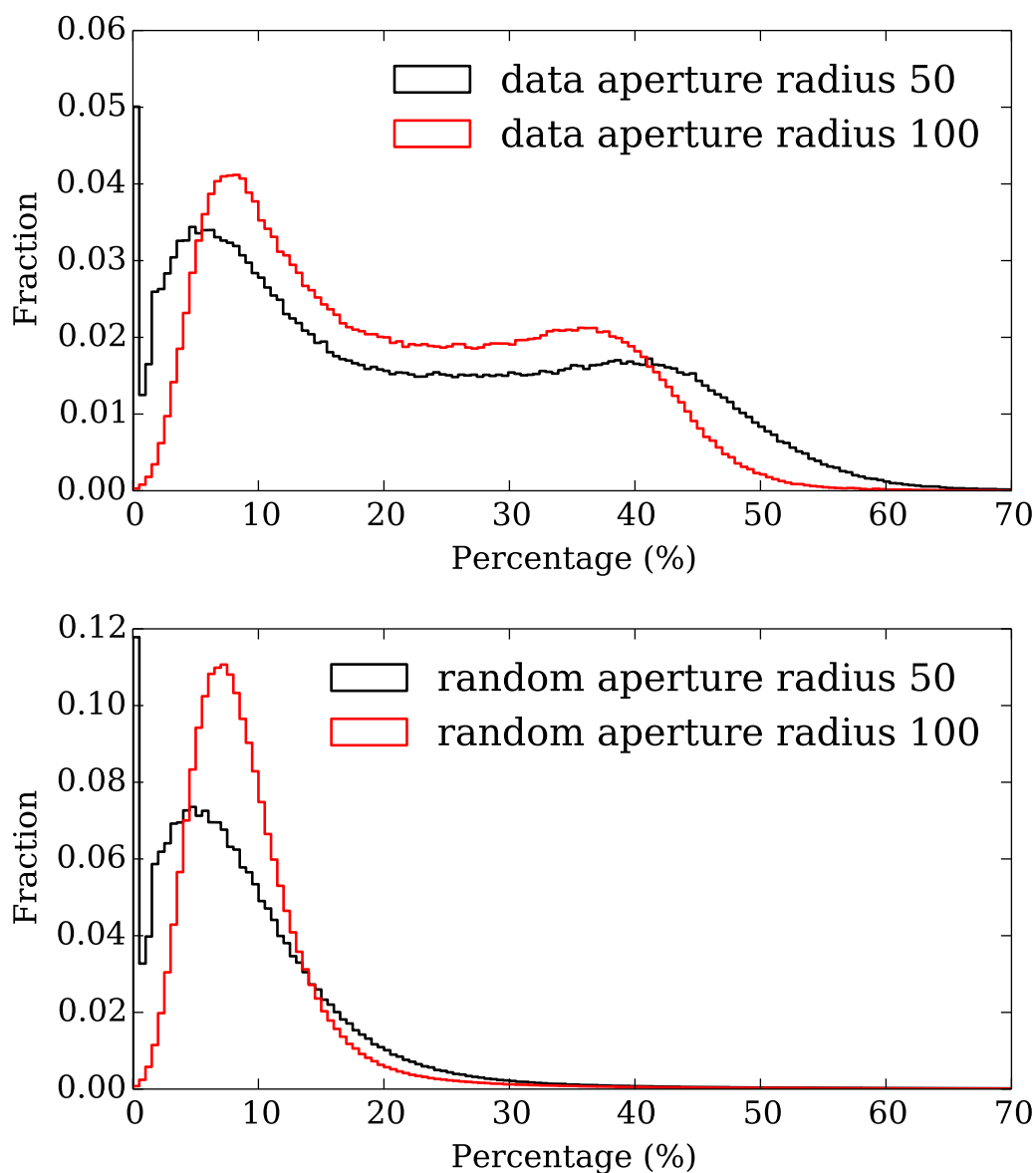


Figure 2.4: The number of masked pixels within a fixed radius is used as a metric to determine whether a detection should be removed. **The top panel** is a histogram of the percentage of masked pixels within the two aperture sizes around each detection given by the detection code. **The bottom panel** shows the distribution found when the apertures were placed randomly across all images. There is an obvious rise in the number of detections with a high number of masked pixels compared to randomly placing the apertures. This is caused by low-surface brightness emission from around brighter objects. Therefore, all objects falling within this second peak can be rejected.

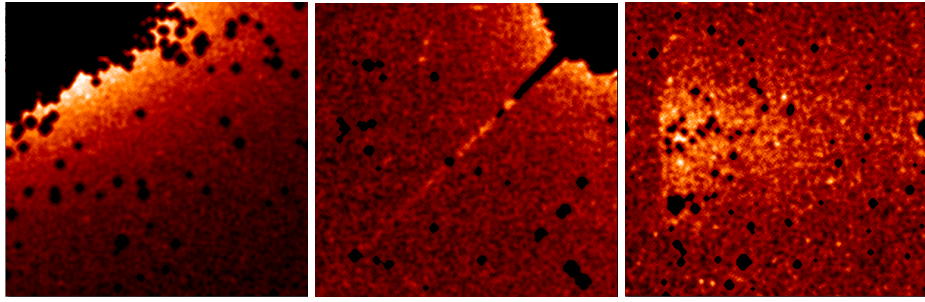


Figure 2.5: A small selection of the problem detections which were able to make it through to the final visual inspection. **The left panel** shows the faint wings of the light distribution of a large galaxy. The emission from the galaxy is well above the level needed to cause a detection and parts of it fall far enough away in the image that it is not masked. **The middle panel** shows a diffraction spike; again the fainter areas of the spike are not masked. **The right panel** shows an artefact from a large star in a neighbouring field, giving a distinctive flat feature parallel to the edge of the image.

A further issue is the detection of scattered light from bright stars which are not in the field where the detection is found but rather in an adjacent field. An example of this is in the right-hand image of Figure 2.5. This shows that parts of the artefact have been detected by the SDSS PHOTO pipeline with the effect of breaking the object up into several smaller detections. In order to try to remove these objects, a constraint is applied to the images whereby all detections which have more than 5 objects within a radius of $120''$ are rejected. A random sample of these objects is visually inspected to ensure that statistically only incorrect detections are removed from the catalogue.

One of the main reasons for conducting this study is to check the completeness of the GAMA survey, which means that galaxies with $r \leq 19.8$ mag are of most interest. To comply with this limit we cut the detections at a magnitude of 21.3 mag within the masked r-band images (1.5 mag deeper than the GAMA sample) and reject anything fainter than this limit. However, some of the detections are, in some cases, only 1 pixel, which is not unexpected as the LSB nature of these systems may lead to only one smoothed pixel of a larger system having a value above the detection threshold of $\text{SNR} > 5$. Two apertures of diameter $10''$ and $15''$ are placed over the objects and the number of counts measured in both in the unsmoothed images. As long as the measured flux is more than the required limit in one of the apertures then the object is allowed through to the final stage of analysis, and all others are rejected. Note that

these apertures were not used to measure the final magnitudes of the sources but as a way to obtain candidate large LSBGs. However due to the size of the apertures at this stage, sky errors could affect the magnitude using these large apertures.

This reduces the number of candidates to ≈ 5000 detections. These needed one final visual check as we expected there to be a proportion of detections which could be ruled out. The detections are given an integer quality ranking from 0 to 2, where 0 means a non-detection i.e. a diffraction spike or other noise, 1 means a possible detection i.e. small object in the smoothed images, no obvious extended structure, and 2 means a definite detection i.e. obvious extended object which has not been masked by SDSS. The number of possible and definite detections after this process was reduced to ≈ 600 detections. All of the removed objects are artefacts like those depicted in Figure 2.5.

The list of 600 positions is finally, visually checked against the same positions in the VIKING Z band data, as this imaging is deeper in magnitude than SDSS and so any detections which are real will also appear in the VIKING data. This final check, along with combining detections of the same object, reduces the final number of catalogued galaxies to 343. Figure 2.6 shows examples of images which were visually checked and proven to be real. Most of these objects were initially determined to have a quality ranking of 1, but on comparison to VIKING Z -band data were confirmed.

As a comparison to deeper imaging figure 2.7 shows how the r -band and Z -band magnitudes of the 343 detected LSBGs compare. These were measured from the SDSS and VIKING imaging using the coordinates determined for the galaxies from the smoothed SDSS images.

2.4 Results

2.4.1 Spatial Distribution

The distribution of large scale structure has been consistently shown to fall into filamentary structures within a Λ CDM universe, in both simulation and through obser-

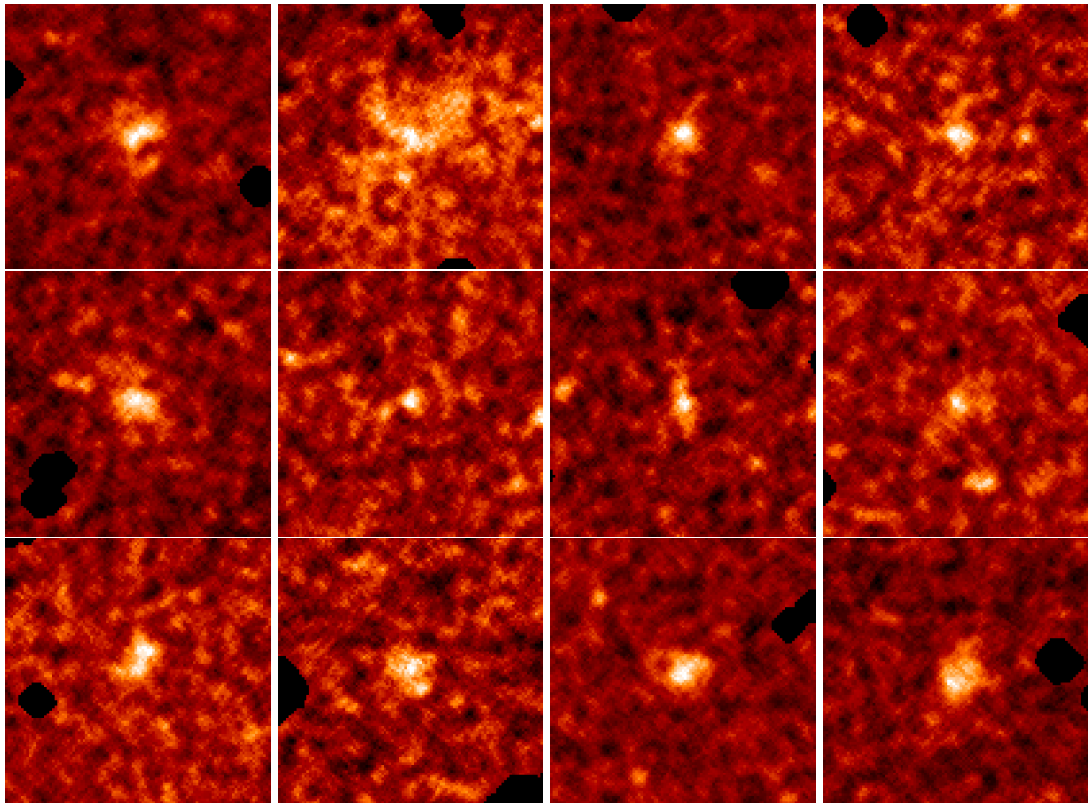


Figure 2.6: Each panel represents a candidate detection from the coadded, masked, smoothed images created from the SDSS g , r , and i bands. Each candidate is positioned at the centre of the panel. Each of these detections was confirmed by the deeper VIKING observations. Each image is $\sim 35'' \times 35''$.

vation (Press & Schechter, 1974; Bahcall, 1988; Alpaslan et al., 2014). It would be expected, therefore, that there would be some clustering of detections even at these low masses. As can be seen from Figure 2.8, the new detections do appear to fall in the same locations as some of these large scale structures. However, this is stated cautiously as without truly accurate redshift information for these objects, it is not possible to state with certainty that they are connected to these structures. It could be possible to define the redshifts of the objects using a clustering technique whereby the detected objects are compared with different redshift slices of the GAMA data. A method such as this has been developed by Morrison et al. (2016) into a sophisticated piece of software, utilising machine learning techniques, which has seen impressive results when using the algorithm on large data sets such as GAMA and KiDS. However when using the method on the objects detected here it shows that the number of detections is too low and causes unreliable results. Due to this it is advised to wait until the objects

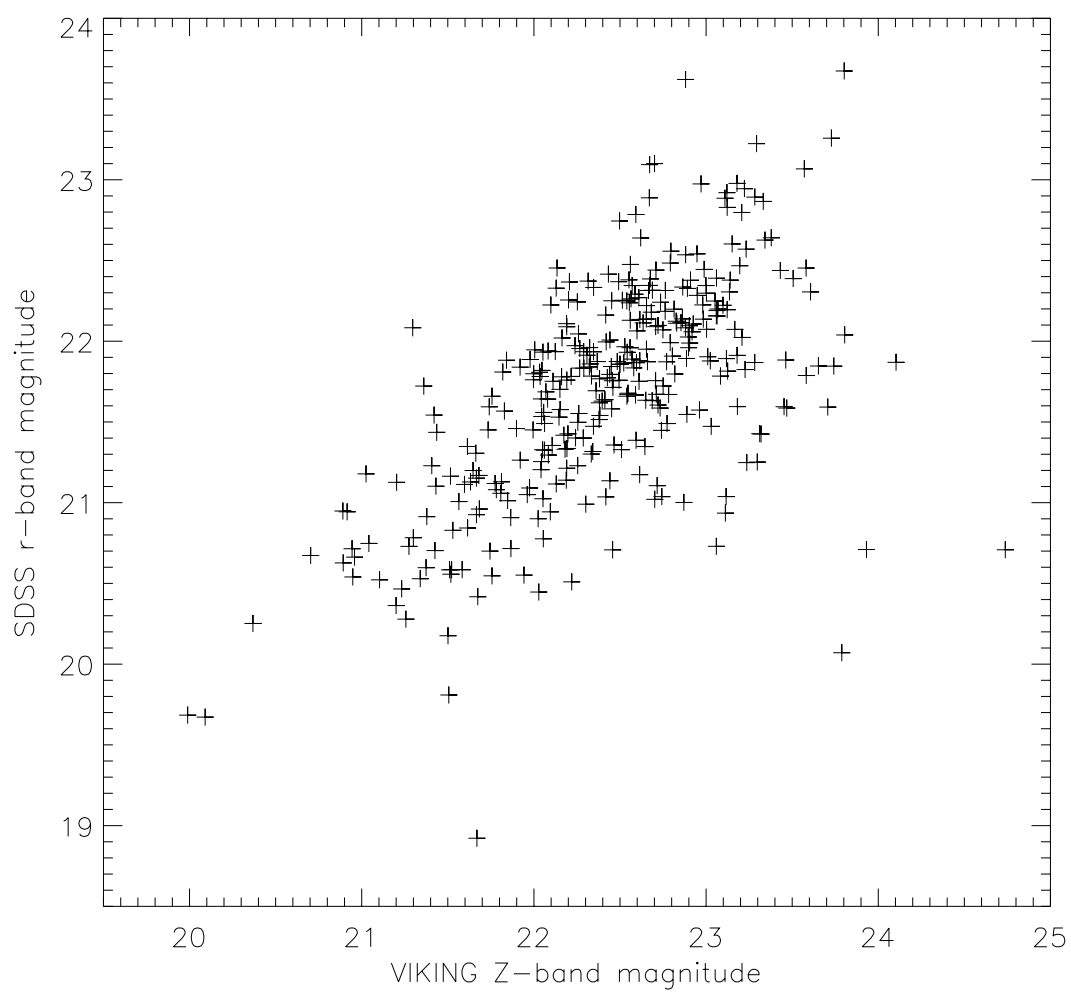


Figure 2.7: A comparison between the SDSS r -band and VIKING Z -band magnitudes for LSBG galaxies in this survey.

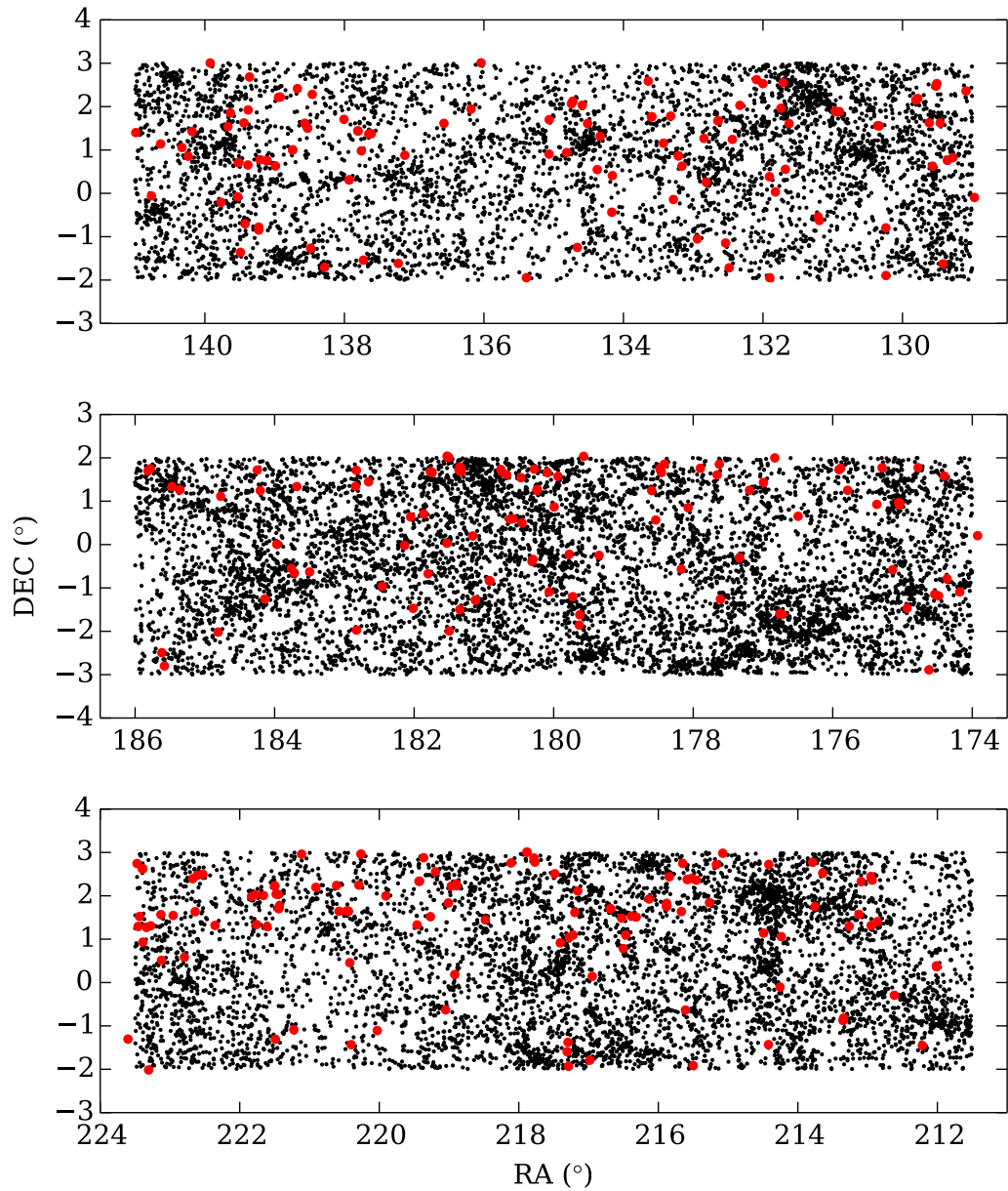


Figure 2.8: Red points define the sky positions of the 343 objects across all fields, G09, G12, and G15 (top, middle, bottom respectively). Black points represent the positions of all confirmed galaxies in the GAMA survey which have known redshifts less than 0.1.

can have accurate spectral measurements made to determine the true redshifts of the objects.

2.4.2 Magnitudes

The magnitudes were calculated using a specially designed wrapper for Source Extractor (SE) called IOTA (Driver et al., 2016). It was first deployed on the main GAMA survey to carry out the SDSS r -band detection on all fields. It works by creating a 1001×1001 pixel cutout area from the detection image centred on coordinates of a detected object. SExtractor is then run over this image and all detections within the image area are measured against the original central coordinate, if a detection falls within $5''$ of the central pixel then a measurement is taken. The aperture created is then applied in the same location across all imaging which is required for the analysis to be carried out. However, due to the smaller sizes of the potential detected candidates a smaller cutout area is employed here to measure the flux of these systems. The VIKING Z -band is used as the reference band as all objects are detected in this imaging.

The SEDs of the detections are constructed with fluxes from both the SDSS and VIKING, giving effectively 10 bands of photometry. Magnitudes are calculated using two apertures, a fixed aperture with a $5''$ diameter, and an auto aperture. Auto apertures are defined as a flexible elliptical aperture, meaning the aperture adapts to the size and shape of source (Kron, 1980), and measures all flux within it. The auto aperture was used as default and compared with the fixed aperture magnitudes using:

$$\Delta_{mag} = \text{auto magnitude} - \text{fixed aperture magnitude} \quad (2.3)$$

and are found to be mostly consistent as shown in Figure 2.9. This meant that the auto magnitudes could be used as a standard for calculating the magnitude. The auto magnitudes tend to be brighter when there is a disparity between the two methods. As stated in the caption of figure 2.9, you don't expect them to agree for sources larger than the fixed aperture so it is not an extreme difference but they should be

checked, and they are all fine in general. Checks were also carried out for those objects which showed the aperture magnitude was brighter ($\Delta_{mag} \geq 0.1$) as this is a less common occurrence. Any objects which are found to be in regions of disrupted imaging are given a magnitude measured using the fixed aperture as the auto aperture will be unreliable, which means that those objects will not have a measured surface brightness in the table. For this work a half light radius was used, meaning the radius contains half the flux of the auto aperture. The auto aperture is assumed to represent close to total flux. Based on these final results, conclusions can be drawn. In total 5 objects used the fixed aperture and 336 used the auto aperture, 2 objects could not be detected in Z-band imaging using IOTA and so had no magnitude measurements.

The measured SDSS r -band magnitudes show that these objects are too faint to be included in the GAMA catalogues, and therefore will not have an effect on the low mass end of the GSMF. Further study is needed to push the imaging to fainter surface brightnesses to further test this.

Upon measuring the surface brightnesses of the systems they were discovered to all be $\mu_r \geq 23.7 \text{ mag arcsec}^{-2}$. These measurements were made using the auto apertures created in SExtractor for each object. This gives a consistent measurement of the objects and will have created a good fit to all of the systems discovered in the survey

For this study we require the SDSS r -band, for comparison with the reference GAMA passband and the VISTA VIKING Z -band, as our deepest band. We also require SDSS g and i and VIKING J and K for colour comparison. Note that even though the sources were not detected in the individual g , r , & i bands, flux measurements can be made using the apertures defined using the Z -band.

2.4.3 Colour Distribution

Redshifts have not yet been determined spectroscopically for these galaxies. However, it can be assumed from the faint magnitudes and surface brightnesses of these objects that they are likely to be at low redshift. A good proxy for determining this is to plot a

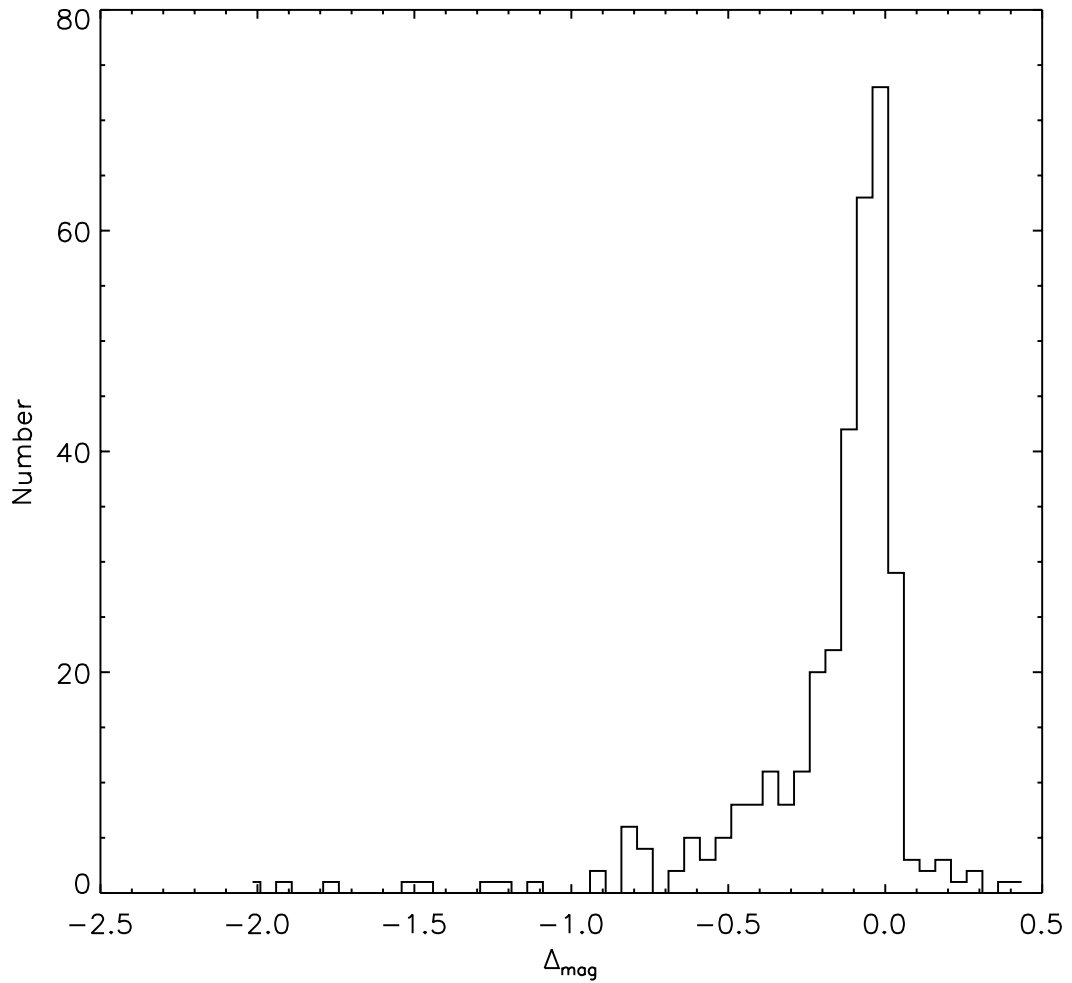


Figure 2.9: Comparing the auto magnitudes with the aperture magnitudes (Δ_{mag}) for the SDSS LSBG catalogue. There is clear consistency with the apertures for the majority of the detected galaxies. Where there is disparity in the wings of the distribution a visual check was carried out on the image quality and those galaxies in noisy image fields in the VIKING Z -band are measured with the fixed aperture rather than the auto aperture.

$J-K$ vs $g-i$ colour-colour plot. As shown in Baldry et al. (2010) this plot gives a good indication of redshift. There is overlap but it can be shown that there is a general trend within the plot which separates the low redshift from higher redshift objects.

Figure 2.10 shows the majority of the 343 objects (35 are unrepresented due to being outside the plot boundaries) detected with the search algorithm plotted on the $J-K$ (VIKING) vs $g-i$ (SDSS) plot. This has been plotted over a contour distribution created using the GAMA r defined APMATCHEDCATV06 (Driver et al., 2016). These data are divided by redshift and contoured to show where the peak density of each redshift range sits on the plot.

A large proportion of the LSBGs sit around the peaks of the lower redshift bands as shown by the median value displayed in Figure 2.10. There is scatter within this distribution, however; this was expected as the LSB nature of the objects means that precise magnitude measurements are difficult. Due to the scatter in the plot and the large errors it cannot be said with certainty that these objects sit at low redshift. Therefore, further follow up is needed with spectroscopy to determine the spectroscopic redshifts of these objects.

2.4.4 Catalogue

The final catalogue of detected LSBG objects numbers 343 with VISTA VIKING confirmation. The full table of detections is given in Table A.1. There are two objects, LSB15269 and LSB15288, which do not have any measurements recorded for magnitude or surface brightness, because IOTA was unable to detect the objects in the frame within $5''$ of the coordinates supplied. However they have been visually confirmed.

When creating the catalogue the main test to tell if the objects were newly discovered or not was to match to the SDSS catalogues. This returned 50 candidates which had already been assigned OBJIDs from the SDSS. This was a concern as it was believed that all detected objects had been masked out using the SDSS PHOTO pipeline output. However, upon inspection of the flags produced by the SDSS it was found that the

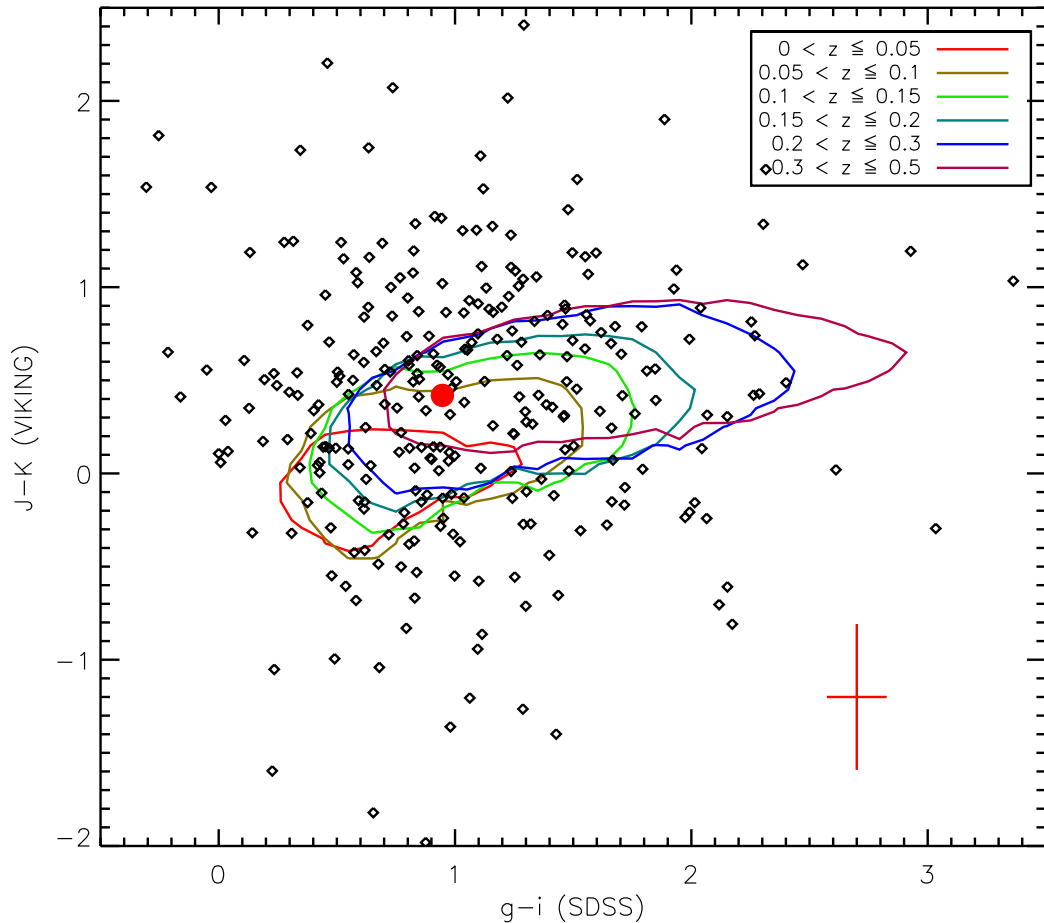


Figure 2.10: A $g-i$ vs $J-K$ colour-colour plot of all LSBGs found using the methods described in this paper. Over-plotted are contours which describe objects found in the GAMA fields, split into bins of increasing redshift described by the numbers of respective colour at the top of the plot. As can be seen this plot can be used as a proxy for redshift (Baldry et al., 2010) to determine if the object is at low redshift or not. The scatter in the plot was expected due to the low surface brightness nature of the objects. In the lower right of the plot is the 1σ error bars for the points (higher values of σ are too large to be displayed within the plotting area). The red circle shows the median value of the distribution of LSBG colours.

objects were only detected in one band within a field and so the SDSS were unable to say if there was a detection so these galaxies were not included in the SDSS catalogues. This meant that the objects could be left in the catalogue created through this work and counted towards the total number of new detections.

2.5 Summary & Conclusions

This work attempts to answer a simple question: are there any LSBGs hidden within the GAMA equatorial regions that could contribute to the low mass end of the GAMA GSMF? Using images from the SDSS, and a specially developed algorithm to process the images and detect the objects it was discovered that whilst there are LSBGs, they do not meet the required magnitude cut of $r \leq 19.8$ mag. Therefore they will not affect the GAMA GSMF at low masses as presented in Baldry et al. (2012).

The algorithm created consisted of several parts, namely the coadding and weighting of the images, the masking of these images, and then finally smoothing the images to bring out any hidden objects within the images. A cut of 5σ was then applied to the smoothed images to identify any pixels with a high enough signal to noise to be considered a detection. After clumping the detected pixels into candidate objects, constraints were applied to the candidate objects, which removed most of them as erroneous detections such as extended wings of bright stars and galaxies which were not masked out by the original masking, or over-densities of candidates hinting at ghosts within the image that have been deblended by the detection algorithm. After a final comparison to VIKING Z band data it was discovered that there were at least 343 new galaxy detections within the data.

In the majority of cases these objects have had their magnitudes measured with an auto aperture, which gives an approximation of the total magnitude for the system. However, if the magnitude differed from that given by a $5''$ fixed aperture as to place the value in the wings of the distribution described in Figure 2.9 ($-1.0 \geq \Delta_{mag} \geq 0.1$) and there was a problem with the imaging (e.g. scattered light or emission from a bright

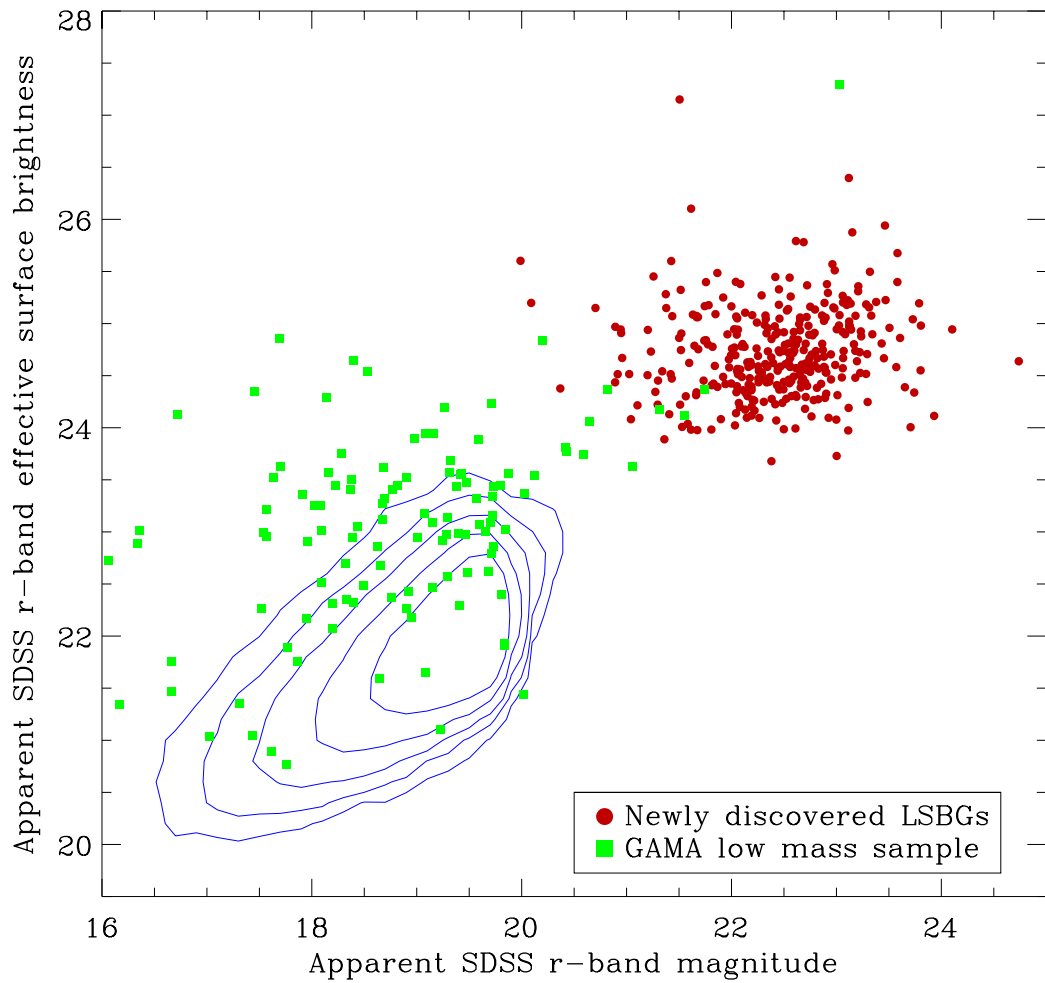


Figure 2.11: This plot shows the GAMA main survey sample (blue contours), newly discovered LSBGs (red points) and the GAMA low mass sample (green squares) which was used to weight the images as described in section 2.2, on a plot of apparent r -band magnitude vs. effective surface brightness. This shows how the newly discovered systems compare to the GAMA sample and show they sit outside the main survey limit of $r \leq 19.8$ mags. This means that they will not affect the GAMA GSMF. There does however seem to be a general trend being followed with no hard limit on the surface brightness being seen, which may suggest there are further systems to be discovered at fainter magnitudes.

source) then the fixed aperture magnitude was used. This means that accurate surface brightness information could not be gathered, and therefore this is missing from Table A.1 for those objects. While the SB of the detected objects within the auto aperture is low ($\gtrsim 25$ mag arcsec², Williams et al., 2016), it is unclear what the half-light SB values of the majority of sources are. This is because the majority of half-light radii are around 1", as shown in Figure 2.12, and the measurements are not corrected for seeing.

The majority of LSBGs seem to be at a low redshift when compared to a $J-K$ vs $g-i$ plot of all galaxies from the r -band defined GAMA survey. This plot is a good proxy for photometric redshift and can give a good idea of whether the objects are at high or low redshift. This is not conclusive however as there is overlap between the contours making any judgements on distance ambiguous at best. Further follow up is needed to obtain good spectra for each object in order to accurately determine the redshifts of the systems.

The measured magnitudes do not, however conform with the original cut made to the data at an apparent magnitude of 21.3 mag and sit fainter than this limit. This is due to several factors. One possibility is that the objects are sitting in areas where there are other faint objects which were not masked out, and which raise the detected flux in the larger apertures compared to the smaller auto apertures defined by IOTA. Another reason could be due to uncertain sky subtraction. There will be larger uncertainties in the larger 15" fixed apertures than there are in the smaller auto apertures.

Figure 2.11 shows how the newly discovered sample compared to the main GAMA survey. This shows how the systems discovered in this work do not fit with the GAMA survey data in that they are too faint to be included in any calculations of the GSMF using the GAMA main survey limit. However, the catalogue can be used in future studies to generate a test sample for upcoming deep redshift surveys in the same regions. Many of the objects seem to have fairly small effective radii, as seen in Figure 2.12 which does mean that they could be distant galaxies, however they are still detected as LSBGs and so they are still included in the discussion of LSBGs. Note also SExtractor returns the circularised half-light radius, along the major axis, this will be

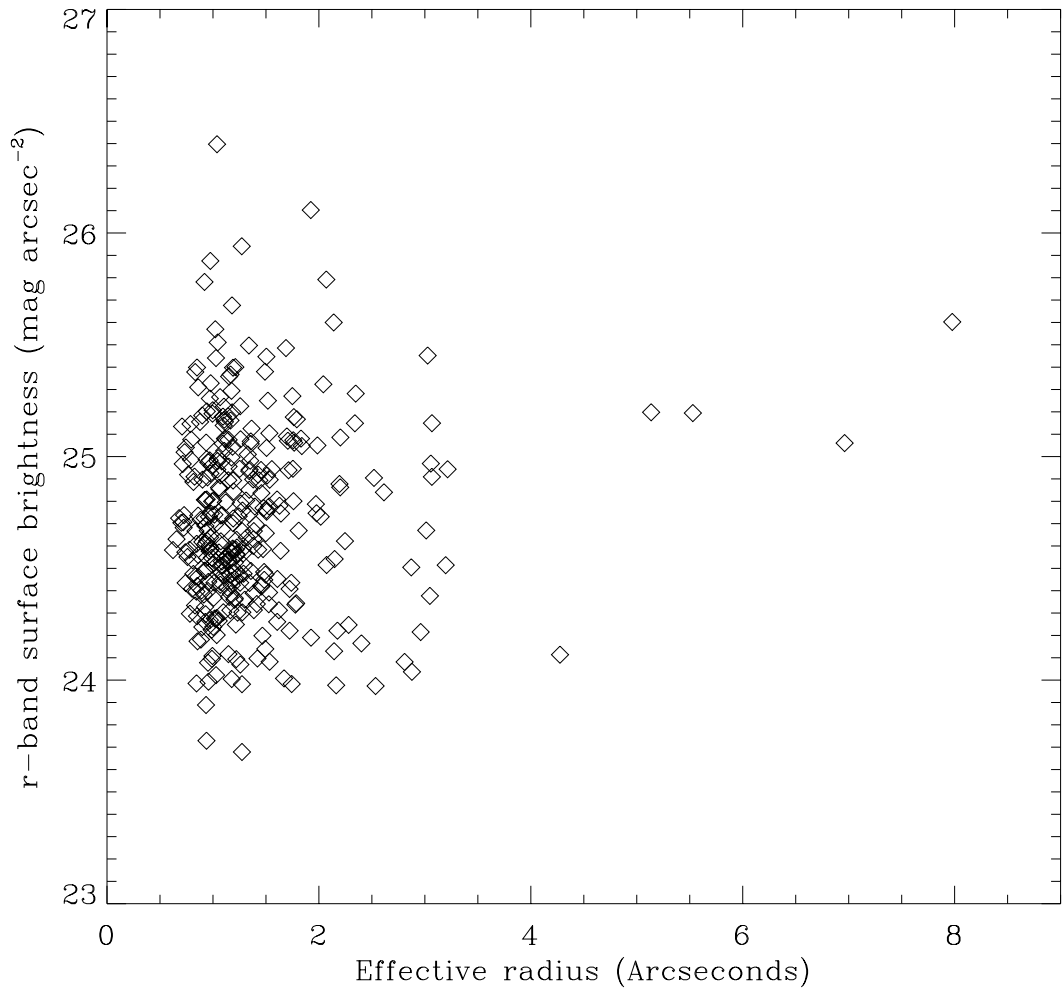


Figure 2.12: The plot describes the distribution of the effective radii (R_e) in arcseconds against the surface brightness measured within that aperture for all confirmed detections. They were measured using the Z -defined auto apertures created using IOTA. Most of the objects are measured to have radii on the order of $1''$ however these are still objects which were not detected in the original SDSS catalogue and so are included in the discussion of LSBGs.

slightly larger in general, and the half-light measurement will be noisy in the r-band data because the total flux measurement is noisy. The median semi-major axis radius for the auto aperture, defined using the VIKING Z-band data, is 3.2 arcseconds. Until true redshifts can be determined for these objects they should remain in the catalogue as LSBGs.

We have run a Z-band source extraction on the the VIKING mosaics to try and complete the low mass end of the GSMF, the results of this analysis will be described in the next chapter.

Chapter 3

Determining the GLF and GSMF using a VIKING-Z band catalogue

GAMA has thus far created a highly complete spectroscopic survey of galaxies in the local universe, to a magnitude of $r = 19.8$, over an area of 286 square degrees. From analysing a $z < 0.06$ sample of galaxies, the Galaxy stellar Mass Function (GSMF) was accurately measured down to a stellar mass of $M_* = 10^8 M_\odot$ (Baldry et al., 2012). However below this limit the GSMF is less complete because of surface brightness effects, and the limiting magnitude of the Sloan Digital Sky Survey data.

This work will be used to extend on the SDSS study discussed within Chapter 2. From the results gathered within the last chapter it is clear that there is a population of previously undetected LSBG galaxies. Whilst the work towards uncovering these objects within the SDSS data retrieved no galaxies within the GAMA survey limits ($r \leq 19.8$ mag), it did show the potential of the technique and the fact that VIKING Z -band imaging is deep enough to detect galaxies with a lower surface brightness than SDSS means it is suitable for expanding the search. This chapter will detail the efforts undertaken to quantify the number of LSBGs within GAMA through the use of deeper imaging in the hunt for these systems.

3.1 Detecting Objects

For the start of the analysis it is necessary to extract all of the objects from the three equatorial GAMA fields in the VIKING Z -band data, SExtractor was used for this task. It should be noted at this stage that a standard SExtractor run recovers the LSBGs that were identified in Chapter 2. Even though these are too faint to be included in a magnitude-limited sample that has a reasonable redshift completeness, it shows that this SExtractor run on the Z -band will identify lower-SB sources than SDSS.

All of the objects detected were compared, spatially, to the original GAMA sample, which gave two lists of objects, those detected in the original survey which had been found again and those newly found from the deeper imaging provided by VIKING. This catalogue was cleaned of any contaminating data, such as bright stars and artefacts, which could affect the GLF or GSMF measurements. Finally the objects included within this catalogue were used to calculate the weighting factors to be applied to all galaxies with a reliable redshift. This is then used to measure the GLF and GSMF within a redshift range of $0.002 \leq z \leq 0.12$.

3.1.1 Source Extraction

The VIKING Z -band data was mosaicked by the GAMA team using the SWARP programme. This combined the individual fields of the VIKING data into three large images each representing one area of the GAMA survey; G09, G12, and G15. The zero point for all images was set to 30^{th} magnitude in the AB magnitude system. The background was estimated and subtracted within the SWARP programme, and is carried out by applying a 128×128 pixel grid to the images. VIKING has a pixel scale of $0.339''$ per pixel, meaning one grid square is $\sim 43'' \times 43''$. This mesh is used to create a histogram of all pixel values within these areas, and measures the mean and median of the values. The histogram is clipped to $\pm 3\sigma$ around the median followed by re-measuring the mean, and if the mean value has not changed by more than 20% then this value is used as the background to be subtracted. In the event that the mean

value changes by more than 20% then a mode is used for the background. Once this background has been subtracted from the image a 3×3 grid is used to smooth the box and a bi-cubic spline is fitted to the image mesh to smooth over the joins between the boxes.

Different background mesh sizes were tested as described in Driver et al. (2016). The chosen initial size, 128 x 128, was considered optimum for GAMA. Flux measurements of galaxies brighter than 14th magnitude were not usually affected when using this mesh size. In general, only sources of size around an arcminute or larger had noticeable flux subtracted. This is significantly larger than the scale of most LSBGs at distances > 10 Mpc.

To extract the sources from the images SOURCE EXTRACTOR (SEXTRACTOR) was used. To use SExtractor a setup file is used to define, for example, the way the background is measured in the images. The parameters that were changed from the defaults, for the detection of sources, were as follows:

```
MAG_ZEROPOINT = 30.0
```

```
BACK_TYPE = MANUAL
```

```
BACK_VALUE = 0.0
```

The zero point was set to the value described in Driver et al. (2016) and a manual background value was chosen to be 0 as background subtraction has already been completed for the mosaicked images as part of the mosaicking process. This was chosen as the run is primarily used for detection, a local background subtraction was used later in the process when determining photometry for the objects.

Despite mostly being used for detection it is still important to correct the magnitudes from the SExtractor run for Galactic Extinction to more accurately apply cuts to the catalogue. As can be seen from Figure 3.1 the GAMA regions had minimal extinction due to dust. This means the corrections will be mostly small, but still important to calculate accurately. To do the corrections the EULER¹ IDL routine is used to convert the RA and Dec coordinates of the objects into Galactic longitude and latitude. These in

¹Supplied through the IDL astronomy library <http://idlastro.gsfc.nasa.gov/contents.html>

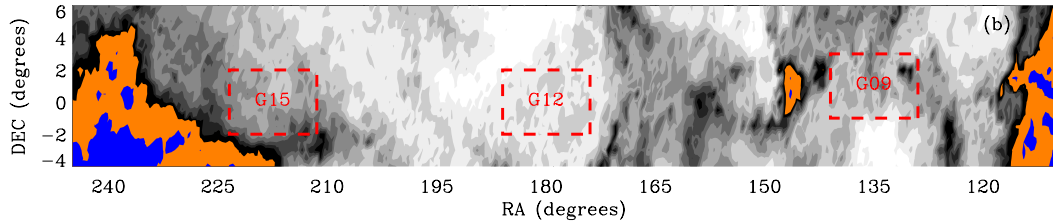


Figure 3.1: This is part of figure 2 taken from Baldry et al. (2010) and shows the area of the sky where the GAMA regions fall in relation to the dust extinction maps of Schlegel, Finkbeiner & Davis (1998). As can be seen from this figure the GAMA regions fall in areas of relatively low extinction which gives, specifically for the reason of being able to probe to deeper magnitudes. The colours describe the r-band extinction in magnitudes: < 0.06 white; $0.06 - 0.20$ grey scale; $0.20 - 0.25$ black; $0.25 - 0.50$ orange; and > 0.50 blue.

turn are used to get the extinction correction for that location from the `DUST_GETVAL`² routine, which took those values from those supplied in Schlegel, Finkbeiner & Davis (1998). This returned the $E(B-V)$ value for the Galactic coordinates which, when corrected using an $A_x/E(B-V)$ value for each band, x gives the extinction value to be applied to the calculated magnitudes. After the corrections were applied to the magnitudes a cut of $Z = 19.5$ was made.

This produced an initial list of objects within the three fields as detected by VIKING. This would contain a large proportion of artefacts and stars and so had to be further filtered using a series of procedures detailed below. The SExtractor run will have detected some LSBGs that exist in the field due to the VIKING imaging having a deeper magnitude limit, however it will have also returned several artefacts which may have come from many sources, such as ghosting, or at the joins between images when the SWARPS were created. Despite problems in the images the limiting magnitude of the VIKING SWARPs is still an improvement over SDSS. This is shown in Figure 5.1 and is discussed further in Chapter 5. This does show an almost 1 magnitude improvement over the SDSS compared to a typical low redshift SED.

3.1.2 Removing Artefacts and Stars

The first cuts to the catalogue are to apply limits of:

²Supplied through SDSS idlutils library https://www.sdss3.org/dr8/software/idlutils_doc.php

$$\text{MAG_AUTO}^3 \leq 19.5$$

$$\text{CLASS_STAR} \leq 0.8$$

The magnitude limit is consistent with the original GAMA catalogues as these images are being used to fill in the gaps where surface brightness means the object was not detected. This cut was decided upon based on the information contained within Figure 3.2, to ensure high spectroscopic completeness within the catalogue from GAMA sources, This is to ensure when correcting the GLF there is a good sample of galaxies with measured redshifts to reflect the redshift distribution of the galaxies. The second parameter is used to remove objects which are determined to be stars. An object is considered to be highly star-like when its Class Star (CS) value approaches 1. As shown in Figure 3.3 there is a strong feature around the CS value of 1 which is removed by the cut. The limit of 0.8 was chosen as a standard cut used on this parameter to separate stars and non stars. This is only an approximation based on the SExtractor output and it is likely that stars are left within the catalogue after this cut. A CS value of 0 however does not mean that the object is a galaxy, it only means it is not star like. This can lead to misunderstanding of this parameter and is the reason why the cut must be placed at such a high value. The cut of $\text{CS} > 0.8$ removed some 600,000 star like objects from the catalogue.

The G15 area in the VIKING Z band images is 99% complete (Driver et al., 2016) and therefore, has some holes where observations do not exist. These appear as 5 thin strips in a north-south orientation within the SWARPed images. SExtractor had created a large number of false detections within these areas. Therefore all detections which fell within the area defined by the missing data were removed. This left holes within the data which needed to be accounted for when testing how many objects were missing from the original catalogues.

The next stage in cleaning the catalogue of detections was to apply masks to the data. As described in section 2.3, bright stars in the images will have an effect on the surrounding pixels. This must be taken into account and so the RA and Dec coordinates of

³This is the magnitude within an SExtractor defined Auto aperture, which is an aperture fit to an object to measure all of the detectable flux of the galaxy.

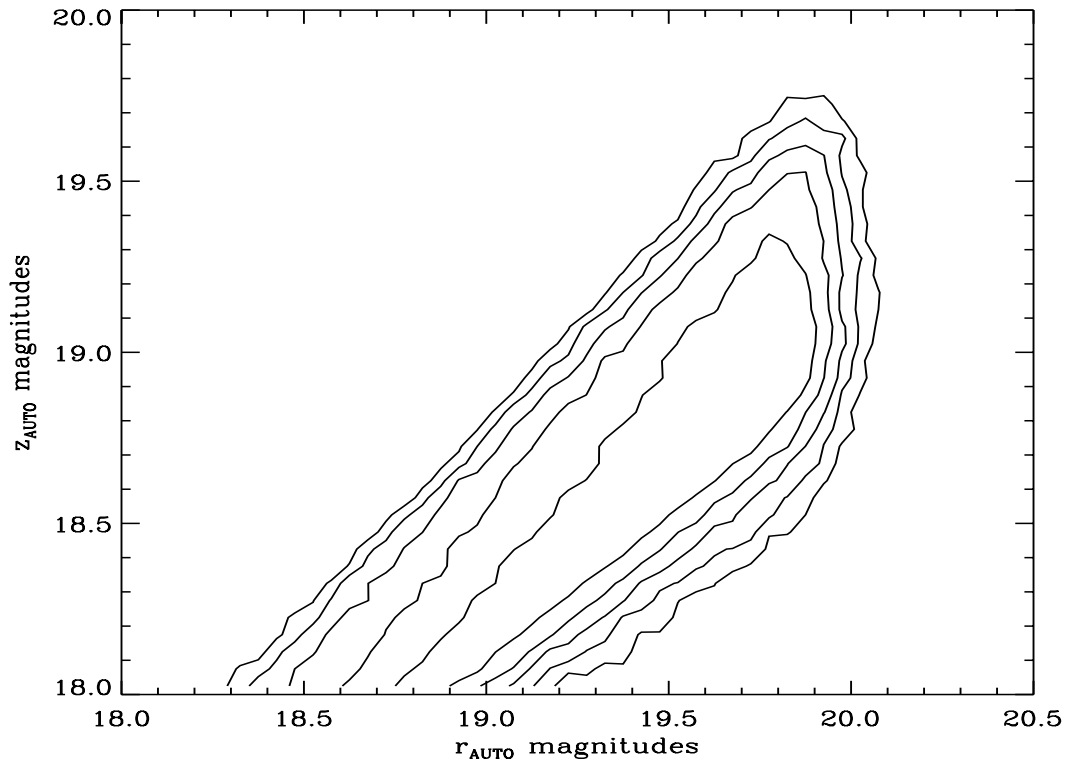


Figure 3.2: Data taken from the r -band aperture matched GAMA catalogue, showing the distribution of Z -band magnitudes against r -band magnitudes for objects with good redshift measurements. The r -band catalogues were cut at 19.8 based on the completeness from the the distribution. Therefore, a Z -band limit of 19.5 was decided upon based on this distribution to ensure that there would be a good sample of galaxies with redshift data to construct a GSMF.

all detections from the SExtractor run are compared to the Tycho catalogue (Høg et al., 2000) with a limit of $V < 12^{th}$ magnitude and assigned a proximity value (`mask_ic`; Baldry et al., 2010) between 1 and 0. Sources with `mask_ic` > 0.5 were removed from the catalogue. This then leaves a list of objects which must be sorted to determine which could be new detections. This was achieved by matching the objects to within $2''$ of the original GAMA Tiling Catalogue objects. This produced three tables: (i) Those already in the GAMA Tiling Catalogues, (ii) New objects within the VIKING images, (iii) Those objects in the Tiling Catalogue which had not been matched to VIKING.

The most troubling of these tables was the third. This showed that $\sim 5\%$ of the galaxies detected within TilingCat were missing from the SExtractor catalogue after false detections had been removed. To check the reasons for this, a random sample of 1000 objects were chosen from the missing sample and visually inspected to determine why

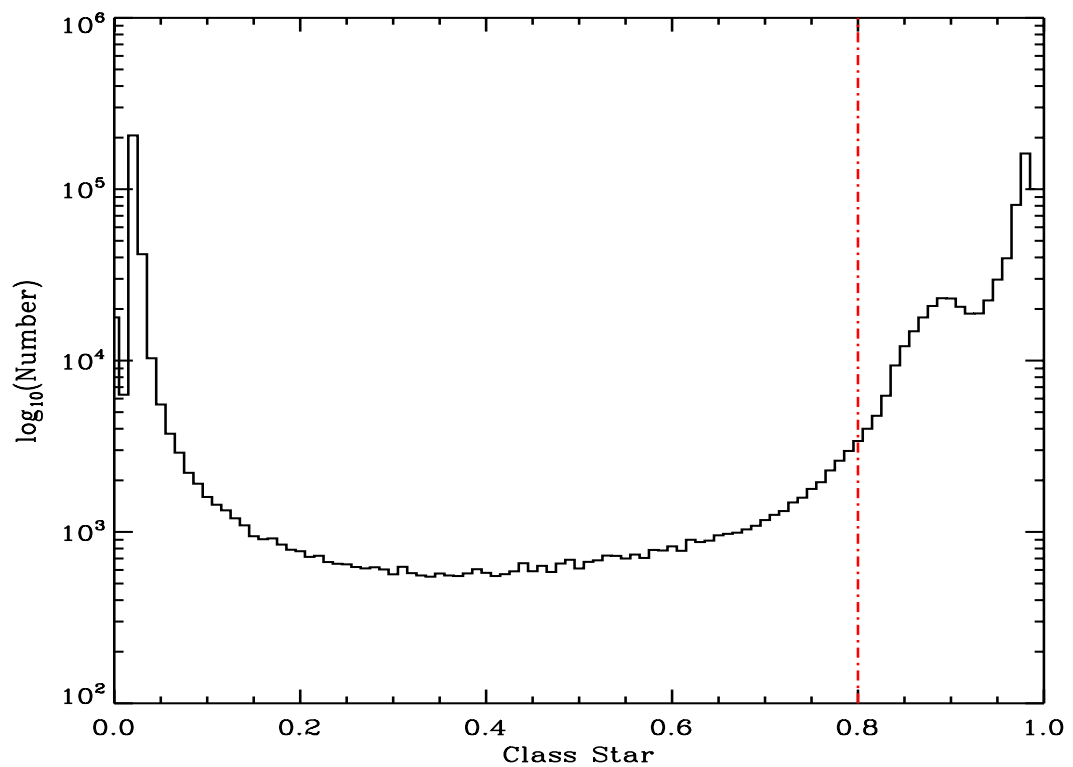


Figure 3.3: Histogram of the class star values output by SExtractor from the initial detection run of the GAMA mosaics. The parameter ranges from 0 (not star like) to 1 (star like). As is shown in the plot there are strong features around these two values. The red dotted line shows the location of the cut applied to the catalogue of a class star value of 0.8. This removes many of the objects deemed to be stars as well as the extra feature which is seen to occur on the approach to a value of 1.

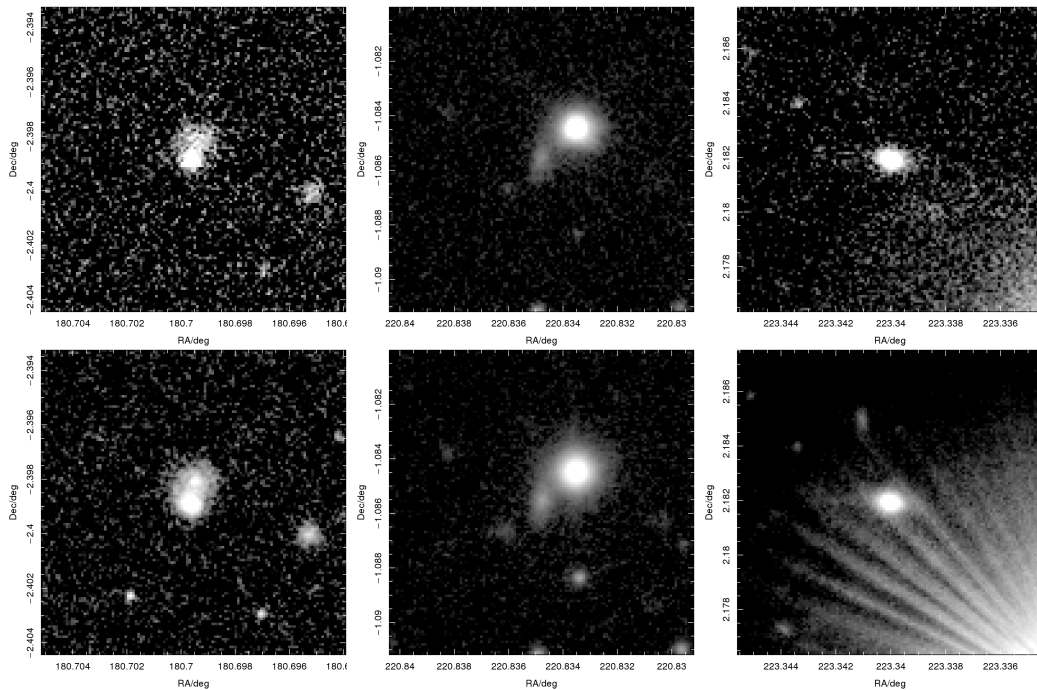


Figure 3.4: 3 examples of objects missing from the VIKING Z -band source extraction catalogues which were detected in the SDSS r -band catalogue. The top row is the objects from the SDSS imaging and the bottom row represents the same objects from the VIKING imaging. As can be seen the VIKING imaging has either detected ‘more’ of the object than the SDSS imaging, thereby moving the centroid by more than $2''$, or has ‘covered’ the object with extra emission from another object.

they were not being detected. It was discovered that many of these galaxies were being obscured by a brighter object, or that the centroid as measured in Z had been relocated by more than $2''$ compared to that measured in r , and so was not matching to the new VIKING catalogue. Both sets of coordinates were kept at this stage to be dealt with later on in the process. Examples of these galaxies are shown in Figure 3.4.

3.1.3 Ghosts in the Images

The VIKING imaging mosaics had a number of quality issues which should be discussed, as they contribute to the troubles with detecting faint objects. Many of the newer objects (those with new ID numbers) have been confirmed to be real objects though visual inspection, however in carrying out this inspection there was a noticeable, recurring error within the imaging. Figure 3.5 gives several examples of this issue. It appears to be a 3×3 grid of sources always oriented in the same way, but

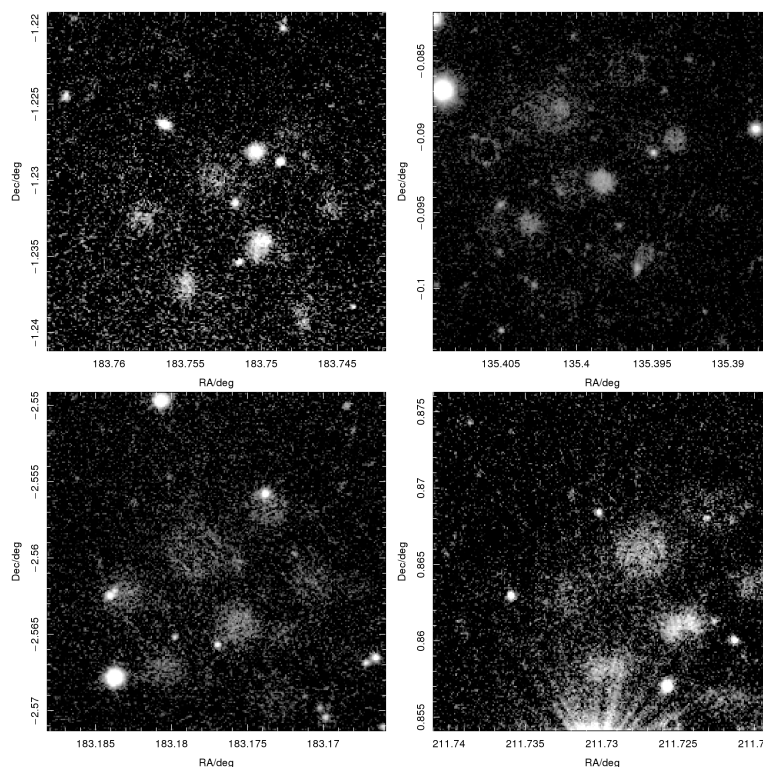


Figure 3.5: These are 4 examples of a common 3×3 grid of ghosted sources which are detected by SExtractor. These are thought to be caused by some internal reflection within the telescope and then exacerbated through the ‘jittering’ process used to create a complete image.

with different effects i.e. different overall signal or aberration. It is still unknown as to why this has happened in the imaging, it was first thought to be due to something on the detector such as a grain of dust however it appears randomly on the sky with no repeating pattern as you might expect if this was causing it. Another possibility is that there is some internal reflection caused by the baffling in the telescope, this would likely appear more randomly in the imaging. Another possible reason for this pattern could be due to an effect known as persistence in one of the detectors, where a previous exposure to a bright star remains into following observations. The reason for the 3×3 grid will most likely be due to the ‘jittering’ the telescope undergoes to fully observe the field and fill in the gaps around the detectors.

Figure 3.6 gives an idea of other issues with the images, these are all ‘easily’ explained as artefacts and internal reflection, apart from that shown in the top middle panel. This describes what looks like a normal detection. However it appears throughout the Z -band imaging multiple times in the same orientation, described as a rectangular source

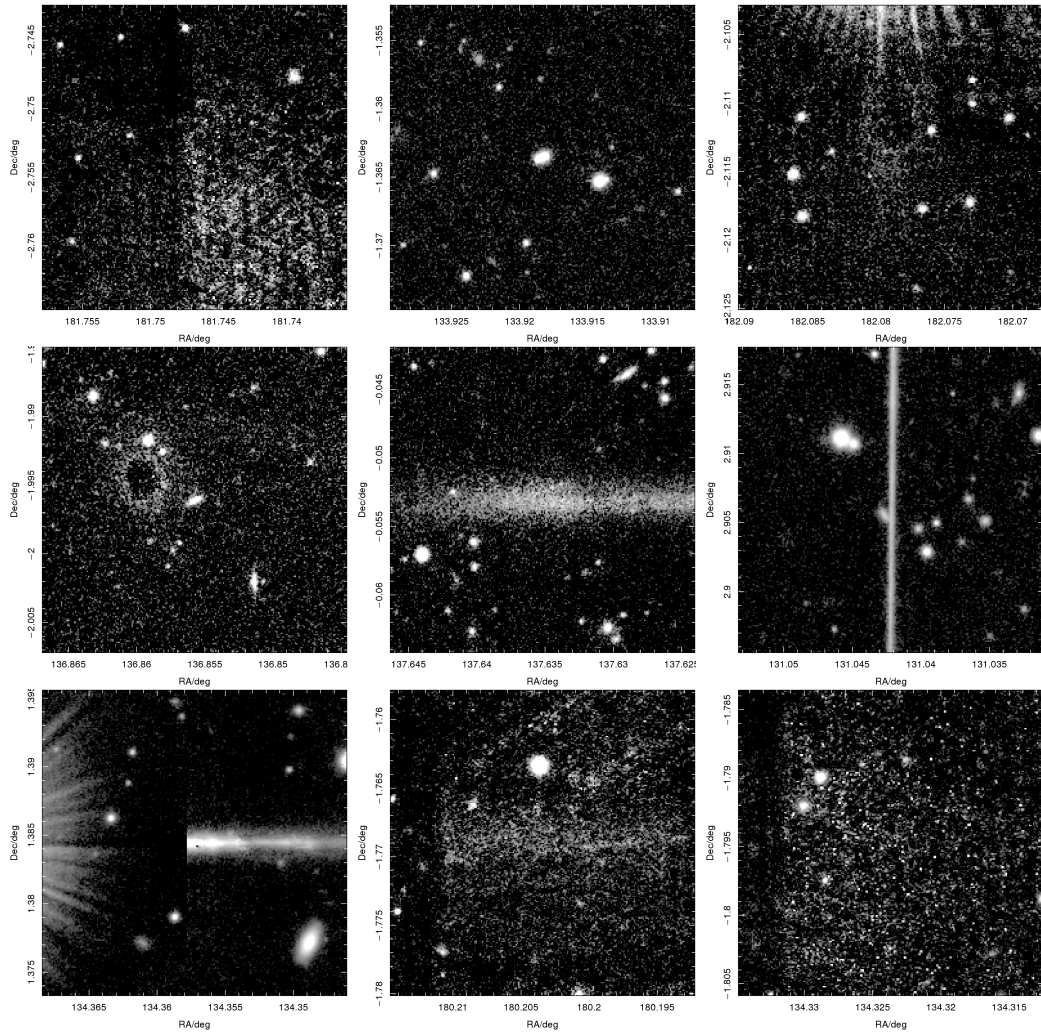


Figure 3.6: Examples of bad imaging quality from the VIKING data. All of the frames are centred on detection coordinates from SExtractor, and gives some idea of the difficulty in detecting new objects within the survey data

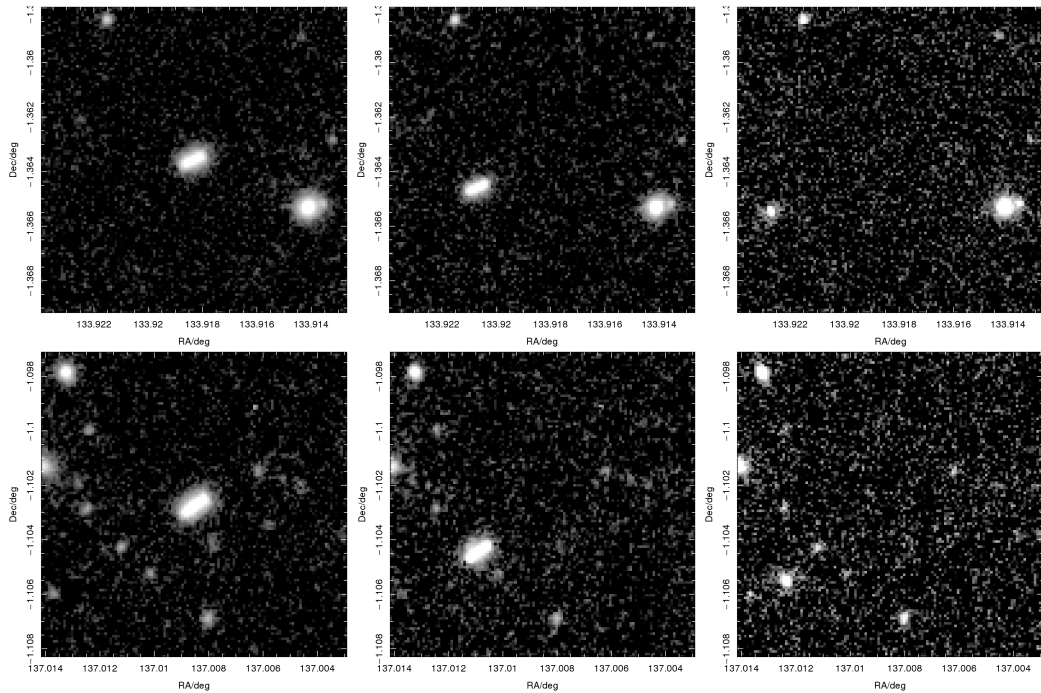


Figure 3.7: The two examples given above are displayed in, from left to right, the $ZY&J$ filters from VIKING, and each row gives an example from a different location on the sky. As can be seen the object ‘moves’ between the filters and is seen in the same orientation between the two different locations. This is most likely an asteroid, as there is movement between frames as well as an elongation along the path of the object. K and H are not shown as they are observed at different times meaning the asteroid will have moved from the frame.

which when viewed in successive filters moves from the original position and becomes fainter until it eventually disappears, this effect is shown with two examples in Figure 3.7. The object is most likely an asteroid, this explains the elongation of the object and its movement between frames in the direction of the elongation. It also explains why it does not appear in the K or H bands. The observing pattern of the survey was to carry out $Z, Y&J$ measurements in one run and the $J, H&K$ in a later run, giving the object time to move from the area being imaged. These objects will be removed as they are discovered visually in the catalogues by assigning a flag to identify them as not stars or galaxies.

3.1.4 Creating a Z selected catalogue

To produce a consistent Z selected catalogue based on the GAMA regions it was necessary to run both the new VIKING detected objects, and the original TilingCat ob-

jects through IOTA, a wrapper for SExtractor, across all SDSS (*ugriz*) and VIKING (*ZYJHK*) bands. IOTA is given the coordinates of the target object and produces a 1001×1001 pixel cutout of the area around the centroid. To avoid running on duplicates, the *Z*-band VIKING catalogue containing all of the detections from the SExtractor run are matched to the original GAMA catalogue and any objects which fall within $1''$ of each other are ‘combined’, i.e. the VIKING object is removed and the matching GAMA source is kept. SExtractor is then run on the ‘primary’ band, in this case the VIKING *Z*-band, with a $5''$ detection radius⁴ from the original point. The new coordinates and the aperture created for MAG_AUTO are then applied to all of the other bands for detection of the same objects.

The VIKING-only and the targets with GAMA IDs, having both been run through IOTA, are combined at this point, and the magnitudes corrected for extinction, following the procedure outlined in Section 3.1.2. Known false detections within TilingCat are also removed using the SURVEY_CLASS and VIS_CLASS parameters outlined in Baldry et al. (2010)⁵. This is to reduce the number of known contaminants from TilingCat. The table is also matched to the SDSS DR7 catalogue of all galaxies in SDSS which reside in the GAMA fields. This is used to gather the r_{psf} a magnitude calculated using a point-source function, and r_{model} parameters (for use in the star galaxy separation) for SDSS objects. The next stage in creating a *Z*-defined galaxy catalogue is to perform an improved star-galaxy separation. This is detailed below and closely follows the process from Baldry et al. (2010), with modifications made to parameters based on the data sets presented in this work.

⁴The $5''$ detection radius is useful for correcting the issue mentioned in Section 3.1.2, where objects are detected in both the original GAMA catalogues and the new VIKING run but their measured coordinates happen to sit more than $2''$ (the original matching radius) away in the different catalogues. This will align the coordinates of these objects into a consistent measurement meaning all duplicates can be effectively removed from the new catalogue.

⁵SURVEY_CLASS is a binary numerical value which describes if the object is real (1) or not (0). This is driven by the textscvis_class parameter, objects are assigned a numerical value after being visually inspected, 1 for a confirmed object and all other values are for detections caused by some error, such as image aberrations.

Star-galaxy separation

The next stage is a more rigorous process to separate the galaxies and the stars. This is only carried out for objects not found in the original TilingCat as all TilingCat objects have already had a star-galaxy separation applied. This can be accomplished by applying constraints to the detections based on several factors. The following constraints are based on those used by Baldry et al. (2010) and outlined in Section 3 of that work, with some expansion and changes due to the nature of using different data.

The first constraint is to use the SDSS main galaxy sample (MGS) star-galaxy separation parameter which was defined following Strauss et al. (2002) as:

$$\Delta_{sg} = r_{psf} - r_{model} \quad (3.1)$$

where r_{psf} is the point spread function (psf) defined magnitude, and r_{model} is the model magnitude, both measured in the r -band. If the model magnitude differed from the psf-defined magnitude by a sufficient amount, $\Delta_{sg} > 0.24$, then it was deemed a galaxy⁶. This parameter, however, was set based on a galaxy sample measured to $r < 17.8$ (Strauss et al., 2002), and would likely include compact galaxies at higher redshift and brighter magnitudes in the cut. Baldry et al. (2010) determined a criterion better suited to fainter samples based on SDSS stripe 82 data (Adelman-McCarthy et al., 2006), which has a magnitude limit of $r < 19.5$, where $\Delta_{sg} > f_{sg,slope}(r_{model})$ is defined as:

$$f_{sg,slope}(x) = \begin{cases} 0.25 & x < 19.0 \\ 0.25 - \frac{1}{15}(x - 19) & \text{for } 19.0 < x < 20.5 \\ 0.15 & x > 20.5 \end{cases} \quad (3.2)$$

It is determined that a more inclusive approach must be used by utilising the colour-colour diagram of $g - i$ vs. $J - K$.

⁶Originally the SDSS MGS limit was set as $\Delta_{sg} > 0.3$ (Strauss et al., 2002) however it was lowered as a result of the way model magnitudes were calculated

This method was used to test how well the star-galaxy separation had performed in the SDSS (Ivezić et al., 2002). It was shown to split stars and galaxies quite cleanly, creating a stellar locus, as is shown by the red plotted line in Figure 3.8. The stellar locus is fitted using a quadratic function and a new star-galaxy separator is defined as the separation of $J - K$ from the locus. By applying a function for the stellar locus it is possible to ‘flatten out’ the stellar locus to enable the application of a simple cut to the data. This function is given as:

$$\Delta_{sg,JK} = J_{AB} - K_{AB} - f_{locus}(g - i) \quad (3.3)$$

where J_{AB} and K_{AB} are the VIKING J and K band magnitudes, and $f_{locus}(g - i)$ is defined as:

$$f_{locus}(x) = \begin{cases} -1.7672 & x < 0.3 \\ -0.94 + 0.615(x) - 0.13(x)^2 & \text{for } 0.3 < x < 2.3 \\ -0.2132 & x > 2.3 \end{cases} \quad (3.4)$$

The cut of $\Delta_{sg,JK} \geq 0.2$ is used to separate stars from galaxies. The corrected plot and the separation parameters are shown in Figure 3.9.

This is used as the main separation parameter between the stars and galaxies. However it must be used in conjunction with the SDSS MGS main parameters, so as not to create too hard a cut on the data and not remove galaxies which should be included in the survey. The overall star galaxy-separation for this survey is given as:

$$\begin{aligned} \Delta_{sg,JK} \geq 0.2 & \quad \text{OR} \\ \Delta_{sg} \geq 0.25 & \quad \text{OR} \\ \Delta_{sg} \geq f_{sg,slope}(x) \text{ AND bad } J - K \text{ colour} & \quad \text{OR} \end{aligned} \quad (3.5)$$

where a bad $J - K$ colour results if the photometric measurement of either J or K was erroneous. This is determined by checking for fluxes with the value -9999 from the SExtractor output. All objects which were not matched to the SDSS catalogues

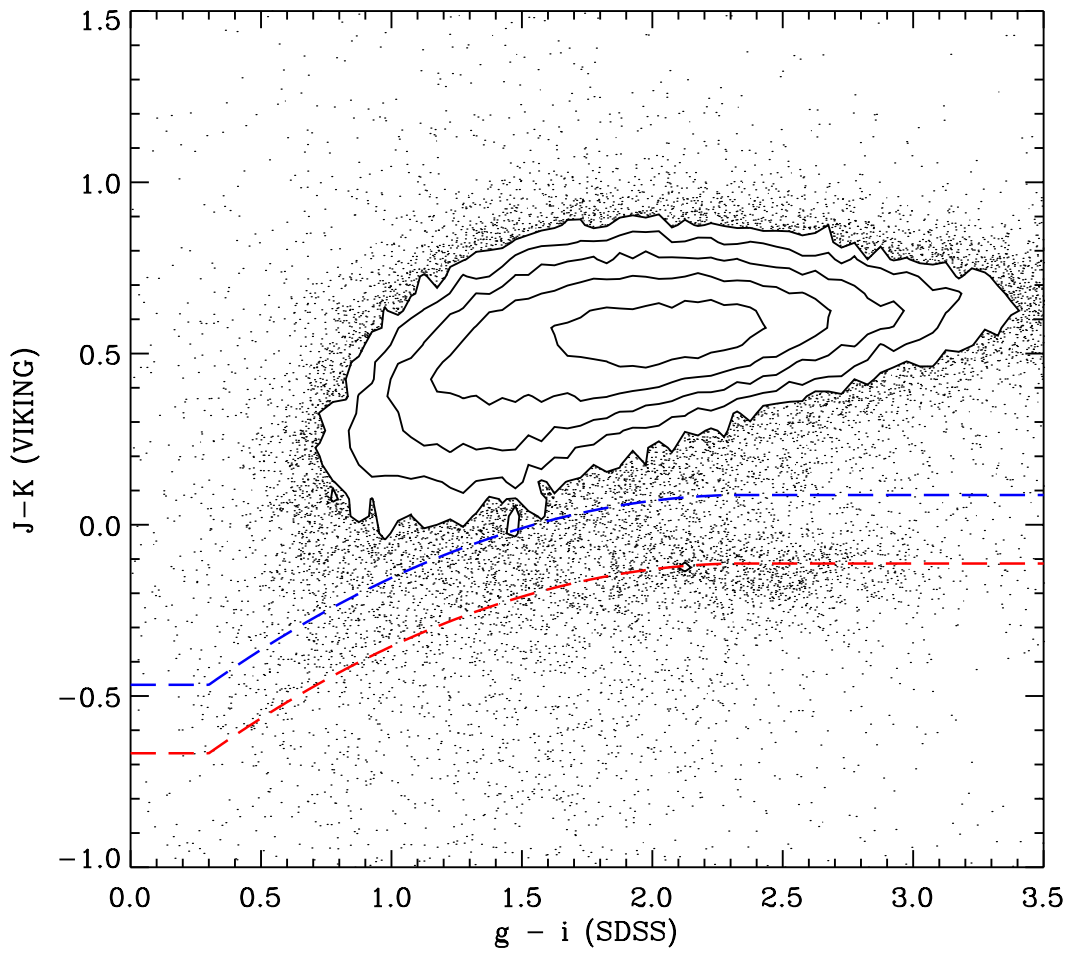


Figure 3.8: $g - i$ vs $J - K$ for all detected VIKING sources. The stellar locus is plotted for clarity. The red line defines this stellar locus as outlined in equation 3.4, and the blue line represents the star-galaxy separation point.

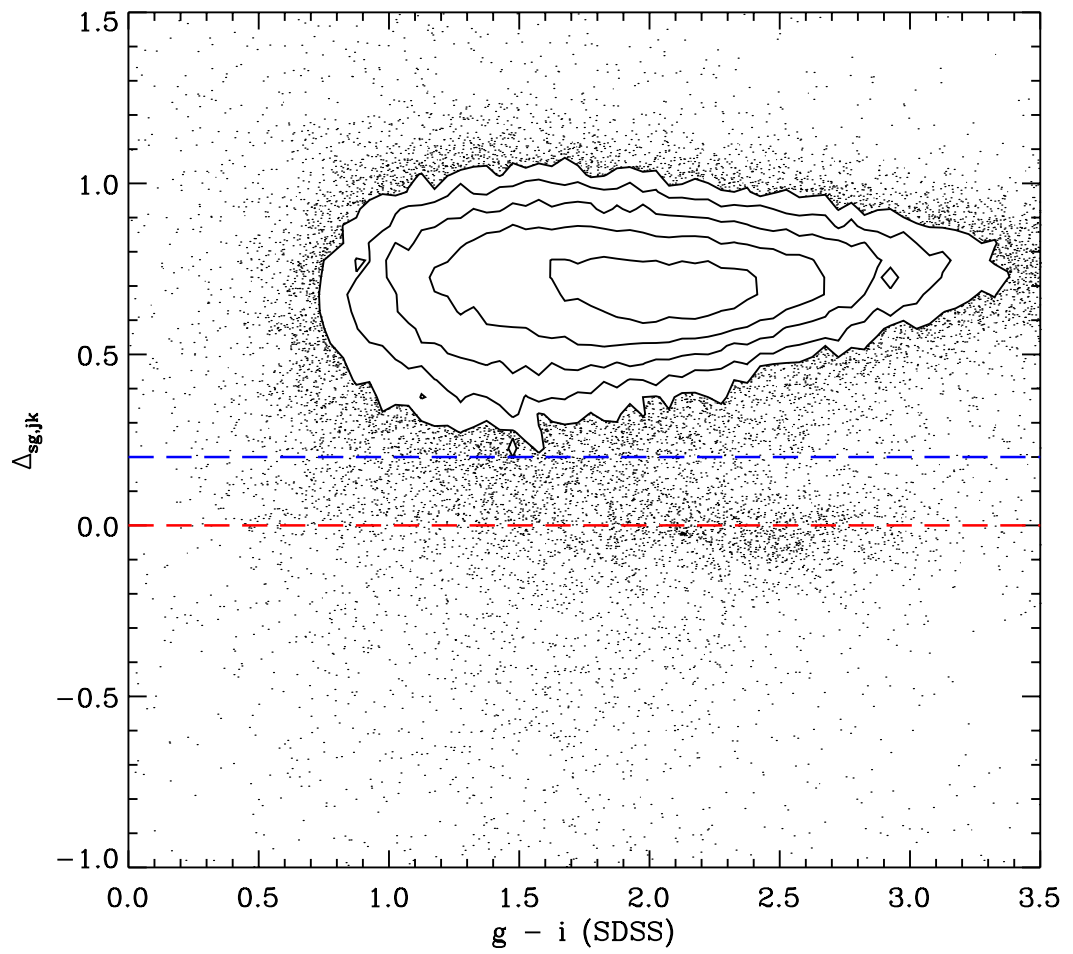


Figure 3.9: Data shown in Figure 3.8 but with the $J - K$ colours corrected by $f_{locus}(g - i)$. This creates a linear cut which can be applied to the data and is shown in blue. The red line defines the stellar locus.

were also kept as this cannot be used as a good metric for those objects. With these parameters applied the stellar locus defined above is removed whilst keeping any objects which cannot be definitely classified, as shown in Figure 3.10. The next step in determining the final object list within the catalogue is to decide on the Z band magnitude limit to be applied. From the original SExtractor run there is already a limit of $Z_{mag} \leq 19.5$ which brought the detections into line with the GAMA catalogues. However with the new, more accurate magnitude measurements from IOTA it is necessary to redefine this limit based on the completeness in the sample.

Setting the Magnitude Limit

The magnitude limit was defined based on the number of discovered objects per magnitude bin in the survey and the difference in the magnitudes measured by the detection run and IOTA for each object. Figure 3.11 shows the difference between the SExtractor detection run magnitudes and those calculated by IOTA. There is little spread in the difference with the majority of objects magnitudes changing by less than 0.05 mags. There are a small number of objects however which have a change in their magnitude of up to 0.2 mags. A survey limit of $Z = 19.3$ magnitudes was therefore chosen based on the IOTA magnitudes, 0.2 mags less than the previous limit chosen. This is supported by Figure 3.12, which shows the number of galaxies per magnitude bin based on the IOTA magnitudes gathered. All detections with a magnitude fainter than this limit are removed from the catalogue.

Refining the Completeness

From Figure 3.13 it can be seen that the spectroscopic completeness at bright magnitude, $Z \leq 16.5$, shows a large dip. Upon visually inspecting a random sample of the objects causing this discrepancy, it was revealed to be due to bright stars, which do not have assigned redshifts from the GAMA survey. To account for this it was decided that these objects should be flagged to indicate that they have been confirmed as not galaxies. This will mean that they are not considered when calculating the complete-

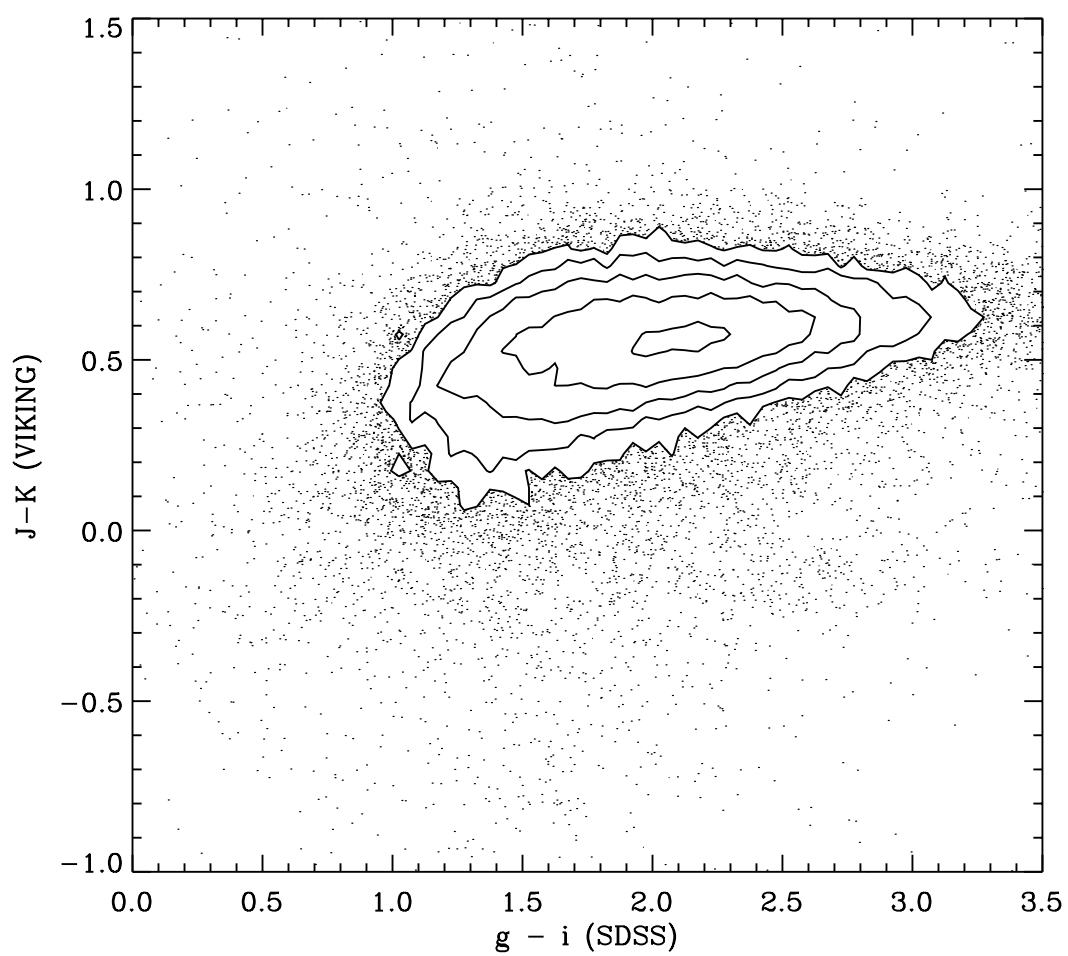


Figure 3.10: As Figure 3.8 but with most of the stellar locus removed from the plot using the processes outlined within this section.

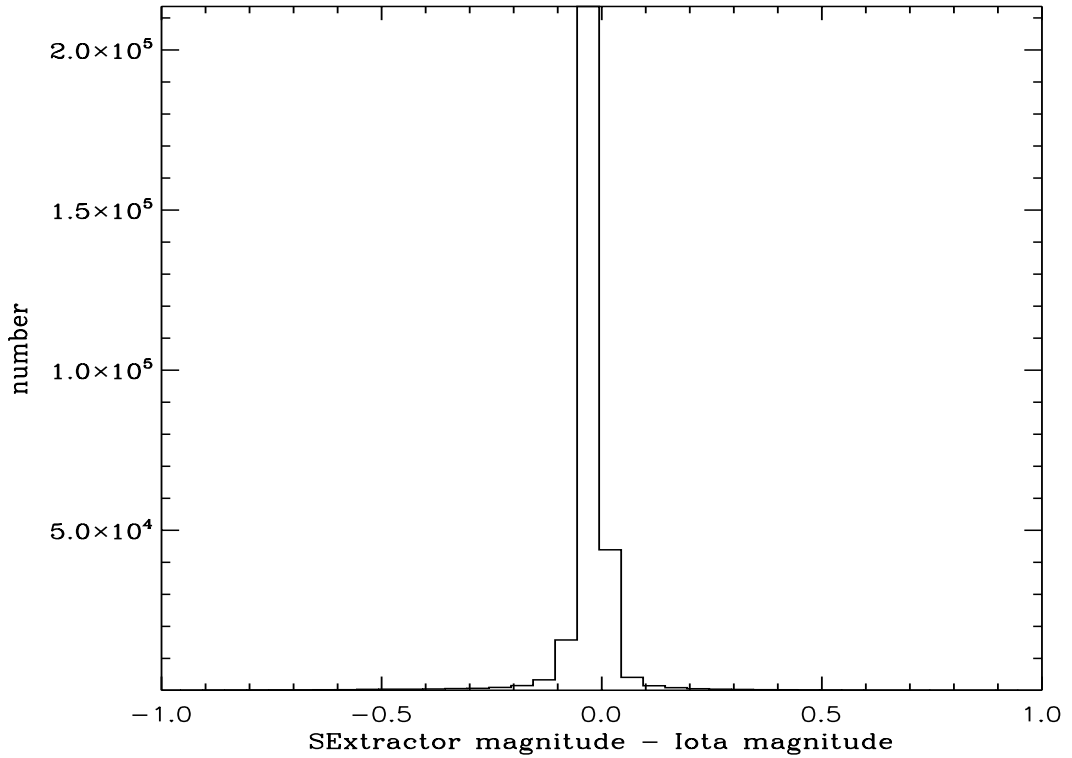


Figure 3.11: The majority magnitudes measured from the detection run of the VIKING data do not change more than 0.05 magnitudes when measured more accurately using IOTA, however there is some spread at the bottom of the distribution meaning that a small proportion of the magnitudes have changed by as much as 0.2 magnitudes. This and also Figure 3.12 are used to define the new magnitude limit.

ness values, to be used in the GLF calculation. As a star-galaxy separation has already been applied to the catalogue, it can be asserted that these objects do not fall into the parameter space already removed from the catalogue.

A new metric was used to discover the bright stars still in the catalogue, using an aperture magnitude. This is measured in IOTA and is set as a $5''$ diameter aperture placed over all target coordinates. This measure was used as a metric to separate galaxies from bright stars which which still remained in the catalogue. This was achieved by defining the difference between the $5''$ aperture and the auto aperture as Δ_{f-m} where:

$$\Delta_{f-m} = 5'' \text{ magnitude} - \text{Automag} \quad (3.6)$$

and plotting this against $\Delta_{sg,JK}$ as defined in Equation 3.3. This gives Figure 3.14,

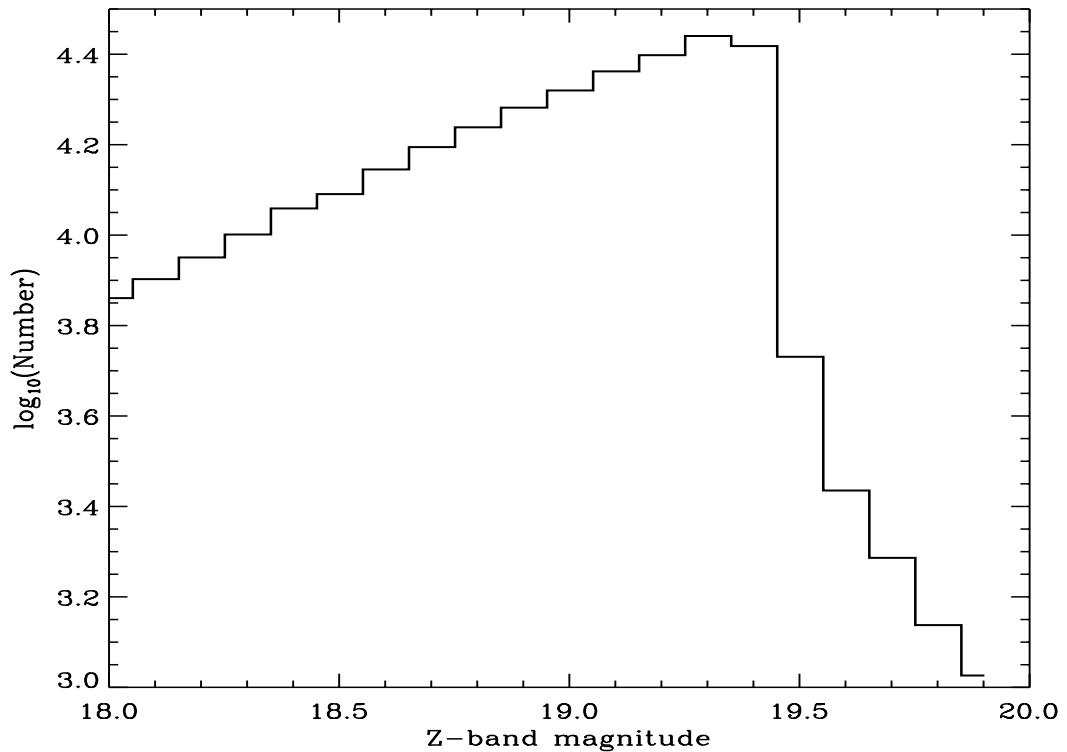


Figure 3.12: The number of galaxies per Z -band magnitude bin over the same range as figure 3.11. The number of objects rises steadily as a power law until an apparent Z -band magnitude of 19.3 where the function turns over. This describes the point where the sample, based on the detection-run magnitudes, becomes incomplete and gives confirmation for using a cut of $Z \leq 19.3$

which shows a clear separation between the stars, defined as having similar fixed and auto magnitudes, and sitting at approximately $\Delta_{sg,JK} = 0$. To define the objects to be removed the following criteria are applied:

$$\begin{aligned}
 \Delta_{sg,JK} &\leq 0.22 \quad \text{AND} \\
 \Delta_{f-m} &\leq 0.22 \quad \text{AND} \\
 Z_{Auto} &\leq 16.5
 \end{aligned}
 \tag{3.7}$$

All objects which fall within this criteria have their `survey_class` values changed to 0 to define them as not being galaxies, and removes them from any analysis to be carried out. This removes the majority of the bright stars from the catalogue whilst only removing one galaxy. This object was visually inspected to check it was a galaxy and had its `survey_class` value manually reset to 1 to define it as a galaxy.

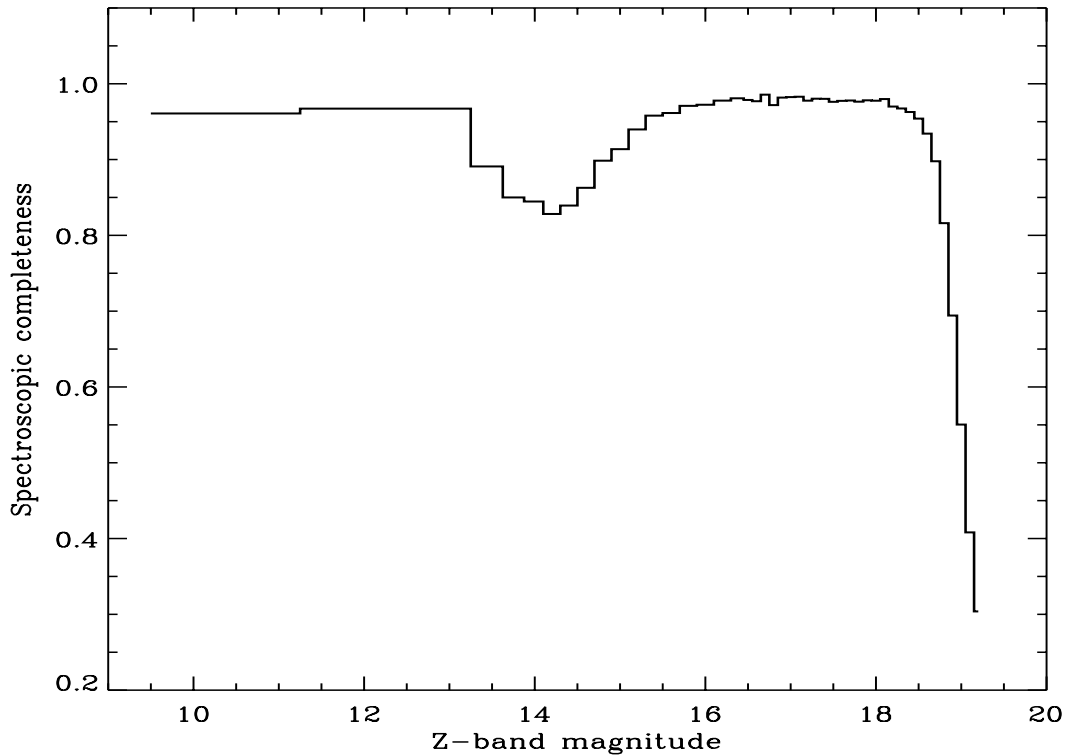


Figure 3.13: Spectroscopic completeness showing that at bright magnitudes there is a dip in the completeness levels of the survey. This has been caused by bright stars remaining in the survey data which have no redshift information.

With these criteria applied it is also necessary to visually inspect all other objects which have a magnitude of $Z \leq 16.5$ to check whether they are part of another object in the catalogues, or are not an object. The `survey_class` is set to zero for sources that are not galaxy targets. This means they will not be considered when calculating the completeness in the magnitude bins. When these changes have been made to the catalogue the spectroscopic completeness is considered corrected, as in Figure 3.15. With the catalogue now finished it is possible to create the GLF for the sample.

3.2 Galaxy Luminosity Function

Using the finished catalogue of sources it is possible to estimate the Galaxy Luminosity Function (GLF) for the data. A completeness value (C_i) must be calculated for each object with a determined redshift. This weights each object when calculating the number density for that magnitude bin to account for incompleteness within the survey

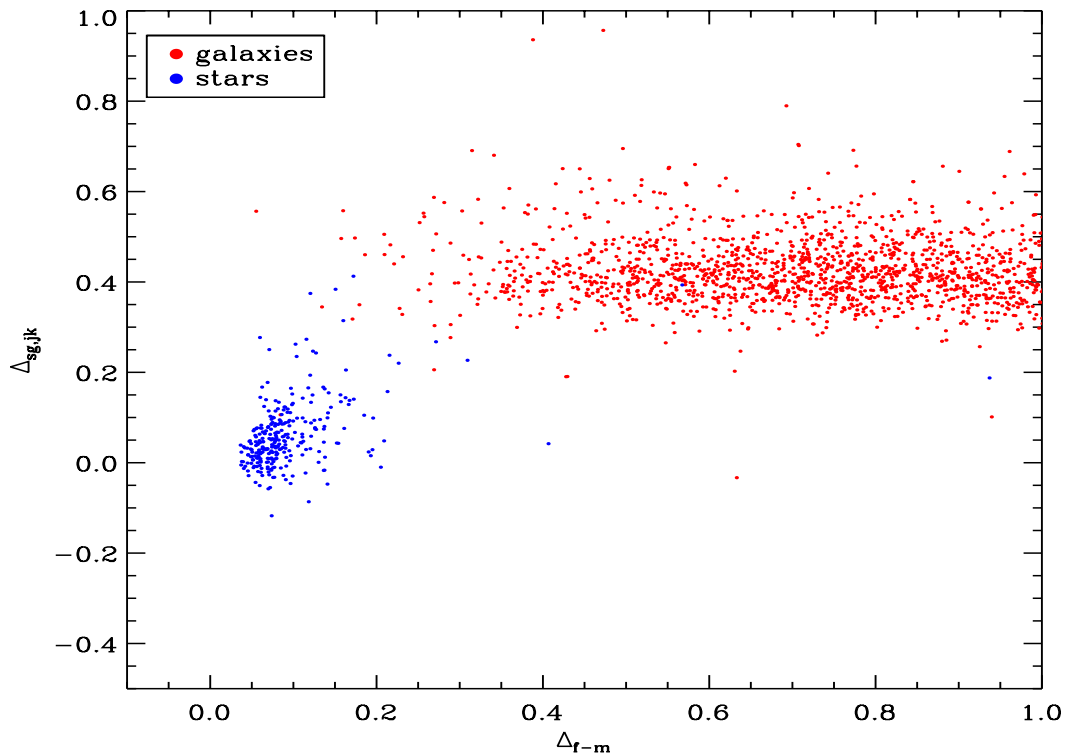


Figure 3.14: The distribution of stars (blue points) and galaxies (red points) for all objects with redshifts and with a magnitude of $Z \leq 16.5$ showing a clear separation. By constraining boundaries for this distribution it is possible to identify the majority of stars which remaining in the galaxy catalogue.

data. Secondly $1/(V_{max}C_i)$ is calculated for each object, as explained in Section 1.4.

3.2.1 Calculating the K-correction

A K-correction is a factor applied to a magnitude (or flux) which corrects for the redshift of the galaxy and represents the magnitude within the galaxy's rest frame (Hudson, Mayall & Sandage, 1956). This correction is not needed when using bolometric measurements, or when looking at a single emission line, as it is only applicable when using a photometric filter to observe objects. Only a fraction of the total emission from the galaxy is seen redshifted into the observer's frame therefore, when comparing objects at a range of redshifts it is imperative to correct all their photometric measurements to their respective rest frame. They are applied through a change to the equation for calculating the absolute magnitude:

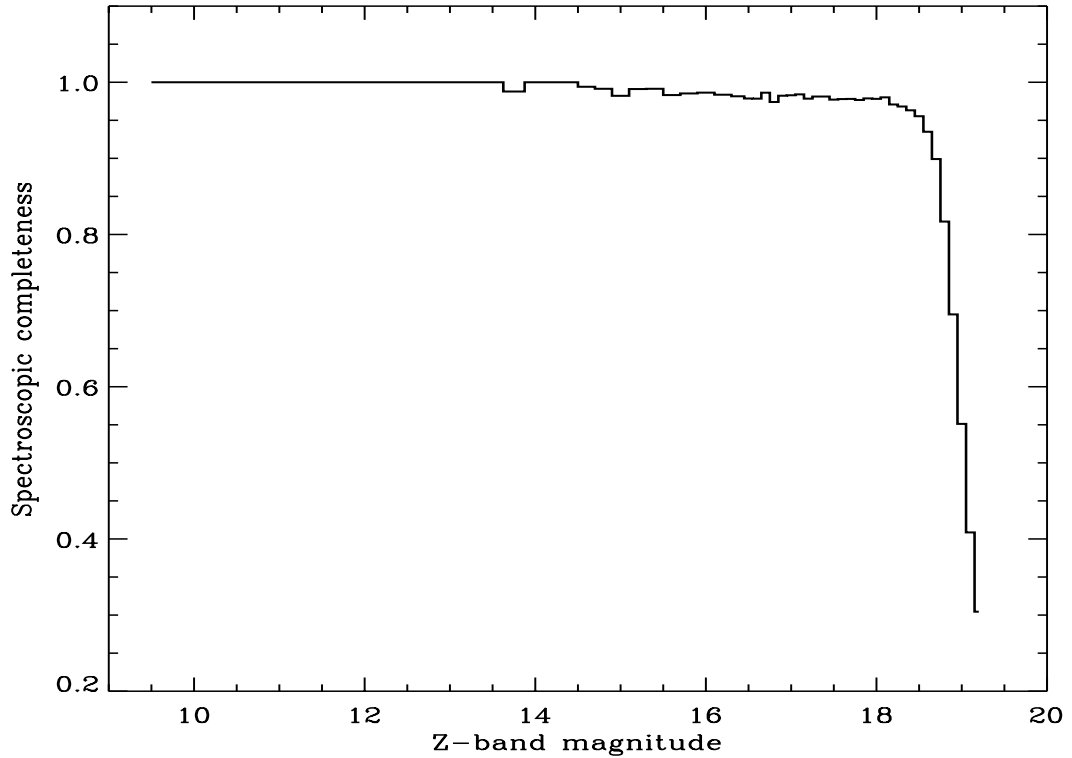


Figure 3.15: Spectroscopic completeness after the constraints to remove bright stars have been applied and visual classification performed. The feature seen in figure 3.13 has been removed.

$$M_x = m_x - DM - K \quad (3.8)$$

where M_x the absolute magnitude in a filter x , m_x is the apparent magnitude in the same filter, DM is the distance modulus of the object defined by its redshift, and K is the K-correction to be applied to the measurement.

In calculating the K-corrections of galaxies within a survey area, several passbands are needed in order to construct the SED for each of the objects. Templates can then be fit to the SED of the galaxy knowing which pass band is being corrected, and the redshift at which the galaxy sits. This fit is constructed through the linear combination of a set of template spectra, and the best fit to the data which is also non-negative is the one used. The code KCORRECT V4₂ (Blanton & Roweis, 2007) follows this method of prescribing K-corrections, also using the templates and an assumed IMF to calculate an estimate of the stellar mass system.

V_{max} is potentially affected by a differential K-correction (dK). This is the difference

between the measured K-correction and what the K-correction would be for the galaxy if it was moved to the most extreme redshift of the sample whilst still being detectable. The volume limit applied to this survey is $0.002 \leq z \leq 0.12$, and as Figure 3.16 shows the K-correction does not vary from a median of 0, therefore on average the dK value will be negligible. The K-correction is therefore only applied to the galaxies when calculating the absolute magnitude and is not important for the V_{max} calculation. This is in part due to the flat nature of the universal SED in νf_ν in the range $\sim 0.8\text{--}0.9$ microns (Baldry & Glazebrook, 2003; Driver et al., 2012).

3.2.2 Density Correction

The final step before plotting the GLF is to calculate the density-corrected V_{max} (V'_{max}) values for the survey being used. As mentioned in Chapter 1 the standard measure of V_{max} is susceptible to over-densities and under-densities along the line of sight. These changes in density must be ‘mapped’ in order to account for them, and to create the density defined population (DDP) described in section 1.4. To define the DDP for the population out to the redshift necessary, a volume limited sample must be defined. This can be done using the information contained within Figure 3.17 showing the absolute Z -band magnitude against redshift for all objects within the catalogue that have redshifts. A cut is applied at the point galaxies are no longer detected as a function of redshift, as described by the blue dashed line in Figure 3.17, in order to define the density variations over the whole survey. However at a redshift of $z = 0.12$ the limiting magnitude of $M_Z = -19.5$, whilst offering good statistics for fitting the turnover in the GLF or GSMF, is not a good fit for truly defining the DDP at fainter magnitudes, and therefore is not sufficient for defining this function. It was shown by Mahtessian (2011) that it is possible to define different volumes within the survey limits and effectively stitch the resulting DDPs together to generate a final DDP for the survey volume. Therefore a second volume limited sample to redshift $z = 0.065$ was defined and by using Figure 3.17 as a guide this gives an absolute magnitude limit of $M_Z = -18$. This gives more accuracy in determining V'_{max} of low magnitude objects.

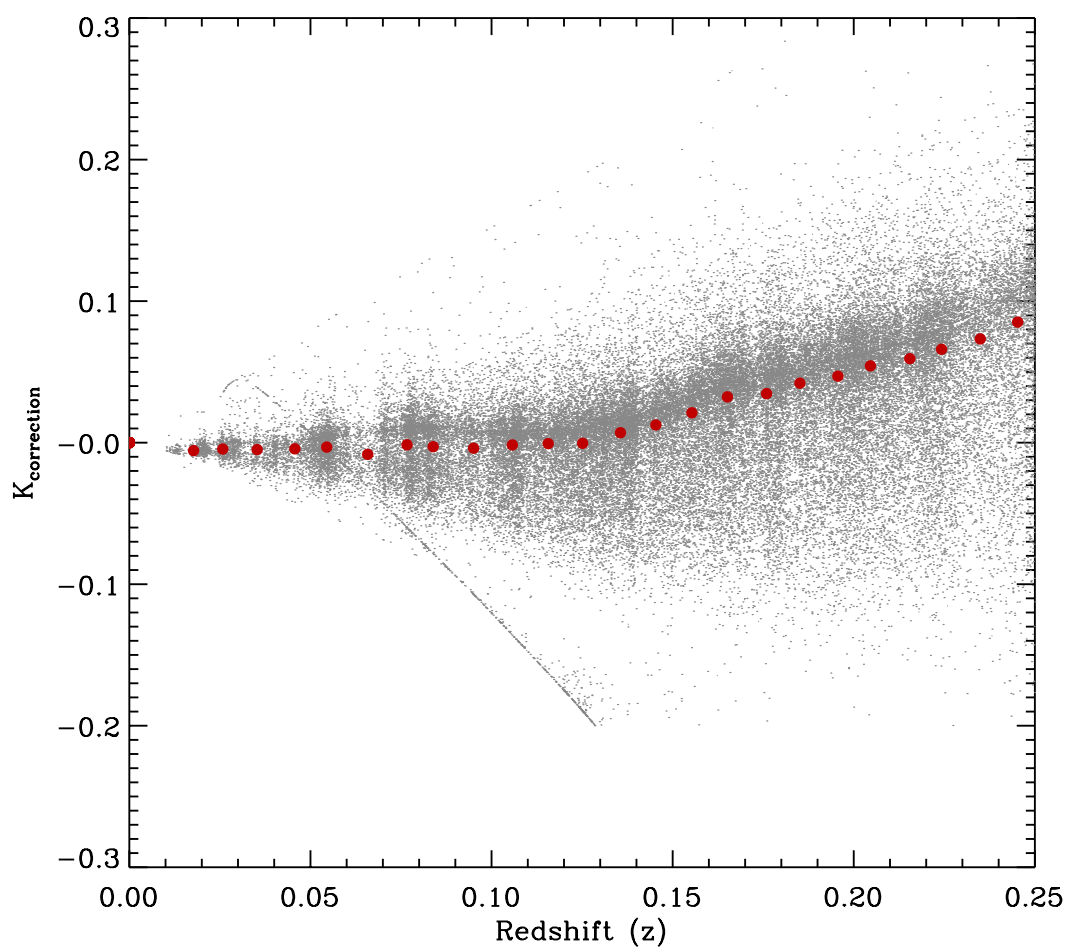


Figure 3.16: The distribution of the measured K-correction in the Z -band against redshift (z). The red points describe the median value for the K-correction at the corresponding z . The median values up to $z = 0.12$ are approximately flat. This means that the dK would be on average 0 and so no correction is needed when determining V_{max}

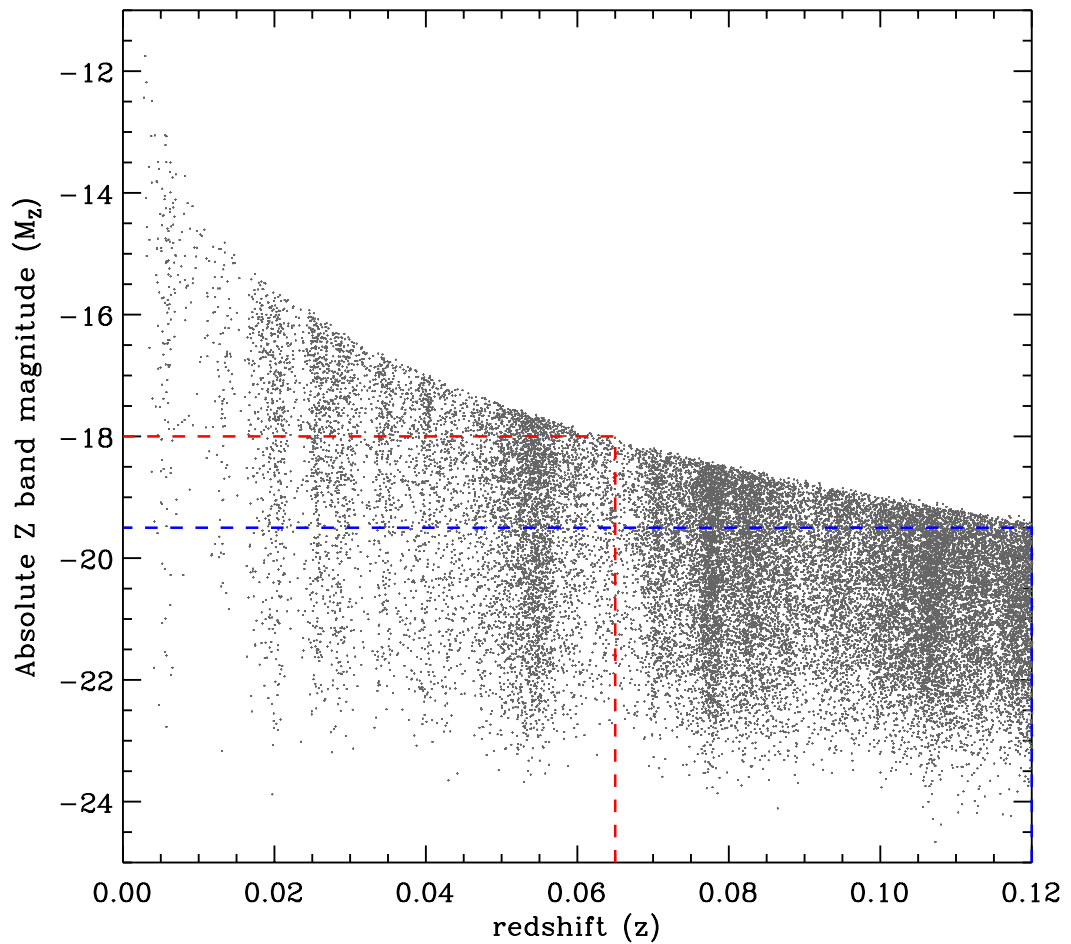


Figure 3.17: Absolute Z -band magnitude versus redshift for all galaxies with a well defined redshift measurement. The range of redshifts describes the limits used in the production of this work's GLF and GSMF. This information was used to create the volume limited samples needed to create the DDP for weighting V_{max} . The red and blue boxes define the population used to calculate the density corrections for the survey at $z = 0.065$ and $z = 0.12$ respectively.

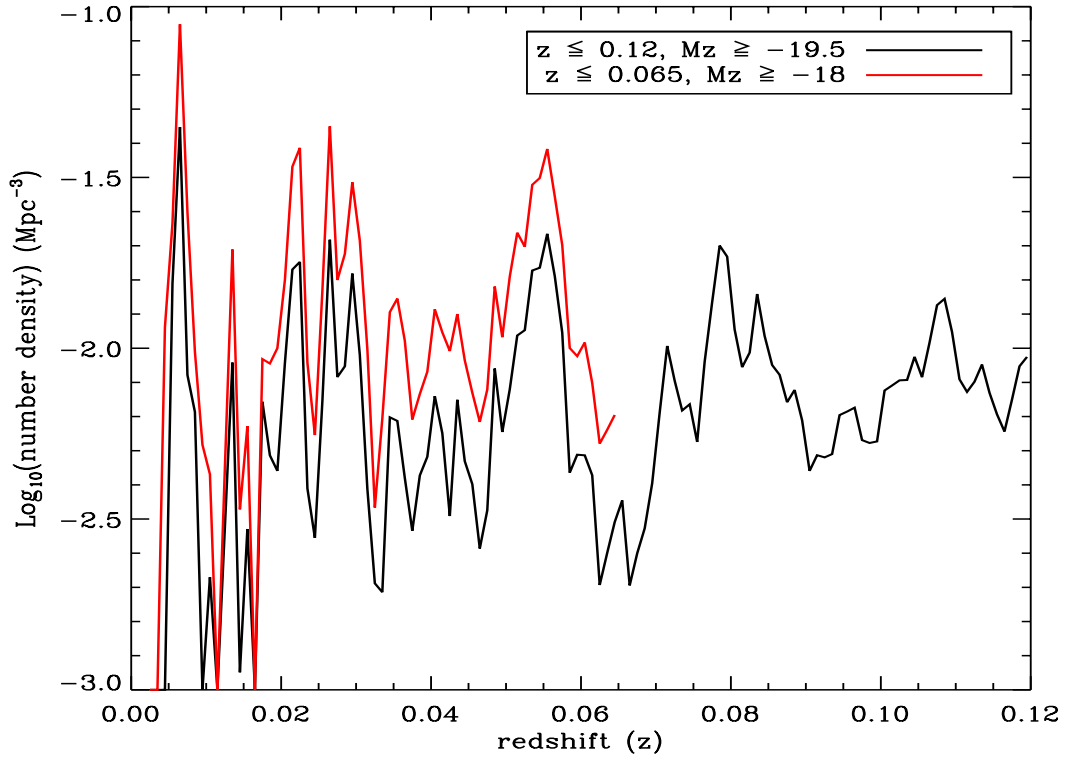


Figure 3.18: The change in number density of the population of galaxies vs redshift bin for two volume limited samples.

Figure 3.18 shows the number density per volume bin for the two volume limited samples to be ‘stitched together’ to create the DDP to be used. As can be seen in this plot there is a lower number density produced by the sample covering the most volume. This is due to the magnitude limit for the larger volume sample covering fewer of the galaxies at the low redshift range. The cumulative number density is plotted and normalised to a value of one at the highest redshift limit of the sample ($z = 0.12$).

Figure 3.19 shows this relative number density ($f_v(z) = \rho_{ddp}(z_1; z) / \rho_{ddp}(z_1; z_2)$) for the complete ‘stitched’ samples. By normalising the distribution by the maximum number density over the survey range a distribution has been created which represents the correction factor in equation 1.5. Therefore by interpolating the z_{max} value calculated for each object, using the method described in section 1.4.2, a value is generated which can be directly applied to V_{max} to create V'_{max} . Figure 3.20 shows a comparison between V_{max} and V'_{max} .

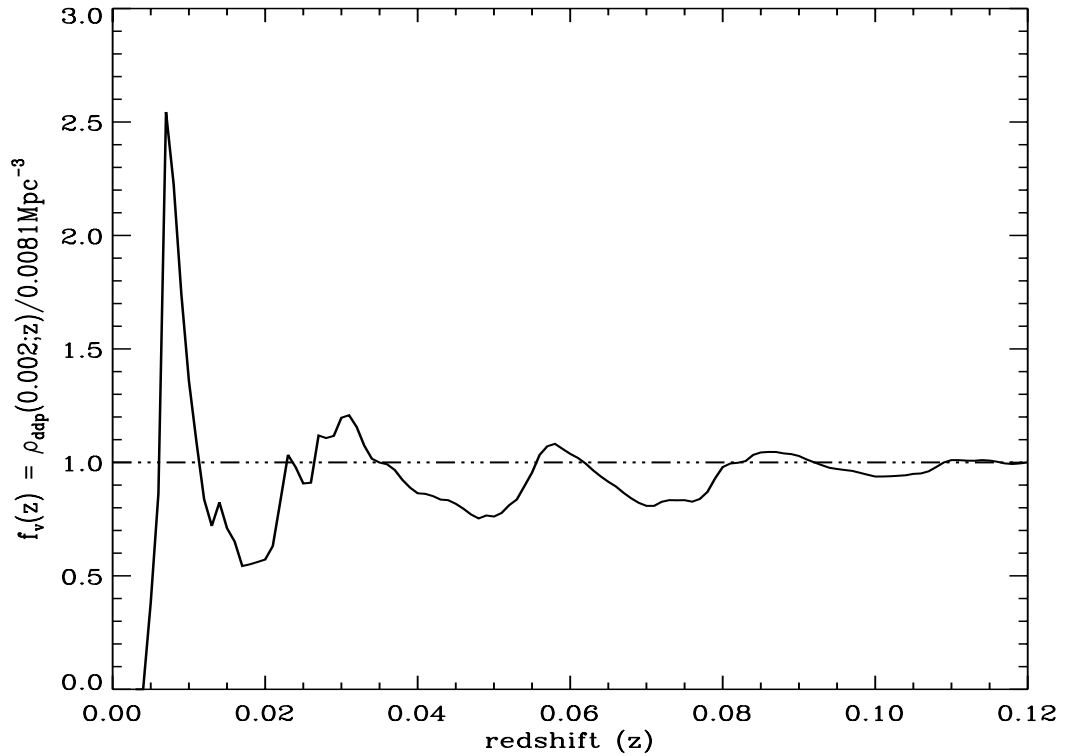


Figure 3.19: Variation in number density shown by the DDP to be used in the density-corrected V'_{max} method. The solid line represents the the number density of the combined volume limited samples divided by the total number density of the survey (0.0081 Mpc^{-3}) from $z = 0.002$ to the maximum redshift of $z = 0.12$ normalised to the highest redshift bin. The dashed line shows where over-densities and under-densities lye compared to this normalised point for clarity.

3.2.3 Calculating Completeness

The data from the GAMA II $r \leq 19.8$ survey is highly complete spectroscopically, and completeness values are near unity regardless of how the sample is divided. Here, we are using a new input catalogue which includes a large number of previously undetected objects, which means the redshift survey is not complete in some areas of the parameter space. In order to account for this, correction values must be calculated based on some physical parameters of the data in order to correct for the missing spectroscopic data in the survey.

The completeness value to be applied to V'_{max} can be calculated, in a simplistic way, by taking the bin values from Figure 3.15 and applying them to the corresponding galaxies within that bin. However, this is unlikely to produce a reliable result because the underlying assumption is that the galaxies without a redshift in a bin have similar

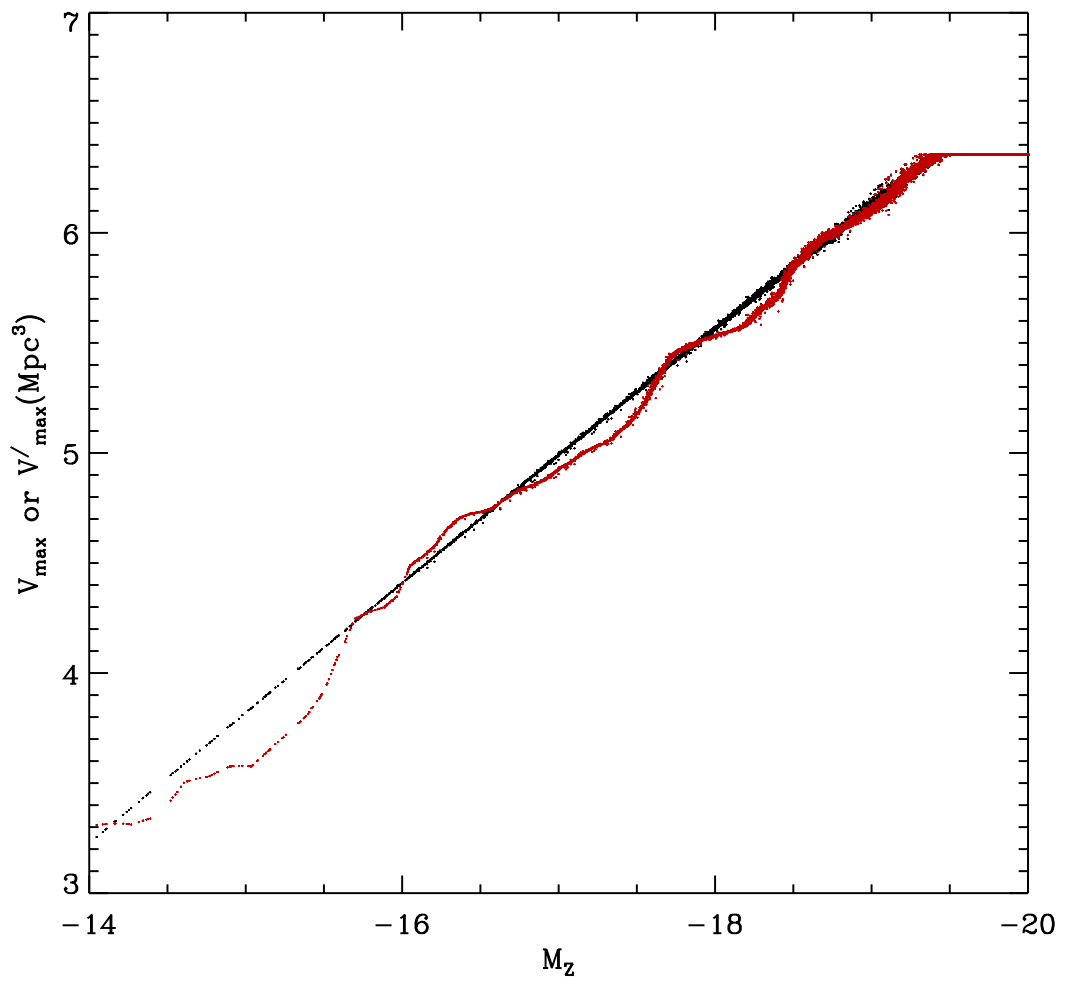


Figure 3.20: Comparison between standard V_{\max} and density-corrected V'_{\max} . The black distribution shows V_{\max} . The scatter at brighter magnitudes is from the inclusion of the K-correction on the magnitudes. The red line represents V'_{\max} . A minimum value was used for V'_{\max} of 100 Mpc³ as the DDP contains very few objects below this volume.

properties to the other galaxies within that bin. A more accurate correction which can be applied is through the use of $g - i$ and $J - K$ colours. As explained in chapter 2 these colours are linked to the redshift and SED of the system. Splitting the catalogue into different magnitude bins, and then using the colour values to two-dimensionally bin objects in the plot, ensuring more than 50 galaxies per bin to be statistically significant, generates a more physically motivated completeness correction for each galaxy. Again the value used is the fraction of photometric objects which have spectroscopy in each bin. These distributions are shown in Figure 3.21. A main assumption of the corrections therefore is that the redshift distribution of the galaxies with redshifts is the same as those without redshifts for each colour-colour-magnitude bin.

As shown on the figure the levels of completeness increase towards brighter magnitudes, however this makes sense as most of the objects in this bin will have been detected in the original GAMA survey, meaning a larger proportion of the objects will have a well defined redshift measurement, compared to the fainter magnitude bin, which has a far larger share of the newer objects found at faint magnitudes. Each object within the plots is then matched with the correction value of the bin in which it resides to obtain its C_i value when calculating the GLF or GSMF.

3.2.4 Determining the GLF

The first thing to do before determining the GLF is to define the sample to be used to create it. As discussed previously not all galaxies in the SExtracted sample can be used. For a galaxy to be included it must first fall within the redshift limits for the analysis, these limits being $0.002 \leq z \leq 0.12$. The upper limit of $z = 0.12$ was chosen as the increased volume allows the accurate measurement of the bright end of the GLF, whilst not being significantly affected by evolution and keeping good statistics for luminosity and mass bins as shown in Figure 3.17. The lower limit of $z = 0.002$ is required to remove any objects which have either been given an incorrect redshift or are stellar in nature. Another criterion to use is a parameter called nQ , which describes how good the redshift determination is for a given object as described by the GAMA samples. A

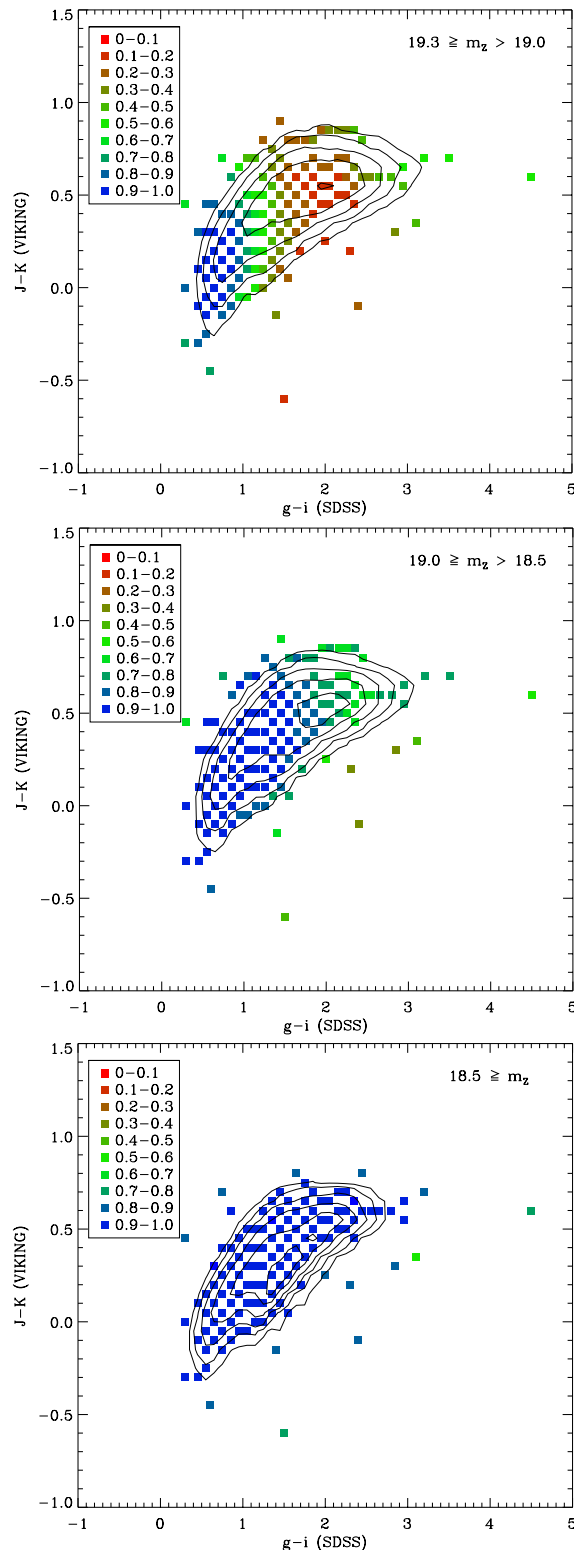


Figure 3.21: Completeness distributions based on the $g - i$ versus $J - K$ colour distribution. The contours represent the overall distribution in the data, overlaid are the bin positions. The colours are defined within the legend of each plot. The three plots represent the three apparent magnitude bins which the data were split into. These are, from left to right; $19.3 \geq m_z > 19.0$, $19.0 \geq m_z > 18.5$, and $18.5 \geq m_z$. The completeness in the brightest magnitude bin is rather uniform and close to 1 for most of the bins, whereas in the faintest bin there is more incomplete as more new objects are added to the distribution from VIKING. This is significantly larger than the magnitude of most LSBGs at distances > 10 Mpc.

limit of $nQ \geq 3$ is used to remove all poor redshift measurements. The final criterion is to use the SURVEY_CLASS parameter. This has been used throughout to ensure only ‘true’ objects are included at all parts of the analysis. Therefore only objects with a SURVEY_CLASS > 0 are used. The final set of criteria is listed below:

$$\begin{aligned}
 z &\leq 0.12 && \text{AND} \\
 z &\geq 0.002 && \text{AND} \\
 nQ &\geq 3 && \text{AND} \\
 \text{SURVEY_CLASS} &> 0
 \end{aligned}
 \tag{3.9}$$

Once all the constituent parts of V'_{max} have been defined, the next step is to combine them to create the GLF. The GLF is an important metric for measuring the number density of galaxies, as it relies only on the flux measurements of the sample.

To plot the GLF requires the application of the C_i values calculated and the density-corrected V'_{max} values calculated for each galaxy. The average C_i applied to an object within a certain magnitude bin is shown in Figure 3.22 and shows how at brighter magnitudes the correction factors approach a value of 1, showing that in terms of their redshift measurements the brightest galaxies are mostly complete.

Figure 3.23 shows the GLF plotted both with and without the correction factor applied to each galaxy. It highlights the importance of applying these correction factors to the galaxies to account for missing objects as the effect is most noticeable and significant at fainter magnitude limits.

Figure 3.24 shows the newly defined Z-band GLF compared to past GLF measurements by Kelvin et al. (2014a) and Loveday et al. (2012). The points plotted from Kelvin et al. (2014a) show the binned values calculated to an absolute magnitude limit of ~ -18 mag. They show a good agreement up to the turn over in the Kelvin et al. (2014a) data at ~ -18.5 , at which point the deeper VIKING data carries on to fainter magnitudes. The Loveday et al. (2012) results plotted here also show good agreement over the range covered by the Kelvin et al. (2014a) results, however at both bright and

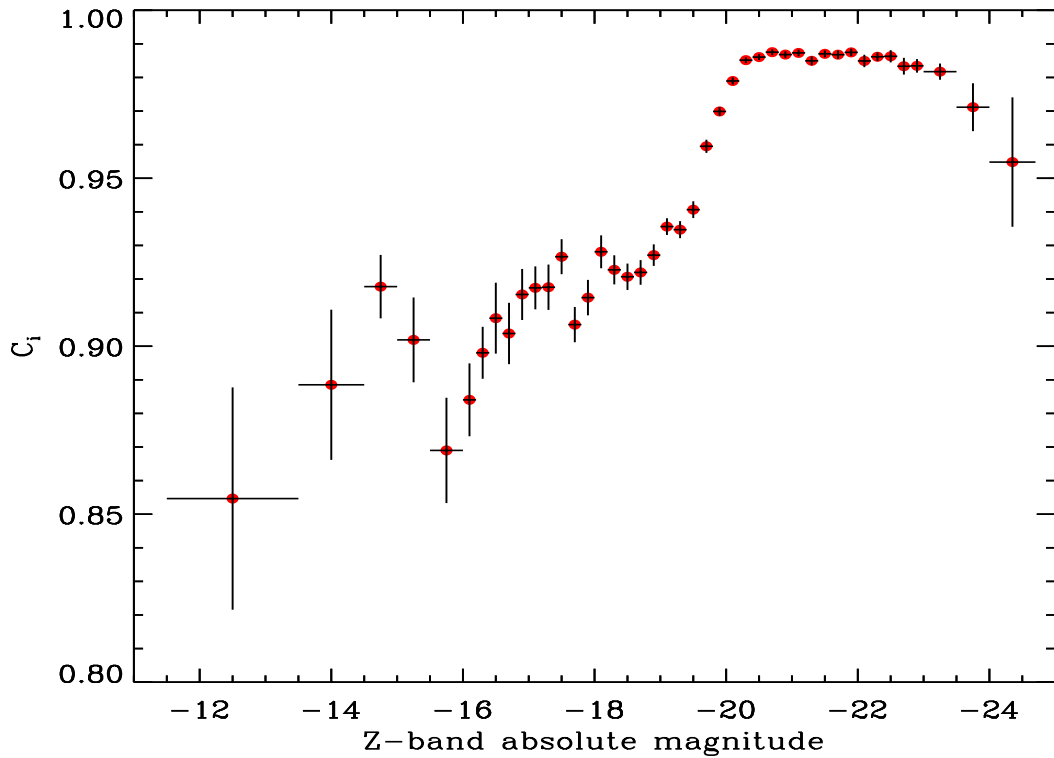


Figure 3.22: Average correction factor applied to the galaxies within each Z-band defined bin. Brighter objects tend to be in complete bins compared to their fainter counterparts. The brightest bin seems to show a decline from this trend. This is due to a small number of objects counting toward this value, and as the error shows the scatter in this bin is relatively large.

faint magnitudes the agreement breaks down. This is believed to have been caused for several reasons. At the bright end of the function it appears that the measured number density is below that of Loveday et al. (2012), this may have been caused by the way the objects fluxes have been measured in the two studies.

As already mentioned the magnitudes in this study were measured using AUTO apertures, whilst those from Loveday et. al. were measured using Sersic apertures. The AUTO apertures may have failed when trying to measure the larger galaxies which would mean the magnitude was being underestimated for the systems meaning the bright end of the GLF looks under-dense. At the faint end the problem is the opposite way round, the Loveday et. al. results are now under-dense compared to the new results. This isn't so much of a problem as an increase was expected due to increased sensitivity to LSBGs within the VIKING Z-band study, however this is a large difference. There are several possible contributing factors to why there is such a large

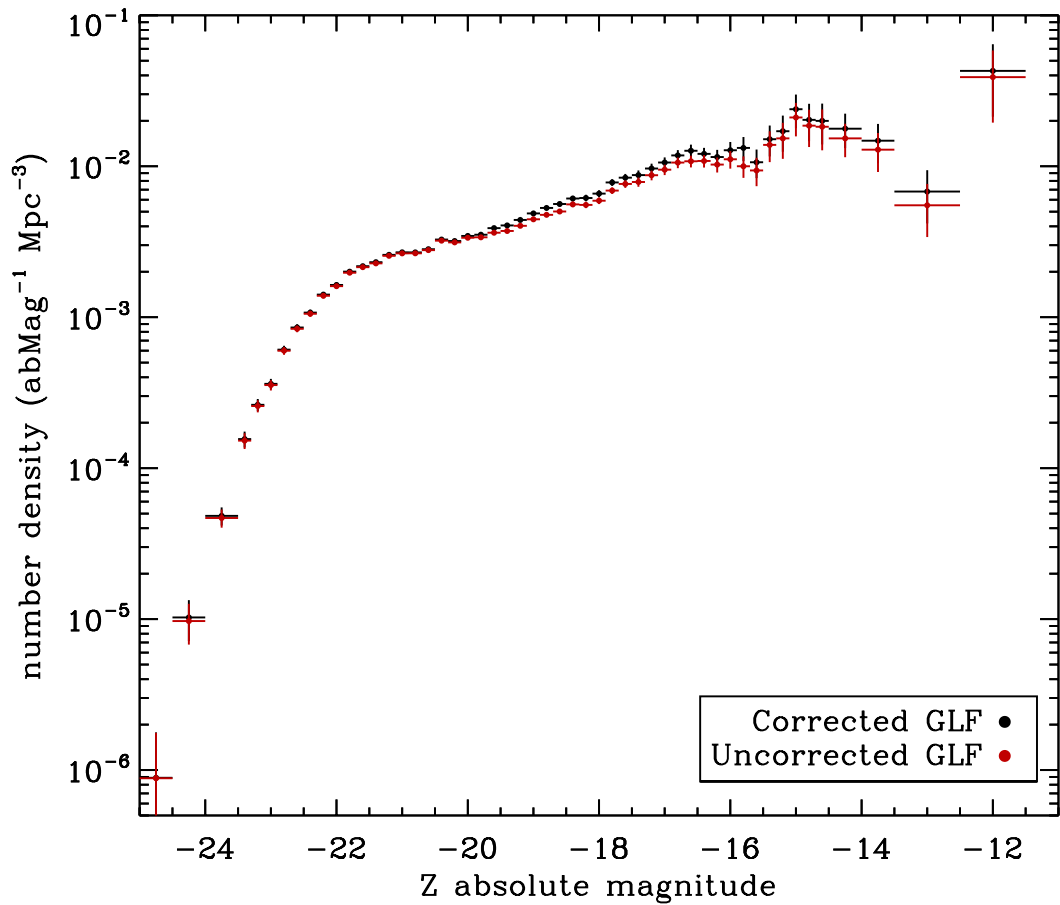


Figure 3.23: The GLF with corrections both applied and not. When taken in conjunction with Figure 3.22 it can be seen why the largest effect is on the fainter bins, where the spread in correction factors is greatest. These corrections mean the V_{max} value decreases for each galaxy thereby making $1/V_{max}$ larger and inflating the value of the bin it is contained in. The effect is most noticeable when a large number of the objects which make up the bin are corrected by values lower than 1.0.

difference between the results of this survey and those of Loveday et al. (2012). A difference in how the C_i values were calculated could lead to a difference especially at the low mass end of the function. Another possible reason could be the density correction, which was performed using a different method to this VIKING Z -band survey. And also the measurements have been made in different images and slightly different filters, the Loveday et al. (2012) results being measured in SDSS z -band and the results of this survey, as already mentioned, being measured in the VIKING Z -band. All of these reasons could have contributed to the eventual discrepancy at the low mass end resulting in a lower correction being applied to the results of Loveday et al. (2012).

A contributing factor to the under-density may be the C_i values calculated for the two studies, as Loveday et al. (2012) used several factors to calculate the incompleteness in each bin, namely the spectroscopic incompleteness, incompleteness due to surface brightness, and incompleteness in the survey in general. This may have led to an overcorrection at the faint end of the distribution and so sits lower than if a similar correction had been applied to the new study.

Comparison with the Cluster Environment

A comparison between clusters and the field when discussing the GLF is interesting at this point. As stated in Chapter 1, when cataloguing a cluster environment focused searches of a fixed region are carried out, making it easier to refine a survey to detect LSBGs in the cluster. Ferguson & Binggeli (1994) did a comparison of GLFs, primarily looking at dwarf ellipticals, within the cluster and field environments. They find that in general the low luminosity end of the functions is where you see the biggest difference with steeper slopes exhibited at the faint end of the function in clusters compared with the field. This conclusion is also supported in this work when comparing Figure 3.24 and Figure 3.25, taken from Popesso et al. (2006). They are a good comparison to the field GLF presented here as they include the SDSS z -band and use a composite of ~ 70 clusters from the RASS-SDSS galaxy cluster survey. There is a clear ‘steepening’ at the low luminosity range in their results. Note that the measurement at the

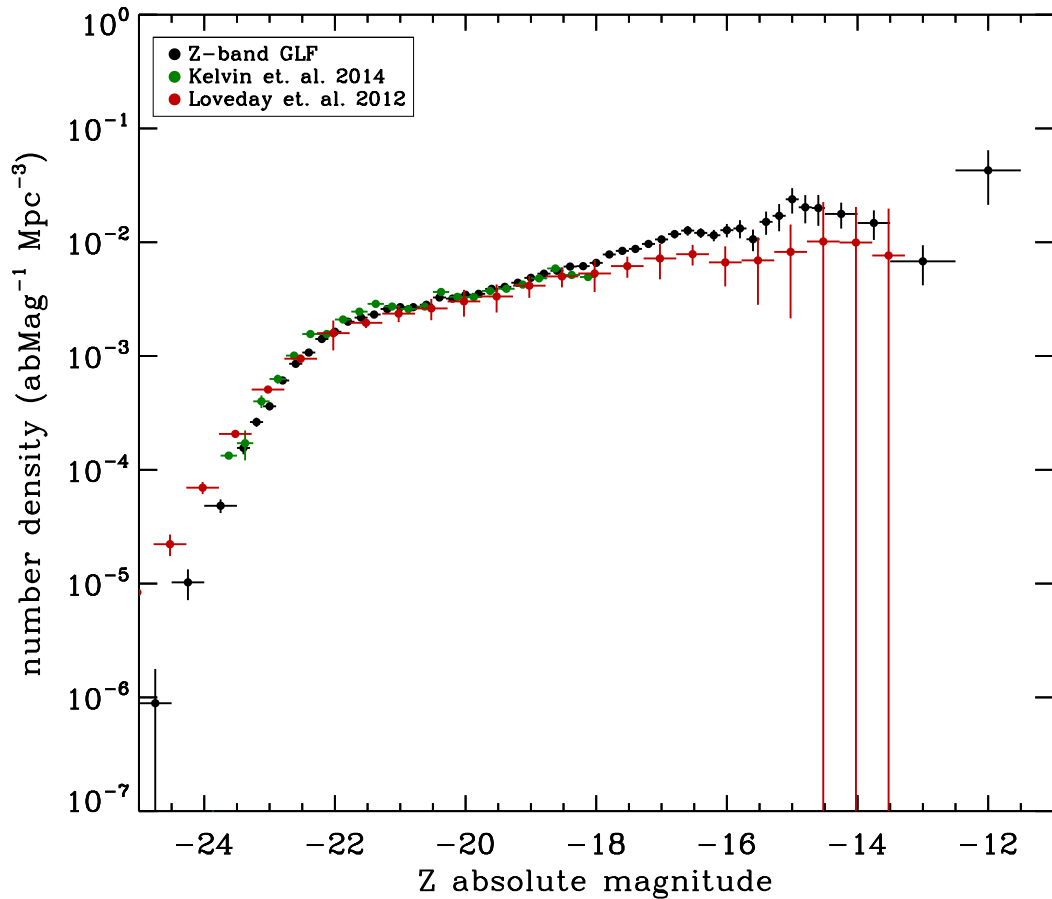


Figure 3.24: The GLF as compared to other studies from Kelvin et al. (2014a) and Loveday et al. (2012). It shows good approximation with both past results at faint around the break luminosity for the distribution. However, at bright and faint magnitudes there appears to be some disagreement with Loveday et al. (2012). At faint magnitudes this is likely due to how the C_i values for each galaxy are calculated in the different studies. Loveday et al. (2012) uses several factors to come to a final result, namely surface brightness, colour and overall completeness of the survey. This may lead to some differences in correction in the faint magnitude bins. The discrepancy at bright magnitudes may be due to the way the magnitudes are measured. Loveday et al. (2012) use a Sersic aperture whereas the apertures from this study are Auto. Some auto apertures may be failing at bright magnitudes meaning the flux may have been underestimated for some galaxies, which may explain the discrepancy.

lowest luminosities relies on photometric selection of cluster galaxies. They do not have redshifts to these low luminosities.

A conclusion of this could be that there are more low luminosity galaxies as a whole in clusters pushing up the number densities compared to the field. Another could be that due to the difficulties in discovering LSBGs in the field compared to the focused survey of a cluster that this is simply a selection bias and a by product of better SNR in cluster surveys. Various studies have been carried out on whether there is a surface brightness selection effect in the construction of the GLFs for the two environments and have concluded that this selection effect could not wholly account for the differences (eg. Lacey et al., 1993). The most compelling argument for the difference other than selection bias is the environmental differences. Clusters are by their nature more gravitationally turbulent than the field with more interaction between systems. Tidally stripping galaxies, mergers, other gravitational effects could all come together to ‘create’ more of these low mass systems than are seen through non turbulent hierarchical formation.

3.3 Galaxy Stellar Mass Function

As well as the luminosity function it is also important to plot the mass function as a cosmological check to simulations. To do this masses must be estimated for the objects in the catalogue with defined redshifts, however none of the corrections or V_{max} values need to be recalculated. This is the strength of the density-corrected V_{max} method (Baldry et al., 2012) as the assumptions of the completeness corrections hold. As stated in the above sections the binning to calculate the completeness was carried out using colour-colour-mag parameters and assumes that the redshift distribution for galaxies without redshifts is the same as those with. Of course when estimating the masses of the systems a mass to light ratio (M/L) is used which will depend on colour, and the method employed to calculate the completeness will be dependent on the M/L and the approximate redshifts of the systems, however this is the procedure for estimating the GSMF given a spectroscopically incomplete Z-band limited sample. The following

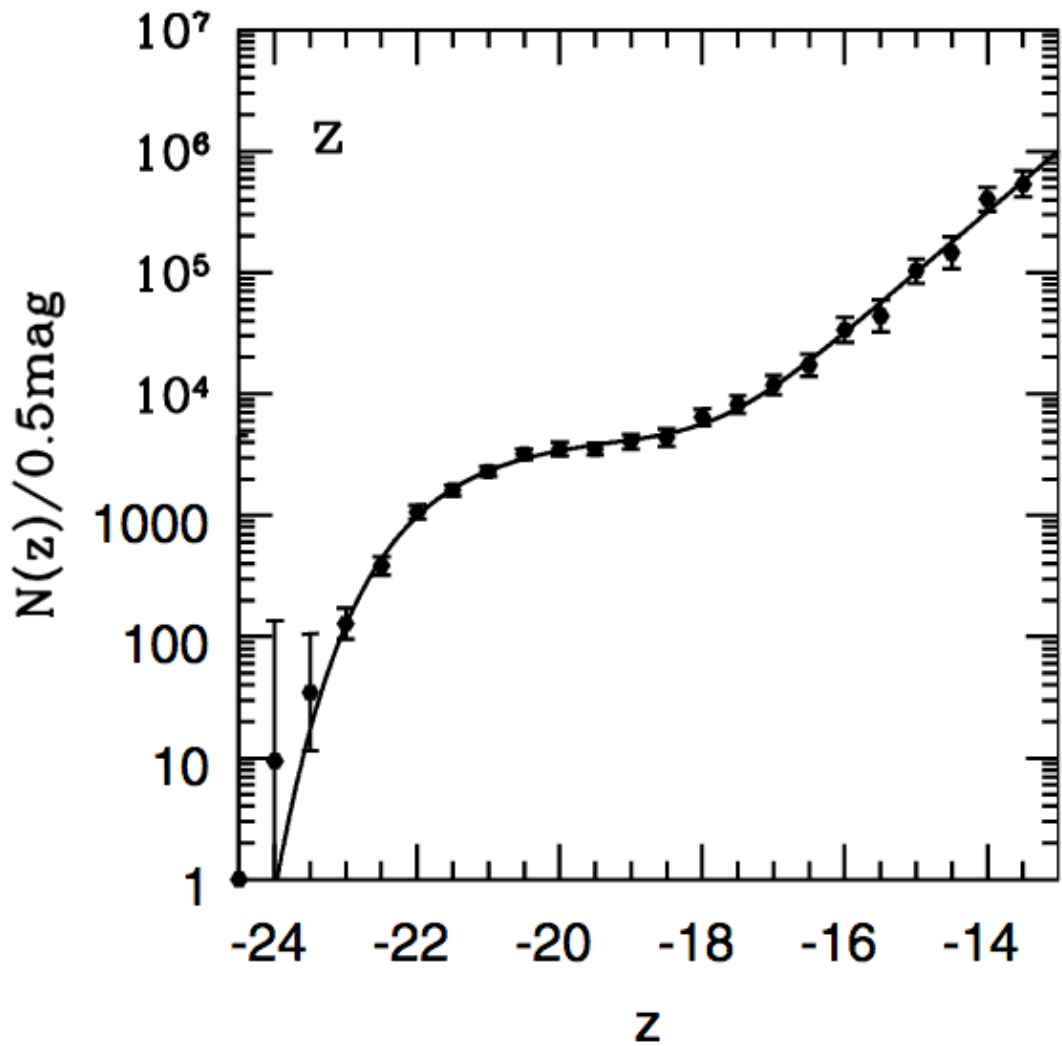


Figure 3.25: A composite GLF taken from Popesso et al. (2006) from the SDSS z -band. The composites are made up of the conglomeration of ~ 70 galaxy clusters. As can be seen there is a clear steepening of the number density of low luminosity objects, compared with that of the field GLF presented in this work and others, as shown in Figure 3.24.

sections will describe estimating the masses for the sample of galaxies and plotting the GSMF.

3.3.1 Mass Estimation

The mass function is created in the same way as the luminosity function, and because the sample being used is the same all of the V_{max} , k-correction, C_i , and density corrections are the same for the objects being plotted. The only noticeable difference is that masses are now assigned to each galaxy. This was carried out using two techniques which have been shown to give good approximations for masses. The first using a linear equation based on the rest frame of the observed systems as laid out in Taylor et al. (2011). The second utilises spectral template fitting as produced by the code to measure the K-corrections for the galaxies (KCORRECT v4.2; Blanton & Roweis, 2007).

It has been shown that the M/L of a system in the i -band or Z -band can be well approximated from the $(g - i)$ colour of the system using a linear approximation (Gallazzi & Bell, 2009; Zibetti, Charlot & Rix, 2009; Taylor et al., 2010):

$$\log\left(\frac{\mathcal{M}}{L_i}\right) = a + b(g - i) \quad (3.10)$$

where \mathcal{M} is the stellar mass and L_i is the luminosity in solar units. Estimates of a and b vary greatly in the literature, for instance Bell et al. (2003) found values of $a = -0.152$ and $b = 0.518$ whereas Zibetti, Charlot & Rix (2009) give $a = -1$ and $b = 1$. However, Taylor et al. (2011) were able to constrain values from fitting to the GAMA data of $a = -0.68$ and $b = 0.73$. These values are close to those obtained in some other studies, for example Kauffmann et al. (2003) fitted to SDSS colours and produced stellar mass estimates.

Blanton & Roweis (2007) use template fitting to SEDs to estimate the stellar masses, and is presented as a by product of their efforts to produce k-correction estimates for objects within the survey. This method however relies heavily on obtaining good pho-

tometry for the templates to be fitted to, if the photometry is bad then the mass estimates will be incorrect.

There is, of course, another factor which must be taken into account when using spectral fitting and that is the effect the initial mass function (IMF) will have on the outcome. The IMF describes initial distribution of stars as a function of their mass within the system. This is important as the assumptions made when choosing the IMF will have a final effect on the mass prescribed to a galaxy. An IMF where the majority of the system is made up of low mass stars will be given a different mass than those with a distribution describing a higher number of high mass stars. This topic is of course a thesis in itself and not something for this work necessarily. There is evidence to suggest that the IMF could be dependent on galaxy mass, based on spectral features and dynamics (van Dokkum & Conroy, 2012; Conroy & van Dokkum, 2012; van Dokkum et al., 2016; Conroy, van Dokkum & Villaume, 2017), which would mean using a fixed IMF may not be pertinent, however direct measures of the IMF, based on star counts in the solar neighbourhood, have shown no deviation from a Chabrier (2003) IMF (Bastian, Covey & Meyer, 2011). Based on this analysis the IMF used is that of Chabrier (2003), in order to stay consistent with the method used by Taylor et al. (2011).

Figure 3.26 shows how the majority of masses calculated using these two methods match with good agreement. There is however, an obvious population of outliers where the masses do not agree. It was initially assumed that the error came from the Taylor et al. (2011) method, and that the masses had been overestimated. However, when the population was checked it was discovered that it was in fact the Blanton & Roweis (2007) method which had caused the errors as all objects with large chi-squared (χ^2) values fell within this region. Therefore, it is decided to use a mixture of the estimated masses from the two methods. Any objects which were $\chi^2 \geq 450$ from the template fitting instead has its mass estimated using equation 3.10.

The obvious question at this point in the analysis is why not just use the linear estimation for the mass? One reason is because equation 3.10 was calculated using a template fitting method to GAMA data, and describes a best fit to those estimates, this means that the errors on these measurements are rather more unconstrained than those given

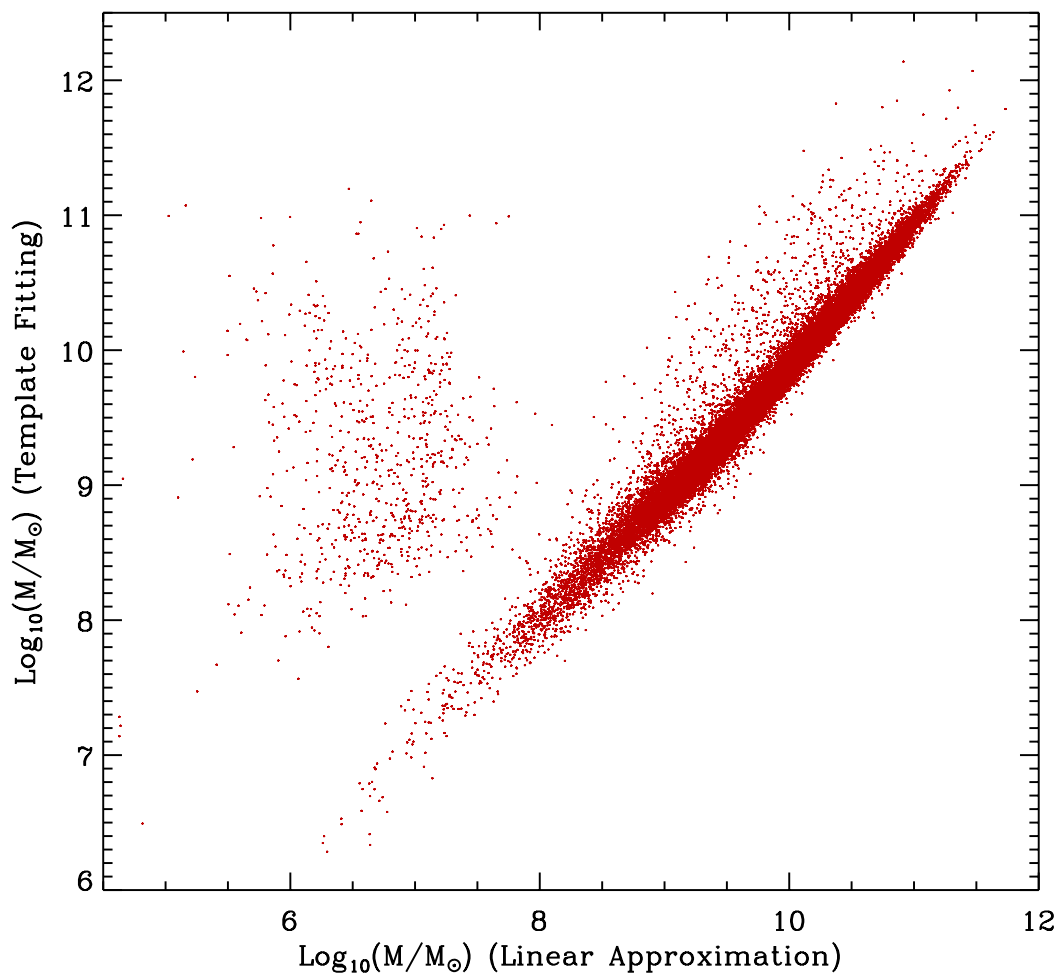


Figure 3.26: This describes the masses estimated through the two methods discussed in this section. There is a clear agreement between the two methods for the most part with some scatter, however there is a clear population where the two estimates disagree. This has been caused by poor photometry in one or more bands meaning the template fitting method has underestimated the mass of these systems. For these objects the linear approximation was used in place of the template fitted estimates.

by purely using the template fitting method. How well the linear estimation works but also the scatter at all points of the distribution can be seen from Figure 12 in Taylor et al. (2011). Also, as already stated, the masses provided through the KCORRECT v4.2 code, come with measured χ^2 values, this makes detecting bad mass estimates easier. If there is a problem with the fitting it is likely to be due to poor photometry in several bands, therefore using the linear approximation is advantageous in this scenario because only two photometric bands (g & i) are required for the estimate.

3.3.2 Plotting the GSMF

Figure 3.27 shows the GSMF of the Z -defined galaxy sample (binned values are shown in Table 3.1 plotted with the non-parameterised results from Baldry et al. (2012)). There is strong agreement between the two sets of results, as one would expect, at $M_* \geq 10^8 M_\odot$. Below this mass the points become much more unconnected as incompleteness becomes a problem. However, as was predicted in Baldry et al. (2012) the low mass end of the GSMF, when plotted using the deeper Z -defined survey data shows a marked increase in the number density.

As when plotting the GLF it is possible to compare the results to those calculated more recently within the same regions. Kelvin et al. (2014b) produced a set of GSMFs based on the GAMA data, split into morphological type in all nine bandwidths of the GAMA survey ($ugrizYJHK$). This is shown in Figure 3.27 by plotting the SDSS z -band parameterised results of all galaxies from the study. It shows that the two surveys are consistent with each other at the mass range covered.

Double Schechter Function

As mentioned in Chapter 1, the GSMF can be well fit by using a double schechter function. This is essentially two power laws which describe the shape of the GSMF generated. Figure 3.28 shows the fit to the data generated from this study, along with a comparison to that found by Baldry et al. (2012). It would seem from first glance that

Table 3.1: Binned values for the Z -band defined GSMF shown in Figure 3.27. ϕ is the number density in each bin. The errors were calculated as the square root of the sum of the weights squared.

$\log(M/M_{\odot})$ mid point	bin width	$\phi/10^{-3}$ $\text{dex}^{-1} \text{Mpc}^{-3}$	error	number
6.25	0.5	49.4	30.4	6
6.75	0.5	75.1	31.4	29
7.1	0.2	33.5	9.2	16
7.3	0.2	47.7	8.7	36
7.5	0.2	31.5	5.8	45
7.7	0.2	24.6	4.4	74
7.9	0.2	25.6	2.7	160
8.1	0.2	28.0	2.0	282
8.3	0.2	25.6	1.4	462
8.5	0.2	20.4	1.1	656
8.7	0.2	14.6	0.62	926
8.9	0.2	13.0	0.44	1402
9.1	0.2	10.9	0.30	1971
9.3	0.2	9.36	0.21	2598
9.5	0.2	7.83	0.16	2908
9.7	0.2	6.85	0.14	2893
9.9	0.2	6.34	0.14	2753
10.1	0.2	5.89	0.12	2623
10.3	0.2	5.39	0.11	2392
10.5	0.2	4.95	0.11	2210
10.7	0.2	3.48	0.088	1558
10.9	0.2	2.18	0.072	958
11.1	0.2	0.889	0.045	389
11.3	0.2	0.269	0.025	117
11.5	0.2	0.0741	0.013	31
11.7	0.2	0.0118	0.0053	5
11.9	0.2	0.0112	0.0056	4

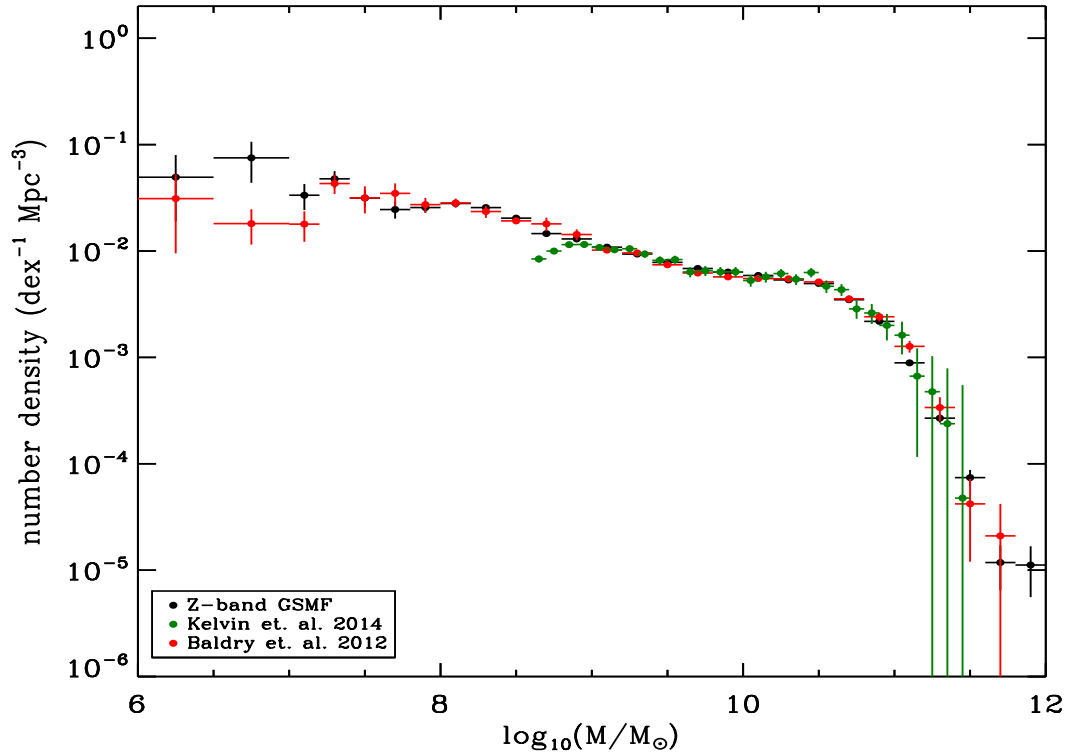


Figure 3.27: The Z -band GSMF represented by the black circles is plotted here with past survey results by Baldry et al. (2012) (red points) and Kelvin et al. (2014b) (green points). There is strong correlation between the three measurements at $M_* \geq 10^8 M_\odot$, however there is a noticeable rise in number density below this mass threshold compared to the quoted results by Baldry et al. (2012).

the data at the low mass end does not, in fact, show a rise in number density compared to Baldry et al. (2012) as stated earlier, but actually shows a shallower function for the low mass end. This is due to the way the two functions were fit to their data. The VIKING data was fit for all data points of $M_* > 10^6 M_\odot$, whereas the Baldry et al. (2012) fit was generated from only $M_* > 10^8 M_\odot$. Until this point in the two data sets there is good agreement, it is only after going to lower masses that a significant rise is seen in the VIKING data. This means therefore that the rise seen in the fit to the Baldry et al. (2012) data is not a representation of the data below $M_* = 10^8 M_\odot$, and is in fact only an extrapolation of the data to that point.

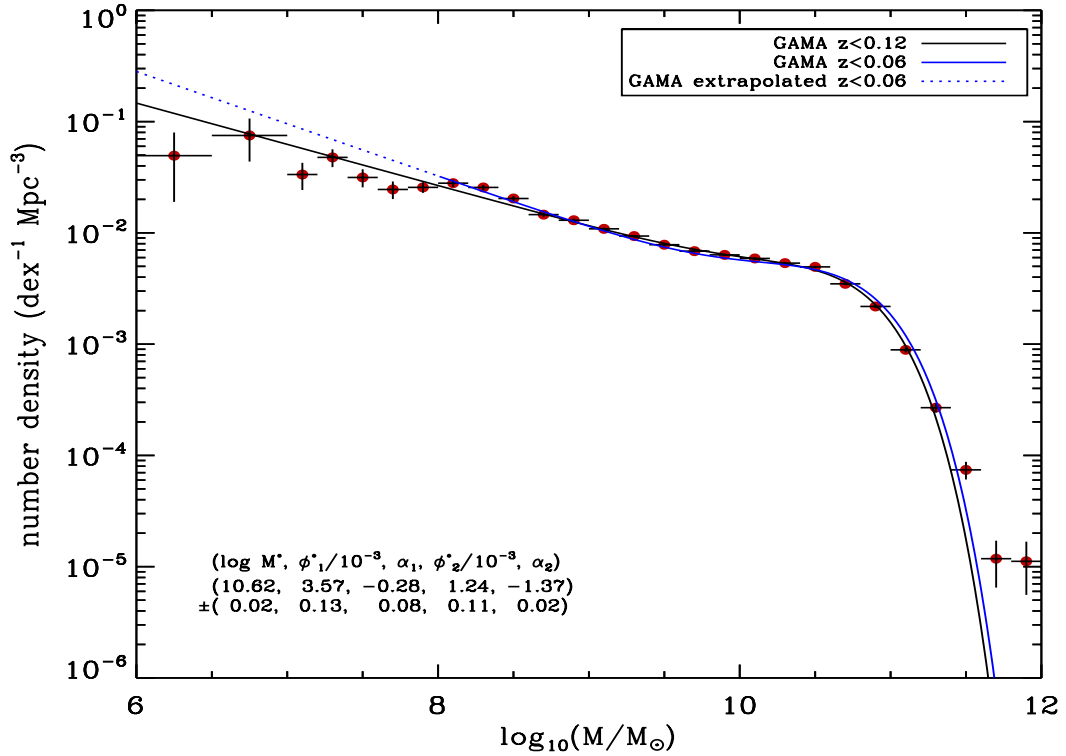


Figure 3.28: The black line represents the fit to the data of $M_* > 10^6 M_\odot$ for all galaxies at redshifts of $z < 0.12$. The blue line is the Schechter function produced from Baldry et al. (2012), which shows good agreement until $\sim 10^{8.5} M_\odot$. This is due to the data only being fit to $10^8 M_\odot$ meaning after that point is just extrapolation of the line.

3.4 Discussion

3.4.1 Defining the completeness correction

In determining the GLF or GSMF for the survey care must be taken to account for those galaxies which do not have accurate redshift measurements. To do this a completeness correction (C_i) is applied to the galaxies with redshifts, which is based on the number of galaxies which have a similar distribution in some parameter space. This means that there is an underlying assumption that the redshift distribution of galaxies with redshifts is the same as those without redshifts.

In section 3.2.3 the process of defining the final C_i values for the galaxies was described. The method used was a 3-dimensional binning of the available data using $g - i$, $J - K$, and finally the apparent Z -band magnitudes of the systems. Other meth-

ods of calculating C_i were tried, one of which is briefly mentioned in section 3.2.3, a 1-Dimensional (1D) method, binning by the apparent Z -band magnitude of the objects and using the spectroscopic completeness in each of these bins to determine a correction factor as defined in Figure 3.15. Another using the surface brightness and apparent magnitude of the objects, to determine the correction, in a similar way to the 3D method with 2D binning. The initial distribution is shown in Figure 3.29 where the newly discovered VIKING objects have been separated from the already defined GAMA sample to indicate the parameter space defined by the new objects. The distribution was broken up into bins, defined by a central point and the spectroscopic completeness of each bin is measured, the resulting C_i values are shown in Figure 3.30.

However, when using these other methods to plot the GLF and GSMF there was a rise in the number densities for $M_* \leq 10^{9.5}M_\odot$ in the GSMF, this is best illustrated in Figure 3.31. The C_i value relies on similar galaxies being grouped together into each bin so as to correctly ascertain where there needs to be a correction, however relying so heavily on the apparent magnitude of the systems leads to a situation where a high mass galaxy is sitting in a bin with very low completeness due to having a faint apparent magnitude. It will not necessarily be grouped together with similar galaxies. This is illustrated in Figure 3.32.

When taken in conjunction with Figure 3.30 it becomes clear why there is an issue in calculating the completeness this way. By plotting the Z -band apparent magnitude against the stellar mass of the systems it becomes apparent that using apparent magnitude as a parameter in this way will not work, as there is a spread in the distribution which covers the lowest masses up to $\sim 10^{9.5}M_\odot$ at the faintest magnitudes, which correspond to the lowest completeness bins in Figure 3.30. This means that although some of these galaxies will have been well sampled due to their higher mass, that the GSMF at $M_* \leq 10^{9.5}M_\odot$ will be artificially raised by the presence of low completeness systems. This is ultimately why a colour distribution was chosen as this bias is not present.

By using the $g-i$ vs $J-K$ distribution split into apparent magnitude bins this problem

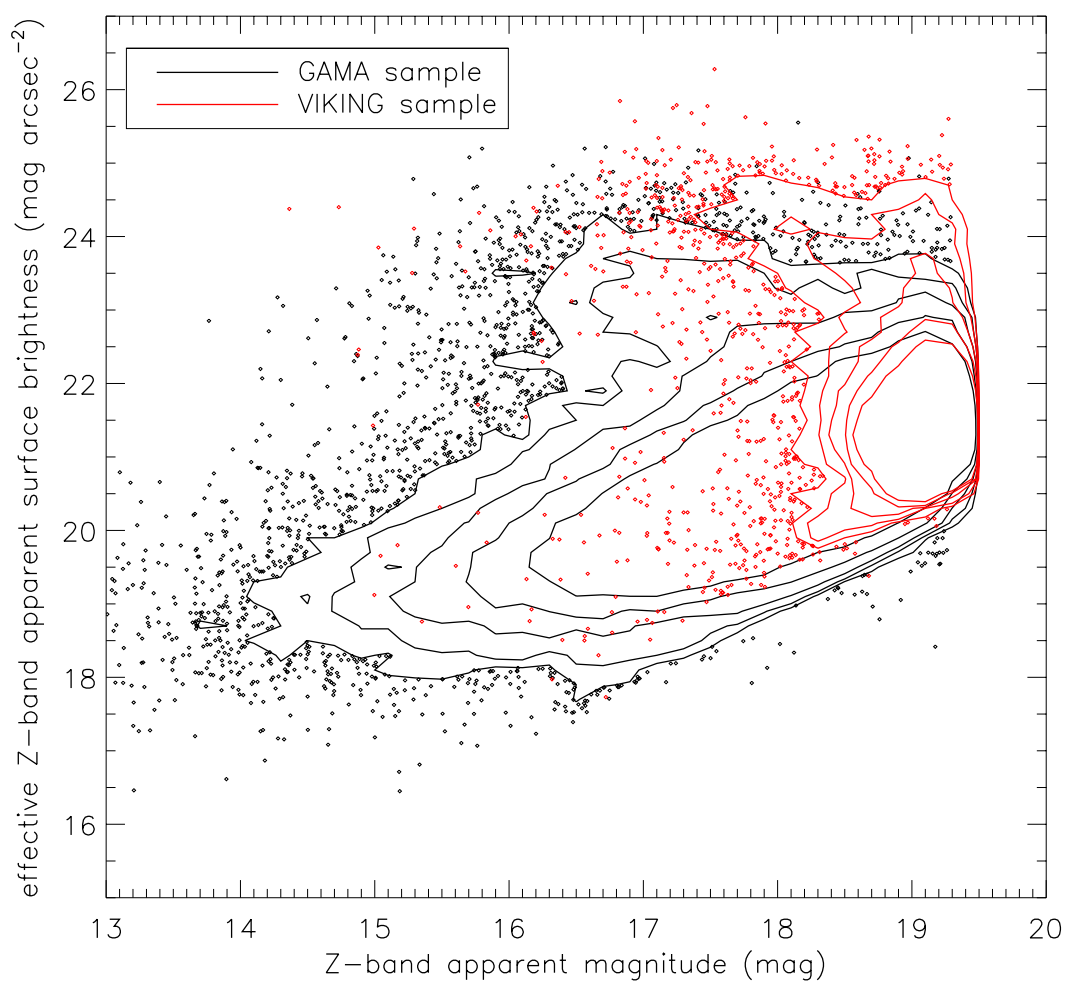


Figure 3.29: The two sets of contours are created using the same binning (0.3×0.3) and levels (10, 20, 40, 80, and 160). All data is selected to have, `survey_class` ≥ 1 which means that they have at least not been confirmed to be erroneous. The bulk of the newly detected VIKING objects sit at the far end of the original distribution, this shows the high completeness of the original study at magnitudes brighter than the SDSS survey limits. There is also seen an extended distribution of objects which have faint magnitudes and surface brightnesses, showing the improved detection rate of LSBGs, however it must be stated that not all objects have been visually checked and some may turn out not to be real.

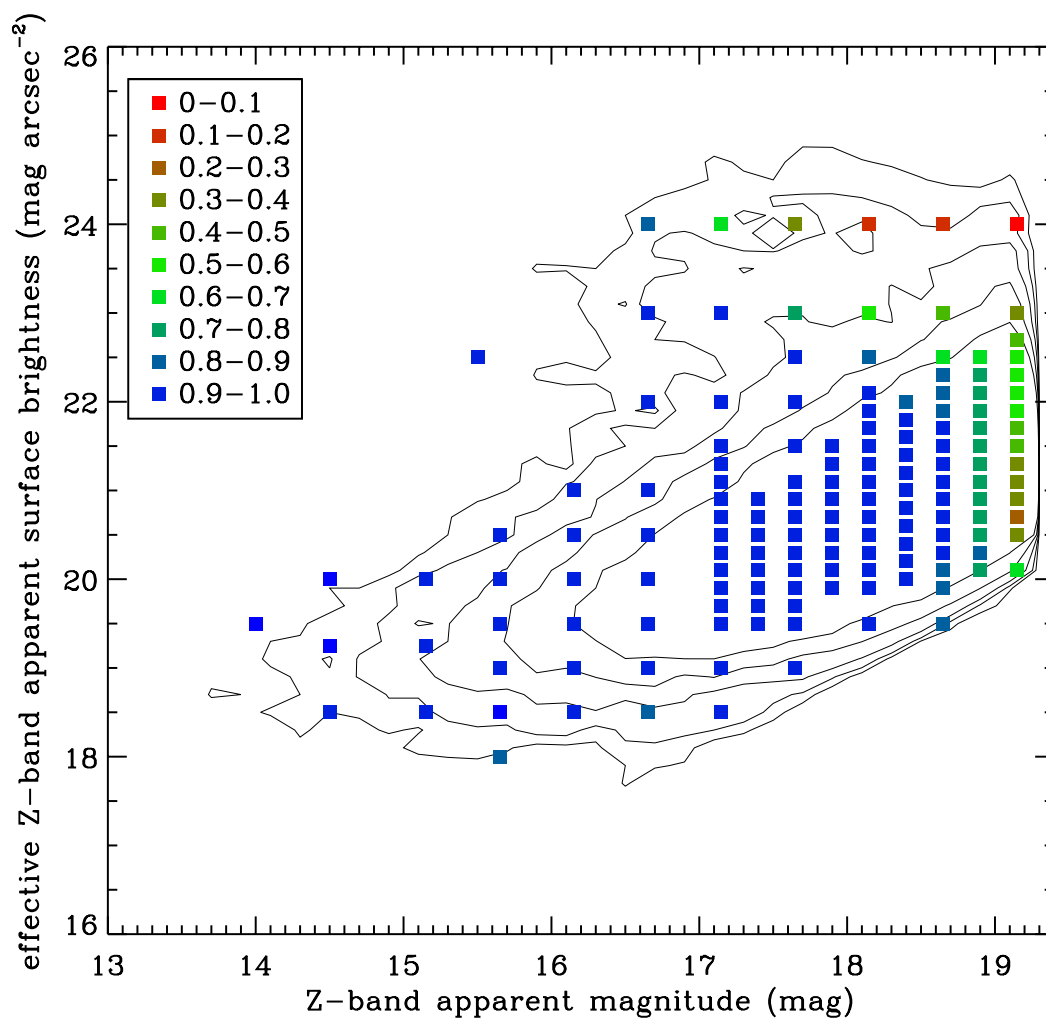


Figure 3.30: Using this information correction factors were generated as the spectroscopic completeness of the bins, represented approximately by the color of the bin. Again showing how as fainter magnitudes are approached more of the galaxies have no defined redshift, due to the newly discovered objects populating that area of the distribution shown in Figure 3.29. The legend describes the completeness of the bins in the plot.

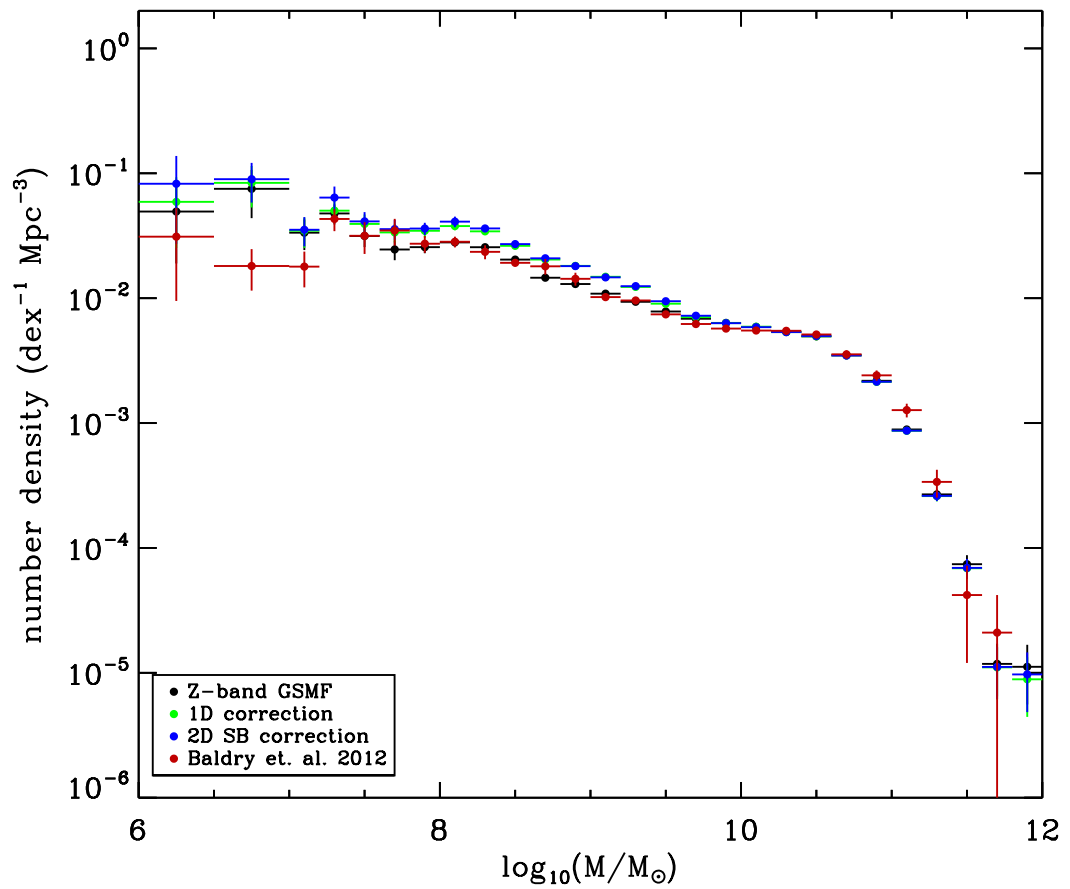


Figure 3.31: The GSMF using different C_i values to determine the final correction. The C_i values were calculated using a 1D method, 2D method using Surface Brightness, the GSMF calculated in Baldry et al. (2012) and the method used in this thesis. The rise in number density in all bins of $M_* \leq 10^{9.5} M_\odot$ is clearly seen, showing a systematic overcorrection as galaxies are grouped which do not have similar redshift distributions.

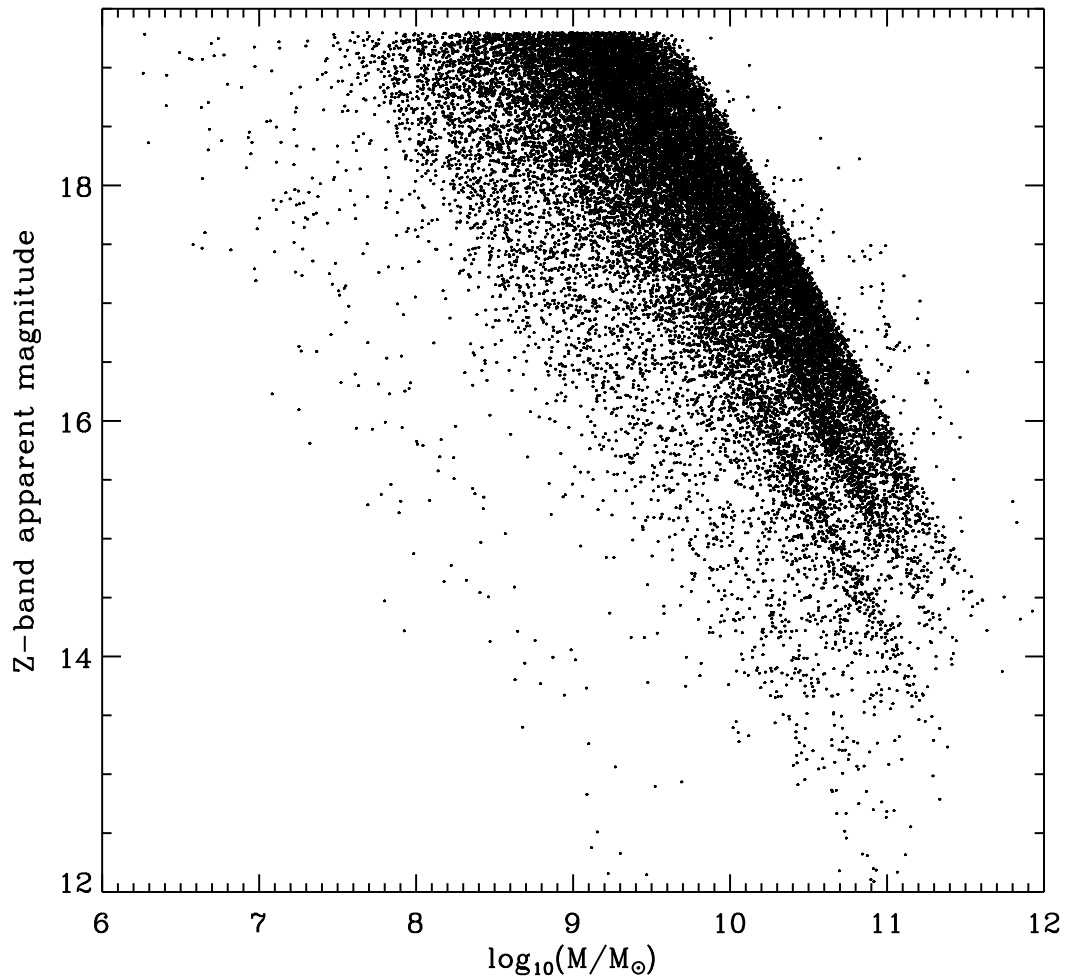


Figure 3.32: Showing the distribution of Z -band apparent magnitude against mass using those galaxies with redshifts. The spread of mass at each apparent magnitude bin shows how galaxies which may be well sampled, for instance those with a mass of $M_* \sim 10^{9.5}M_{\odot}$, are being affected by the large number of new objects at faint apparent magnitude. When taken in conjunction with Figure 3.29, where it is clear to see the low completeness bins at faint magnitudes, the issue becomes more apparent. Because of this bins of $M_* \leq 10^{9.5}M_{\odot}$ have their values increased due to low completeness. The stripes are naturally occurring due to large scale structure in the GAMA regions.

can be reduced. As the distribution has some connection to the redshift of the objects creating it as outlined in Chapter 2, means that it is more likely that objects in a bin are more closely related to the objects occupying that same bin. This in the end is why this distribution is used to correct for missing redshifts in the volume.

The problem with completeness

During this chapter great emphasis was placed on measuring the completeness of the survey, based on the number of photometric objects with spectroscopy, using different constraints to quantify completeness values (magnitude, surface brightness, and colour). However these completeness corrections were based on the idea that the photometric survey had a completeness of 1 across all magnitudes within the survey limits. Whilst this may be true for brighter magnitudes ($Z \lesssim 17.5$) the same cannot be said for fainter magnitudes. As the magnitude and surface brightness limits are approached for a survey the completeness of that survey will start to go down as objects are not detected due to surface brightness.

The cut of $Z = 19.3$ in this survey was based mostly on using Figures 3.12. This shows that the number of galaxies increases as a power law when measured as a function of apparent magnitude. When this distribution turns over it is assumed that the completeness limit in magnitude is reached for the survey. However is this really true? It must be assumed that this is the case when conducting a survey, as it is impossible to quantify what one does not know is there, but in reality it is a harder question to answer. This is a technique used in other surveys to determine where the completeness limit of said survey lies, for instance GAMA, but using deeper imaging more objects are discovered which fall in the parameter space of the original survey e.g. Figure 3.29, therefore the assumption that the photometric completeness is 1 is unlikely to be accurate. In the next Chapter, we describe a pilot study to search for LSBGs missed in the Z-band by the standard SExtractor run.

There will always be an issue with surface brightness limits when conducting a large survey, and therefore the true photometric completeness of the survey will always be a

problem. However the method used here at least limits the chances of missed objects by using the apparent magnitude of the objects to limit what goes into the final catalogue. As advances in telescope and detector technology continue to push to fainter magnitudes the lower limit imposed on the data for being complete will continue to be pushed also. The author of this work fully expects that the catalogue presented here will have new objects included within the survey limits of this survey from future work.

3.4.2 LSBGs within the study

Figure 3.29 gives an indication that the number of known LSBGs within the survey area has been increased relative to the original GAMA catalogues. These have been checked to ensure the detections are not due to image quality issues. As discussed earlier in the thesis the definition of an LSBG is not completely set, the main threshold of surface brightness has not been definitively tied down in the literature, however most studies of these objects use the definition Impey, Burkholder & Sprayberry (2001) of $\mu_{central,B} \geq 23 \text{ mag arcsec}^{-2}$. This is not useful in this case as information is not gathered on the objects in the B -band therefore, using Figure 3.29, and the definitions defined in Chapter 1, a limit is set of $\mu_Z \geq 23 \text{ mag arcsec}^{-2}$, based on the maximum limit of the main bulk of objects in the survey at low magnitudes. This limit more than doubles the number of objects within this range, from 1021 objects from the GAMA catalogues to a total of 2692 objects in the newly created catalogue, an increase of $\sim 164\%$ over the old survey. Some examples of LSBGs found within the survey are given in Figure 3.33, this is only a small selection of the LSBGs from the study, and only includes galaxies with a surface brightness greater than $\sim 23.5 \text{ mag arcsec}^{-2}$. This was just the parameter space visually searched for erroneous detections and notes were made as to any good examples of LSBGs which had been discovered.

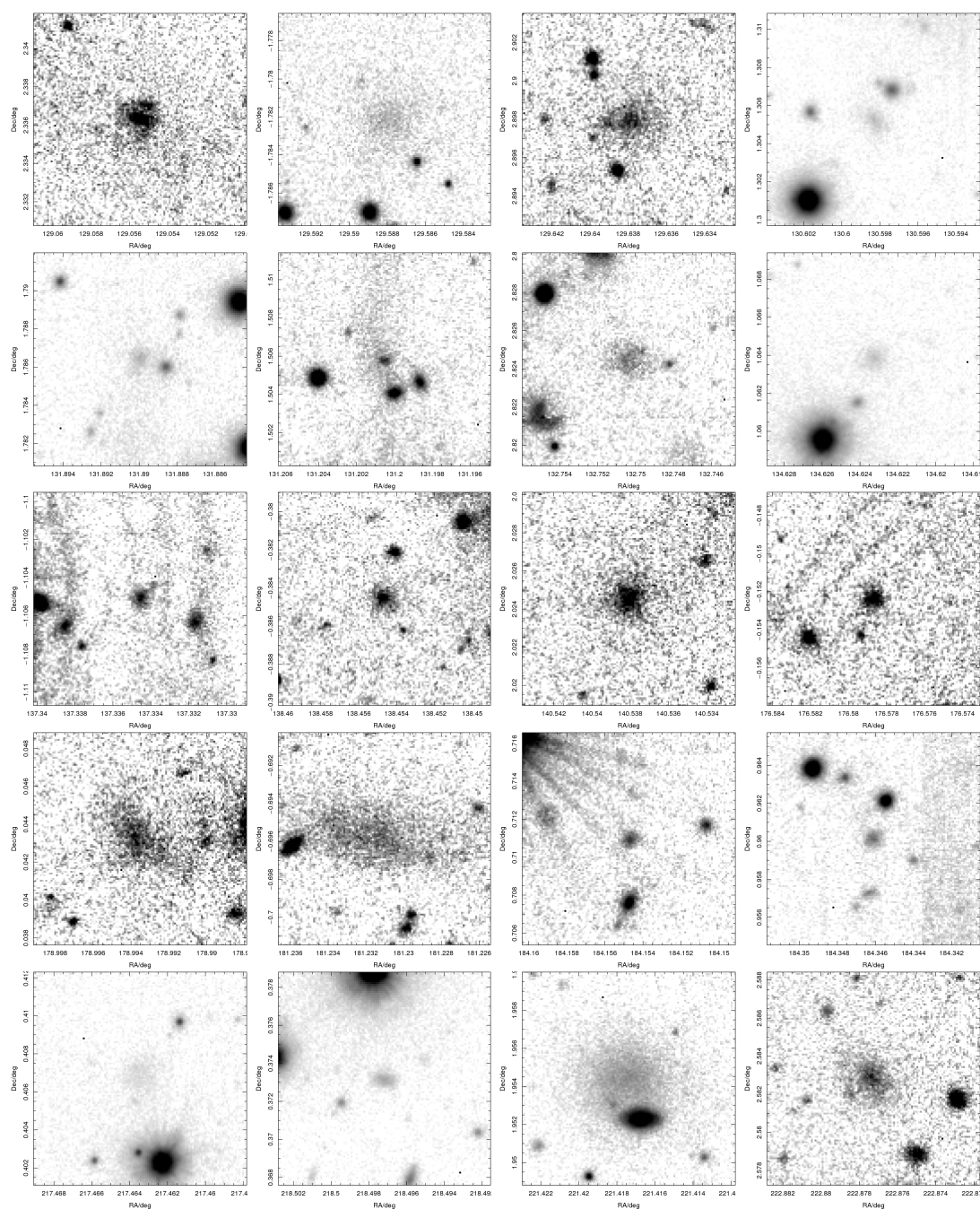


Figure 3.33: The figure shows a small sample of some of the LSBGs which were detected using the VIKING image data. As can be seen most are diffuse objects which are difficult to pick out against the background even with the eye, which is good at pattern recognition. The frames are centred on the objects of interest and are $20'' \times 20''$

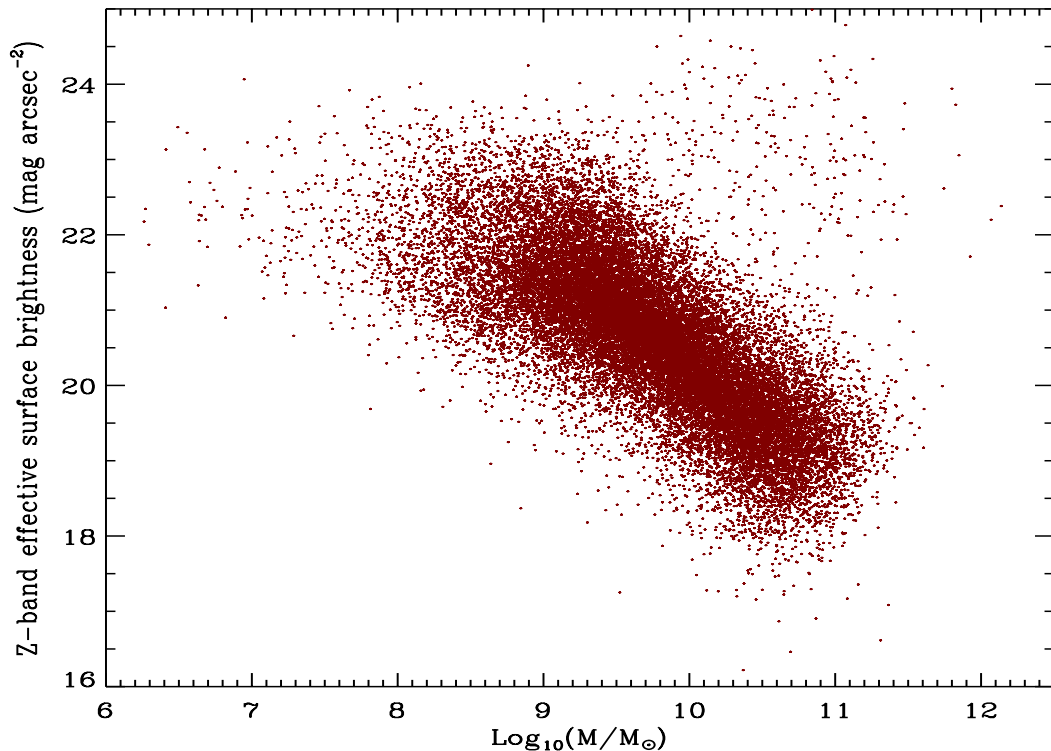


Figure 3.34: Only galaxies with good redshifts i.e. $nQ \geq 3$ are included in the plot. This was to be compared to Figure 11 in Baldry et al. (2012) as a sanity check that the surface brightnesses were sensible and followed a similar trend to the original GAMA survey. The points which fall in the upper right of the plot however needed to be checked as they lie suspiciously outside the boundaries of the main grouping. This led to the discovery of the bad images represented in Figure 3.35

3.4.3 Surface brightness, limits and challenges

In imaging surveys there is an implicit problem with surface brightness. It is difficult to define the surface brightness limit within a survey and this can have real effects on the faint end of the GLF, making it difficult to know when you are approaching a maximum value for the distribution at this end (Phillipps & Disney, 1986; Cross & Driver, 2002). This is why surveys such as VIKING are important to really push the understanding of these systems and how they contribute to the distribution of matter throughout the Universe. However, defining the surface brightness limit is still difficult, especially with VIKING. As noted in Section 3.1.3 there are a large number of image quality issues, to the extent that by plotting the number of galaxies per surface brightness bin would not reliably return a true turn over to help define the limit of the survey.

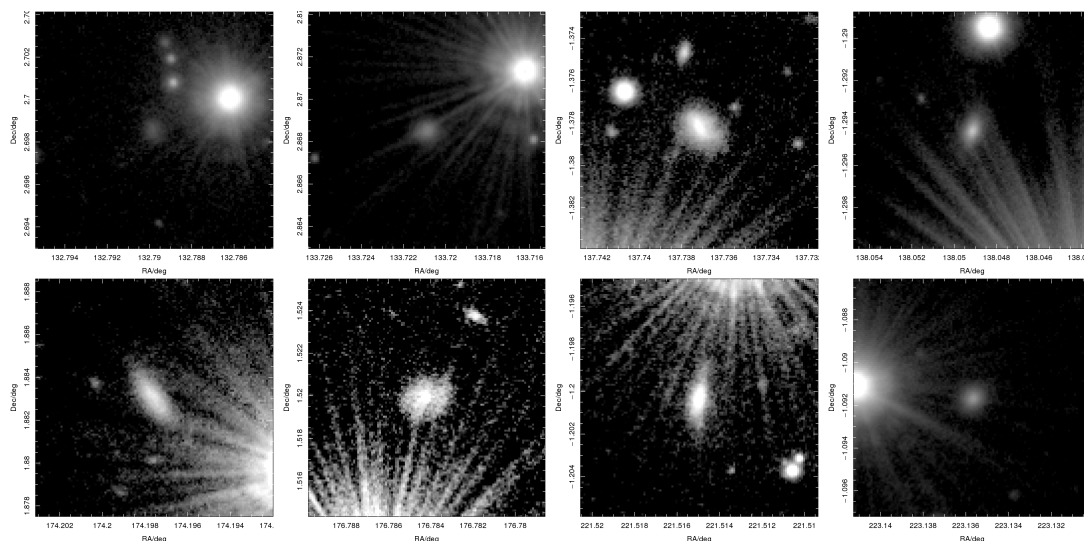


Figure 3.35: These have clearly been affected by bright sources in the field where a diffraction spike have affected the measured aperture which have affected the surface brightness measurement. They have not had a affect on the overall GSMF population however as they fall at high mass and have not changed the bin values.

These same image quality issues have also had an impact on the known galaxies within the survey. When plotting the Z -band half light surface brightness for the survey against stellar mass (Figure 3.34) it became obvious that there was a problem. As illustrated in Figure 3.35 there is a population of galaxies which had been discovered with faint surface brightness measurements and high masses. These objects were visually inspected to determine if this was a real effect. Some of these galaxies were discovered to be real with no obvious ill affects to distort the detection. However, there were several examples of galaxies which were being affected by bright sources in the nearby field and therefore affecting the profile of the galaxies. As can be seen in Figure 3.35 this is mostly caused by diffraction spikes from nearby bright stars going through the centre of the galaxy in the images. This likely had an affect on the C_i values as determined through binning in surface brightness and apparent magnitude, as it may have led to some actually bright galaxies being placed in incorrect incomplete bins. This will need to be cleared up with future surveys.

There are a number of potential issues which may be present in the calculation of the number density, when considering the more complete GSMF shown in figure 3.27. As stated earlier in this work, the most easily detectable galaxies are those with lower

mass to light ratios e.g. LSBGs with active star forming regions, if galaxies have higher mass to light ratios it is likely they will have been missed by the detection algorithms applied to the images by SExtractor and so will be missing from the completeness corrections applied to the GSMF. There is also the possibility that any new LSBGs detected will have had different properties to those galaxies in the same colour-colour-magnitude bins when calculating the completeness corrections, which may have adversely affected the correction of those galaxies. This can be rectified by obtaining spectroscopic redshifts for a significant fraction of these new LSBGs.

3.5 Summary & Conclusions

Using VIKING Z -band imaging data centred around the GAMA equatorial regions, a catalogue was constructed of all objects whose magnitudes fall within the range $Z \leq 19.3$ mags. This was achieved running SExtractor on the images to detect all objects in the survey data, and then using the information obtained from this SExtractor run to refine the catalogue to include only objects which could be considered real. This involved using several tests to separate stars and galaxies, and to compile lists of detections which fell outside ‘standard’ parameters and visually inspecting them. The final catalogue of VIKING sources was matched to the GAMA input catalogues so as to identify all new detections. Figure 3.29 shows where the ‘new’ objects fall in relation to the GAMA input catalogues, mostly the new detections fall at the fainter end of the distribution and have also increased the number of detected LSBGs in the survey area.

The collated data was then used to construct a GLF and GSMF, through calculating density corrected V'_{max} values for all of the candidate objects which had reliable redshifts. Correction values were calculated for each V'_{max} based on the fraction of galaxies which had spectroscopy compared to the number of photometric objects within a defined bin. Three different methods for defining the bins were tested, using a 1 dimensional approximation based on the apparent magnitude of the detection, a 3 dimensional approximation using $g - i$ versus $J - K$ colours and apparent magnitude,

and a final 2 dimensional approximation using surface brightness and apparent magnitude. It was decided to use the colour-colour method as it is more closely linked with physical characteristics of the objects. These parameters were used to construct the GLF, which is then compared to earlier versions to determine if there has been significant change at the faint end of the distribution. The final stage in the analysis was to calculate the masses for all objects with a known distance, again the ones with good spectroscopy, in order to calculate the GSMF for the observations.

It was hoped coming into this work that the deeper VIKING imaging would improve the accuracy of the low mass end ($M_* < 10^8 M_\odot$) of the GSMF. And whilst the statistics, when looking at the lowest mass bins, is still poor there can still be seen a marked increase in the number density of galaxies at $M_* < 10^8 M_\odot$. This shows that the surface brightness of objects has had an effect and that there are still more galaxies to be discovered within the data at these lower masses and luminosities. Below will be a discussion of issues from the work and general points from the analysis.

One of the main objectives of this study was to determine whether deeper imaging would reveal more sources at or below the limits of previous studies conducted within the GAMA survey. Using the VIKING Z -band imaging, which is ~ 1 magnitude deeper than the SDSS r -band imaging when compared to the local SED, it has been possible to show there is a rise in the number density at the low mass end ($M_* \leq 10^8 M_\odot$) of the GSMF. It is not, however, a large increase and could be argued that it has only served to improve the accuracy of the low mass end of the GSMF, as the ‘new’ points still sit mostly within the errors of the ‘old’ GAMA GSMF. It is unlikely that a significant population of these low surface brightness galaxies are sitting below the SB limits of the GAMA populations, however the fact is that new systems have been found, whilst the Z -band does hint towards the idea that there could be more. Of course this will need improved instrumentation before being a ‘closed’ topic.

This work has gone some way to addressing the issue of surface brightness in galaxy detection and has shown that low surface brightness objects have affected the completeness of past surveys within GAMA and presumably others. However one thing it has not done is given any sort of upper limit to surface brightness effects. The fact

that new galaxies have been found within the magnitude limits of past surveys based on their surface brightness suggests that there will still be more to find as improved search techniques and telescopes are deployed. This hints at the possibility that the GSMF may continue to rise steeply even past the magnitude limits of this survey. Of course it would be remiss to suggest that the distribution will carry on all the way to the faintest magnitudes, the fact we don't know when it stops means that it could stop rising very soon after the magnitude survey limits given in this work. Therefore, more work is needed before any upper limits can be applied to this population.

Another main result which can be taken from this work is that the GSMF and GLF at high masses and luminosities respectively have not changed and show strong consistency with previous results. This is useful as it shows the results are at least consistent with what was previously known, and that untrue detections have been effectively removed from the survey data at high masses.

The GSMF produced from the survey data can be used in simulations to constrain galaxy formation, by acting as a tuning mechanism within the simulations. It is still important to remember that at lower masses the data cannot be seen as complete, and is an improved lower limit over those produced so far from these regions. Moving forward it is important to continue the search for these systems by improving surveys and technology so as to push to deeper magnitudes and uncover new LSBGs.

Chapter 4

Detecting VIKING LSBGs

Using a specially designed algorithm on SDSS data in Chapter 2 it was shown that imaging, if treated properly, could be used to push detection limits to search for hidden LSBGs within them. Therefore, using the same method on deeper imaging should turn up more of these elusive galaxies. It was also shown in Chapter 3 that the VIKING Z-band imaging was about one magnitude deeper than SDSS r-band imaging, meaning more objects were detected when standard detection techniques were used on VIKING mosaics produced by GAMA.

This Chapter will detail a pilot study, using the VIKING data mosaics and the same method developed and employed within Chapter 2 to push deeper into the GAMA fields to detect more undiscovered LSBGs, and to determine the possibility of using the algorithm on the entirety of the three GAMA fields in VIKING. There are some differences, the number of bands with a similar signal to noise at the start is 2 (Z & Y) compared to the SDSS's 3 (g, r, & i), and the fact that the images being used are the mosaicked images produced by GAMA and not the original raw images produced by the VIKING survey.

Region	RA	DEC
G09	131.5	2.25
G12	177.0	-2.0
G15	214.5	2.0

Table 4.1: The central coordinates of the cutouts used in the pilot study. The area of each cutout was 0.25 deg^2

4.1 Images

As already mentioned in Chapter 3 the GAMA team have produced large mosaics of each region for each band. Background subtraction is employed across the entirety of each mosaic using a mesh¹, and each image has its Zero Point set, in the case of VIKING this Zero Point is 30. The mosaics were not used in Chapter 2 for a number of reasons, however the most prominent of those being that SDSS had produced specialised pixel masks for the SDSS files which could not be effectively used on the mosaics, therefore the decision was taken to not use the mosaic for that study.

For this pilot study, a $0.5 \times 0.5 \text{ deg}^2$ region has been chosen from each field. It can be seen in Figure 2.8 that the majority of the discovered LSBGs in the SDSS imaging were found in and around densely populated regions of the fields when considering galaxies with $z < 0.1$. Therefore to improve the chances of detecting new galaxies, the cutouts used have been determined based on a similar idea, of focusing on the denser regions of the images. This is where the mosaics become very useful as it is a fairly simple task to extract the relevant regions from the image using a simple cutout tool. The regions chosen were defined as described in table 4.1.

4.1.1 Image Reduction

Creating suitable images for detection was a more straight forward process than when using individual frames, as the areas are already aligned to each other, so coadding is simpler. For this study the Z and Y frames are used from VIKING as these have the

¹The size of the mesh is determined separately for each survey. In the case of VIKING images, the mesh size used was 256×256 pixels.

Filter	m	Counts	σ	Weights (ω)
Z	18.95	26419	9.5 - 20	1
Y	18.87	28434	21.2 - 41.9	0.21-0.25

Table 4.2: The filter, apparent magnitude (m) as compared with an *i*-band magnitude of 19.0, the range of signals calculated for the different images (Counts), noise (σ), and the range of weightings (ω) to be applied to the images. The counts are calculated using an *i*-band magnitude of 19 mag, and are included to show the spread in counts across the images due to different conditions based on the night the image was taken.

better signal to noise ratio (SNR) for low-redshift galaxies. After *Y*, the SNR of the other three frames is significantly lower such that including these frames would result in negligible improvement. Before the images can be coadded they must be weighted.

Using the same method as outlined in chapter 2 it is possible to weight the images. Figure 4.1 describes the median colours of the low mass GAMA galaxy sample used in Chapter 2 compared to the *i*-band. Applying these colours to the *Z* and *Y* bands, using the same arbitrary magnitude in the *i*-band (19th mag) gives the magnitudes shown in Table 4.2, the *i* – *Z* colour is measured at ~ 0.055 and the *Z* – *Y* colour at ~ 0.080 , this gives the relative magnitudes used to calculate the weights for the images as in the method described in Chapter 2. The calculated weighting values are shown in Table 4.2. A pixel map also had to be created in order to mask the images in the same way as the original method. As no mask files currently exist for the VIKING imaging they needed to be created using SExtractor. SExtractor gives the user the option of creating and saving the segmentation map, this is a map of ‘detected’ pixels which the program then uses to define ‘detected’ objects. It is possible to take this map and use it as a pixel map on the image regions, thereby masking any detected pixel in a similar way to the original method.

Now that weighting factors and masks have been applied to the images smoothing must take place. Again, similarly to the method in chapter 2, a kernel of diameter 7 pixels was used as the pixel sizes between SDSS and VIKING are fairly similar, $0.399''$ pixel^{-1} and $0.339''$ pixel^{-1} respectively, this means that the relative size of the kernel on the sky is approximately the same. How the images change over the course of these corrections are shown in Figure 4.2.

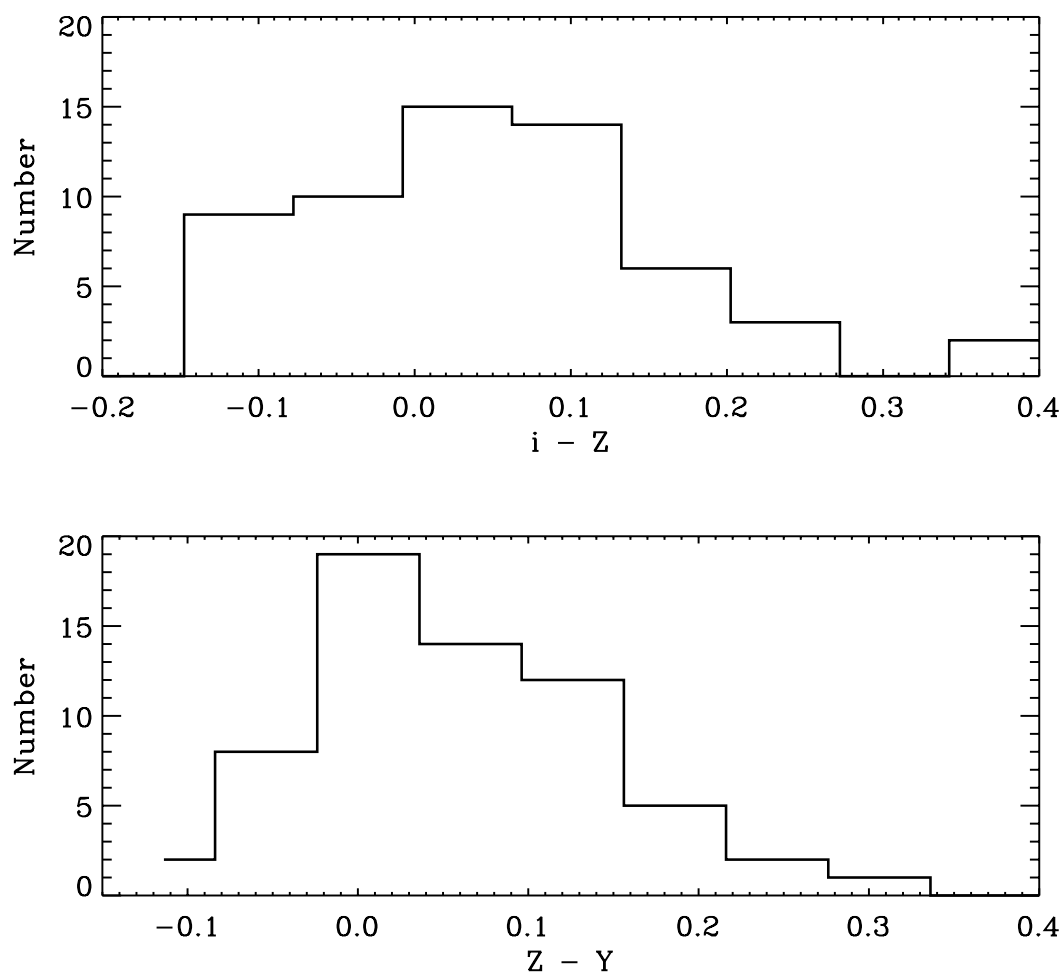


Figure 4.1: **Top panel** shows the $i - Z$ colour distribution of the GAMA low mass sample with a median colour of 0.0548. **Bottom panel** shows the $Z - Y$ colour distribution of the same sample with a median colour of 0.0798. Each of these metrics were used in the calculation of the weights of the corresponding images.

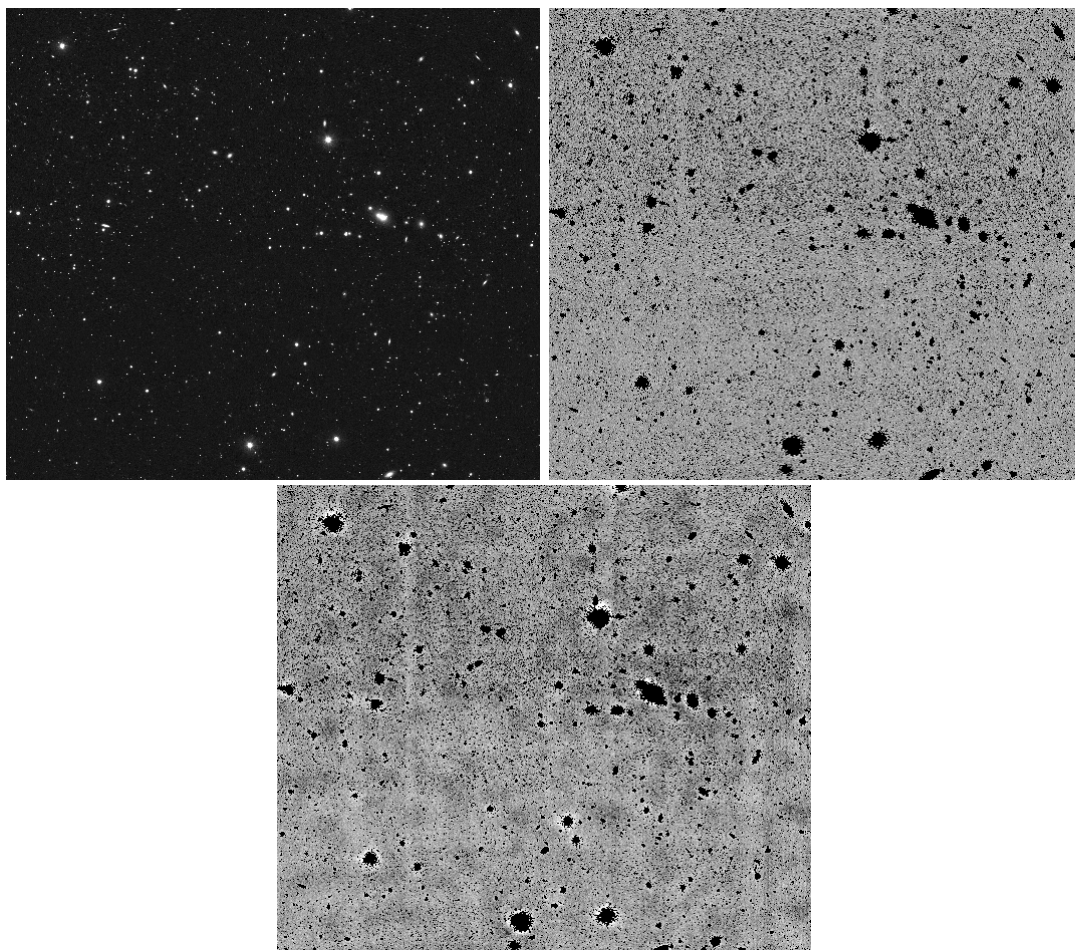


Figure 4.2: These panels show how the image files are affected through the processes described in § 2.2. **The top left panel** shows the initial image file of the field in question. This particular image is from the G15 region centred on the coordinates shown in table 4.1. **The top right panel** is this same field after masking of known sources detected using the pixel map created using SExtractor run on the Z -band imaging. **The bottom panel** shows the field after smoothing and coadding has taken place. This brings out the low surface brightness features around the brighter detected objects within the field and gives a good representation of the challenges faced when trying to detect LSBGs in the field. There were no confirmed LSBGs in the shown field.

This method, when applied to the SDSS imaging in Chapter 2 led to an ~ 1 mag arcsec $^{-2}$ improvement over the SDSS pipeline. The VIKING imaging using SExtractor was at least as deep as this because the LSBGs were detected. Using the masking and smoothing technique on the VIKING data, we expect ~ 2 mag arcsec $^{-2}$ improvement over the SDSS imaging and pipeline (for a low-redshift SED).

4.2 Object Detection

Before continuing it should be noted that the full area searched in the original method in Chapter 2 was some 180 deg 2 . In this pilot study three regions of $0.5^\circ \times 0.5^\circ$ were cut from the three equatorial regions of the GAMA survey. This means that in total for the pilot study an area of 0.75 deg 2 is being searched, which equates to $\sim 0.4\%$ of the original search area. Therefore it would be expected that the total number of detections before cutting would be in the order of 1000's of detections, and that one might expect to find 1 - 2 of the catalogued LSBG sample on average, but many more than that if the number of LSBGs increases significantly when probing a magnitude fainter in SB. This is of course only an estimate and will be mostly affected by the quality of the imaging in VIKING. Whilst the overall surface brightness limit has improved in the VIKING images, especially when compared with a 'universal' SED as shown in Figure 5.1, the number of imaging issues seems to have increase as discussed in Chapter 3, this has an impact on the ability to distinguish between artefacts and genuine LSBGs, and reduces the effective area of the search.

In order to attempt to increase the likelihood of detection the search areas were chosen based on the distribution of objects within the same redshift range as that explored in Chapter 2. This increases the chances of detection based on the idea that most objects in the Universe tend to be found in higher density regions (Press & Schechter, 1974; Bahcall, 1988; Alpaslan et al., 2014).

Similar to the method used in Chapter 2 a $\text{SNR} > 5$ was used in an attempt to detect any objects which may have been hidden by the noise in the original images. Any pixels

detected through this method were grouped based on their proximity to one another. If pixels are touching in any direction they are considered to be part of the same object, meaning that like in the original search one will end up with single pixel detections within the smoothed image. This returned ~ 1500 detections across all images, which is a similar number to that expected from scaling the search area down from the three equatorial regions in the GAMA survey.

In an attempt to cut the number of detections it was decided to use another of the methods used in the original study. By analysing the number of masked pixels near the object it should be possible to remove some of the detections which are too close to the parent object. In an attempt to define what this number should be for the study the percentage of masked pixels within a 50 and 100 pixel radius of the centre of the detection is calculated and the distribution compared to that of a random distribution of the same size apertures over the same image fields to determine how likely an LSBG would be to appear within the LSB halo of a larger object. As can be seen in Figure 4.3 the natural cut for this test would be at approximately 20% - 30%, based on a random sample of 30000 positions. This gives a total number of detections to visually inspect of 24 – 110.

The distribution shown in the top panel of Figure 4.3 has a wider peak than its equivalent, the bottom panel in Figure 2.4. This is due entirely to the larger number of pixels being masked on average in the VIKING images compared with the SDSS images. On average across the whole survey $\sim 7\%$ of pixels are masked in the SDSS images, whereas in the VIKING images this increases to $\sim 10\%$ of pixels being masked, widening the peak of the distribution. This also places a larger proportion of objects in the LSB halos of larger objects. Some examples of the detections are shown in Figure 4.4.

Through the visual inspection no objects were found at the coordinates detected through the algorithm. It should be noted that the method of cutting the number of objects down using the number of masked pixels within a certain radius from the centre of the object would be used in a full roll out of the detection algorithm to the whole VIKING dataset, it is only because of the small number of detections that this method was not

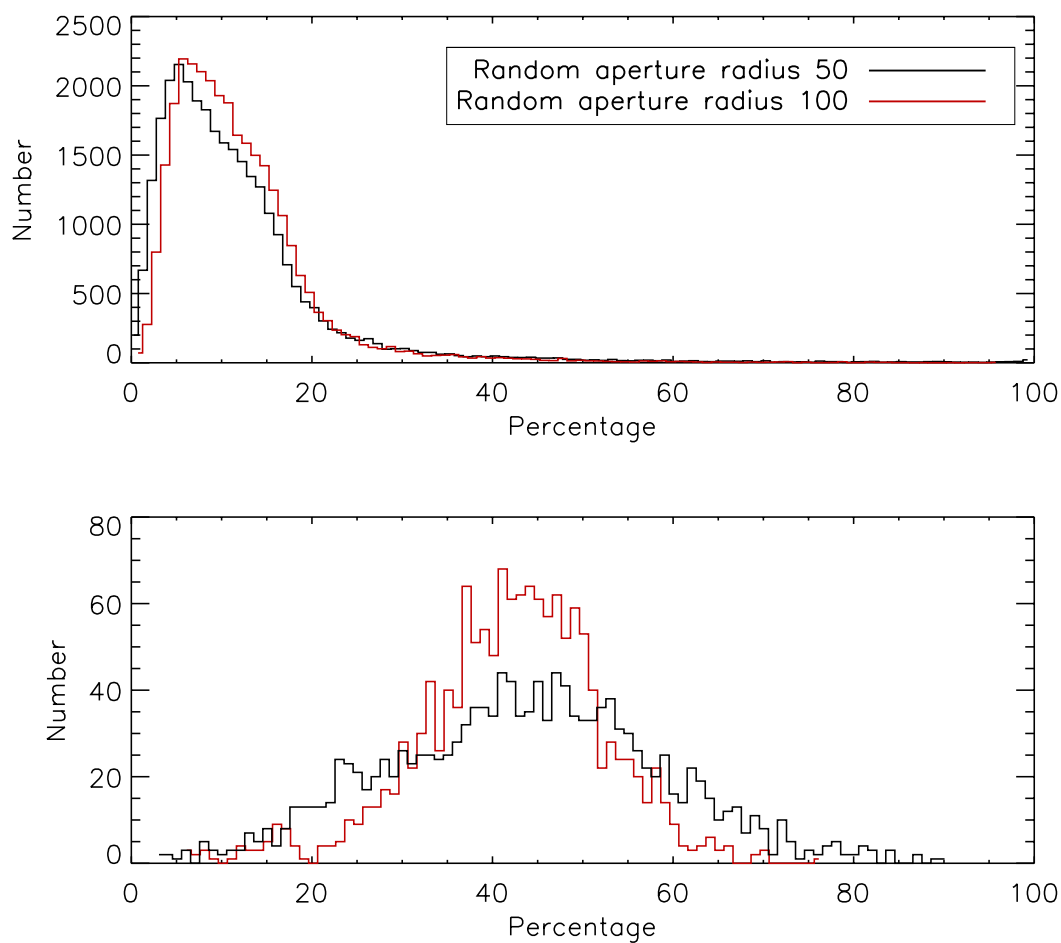


Figure 4.3: **Top panel** shows the distribution the percentage of NaN values within 50 and 100 pixel radius apertures placed randomly within the three regions used for the analysis. A total of 30000 random apertures were placed in the images to obtain a statistically significant sample for comaprison to actual detections. **The bottom panel** shows the distribution of the same apertures placed around detections from the three pilot regions.

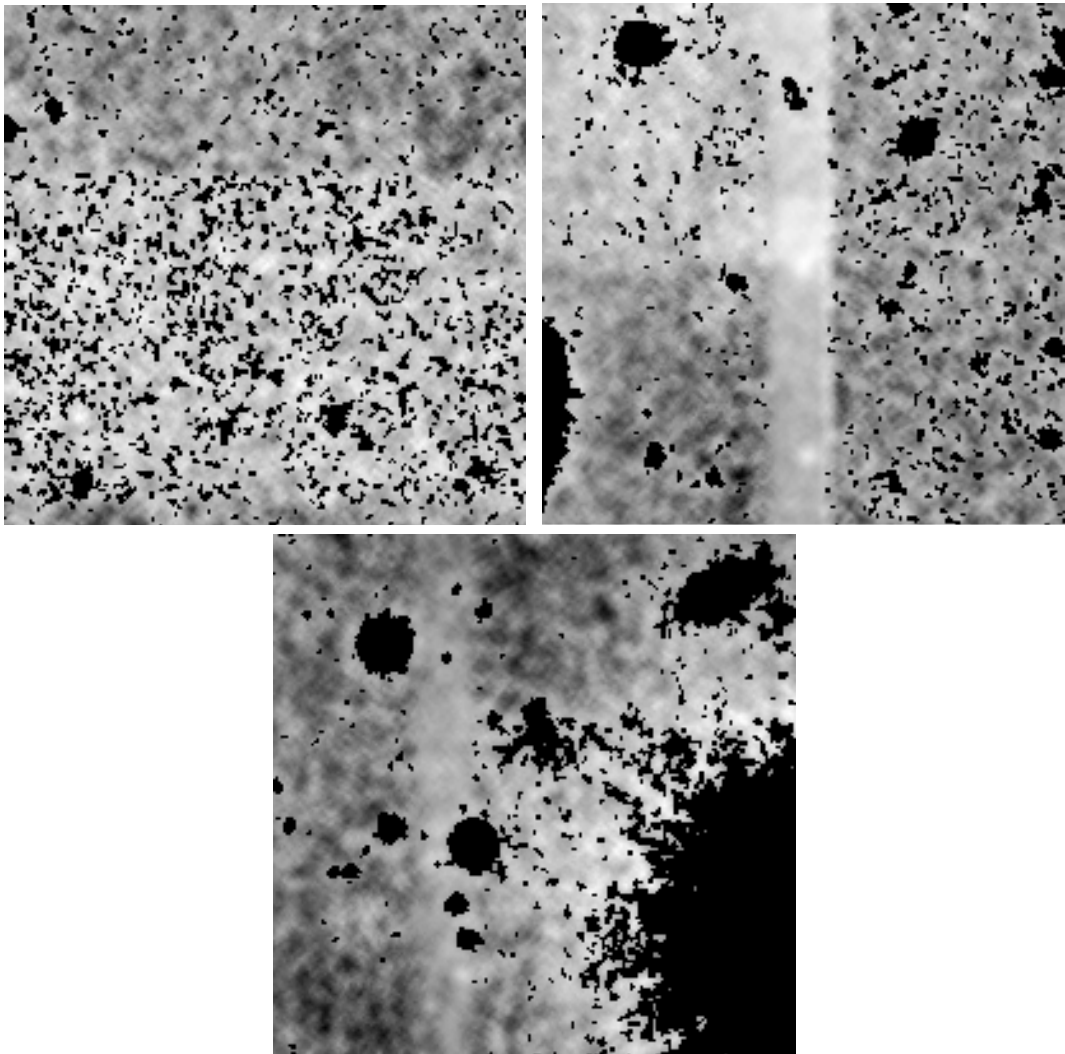


Figure 4.4: The images shown here are taken from the detection pipeline deployed on the VIKING data, which was based on the method explored in Chapter 2. The detections are always in the centre of the frames above. They clearly show some of the issues which were found across the imaging which seemed only to cause issues when trying to detect. If these could be effectively dealt with through accurate masking or some other means then it is likely the images would become more easily searchable.

fully utilised.

It could be that there are no LSBGs to find in this area of the imaging which were not already detected using SExtractor. There is also the possibility that the objects are ‘hiding in plain sight’, they have been detected but not properly classified by the detection algorithm. There were also some issues with the imaging, identified in Chapter 3 which may have had an effect on the overall detectability of LSBGs in the imaging, such as a too harsh background subtraction when the mosaics were created, or imaging issues, also mentioned in Chapter 3, such as persistence or ghosting causing a reduction in the overall quality of the images being searched.

That being said this method still produced images which showed LSB artefacts around bright objects which gives validity to the claim that the method should work when applied to the GAMA area as a whole as imaged in VIKING. This however is out of scope for this work.

4.3 Conclusions

No extra LSBGs were found through this pilot study, however this does not mean that the objects are not there to be found. This places an upper limit on the number of LSBGs to be found using this method. A detection of zero is equivalent to a 95% upper limit of 3. That is given a mean value of 3 per 0.75 deg^2 , we would obtain no detections, 5% of the time.

The true test of the pilot study was to show that it was possible to use the same method as that used on the SDSS imaging to treat the VIKING mosaicked images in such a way as to find LSBGs. It had been a hope of this study that the image quality problems noted in Chapter 3 could be overcome through careful application of weighting and smoothing to improve the SNR within the image frames to make the discovery of hidden LSBGs easier. This is the case in areas that are sufficiently free of aberrations. The improvement in the images from coadding 2 frames, Z & Y , from VIKING yielded an increase in the surface brightness limit of ~ 1 magnitude when compared to the limit

achieved by the detection run from SExtractor. This would be more than enough for detection of LSBGs in the frames. Rolling this method out into the rest of the imaging should yield the discovery of more of the galaxies.

The majority of the problems with the imaging in the VIKING data set were explored in Chapter 3. An issue was the background subtraction also described in §3.1.1, this may have been done using a mesh size which was too small and ‘over-subtracted’ as it appears to have caused some issues around bright sources, as shown in Figure 4.5. This should not affect the entire survey though it will limit the effective search area of the GAMA regions significantly.

In this pilot study the method presented in chapter 2 was utilised to search for LSBGs which could not be detected using other techniques. Two frames, Z & Y were coadded and weighted, masked and then finally smoothed to bring out any hidden LSBGs in the images. Again similar to chapter 2 a cut of 5σ was applied to the smoothed images to identify any pixels with a high enough signal to noise to be considered a detection.

After clumping the detected pixels into candidate objects, constraints were applied to the candidate objects, which removed most of them as erroneous detections such as extended wings of bright stars and galaxies which were not masked out by the original masking. After a final visual inspection of the remaining detections it was discovered that there were no new galaxies in the searched area of the VIKING images. This has placed some constraints on the number of detections we would expect to find in the VIKING imaging and means one would expect to detect between 0 and 700 new galaxies in the imaging. However, even with 700 new detections, this would not have a significant effect on the number density of low-mass galaxies if the new detections are spread over a range of redshifts to $z < 0.2$ as is likely the case for the new SDSS detections (see Figure 2.10), for example. Therefore the GSMF at lower masses is likely nearly complete.

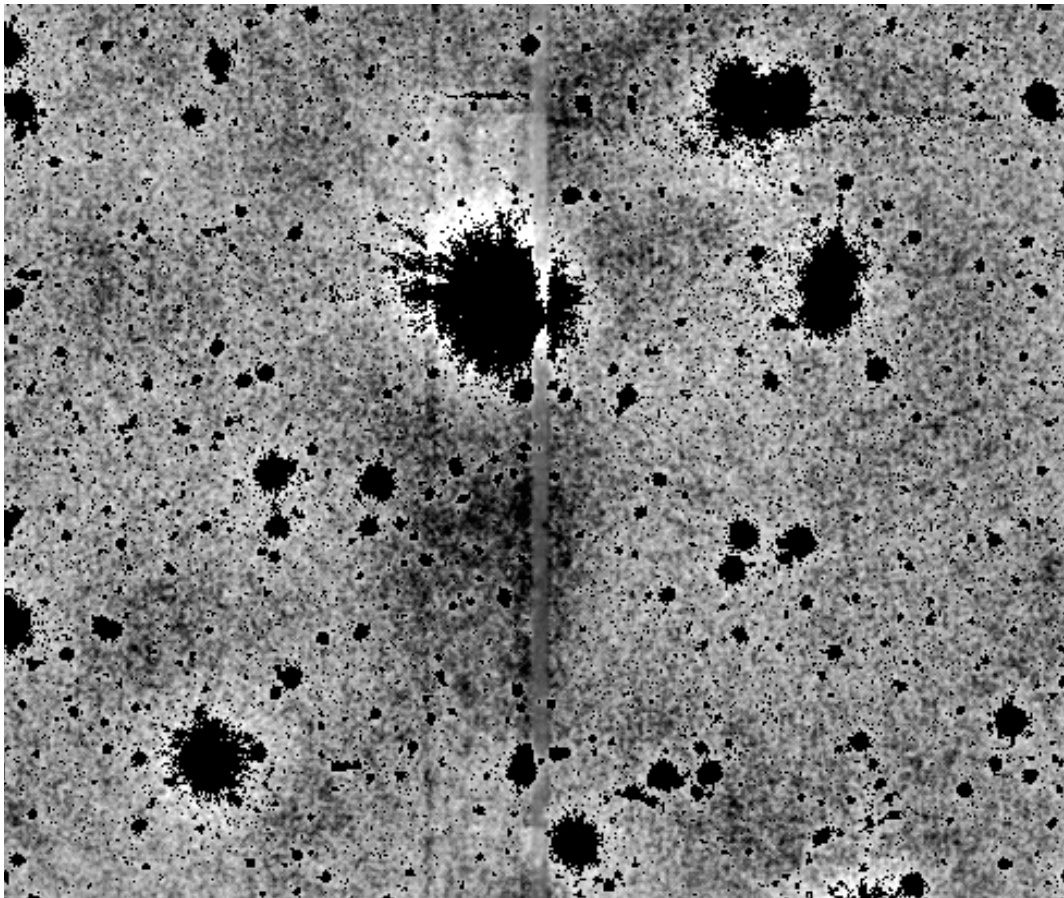


Figure 4.5: The image shown describes some of the issues caused from the mosaicing of the VIKING fields and the subtraction applied to the fields during the swarping process. Clear joins can be seen in the imaging which have caused issues within the detection algorithm. This is taken from the G09 field which was an area with few of the issues of other area.

Chapter 5

Future Work

5.1 LSBG Follow Up

The work on the 343 galaxies identified in Chapter 2 is not complete as the galaxies are still without accurate distance estimates. Using the methods from Chapter 2 we have shown that several of these systems may sit at low redshift, however due to large errors in the photometry, it is necessary to take redshift measurements for the objects to determine accurate distances. This is best achieved through spectroscopy as photometric redshifts would also provide little in the way of accuracy due to the large errors inherent in the method. With well defined distance measurements it will be possible to fit the systems into the current model for the formation of the Universe, which will help in our wider understanding of galaxy formation.

To this end several of the galaxies discovered in Chapter 2 have been included as part of a proposal to the southern African large telescope (SALT; Buckley, Swart & Meiring, 2006), to obtain spectra for the galaxies and therefore distances.

Throughout this study LSBGs have been a central theme in the work and results presented, and whilst constraints have still not been placed on the number of these galaxies likely to be in the local universe, it has added to the overall census. The pilot study has also shown that there appears to be a reduction in the number of galaxies which

might be detected, this hints to the idea that the GSMF is near completion in the local universe. As stated above not much can be said about the new detections presented within this work until further follow up of individual systems has taken place. Until then the search for missing LSBGs will likely continue. This is important for the field of galaxy study as a whole as it is useful to get a complete census of these systems for comparison with simulations. It is important, as it is one of the remaining frontiers in delivering a complete census of the galaxy population.

5.2 Future measurements of the GLF and GSMF

The GAMA survey has produced some important results in our understanding of how the Universe around us formed. It is the most complete redshift survey to date, but like all big surveys it lacks the capability to really explore the low surface brightness regime. This means that whilst the high mass end of the GSMF and the bright end of the GLF at low redshift are complete, the low mass and faint end of the two functions are far from complete. Low surface brightness effects stop surveys from truly exploring the full regime of galaxies within the volume they are exploring.

The work within this thesis has pointed to one solution of this, by employing better telescopes, detectors and techniques to explore fainter magnitude limits then it may be possible to further improve the completeness of low mass systems. The VIKING imaging has already shown how much better it is at finding LSBGs as a large number of new galaxies have been added in that regime just from a fairly standard analysis of the data. This is due to the improvement in the depth of the imaging over the SDSS imaging, as seen in Figure 5.1. Some improvements in the sky subtraction and mosaicking could help to reduce the number of artefacts at the seams.

As can also be seen from Figure 5.1, KiDS data has also improved the depth which can be reached with large surveys. This survey can also be used to carry out further searches for LSBGs within the field, and is likely to improve the understanding of the number density of these low-mass low-redshift systems greatly. By gaining a more

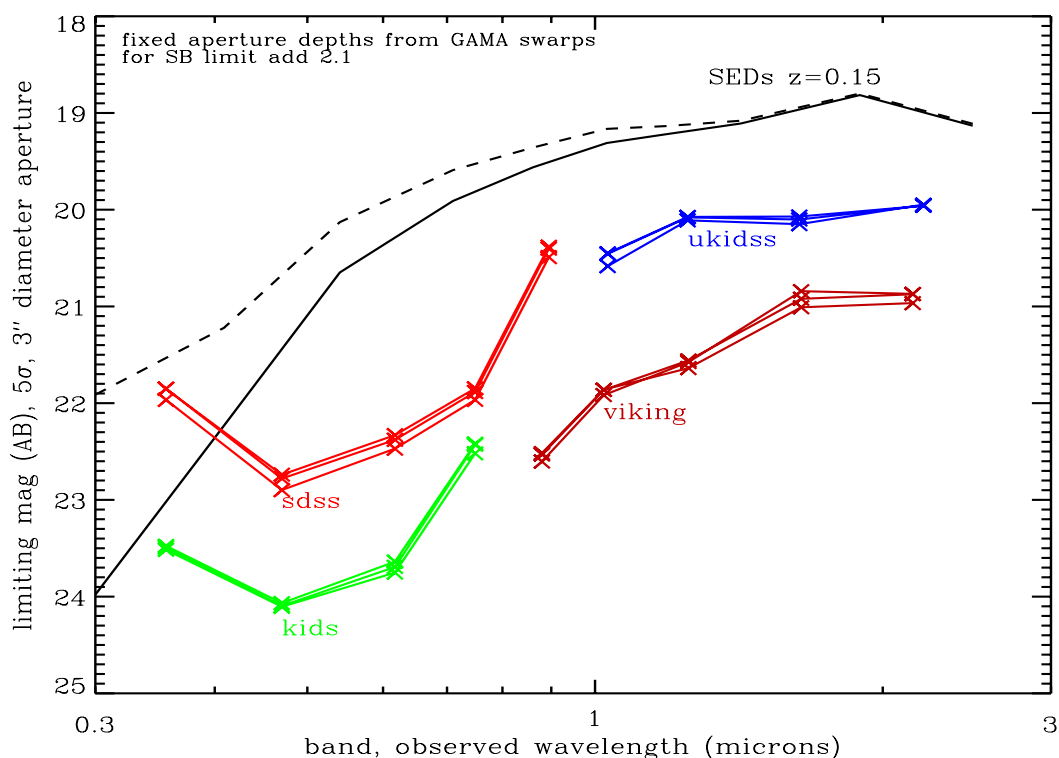


Figure 5.1: The improvement in the limiting magnitude as compared with the low redshift SED between SDSS, VIKING, KiDS, and ukidss is shown. These were produced by placing 2.5'' radius apertures randomly across all three survey areas produced from the survey data from the four surveys. This is what produces the three different lines for each survey. The improvement by moving onto the KiDs and VIKING imaging is obvious with the improved depth each gives.

detailed understanding of where the GLF and GSMF may turn over at low masses will help in the understanding of processes which may suppress them. Currently there is little constraint on when this turnover may occur below the limit of $10^8 M_{\odot}$.

It was however found that there is unlikely to be a large population of LSBGs hiding below the SB limit of the original GAMA catalogues. This is seen most keenly in the apparent magnitude distribution of the objects found in Chapters 2 and 4, but also in the small gains in the number density measurements of Chapter 3. Whilst the number in the bins did go up it was still within the errors of the old points.

5.3 Future Surveys

GAMA is due for a final data release at the end of 2017. However, with further surveys coming online, it will be necessary to carry the work of GAMA on throughout a new era of searches. The Wide Area Vista Extragalactic Survey (WAVES; Driver et al., 2015) is a new survey based on expanding the work of GAMA. This will be a survey split into two parts, WAVES-Deep and WAVES-Wide, which is set to collect spectroscopy on ~ 2 million galaxies to a magnitude of $r < 22$ mag. WAVES-Wide is set to cover an area of ~ 750 sq. deg. to a redshift of $z < 0.2$, and will be integral in determining a more accurate measurement of the number density of galaxies to a lower limit of $M_* \sim 10^6 M_\odot$. This will give a good idea on the constraints to be applied to simulations to be able to fully test theories of low mass galaxy formation.

Other than deep surveys, telescopes such as the Dragonfly Array as mentioned in section 1.6.1 are being built to specifically fill the need of detecting these LSBGs in the Universe. Telescopes such as these can be used to carry out surveys specifically for LSBGs. However due to the relative ease of finding satellite LSBGs around large nearby galaxies, compared to detection in the field, the current focus of the Dragonfly telescope array in particular is to survey these galaxies first before considering looking for galaxies in the field through a large area survey.

As field LSBGs are likely to have had a very isolated formation history and low star formation rate, they will still be gas rich. Therefore H I surveys of the local Universe will likely uncover more of these systems with the added benefit of being able to obtain the redshift simultaneously, removing the need for some of the corrections in the determination of the GSMF. Obtaining masses from the H I measurements will also be possible using these instruments, again increasing the accuracy of measurement at the low mass end of the GSMF. Telescopes such as the Square Kilometre Array (SKA, Carilli & Rawlings, 2004), and surveys such as the Deep Investigation of Neutral Gas Origins (DINGO; Meyer, 2009) will help push our understanding of the overall population of these galaxies.

WEAVE is a next generation survey facility for the William Herschel Telescope (WHT)

(Balcells et al., 2010). Based in the Northern hemisphere it will provide optical and spectroscopic support services for several new large scale surveys. Several of these could be used to find or confirm the presence of LSBGs in the local universe and around the Milky Way. For searches of systems around the Milky Way the collaboration and follow up of Gaia (Prusti, 2011) sources will yield ultra faint dwarf satellites. Follow up of sources can be carried out using APERTIF (Verheijen et al., 2008), which will be deployed on the Westbork Radio Telescope, which will measure HI sources out to a redshifts of $z \sim 0.2$. Using the small Integral field units (IFU's) deployed on WEAVE would give spectral information on any small, nearby, gas rich, galaxies such as field LSBGs.

Looking further into the future brings the completion and launch of the Euclid space telescope (Laureijs et al., 2011). This will be a survey telescope with three instruments which work in the visible and NIR. The main science goal of the mission is to provide imaging for \sim billions of galaxies and redshifts for a large proportion of that survey, which will help in the understanding of galaxy clustering on large scales out to a redshift of 2. The NIR imager will carry Y , J and H filters, which means carrying out algorithm searches, like that detailed in Chapters 2 and 4 of this Thesis, for low redshift LSBGs will be a real possibility. With the Euclid's low sky background, the chances of discovering these low mass, low luminosity systems is high. This would enable good quality morphological studies to be carried out on these systems, which would enable the growth in our understanding of the formation and of some of the lowest luminosity systems in the Universe.

Appendix A

Table of LSBG sources from SDSS

Table A.1: a and b are the semi-major and semi-minor axis measured in arcseconds of the aperture fit by IOTA, m_r and m_Z are the r -band and Z -band apparent magnitudes of the measured objects, and μ_r is the effective surface brightness as measured with the IOTA.

ID	RA	DEC	a	b	m_r	m_Z	μ_r
LSB09001	128.9691	-0.0957943	3.4839	2.6692	21.8408	21.8821	24.5936
LSB09002	129.09009	2.361468	2.7996	2.0884	22.8293	22.1117	24.5670
LSB09003	129.27756	0.8226802	2.8844	2.4205	22.2543	21.229	24.5890
LSB09004	129.35783	0.7595266	2.5037	1.9720	22.7923	22.4842	24.5994
LSB09005	129.41878	-1.6270162	6.0633	3.9586	21.2025	21.1259	24.9391
LSB09006	129.45963	1.6240747	5.6902	4.9250	21.522	20.5847	24.9046
LSB09007	129.50839	2.5296433	1.8882	1.6193	23.1208	22.9203	25.0196
LSB09008	129.51918	2.4740963	1.9518	1.3597	22.8143	22.1985	24.3831
LSB09009	129.52092	2.479978	3.5729	2.3249	22.1895	22.1088	24.3595
LSB09010	129.56984	0.6258908	3.2690	3.1882	22.6541	22.2208	25.0388
LSB09011	129.61598	1.6278003	3.0195	2.8554	23.3115	21.4271	25.1555
LSB09012	129.78062	2.1855922	1.3550	1.0572	23.5704	23.0673	24.5818
LSB09013	129.80873	2.1495922	4.7501	4.3810	21.4253	20.7033	25.6001
LSB09014	130.23743	-1.8956712	3.0878	2.5955	21.9971	21.7614	24.4246
LSB09015	130.23872	-0.7973136	2.6779	1.9435	22.1919	21.3356	24.2017
LSB09016	130.33524	1.5544444	3.4216	3.1466	22.0526	21.0246	24.5425
LSB09017	130.35611	1.559922	2.7835	2.2947	22.5085	21.3285	24.7951
LSB09018	130.90485	1.8834378	3.8699	3.4341	22.4177	21.036	25.4470
LSB09019	130.9658	1.898082	3.4413	2.4460	22.0465	21.8194	24.3405

LSB09020	131.19133	-0.626201	4.0569	2.8533	23.4527	21.5943	24.6668
LSB09021	131.2082	-0.5417988	4.0389	3.1836	22.3345	21.7841	24.4358
LSB09022	131.62434	1.6057427	2.3861	1.7204	22.8885	21.5467	24.5769
LSB09023	131.67816	0.5540369	1.9430	1.4810	22.8808	23.6211	24.6819
LSB09024	131.70927	2.5544965	2.0206	1.5104	23.5808	22.4531	25.3987
LSB09025	131.74373	1.9609236	1.8794	1.7335	23.0595	22.158	24.9193
LSB09026	131.82164	0.0318748	2.3730	1.9435	22.9885	22.4449	24.6022
LSB09027	131.90256	-1.9465204	2.8932	2.0118	22.1521	21.5768	24.3036
LSB09028	131.90715	0.3836737	3.0859	2.0369	23.2325	22.5703	24.9249
LSB09029	132.00081	2.5286186	2.9888	2.4620	22.2552	21.4978	24.4718
LSB09030	132.09196	2.6214356	3.2768	2.6615	22.6536	21.9504	25.0580
LSB09031	132.3307	2.0279646	3.1380	2.3038	22.1112	21.7518	24.3599
LSB09032	132.43839	1.2431616	7.1974	5.7464	20.7033	20.6727	25.1495
LSB09033	132.48506	-1.7177159	2.2674	1.5258	22.4169	22.1619	24.2253
LSB09034	132.5346	-1.1465303	9.2143	4.4846	21.1037	20.5223	24.2151
LSB09035	132.63809	1.6759123	5.8105	4.6113	23.2363	21.2483	24.8774
LSB09036	132.647	1.6729075	3.1300	2.5308	21.8287	21.5672	24.4231
LSB09037	132.81346	0.2577216	10.5486	8.4383	19.989	19.6842	25.6023
LSB09038	132.8455	1.2667147	2.6353	2.1090	22.7068	21.7559	24.8065
LSB09039	132.94164	-1.0513489	2.7940	2.7199	22.036	21.7816	24.6964
LSB09040	133.16144	0.6260146	6.7667	3.5123	21.7448	20.7	25.1670
LSB09041	133.21152	0.8644454	6.3500	3.8309	23.1162	21.0379	24.1901
LSB09042	133.21306	0.8662705	6.8458	5.2644	21.6738	20.4173	23.9770
LSB09043	133.28322	-0.1422893	3.1502	1.9162	22.6819	22.1797	24.4709
LSB09044	133.32228	1.781779	4.7276	2.8541	22.0609	21.3249	24.9416
LSB09045	133.4274	1.1548774	5.4686	3.8521	20.8906	20.9484	24.4357
LSB09046	133.59279	1.7682099	2.6934	1.2957	22.9254	22.1066	24.0952
LSB09047	133.59885	1.7617161	5.7074	3.4198	23.1123	20.9356	23.9738
LSB09048	133.64407	2.5873106	3.5251	2.6447	22.1882	21.1393	24.6005
LSB09049	134.15878	0.4081352	1.7465	1.3953	22.62	22.6395	24.2970
LSB09050	134.16707	-0.4362263	2.1138	1.8273	23.3319	22.8658	25.0760
LSB09051	134.33273	1.3130533	2.5688	1.6314	22.0328	21.8077	24.0225
LSB09052	134.37553	0.5472311	3.3048	2.4004	22.151	21.7018	24.6277
LSB09053	134.5145	1.6115811	2.4655	2.2816	23.0299	21.4726	25.0810
LSB09054	134.58984	2.0320573	1.7513	1.6967	22.5439	21.6711	24.6304
LSB09055	134.65999	-1.2479839	4.0649	3.5619	21.5179	20.557	24.7452
LSB09056	134.72519	2.119218	2.8215	1.8937	22.7109	21.6715	24.5559

LSB09057	134.7253	2.1220298	2.4359	1.4819	22.9027	22.096	24.3269
LSB09058	134.74567	2.0654442	3.1911	2.2998	22.3148	22.3722	24.9882
LSB09059	134.81429	0.9385294	3.6402	3.2541	23.4686	21.586	25.2253
LSB09060	135.06487	1.698353	4.3513	3.4421	22.2869	21.4004	25.2705
LSB09061	135.06609	0.9048426	2.6566	2.1523	22.379	21.5148	24.6755
LSB09062	135.39142	-1.9454952	1.8313	0.8673	23.8021	23.6738	24.5508
LSB09063	136.04141	3.0091252	3.1024	2.9219	22.1807	21.3307	24.6307
LSB09064	136.18439	1.9427997	5.2891	2.9928	21.5293	20.8289	24.0079
LSB09065	136.5729	1.6134504	2.3338	2.0064	21.3603	21.722	23.8888
LSB09066	137.13354	0.8772332	3.0048	2.6818	22.3457	21.473	24.4394
LSB09067	137.22768	-1.6154053	2.7230	2.4169	22.1606	21.7795	24.5838
LSB09068	137.61453	1.3752298	2.8066	2.4156	23.0627	22.1898	25.2021
LSB09069	137.6503	1.3694515	4.7203	2.7399	22.1457	21.5298	24.0968
LSB09070	137.72789	-1.5410286	2.1440	1.8343	22.5603	22.4758	24.5866
LSB09071	137.757	0.9791696	3.0042	2.4976	22.1904	21.2132	24.3723
LSB09072	137.80484	1.438227	1.9708	1.7987	22.7493	22.0706	24.5362
LSB09073	137.80612	1.4389397	2.4349	2.0076	23.1513	22.6026	25.8752
LSB09074	137.93143	0.3099527	1.6089	1.3502	23.7278	23.2576	25.0408
LSB09075	137.93257	0.3094449	3.2747	1.9803	22.1912	21.7591	24.1166
LSB09076	138.00546	1.7058905	3.0604	1.7821	23.1096	22.8857	25.2233
LSB09077	138.28464	-1.706602	2.6091	1.8320	23.1668	22.0732	24.8016
LSB09078	138.46062	2.2821953	5.1054	2.7712	22.0795	21.6417	24.1988
LSB09079	138.48352	-1.2679889	4.4570	2.9403	21.8191	21.809	24.7770
LSB09080	138.5267	1.5053807	4.0378	2.9260	22.45	21.8434	24.7423
LSB09081	138.52826	1.5054741	2.7052	1.5365	22.7623	22.1851	24.1081
LSB09082	138.56844	1.6155249	6.0701	4.4185	21.3778	20.9135	25.1489
LSB09083	138.67357	2.4148436	3.4337	3.2247	22.6141	21.1735	25.7918
LSB09084	138.7421	1.0007017	2.8915	2.6484	22.5902	21.6669	24.8549
LSB09085	138.74261	1.0013458	3.9447	2.8811	23.1183	21.8923	26.3972
LSB09086	138.91884	2.2210083	2.3338	1.4036	22.9988	22.3447	24.0778
LSB09087	138.94423	2.2148294	2.2021	1.6255	22.2063	22.3669	24.2605
LSB09088	138.98769	0.6306243	7.8799	6.1561	20.9482	20.5399	24.9093
LSB09089	139.10703	0.7560009	2.0704	1.6504	23.4311	22.4382	24.8087
LSB09090	139.11559	0.7544283	1.8981	1.5243	22.9473	22.5411	24.7039
LSB09091	139.20633	0.775165	3.8970	3.7876	24.7379	20.7083	24.6380
LSB09092	139.22705	-0.8472468	2.7010	2.0741	23.5818	21.7876	25.6762
LSB09093	139.2284	-0.7800562	4.4006	3.3669	21.666	21.152	24.3396

LSB09094	139.36052	2.6827922	2.5876	2.2481	22.2526	22.243	24.6895
LSB09095	139.37987	1.9229083	5.0157	3.2297	21.2741	20.7292	24.3440
LSB09096	139.38275	0.6529995	3.4006	2.9804	22.5586	21.9596	24.5835
LSB09097	139.42352	-0.7028235	1.8153	1.2482	22.8916	22.327	24.2865
LSB09098	139.4405	1.6241711	2.8666	2.5213	22.3611	21.6933	24.4435
LSB09099	139.48991	-1.3613256	4.1892	2.0955	22.4266	21.7735	24.0698
LSB09100	139.5178	0.7065429	2.8547	1.9898	22.368	21.8742	24.4875
LSB09101	139.5301	-0.0804536	1.9485	1.5660	22.1293	22.3286	24.1738
LSB09102	139.63446	1.8534511	1.7987	1.5365	22.8812	22.5354	24.5835
LSB09103	139.66922	1.5397595	4.0856	2.3804	22.5394	22.2491	24.7230
LSB09104	139.76797	-0.208377	2.7432	1.8509	22.308	21.913	24.2487
LSB09105	139.92413	3.0058315	3.6559	2.3711	23.6525	21.8466	24.3888
LSB09106	140.18279	1.426879	3.9908	3.7343	21.7406	21.5936	24.8364
LSB09107	140.23875	0.8548871	2.5893	2.3273	22.7407	21.4478	24.8929
LSB09108	140.32802	1.0559605	3.7968	3.0766	22.0282	20.4465	24.7700
LSB09109	140.63448	1.1391636	2.9318	2.0977	22.5958	21.8674	24.7906
LSB09110	140.76613	-0.0599354	4.8324	4.1426	21.4353	21.4355	25.0707
LSB09111	140.99066	1.4006438	5.7960	4.9720	21.6316	21.1286	25.0856
LSB12112	173.9233	0.205801	2.9741	2.3545	22.5464	21.6778	24.4613
LSB12113	174.17957	-1.0928775	3.4067	1.4008	22.6703	22.8881	24.6058
LSB12114	174.36147	-0.7890107	2.2867	2.1068	22.743	21.0376	24.6668
LSB12115	174.40137	1.5795437	9.2449	5.2165	20.8924	20.6269	24.9688
LSB12116	174.48265	-1.1832247	1.9154	1.7075	22.6147	21.8792	24.5722
LSB12117	174.53708	-1.147327	2.0420	1.8616	22.5799	21.8348	24.7308
LSB12118	174.62082	-2.8892057	2.5543	1.8633	22.7356	22.2415	24.6230
LSB12119	174.77713	1.7734306	5.4499	3.7214	21.025	21.1784	24.5150
LSB12120	174.93382	-1.467522	3.3258	2.1167	21.6137	21.3479	23.9818
LSB12121	175.03545	0.9513121	2.4113	2.2501	22.6872	21.632	25.7813
LSB12122	175.04352	0.9102873	3.4320	1.7364	22.6105	21.7517	24.3133
LSB12123	175.05731	0.967329	2.8448	2.5447	22.4122	21.6379	24.9737
LSB12124	175.1419	-0.5818876	2.1433	1.6628	22.8042	21.9078	24.7361
LSB12125	175.2921	1.7724499	4.2043	2.6174	22.2419	21.4009	25.0097
LSB12126	175.36784	0.9274588	3.3515	2.8032	22.7331	21.5861	24.9786
LSB12127	175.78618	1.252386	3.9941	3.0229	21.8663	20.7158	24.3919
LSB12128	175.88477	1.7603557	3.1843	1.8504	22.6593	21.8728	24.3857
LSB12129	175.90956	1.7273678	3.0232	1.9601	23.1801	21.9125	24.4799
LSB12130	176.49602	0.6523666	4.3286	2.9867	21.9613	21.05	24.8964

LSB12131	176.72353	-1.6123807	2.3861	2.0859	22.7158	21.1053	25.0629
LSB12132	176.75803	-1.5941678	2.3856	2.1237	22.322	21.841	24.6113
LSB12133	176.83034	1.9986892	10.9619	9.1340	21.669	18.9216	25.0604
LSB12134	176.9922	1.432386	3.3140	2.3243	22.1738	21.4179	24.4761
LSB12135	177.19293	1.2535808	3.5600	2.8673	22.0955	20.943	24.7802
LSB12136	177.33577	-0.3035734	3.3313	1.9308	23.6066	22.3053	24.8614
LSB12137	177.33617	-0.3053225	3.4058	2.0596	22.6343	22.1134	24.8441
LSB12138	177.6101	-1.2572414	2.2847	1.5870	22.9486	22.2838	24.4635
LSB12139	177.62619	1.8526418	2.4599	2.2743	22.3332	21.3011	24.9069
LSB12140	177.65651	1.6073139	3.1859	2.5276	22.6447	21.3474	24.9963
LSB12141	177.89755	1.7597286	3.1051	2.7206	21.5643	21.0069	24.3020
LSB12142 ²	178.07336	0.8470706	3.7494	1.6078	99	23.4863	
LSB12143	178.16978	-0.5662372	4.8266	3.1586	22.8708	21.0014	24.7465
LSB12144	178.41335	1.855143	3.2498	3.0256	22.0443	21.2545	24.9401
LSB12145	178.45589	1.6617416	3.1525	2.2757	22.7827	21.6702	24.2650
LSB12146	178.47293	1.7234395	4.2360	2.7059	23.7067	21.5923	24.0050
LSB12147	178.47678	1.7599995	3.5236	1.9121	22.7206	22.0976	25.3672
LSB12148	178.5363	0.5668178	3.7246	2.4293	22.7504	21.7227	25.1615
LSB12149	178.59483	1.2463651	2.7088	1.4369	23.3421	22.6263	24.8971
LSB12150	179.34868	-0.2494439	3.9397	3.2038	21.7565	21.6592	25.3978
LSB12151	179.57104	2.0353901	2.1894	1.9312	22.7918	21.9913	24.9102
LSB12152	179.62598	-1.6185286	2.6060	2.2866	22.6154	22.135	24.7996
LSB12153	179.6332	-1.8577418	5.1130	4.2788	20.9437	20.7148	24.9434
LSB12154	179.7254	-1.2016097	4.0550	3.3242	21.9207	21.2633	25.2500
LSB12155	179.77655	-0.223316	1.8889	1.8367	22.587	22.2911	24.7172
LSB12156	179.93796	1.5709707	5.0330	2.9491	21.8079	21.0581	23.9826
LSB12157	179.99298	0.8694392	4.3812	2.2628	23.7416	21.8459	24.3379
LSB12158	180.0649	-1.0910075	4.0375	3.2361	21.6625	21.3062	24.3126
LSB12159	180.09084	1.6641341	6.2180	4.7826	21.3399	20.5291	24.5418
LSB12160	180.23477	1.2714336	2.3797	2.0077	22.2897	21.8329	24.4680
LSB12161	180.23889	1.2497051	3.8117	2.6043	21.9423	20.5515	24.4190
LSB12162	180.23979	1.2500044	2.7360	2.3824	22.0697	21.6866	24.2376
LSB12163	180.27849	1.7402687	3.1579	2.2754	22.5595	22.1297	24.6685
LSB12164	180.29556	-0.3427207	4.2438	3.0574	21.9778	21.8868	24.5786
LSB12165	180.31091	-0.3904342	3.1982	1.9346	23.0518	22.2488	24.4825
LSB12166	180.4537	0.5013138	2.2947	1.4333	22.4987	21.857	23.9854
LSB12167	180.46867	1.5413707	6.1478	3.7875	22.2195	20.5095	24.1644

LSB12168	180.58229	0.5963532	7.3095	3.9374	21.51	20.5845	24.2213
LSB12169	180.62883	0.5836311	2.7261	1.7114	22.514	22.2537	24.6101
LSB12170	180.67502	1.6126244	3.6333	2.4127	22.4513	21.5812	25.1804
LSB12171	180.74254	1.6796645	2.4316	2.0513	23.2069	22.7973	25.3099
LSB12172	180.75688	1.7319756	2.8365	1.8016	23.0097	21.9038	24.3127
LSB12173	180.91248	-0.8400798	2.5155	2.3688	22.688	22.3156	24.7452
LSB12174	180.92369	-0.8286511	3.7642	2.9615	23.0026	22.0737	24.9451
LSB12175	181.1209	-1.280674	2.9608	2.4291	23.2085	22.0234	25.3580
LSB12176	181.12163	-1.2811337	1.6419	1.5897	23.283	22.8926	25.1839
LSB12177	181.1599	0.1987569	2.3107	1.7598	22.7207	21.6049	24.4012
LSB12178	181.32521	1.7428979	1.8652	1.2968	22.7006	23.1002	24.1816
LSB12179	181.32837	1.6822639	2.0384	1.7489	22.8645	22.3354	24.8057
LSB12180	181.32903	1.741355	2.4860	1.9278	23.1401	22.3783	24.9420
LSB12181	181.3327	1.7257106	8.1721	7.5726	23.7881	20.0705	25.1946
LSB12182	181.34561	-1.5001056	4.2545	2.7538	22.0502	21.3278	24.8935
LSB12183	181.3454	1.7918327	11.8993	10.5825	20.0905	19.6719	25.1982
LSB12184	181.34644	1.7691823	3.5425	3.4210	22.3812	21.7672	24.8515
LSB12185	181.35828	1.7237722	2.4810	1.5792	23.0603	22.3904	24.5714
LSB12186	181.49654	-1.9934142	3.4890	2.0512	22.2892	21.9351	24.5325
LSB12187	181.50473	2.0089517	4.2901	3.7760	22.8969	22.026	25.0568
LSB12188	181.5146	2.0151854	2.1451	1.9093	22.7955	22.5576	25.1346
LSB12189	181.5163	2.0187263	3.7723	3.0276	23.2263	21.8246	24.5256
LSB12190	181.52672	2.0392444	2.8158	2.4674	22.4591	21.7142	24.7245
LSB12191	181.52946	0.0310497	2.9231	2.7348	22.5541	22.2377	25.4409
LSB12192	181.7427	1.6592497	3.1856	2.8347	22.5002	21.8574	24.9162
LSB12193	181.76764	1.6814373	3.9407	3.1025	22.7708	21.8727	24.5872
LSB12194	181.8006	-0.6729135	1.7911	1.6068	22.9095	22.3777	25.3783
LSB12195	181.86287	0.7062755	2.4294	1.6985	22.9707	22.9744	25.1551
LSB12196	182.0135	-1.4697771	7.8254	4.7470	21.7565	20.5469	24.8403
LSB12197	182.0516	0.6398589	3.8015	1.8830	22.5934	21.3866	24.9194
LSB12198	182.1366	-0.0214293	2.2508	1.6979	23.0982	22.2226	25.1788
LSB12199	182.45735	-0.9658678	3.1232	2.5267	22.0048	21.9464	24.7589
LSB12200	182.65347	1.4475459	5.5006	3.9409	21.5969	21.1131	24.6220
LSB12201	182.82574	-1.9730686	2.6554	1.9387	22.5219	21.865	24.2779
LSB12202	182.82802	1.7124265	3.6965	2.4210	22.3466	22.3328	24.7331
LSB12203	182.83902	1.342883	3.1245	2.5129	22.8863	21.8932	25.1982
LSB12204	183.49693	-0.6315207	3.9527	3.5215	22.7019	21.0208	24.4347

LSB12205	183.68134	1.3380415	3.1854	2.1166	22.1634	22.0201	24.4138
LSB12206	183.7167	-0.6548752	4.0800	2.7484	21.9198	21.8394	24.4887
LSB12207	183.76077	-0.5481748	3.5106	2.9726	21.6831	20.9607	24.7534
LSB12208	183.96555	0.0054639	2.2193	1.7644	23.3786	22.6406	25.2074
LSB12209	183.9665	0.0074475	1.7590	1.5033	22.672	23.0936	24.5593
LSB12210	184.14024	-1.2544146	2.2763	1.7757	22.1908	22.0894	24.3961
LSB12211	184.20561	1.2457364	4.0698	3.2799	21.6663	20.9255	25.0732
LSB12212	184.24861	1.7189575	3.0016	2.3962	22.4416	22.0071	24.5727
LSB12213 ^{2,3}	184.77385	1.1144433	13.9582	9.1267	22.7709	20.8732	
LSB12214	184.81006	-2.0190814	5.2018	4.5830	21.6148	20.8433	26.1027
LSB12215	185.35762	1.2624848	2.3015	1.6540	22.6713	22.3454	24.4750
LSB12216	185.36206	1.2632841	2.7864	1.8035	22.8541	22.115	24.4214
LSB12217	185.47128	1.3389038	4.3113	2.9814	21.4067	21.229	24.1295
LSB12218 ³	185.57948	-2.799344	7.0016	6.8729	22.8493	21.0653	
LSB12219	185.61594	-2.493291	2.4074	1.6504	23.2825	21.8679	24.5164
LSB12220	185.78307	1.747889	3.0914	2.7813	22.3237	21.9607	25.0775
LSB12221	185.81627	1.6985523	4.8858	3.7927	22.0245	20.9003	24.9453
LSB15222	212.01245	0.3628651	2.8989	2.3560	22.5402	21.6595	25.1393
LSB15223	212.01396	0.3853621	2.7955	2.2325	23.125	21.8148	24.9832
LSB15224	212.21507	-1.4532537	3.1466	2.7212	23.0597	20.7297	25.2659
LSB15225	212.6163	-0.2938791	2.1025	1.9494	22.7732	21.4903	24.8867
LSB15226	212.85986	1.4047865	3.3408	3.0272	21.42	21.5425	24.5141
LSB15227	212.93446	2.359877	2.0035	1.5720	23.1225	22.8289	24.9671
LSB15228	212.9486	1.3155879	3.7386	2.7693	22.4551	21.7557	24.3660
LSB15229	212.95381	2.4460514	3.5167	3.1923	23.0836	21.7839	24.8980
LSB15230	213.0923	2.3291068	2.1747	2.0933	22.0522	21.9321	24.3985
LSB15231	213.12363	1.5703441	1.4974	1.4677	23.1794	22.9777	24.7382
LSB15232	213.26299	1.2982538	5.2169	3.8211	21.2997	20.7831	24.4528
LSB15233	213.34418	-0.81815	4.0969	3.1337	22.0448	21.5342	25.0680
LSB15234	213.3494	-0.8712878	2.1023	1.3088	23.293	23.2237	24.7067
LSB15235	213.35158	-0.8718236	3.9266	2.0693	22.5697	21.8892	24.4485
LSB15236	213.64421	2.5213983	2.4935	2.0181	22.7088	22.4407	24.6181
LSB15237	213.75583	1.751082	5.8232	4.2661	21.6467	21.1992	24.7872
LSB15238	213.78859	2.7727916	2.1625	1.7623	22.2011	22.2554	24.2681
LSB15239	214.23706	1.0575188	5.0011	3.8612	21.7819	21.0805	25.1766
LSB15240	214.25511	-0.1038975	3.0599	2.2411	27.4436	22.5787	24.9931
LSB15241	214.41643	2.723527	3.7849	2.1867	21.8987	21.4594	24.0822

LSB15242	214.42212	-1.4310743	4.5088	3.0043	21.8114	21.1293	24.4078
LSB15243	214.49028	1.1398729	2.3208	1.7347	22.8981	21.9599	24.5308
LSB15244	215.07664	2.9822013	9.2058	4.1008	21.5831	20.5849	24.0372
LSB15245	215.16891	2.7183402	6.2513	3.8374	21.5009	20.176	24.8624
LSB15246	215.2661	1.8424808	3.2153	2.7613	22.346	21.9349	24.9555
LSB15247	215.45395	2.360148	2.5775	1.4997	23.5057	22.388	24.9587
LSB15248	215.49884	-1.9169383	3.5554	2.8379	22.4413	21.1357	24.9157
LSB15249	215.51984	2.4001007	5.5793	3.9587	21.8653	20.9074	25.4855
LSB15250	215.58328	2.3778696	8.2672	4.3520	20.9581	20.6627	24.6698
LSB15251	215.58316	2.3788528	5.1604	2.8349	22.1976	21.4262	25.0805
LSB15252	215.60982	-0.6347965	2.3066	1.8877	22.9838	22.1365	25.5107
LSB15253	215.6517	2.7481184	4.1599	3.5548	22.0839	21.295	25.3799
LSB15254	215.66957	1.6374352	2.2822	1.4432	22.8263	22.1237	24.2730
LSB15255	215.84384	2.4398584	3.8716	2.7314	22.6528	22.1374	24.9349
LSB15256	215.88019	1.7564328	2.6011	2.1331	22.0983	22.2244	24.4874
LSB15257	215.88058	1.8284869	2.5591	1.8360	22.4326	22.4153	24.4088
LSB15258	215.88113	1.7603627	2.3623	1.4060	22.9045	21.9887	24.5299
LSB15259	215.8812	1.7555268	2.2444	1.7466	22.6654	22.3142	24.4350
LSB15260 ^{2,3}	216.1322	1.925543	6.1683	5.5577	22.966	21.4861	
LSB15261	216.31714	1.5095775	3.1076	2.4128	22.4403	21.7946	24.5472
LSB15262	216.38608	1.5288144	4.7918	2.4238	22.0567	21.5589	24.5643
LSB15263	216.46811	1.099148	2.3555	2.2113	22.8809	22.0831	25.0258
LSB15264	216.50253	0.7832083	2.3054	2.1891	23.1359	22.3052	25.1919
LSB15265	216.5263	1.4843765	2.0701	1.7640	22.1344	22.4535	24.3341
LSB15266	216.68579	1.701667	2.8990	1.9269	22.4946	21.7585	24.3685
LSB15267	216.68654	1.6995683	5.2923	4.4750	22.4571	20.7078	25.0473
LSB15268	216.947	0.142472	4.7945	2.9865	22.0412	21.2044	25.4003
LSB15269 ¹	216.98161	-1.7907					
LSB15270	217.15456	2.112728	3.4753	2.1235	22.528	21.9661	25.1253
LSB15271	217.19711	1.6153454	3.3737	2.2428	22.3417	21.3169	24.5836
LSB15272	217.22205	1.0953273	2.9786	2.5166	22.4922	22.3686	24.7379
LSB15273	217.27626	1.0433937	1.7264	1.5994	23.1226	22.1951	24.9860
LSB15274	217.2868	-1.93128	5.2554	3.0626	21.2961	22.0833	24.2213
LSB15275	217.29424	-1.3773935	1.4001	1.3372	23.2225	22.9446	24.7245
LSB15276	217.30716	-1.5949094	3.6453	2.6207	23.4626	21.8834	25.9408
LSB15277	217.40565	0.9152898	2.4145	2.0242	22.2606	21.5524	24.5473
LSB15278	217.48491	2.5091927	3.6867	2.7736	21.9952	21.4506	24.6959

LSB15279	217.76918	2.7777164	3.5081	3.3010	21.9747	21.0911	24.6568
LSB15280	217.78322	2.8719597	5.3644	3.7736	21.7746	21.1188	24.8006
LSB15281	217.88286	3.0051112	3.8736	3.3048	22.3014	20.9905	24.4837
LSB15282	217.88359	3.006272	2.3502	1.7318	22.9807	22.2247	25.1456
LSB15283	218.11156	2.757457	5.7043	2.9126	21.0413	20.7476	24.0815
LSB15284	218.47939	1.4447011	5.0788	4.6882	21.2318	20.4658	24.7310
LSB15285	218.89374	2.230398	2.9860	2.2020	22.7634	22.3144	24.7020
LSB15286	218.89958	2.2758565	5.7927	3.8739	23.2974	21.2514	24.2470
LSB15287 ³	218.91776	0.1843939	9.3885	4.6930	22.9608	21.819	
LSB15288 ¹	218.96835	2.22201					
LSB15289	219.0085	1.8360158	2.7384	1.2945	22.6094	22.2699	23.9930
LSB15290	219.04901	-0.6291455	5.2830	3.0928	24.1033	21.8695	24.9439
LSB15291	219.194	2.5529473	3.2830	2.5505	22.3269	21.859	25.0441
LSB15292	219.26688	1.5194068	4.1838	3.5282	21.8473	21.0123	25.0904
LSB15293	219.36504	2.8793623	2.8206	2.6282	21.9988	21.7984	25.1650
LSB15294	219.4219	2.337313	4.1298	3.5499	22.2388	21.9726	24.7609
LSB15295	219.4315	2.3358986	2.3410	1.9091	22.2588	22.0451	24.4361
LSB15296	219.45819	1.3294305	3.8735	3.0764	22.1061	21.3545	24.8036
LSB15297	219.90555	1.9979037	6.8005	4.4626	20.9152	20.9435	24.5143
LSB15298	220.02882	-1.1069613	2.3925	1.7362	22.4974	22.7445	24.4395
LSB15299	220.26273	2.9642181	4.6941	2.5013	22.043	21.6427	24.1395
LSB15300	220.29239	2.2466714	3.3311	2.3078	22.124	21.9357	24.7767
LSB15301	220.40186	-1.4333202	3.1296	2.5543	22.4196	21.9957	24.8943
LSB15302	220.42247	0.456498	2.3335	1.5626	22.5921	22.7848	24.4903
LSB15303	220.44278	1.6378729	3.7992	2.5358	21.734	21.4507	24.4525
LSB15304	220.4465	1.6491683	3.1417	2.0902	22.4841	21.8745	24.2383
LSB15305	220.46707	1.651671	8.7260	4.5641	21.2565	20.2786	25.4519
LSB15306	220.57628	1.6435302	2.5759	1.5448	23.0687	22.1991	24.7366
LSB15307	220.61205	2.2385256	6.4516	4.8088	21.3737	20.5975	25.2818
LSB15308	220.90857	2.1950765	5.2149	3.1358	21.4308	21.1022	24.4723
LSB15309	221.11299	2.9608457	3.9417	3.0817	21.6805	21.1686	25.0622
LSB15310	221.22421	-1.088718	2.9310	2.4425	22.9617	21.5735	25.5695
LSB15311	221.43217	1.767052	2.2421	1.7017	23.1957	22.4674	24.6384
LSB15312	221.44225	1.7013263	3.1709	1.8192	22.2657	21.8336	24.0940
LSB15313	221.44775	2.030775	3.5549	2.5498	22.8185	21.797	24.6678
LSB15314	221.47849	2.0382676	2.5332	1.8853	22.3964	21.6288	24.6213
LSB15315	221.48917	-1.3080446	2.1689	0.9255	23.0021	22.2978	23.7290

LSB15316	221.49748	2.2284212	2.6476	2.2031	22.5641	22.2624	25.2595
LSB15317	221.49748	2.2284184	2.8166	2.4094	22.4519	22.2503	25.3281
LSB15318	221.6079	1.2898256	1.9954	1.6048	22.7072	22.0904	24.2950
LSB15319	221.66093	2.0068934	4.6155	2.8088	22.2164	21.7818	24.2607
LSB15320	221.75862	1.3366328	3.3449	2.3478	22.6762	22.3859	24.5721
LSB15321	221.77289	2.025102	2.9089	2.5663	22.8627	22.1384	25.0776
LSB15322	221.83115	1.9851593	3.0339	1.8260	22.0824	21.9392	24.5590
LSB15323	222.3539	1.316313	2.2342	1.6611	22.599	22.0638	24.7403
LSB15324	222.52922	2.4952686	3.0989	2.7323	22.9187	22.0582	25.2943
LSB15325	222.53416	2.4948723	3.6279	2.4449	23.0245	21.8779	24.9815
LSB15326	222.60628	2.4770982	7.9614	4.9202	21.1996	20.3628	24.5045
LSB15327	222.6398	1.6344391	2.7906	1.4238	22.5523	22.38	24.4269
LSB15328	222.67342	2.3949728	3.1409	2.7978	23.3191	21.4249	25.4970
LSB15329	222.79291	0.5823522	4.7851	3.7669	22.0545	20.7761	25.0499
LSB15330	222.95473	1.5464424	4.8115	4.7773	21.5156	21.164	25.3233
LSB15331	223.12216	0.5128352	2.7299	2.4651	23.1818	21.5951	25.0747
LSB15332	223.13011	1.5667046	2.6530	1.8687	22.6496	21.6343	24.5128
LSB15333	223.27786	1.3067464	4.1110	2.0644	22.3804	21.6186	23.6786
LSB15334	223.30606	-2.015525	4.1943	2.8873	22.5415	21.9313	24.8084
LSB15335	223.3376	1.2702814	2.6789	2.2412	22.2664	21.9547	24.5388
LSB15336	223.38821	0.9306897	8.4073	4.9475	20.3682	20.2519	24.3769
LSB15337	223.39296	2.6237004	3.0545	2.7246	23.805	22.0389	24.9804
LSB15338	223.39351	2.6212687	3.2029	1.6962	22.5706	22.3449	24.3038
LSB15339	223.39392	2.6257772	3.1044	2.1833	22.3827	21.5402	24.2763
LSB15340	223.4361	1.5238143	3.8430	3.2012	22.1299	21.1157	25.1043
LSB15341	223.45651	1.2934494	3.0296	2.7476	22.0619	21.4904	24.5127
LSB15342	223.47292	2.744899	3.7367	2.2180	22.4655	21.3574	24.5864
LSB15343	223.60176	-1.3043734	3.3827	1.2239	23.0637	22.156	24.6689

¹Objects which could not be identified within $5''$ of the centre of the frame using IOTA but which were confirmed through visual checks.

²These objects were detected in the Z -band however their flux in the r -band was so low that only errors were returned. These objects have been given the magnitudes from the $5''$ fixed aperture measurement, and so have half light surface brightness. Even with this change LSB12142 was still not detectable in the r -band.

³Objects falling in the wings of the Δ_{mag} distribution whose imaging has obvious imperfections which have skewed the measurement of the magnitudes.

Appendix B

LSBG images from SDSS search algorithm

The images in this appendix represent a selection of the 343 objects (123) galaxies which were discovered through the methods detailed in Chapter 2. Included are those objects which are large and show promise for future follow up and a random selection of other objects from the catalogue. Also included are objects which IOTA had difficulty in getting accurate detections All images are produced as $20'' \times 20''$ cutouts from the VIKING Z -band imaging. It is difficult to see each object so all frames are centred on the central coordinates of the discovered objects. It is also possible to see why IOTA struggled to get accurate information for all of the galaxies and highlights why it struggled to detect LSB15269 & LSB15288. There is a clear effect from a nearby object in the image, however it is clear that there is an object in the centre of the frame. IOTA struggled in these edge cases and produced erroneous results as discussed in Chapter 2.

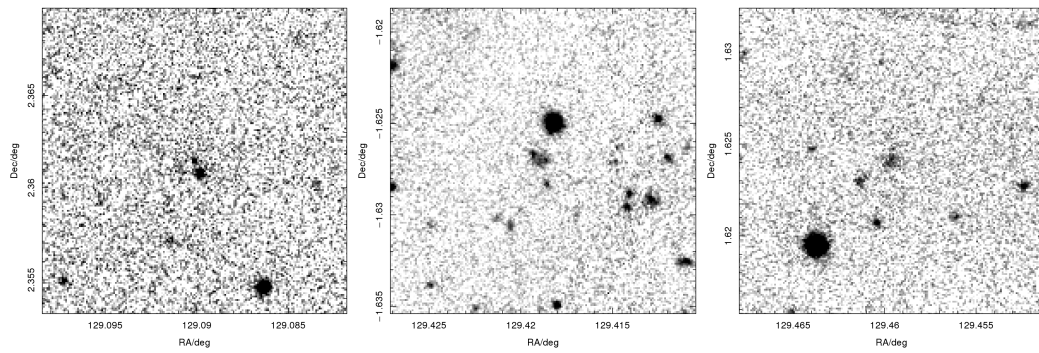


Figure B.1: LSB09002, LSB09005, LSB09006

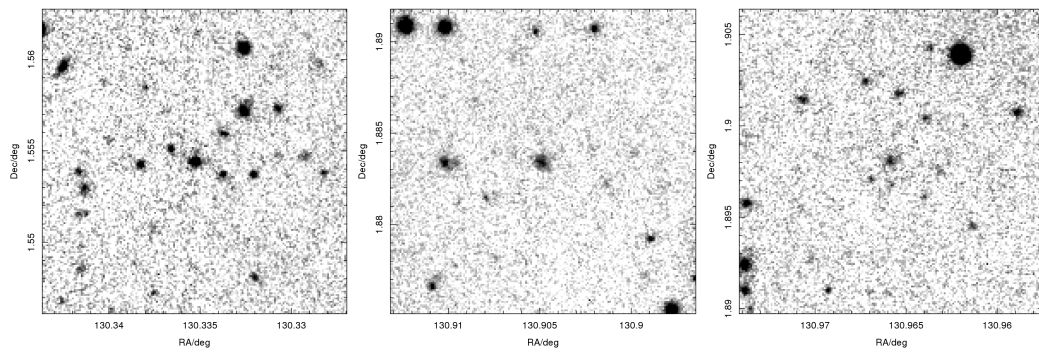


Figure B.2: LSB09016, LSB09018, LSB09019

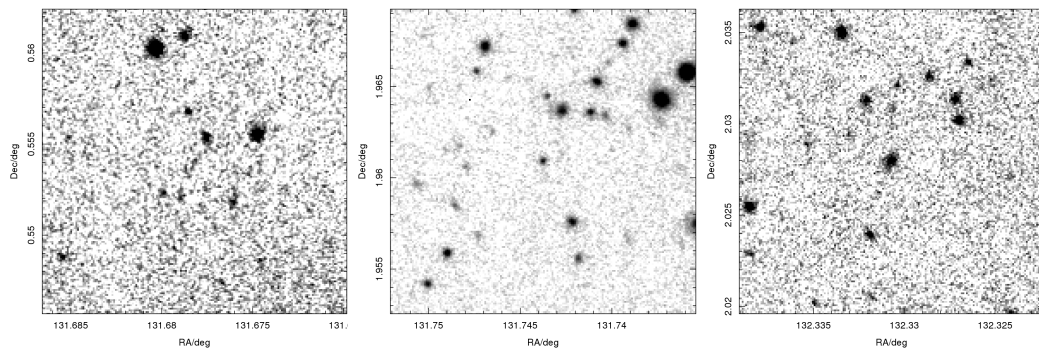


Figure B.3: LSB09023, LSB09025, LSB09031

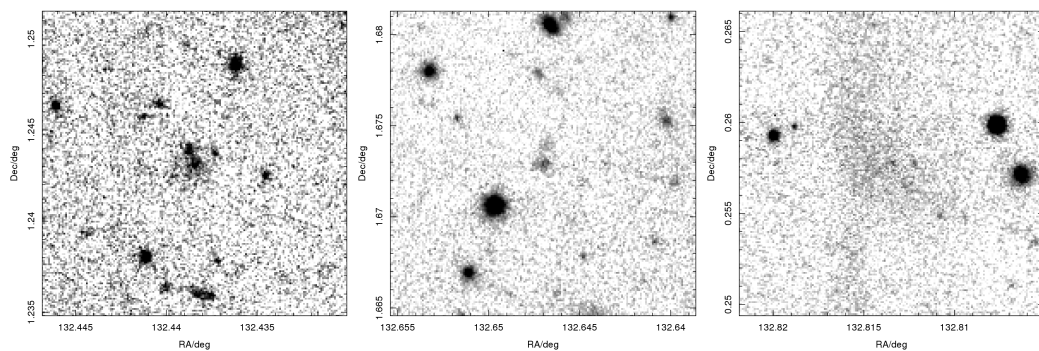


Figure B.4: LSB09032, LSB09036, LSB09037

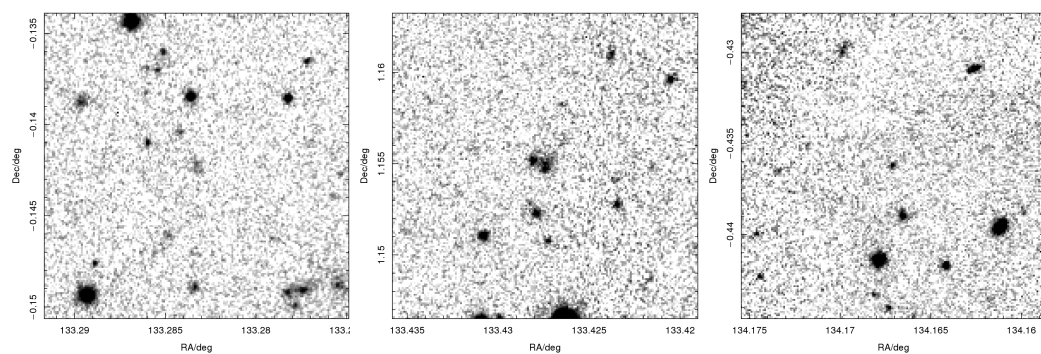


Figure B.5: LSB09043, LSB09045, LSB09050

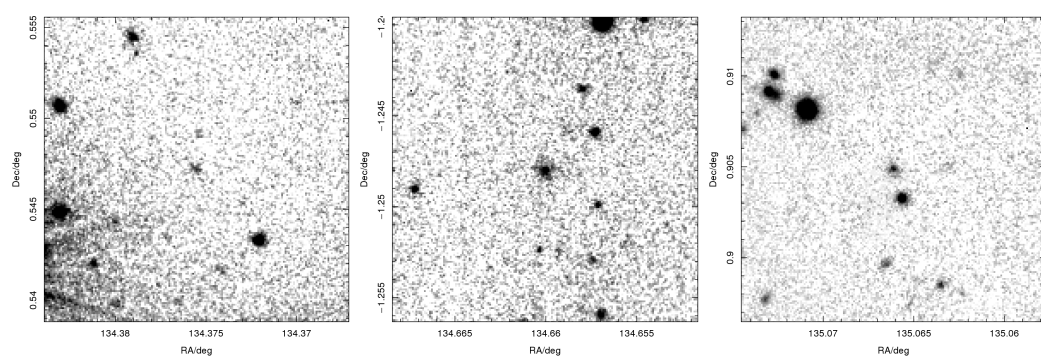


Figure B.6: LSB09052, LSB09055, LSB09061

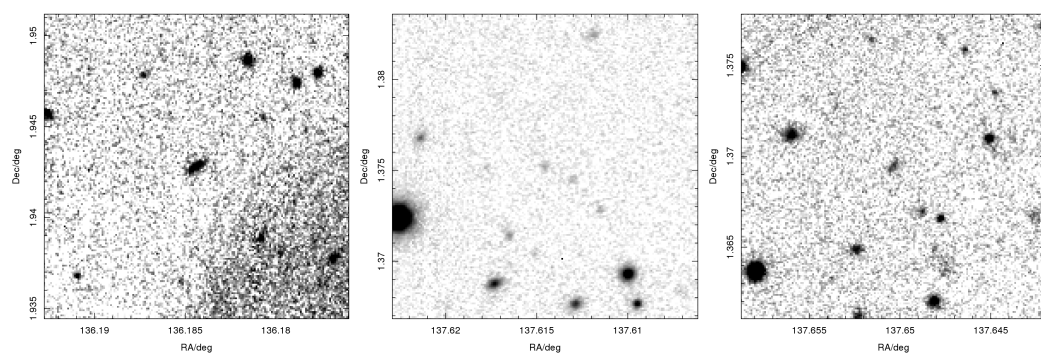


Figure B.7: LSB09064, LSB09068, LSB09069

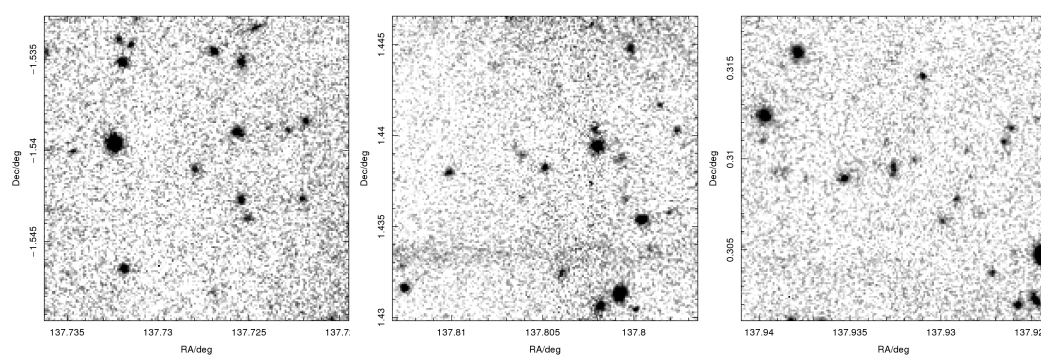


Figure B.8: LSB09070, LSB09072, LSB09075

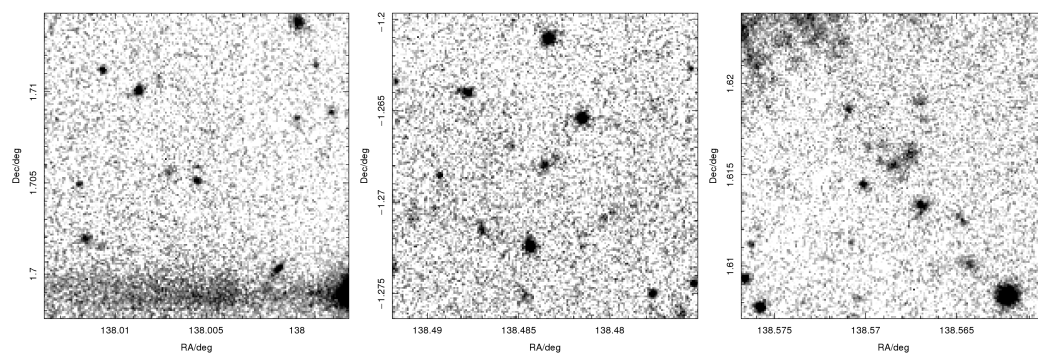


Figure B.9: LSB09076, LSB09079, LSB09082

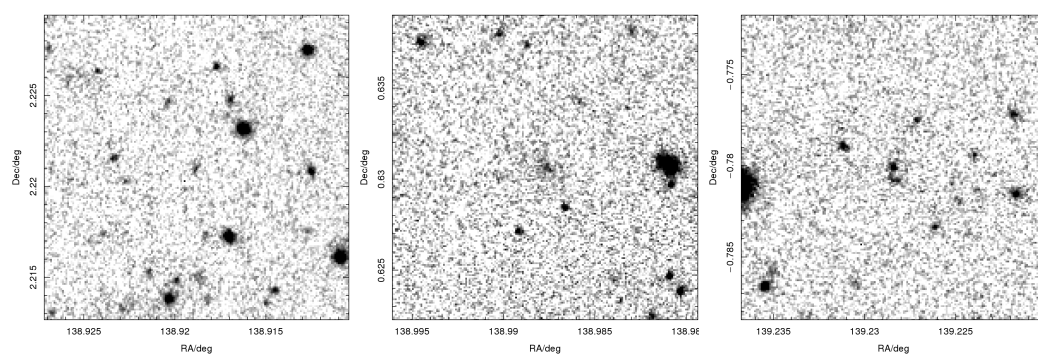


Figure B.10: LSB09086, LSB09088, LSB09093

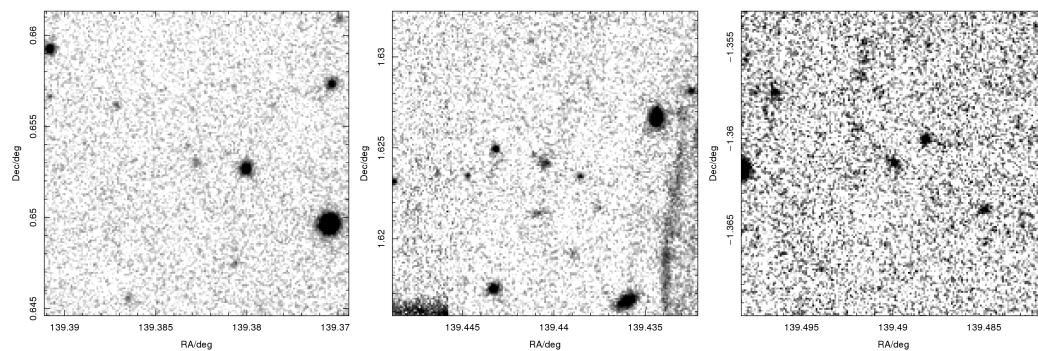


Figure B.11: LSB09096, LSB09098, LSB09099

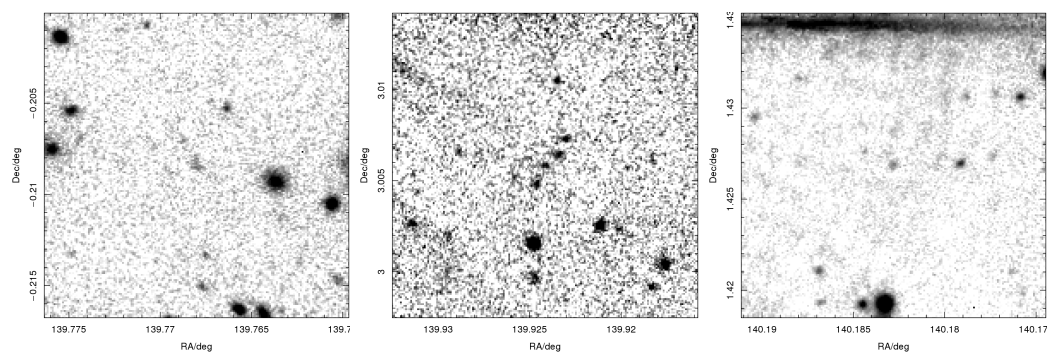


Figure B.12: LSB09104, LSB09105, LSB09106

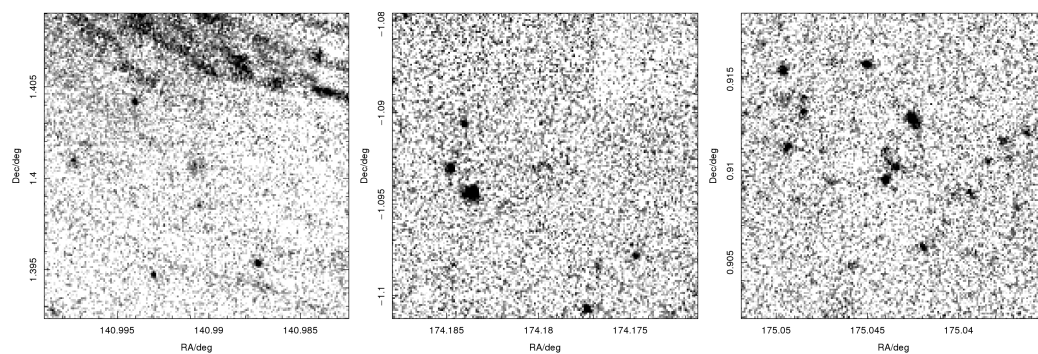


Figure B.13: LSB09111, LSB12113, LSB12122

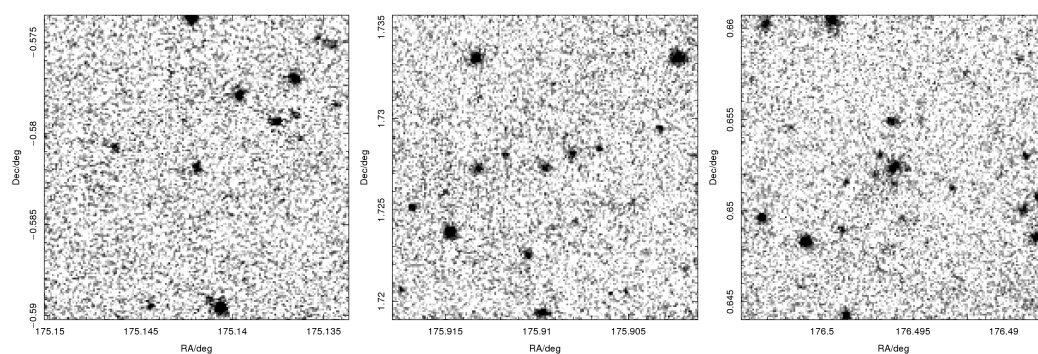


Figure B.14: LSB12124, LSB12129, LSB12130

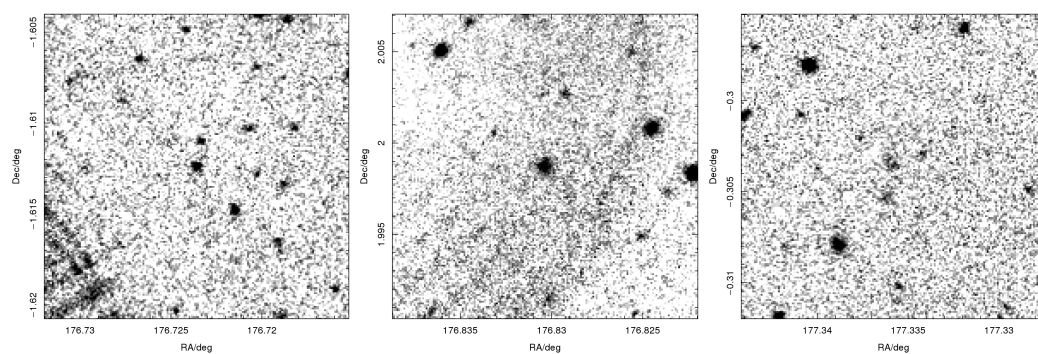


Figure B.15: LSB12131, LSB12133, LSB12136

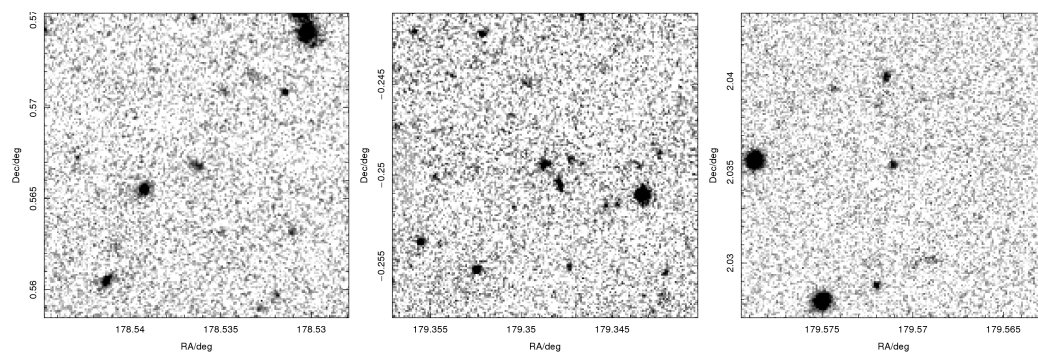


Figure B.16: LSB12148, LSB12150, LSB12151

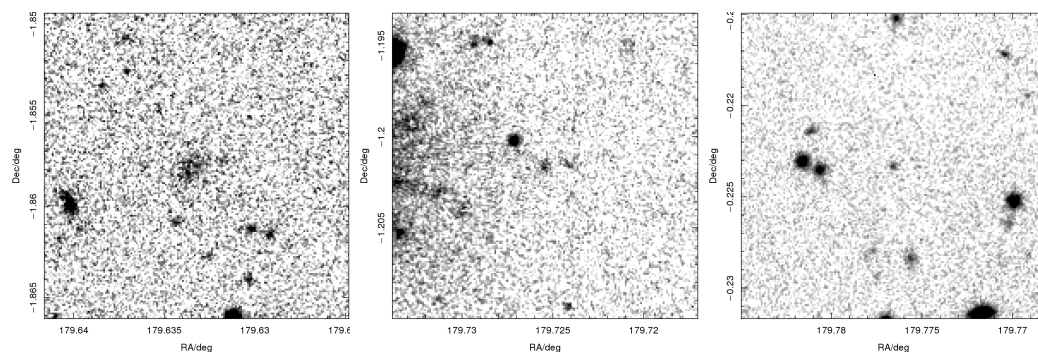


Figure B.17: LSB12153, LSB12154, LSB12155

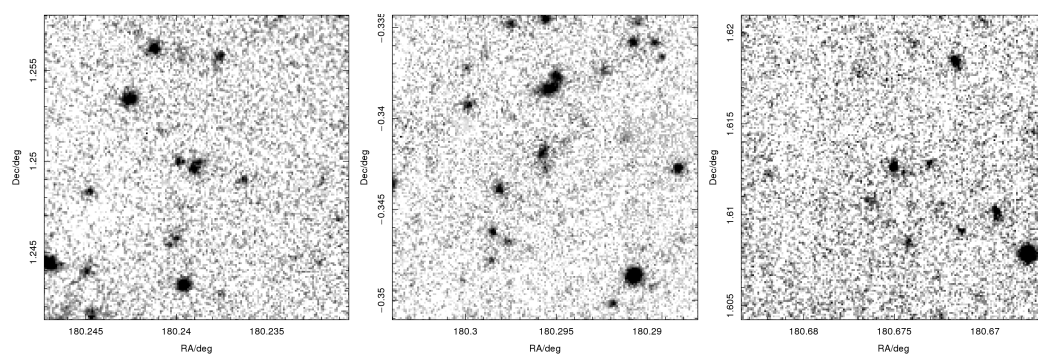


Figure B.18: LSB12161, LSB12164, LSB12170

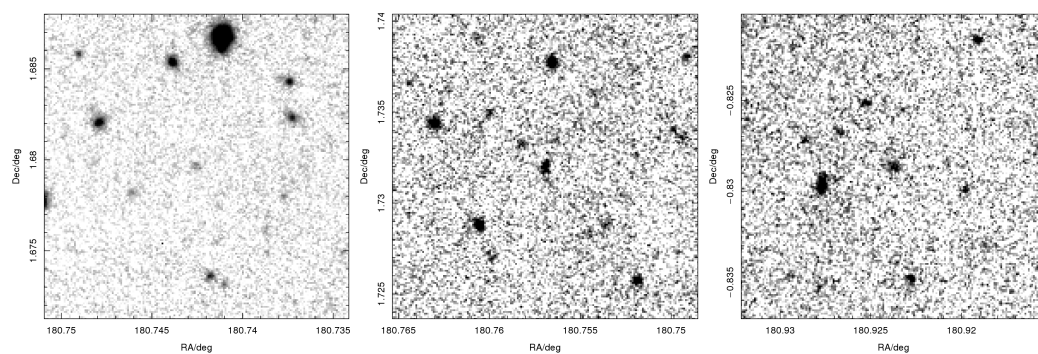


Figure B.19: LSB12171, LSB12172, LSB12174

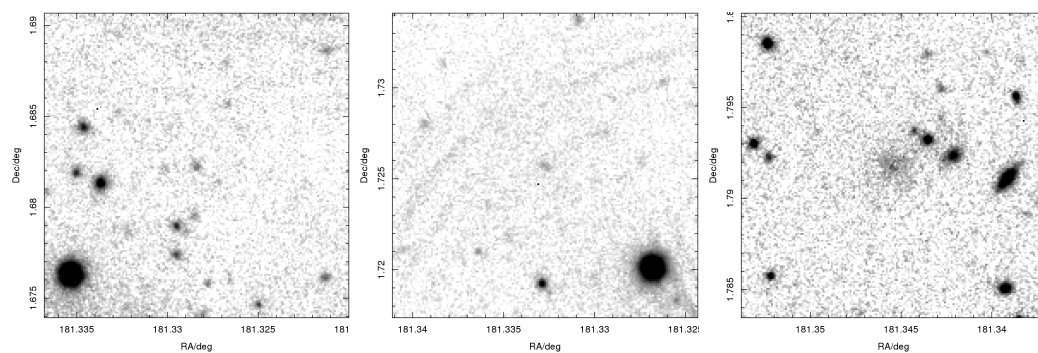


Figure B.20: LSB12179, LSB12181, LSB12183

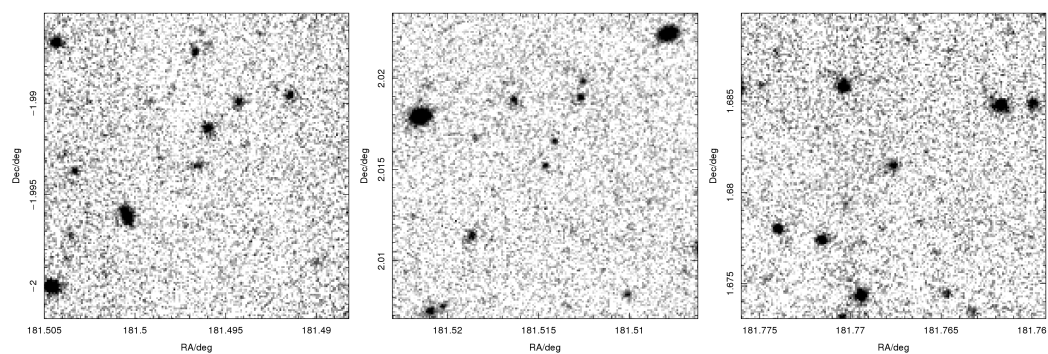


Figure B.21: LSB12186, LSB12188, LSB12193

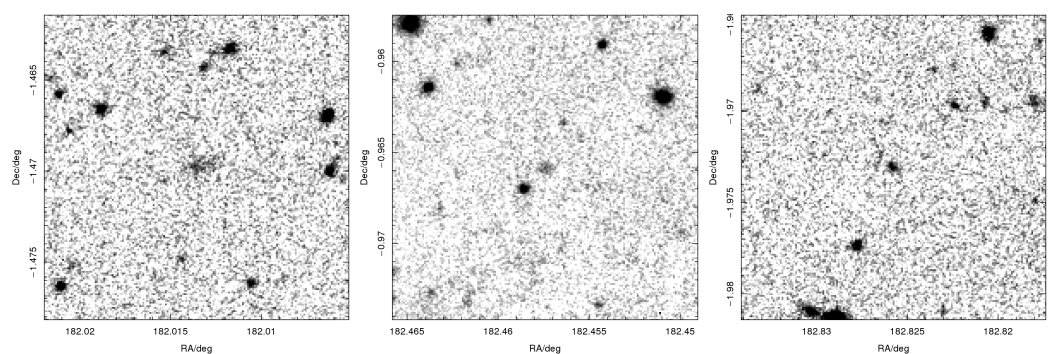


Figure B.22: LSB12196, LSB12199, LSB12201

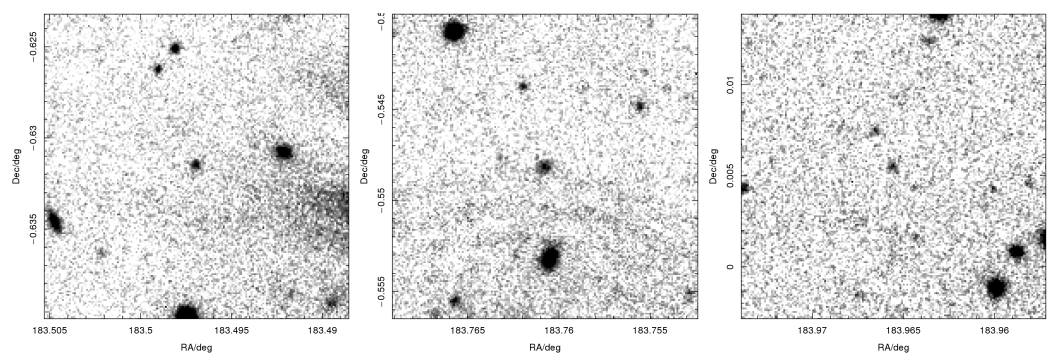


Figure B.23: LSB12204, LSB12207, LSB12208

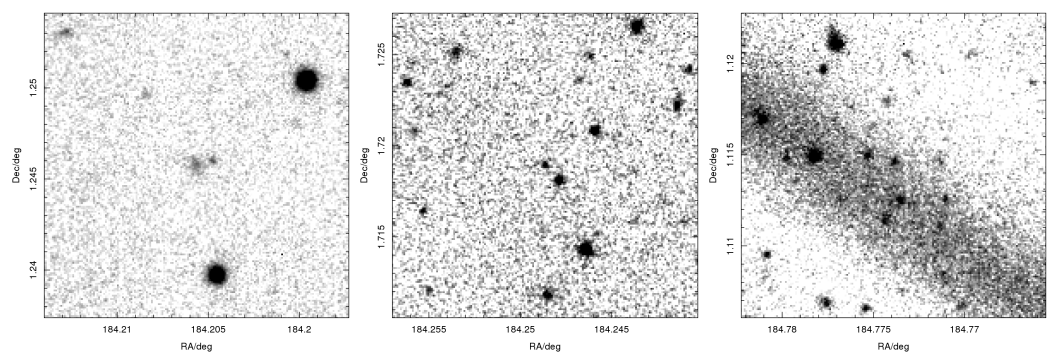


Figure B.24: LSB12211, LSB12212, LSB12213

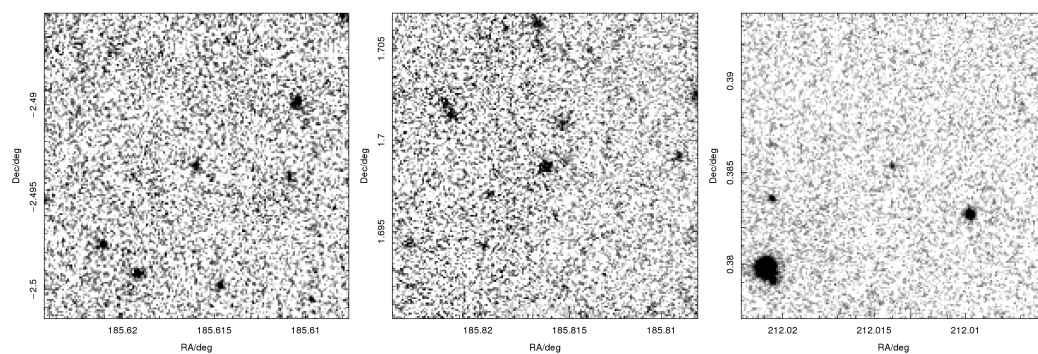


Figure B.25: LSB12219, LSB12221, LSB15223

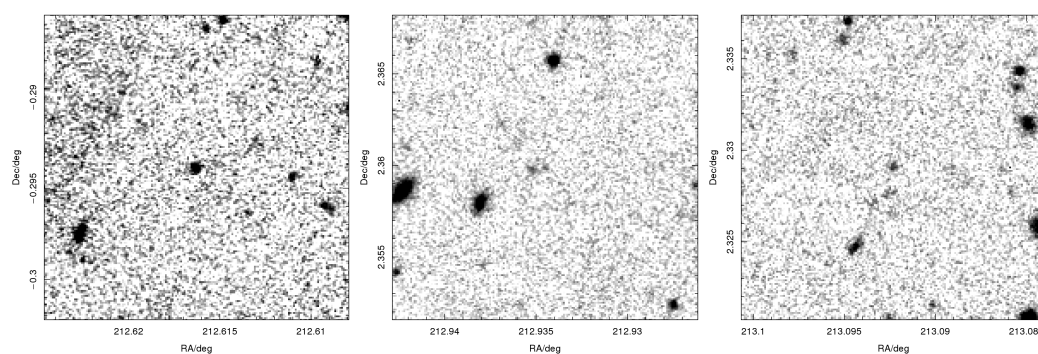


Figure B.26: LSB15225, LSB15227, LSB15230

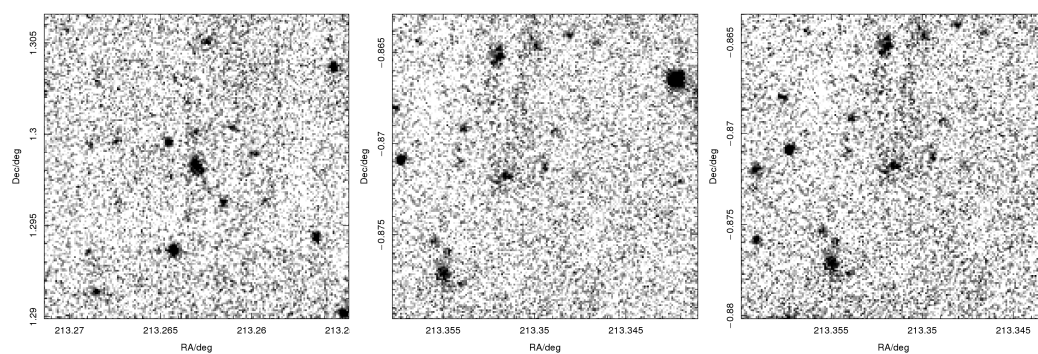


Figure B.27: LSB15232, LSB15234, LSB15235

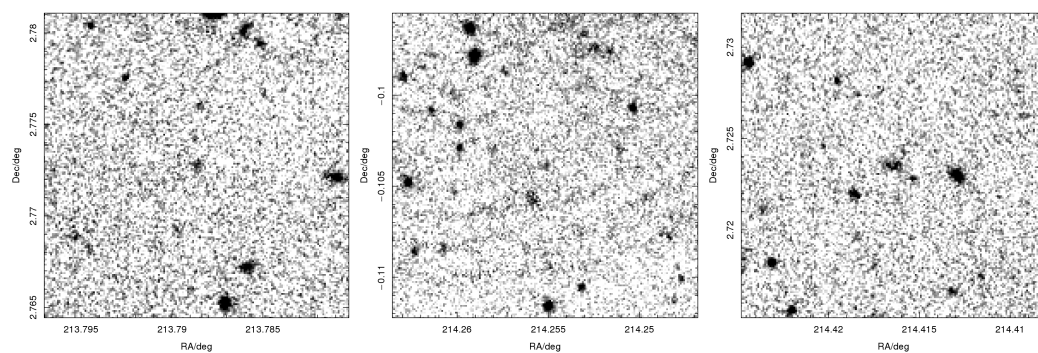


Figure B.28: LSB15238, LSB15240, LSB15241

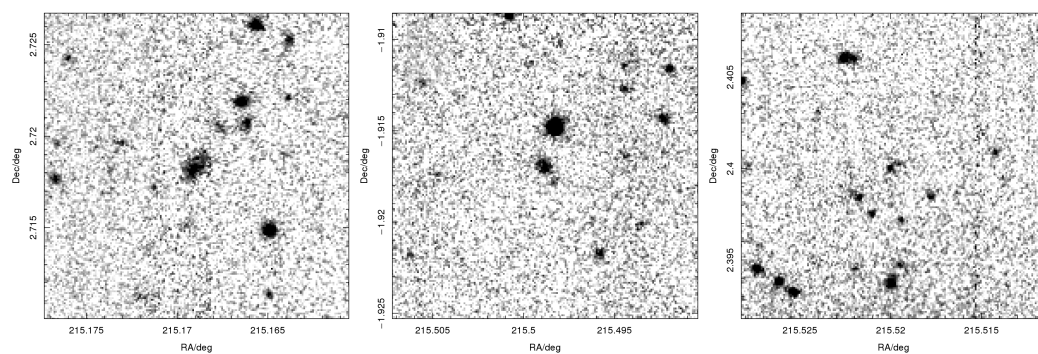


Figure B.29: LSB15245, LSB15248, LSB15249

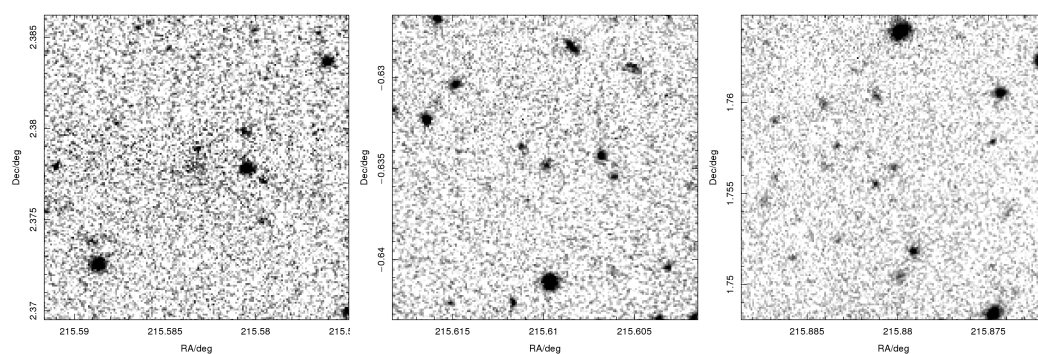


Figure B.30: LSB15251, LSB15252, LSB15256

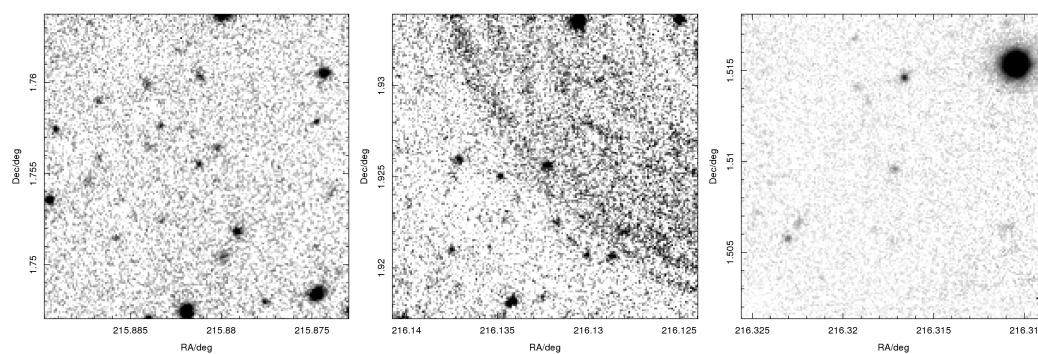


Figure B.31: LSB15259, LSB15260, LSB15261

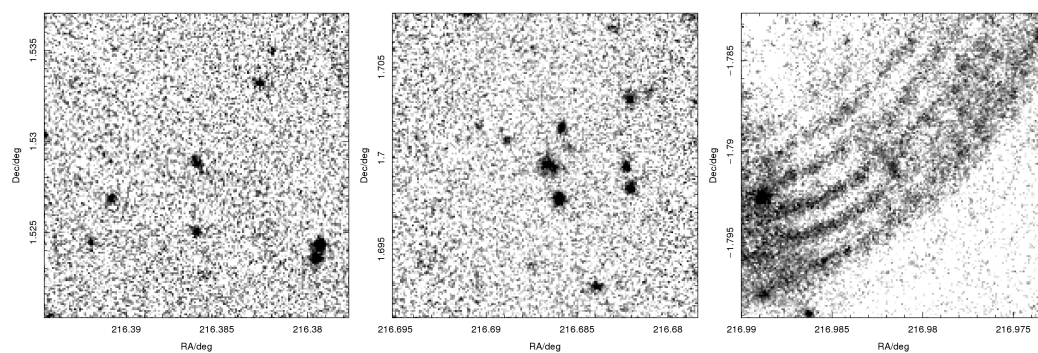


Figure B.32: LSB15262, LSB15267, LSB15269

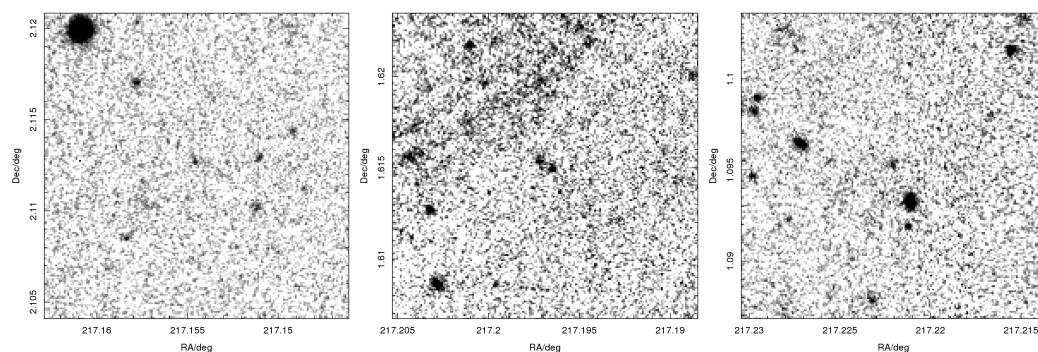


Figure B.33: LSB15270, LSB15271, LSB15272

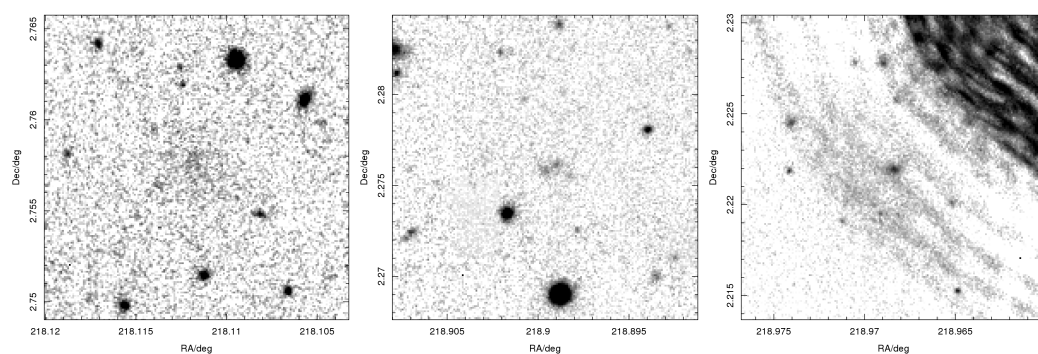


Figure B.34: LSB15283, LSB15286, LSB15288

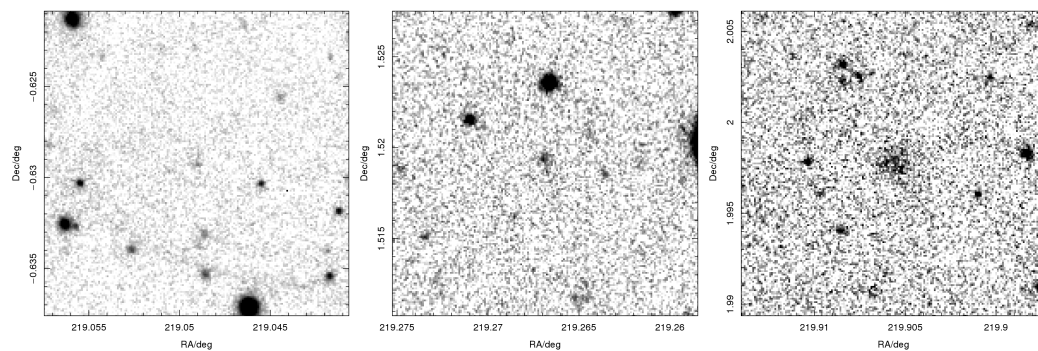


Figure B.35: LSB15290, LSB15292, LSB15297

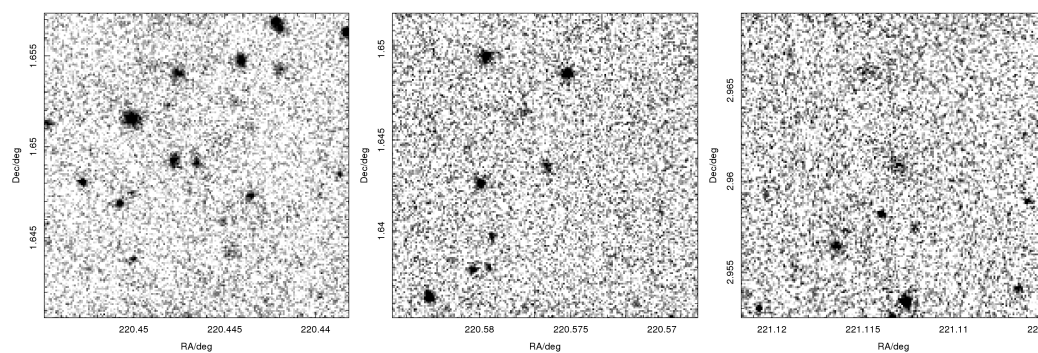


Figure B.36: LSB15304, LSB15306, LSB15309

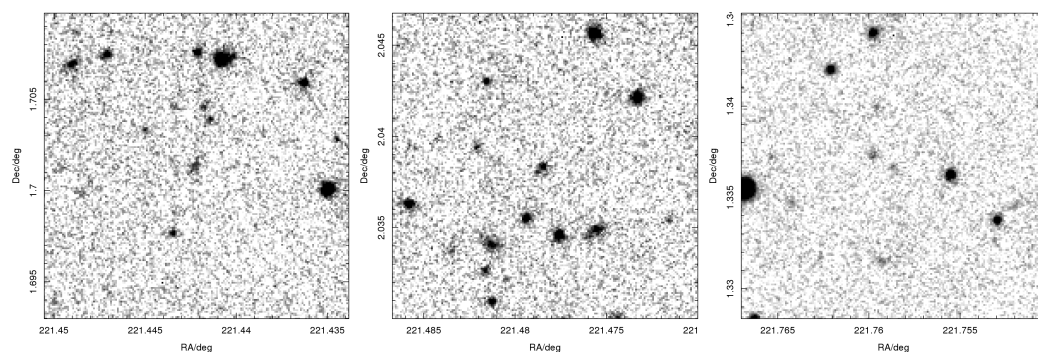


Figure B.37: LSB15312, LSB15314, LSB15320

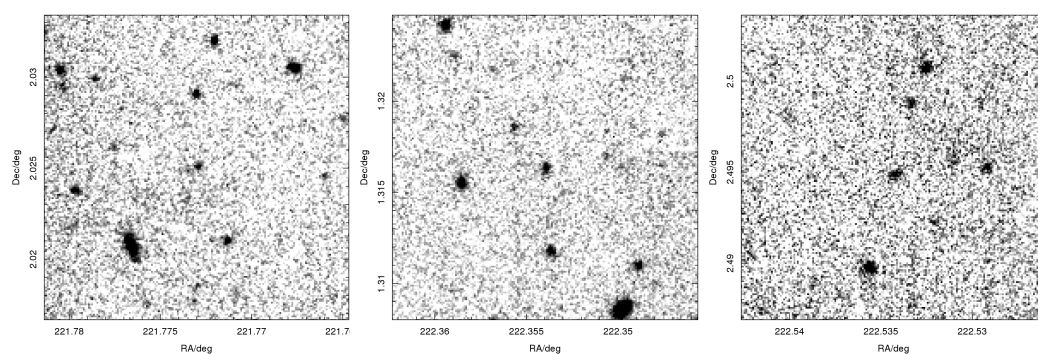


Figure B.38: LSB15321, LSB15323, LSB15325

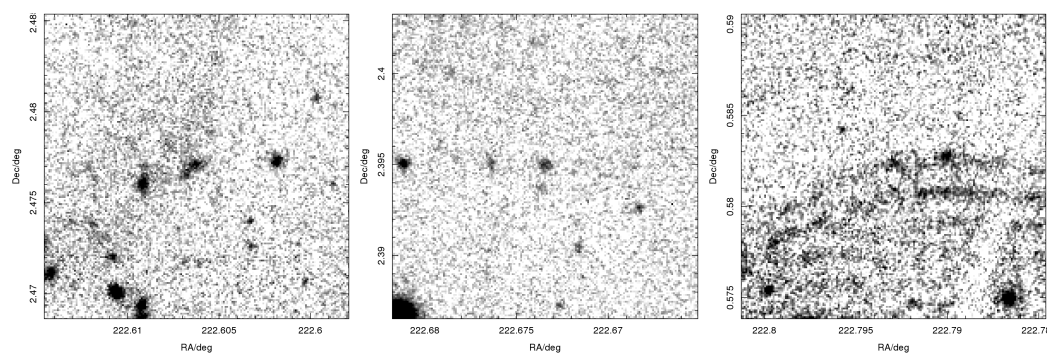


Figure B.39: LSB15326, LSB15328, LSB15329

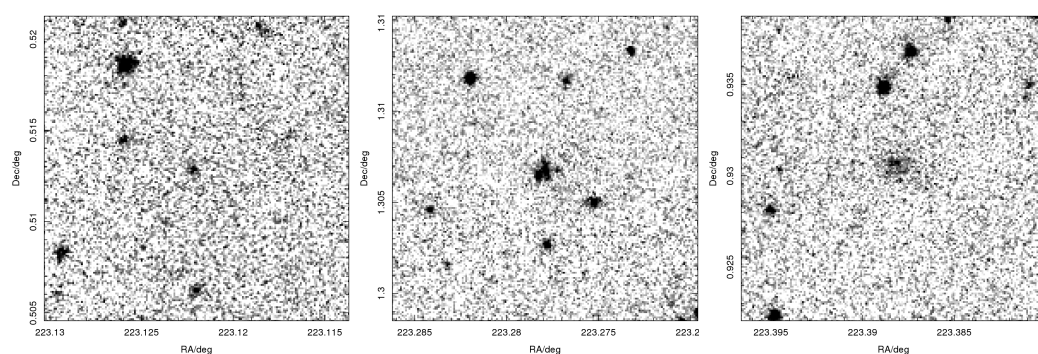


Figure B.40: LSB15331, LSB15333, LSB15336

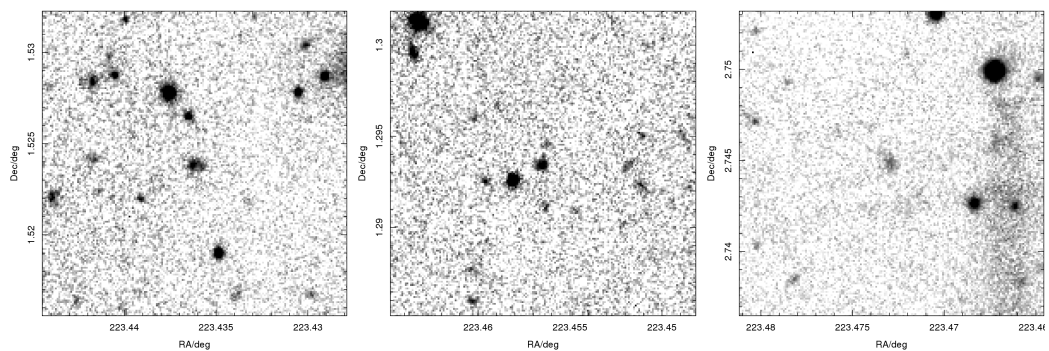


Figure B.41: LSB15340, LSB15341, LSB15342

Bibliography

Abazajian K. et al., 2004, AJ, 128, 502

Abazajian K. N. et al., 2009, ApJS, 182, 543

Abraham R. G., van Dokkum P. G., 2014, PASP, 126, 55

Adelman-McCarthy J. K. et al., 2006, ApJS, 162, 38

Alpaslan M. et al., 2014, MNRAS, 438, 177

Arnaboldi M., Neeser M. J., Parker L. C., Rosati P., Lombardi M., Dietrich J. P., Hummel W., 2007, The Messenger, 127, 28

Atkinson A. M., Abraham R. G., Ferguson A. M. N., 2013, ApJ, 765, 28

Bahcall N. A., 1988, ARA&A, 26, 631

Balbinot E. et al., 2013, ApJ, 767, 101

Balcells M. et al., 2010, in procSPIE, Vol. 7735, Ground-based and Airborne Instrumentation for Astronomy III, p. 77357G

Baldry I. K. et al., 2012, MNRAS, 421, 621

Baldry I. K., Glazebrook K., 2003, ApJ, 593, 258

Baldry I. K., Glazebrook K., Driver S. P., 2008, MNRAS, 388, 945

Baldry I. K. et al., 2010, MNRAS, 404, 86

Barkana R., Loeb A., 2001, Physics Reports, 349, 125

-
- Bastian N., Covey K. R., Meyer M. R., 2011, in *Astronomical Society of the Pacific Conference Series*, Vol. 448, 16th Cambridge Workshop on Cool Stars, Stellar Systems, and the Sun, Johns-Krull C., Browning M. K., West A. A., eds., p. 361
- Bell E. F., de Jong R. S., 2001, *ApJ*, 550, 212
- Bell E. F., McIntosh D. H., Katz N., Weinberg M. D., 2003, *ApJS*, 149, 289
- Belokurov V. et al., 2010, *ApJ*, 712, L103
- Belokurov V., Zucker D. B., Evans N. W., Wilkinson M. I., Irwin M. J., Hodgkin S., 2006, *ApJ*, 647, L111
- Bennett C. L. et al., 2013, *ApJS*, 208, 20
- Benson A. J., 2010, *Physics Reports*, 495, 33
- Benson A. J., Frenk C. S., Lacey C. G., Baugh C. M., Cole S., 2002a, *MNRAS*, 333, 177
- Benson A. J., Lacey C. G., Baugh C. M., Cole S., Frenk C. S., 2002b, *MNRAS*, 333, 156
- Binggeli B., 1994, in *European Southern Observatory Conference and Workshop Proceedings*, Vol. 49, European Southern Observatory Conference and Workshop Proceedings, Meylan G., Prugniel P., eds., p. 13
- Binggeli B., Sandage A., Tammann G. A., 1985, *AJ*, 90, 1681
- Binggeli B., Sandage A., Tammann G. A., 1988, *ARA&A*, 26, 509
- Binggeli B., Sandage A., Tarenghi M., 1984, *AJ*, 89, 64
- Binggeli B., Tammann G. A., Sandage A., 1987, *AJ*, 94, 251
- Blanton M. R., Eisenstein D., Hogg D. W., Schlegel D. J., Brinkmann J., 2005a, *ApJ*, 629, 143
- Blanton M. R. et al., 2003, *ApJ*, 592, 819

-
- Blanton M. R., Lupton R. H., Schlegel D. J., Strauss M. A., Brinkmann J., Fukugita M., Loveday J., 2005b, *ApJ*, 631, 208
- Blanton M. R., Roweis S., 2007, *AJ*, 133, 734
- Bolton J. S., Becker G. D., Raskutti S., Wyithe J. S. B., Haehnelt M. G., Sargent W. L. W., 2012, *MNRAS*, 419, 2880
- Bolton J. S., Haehnelt M. G., Warren S. J., Hewett P. C., Mortlock D. J., Venemans B. P., McMahon R. G., Simpson C., 2011, *MNRAS*, 416, L70
- Bouwens R. J. et al., 2015, ArXiv e-prints
- Boylan-Kolchin M., Springel V., White S. D. M., Jenkins A., Lemson G., 2009, *MNRAS*, 398, 1150
- Brown W. R., Geller M. J., Fabricant D. G., Kurtz M. J., 2001, *AJ*, 122, 714
- Buckley D. A. H., Swart G. P., Meiring J. G., 2006, in *procSPIE*, Vol. 6267, Society of Photo-Optical Instrumentation Engineers (SPIE) Conference Series, p. 62670Z
- Carilli C. L., Rawlings S., 2004, *NAR*, 48, 979
- Carter D. et al., 2008, *ApJS*, 176, 424
- Chabrier G., 2003, *ApJ*, 586, L133
- Chambers K. C., 2005, in *Astronomical Society of the Pacific Conference Series*, Vol. 338, *Astrometry in the Age of the Next Generation of Large Telescopes*, Seidelmann P. K., Monet A. K. B., eds., p. 134
- Cole S., 2011, *MNRAS*, 416, 739
- Cole S. et al., 2001, *MNRAS*, 326, 255
- Cole S. et al., 2005, *MNRAS*, 362, 505
- Conroy C., van Dokkum P. G., 2012, *ApJ*, 760, 71
- Conroy C., van Dokkum P. G., Villaume A., 2017, *ApJ*, 837, 166

-
- Cooper A. P. et al., 2010, MNRAS, 406, 744
- Couchman H. M. P., Rees M. J., 1986, MNRAS, 221, 53
- Crain R. A. et al., 2016, ArXiv e-prints
- Cross N., Driver S. P., 2002, MNRAS, 329, 579
- Dalcanton J. J., Spergel D. N., Gunn J. E., Schmidt M., Schneider D. P., 1997, AJ, 114, 635
- Davies J. I., Davies L. J. M., Keenan O. C., 2015, ArXiv e-prints
- Davis M., Efstathiou G., Frenk C. S., White S. D. M., 1985, ApJ, 292, 371
- de Jong J. T. A., Verdoes Kleijn G. A., Kuijken K. H., Valentijn E. A., 2013, Experimental Astronomy, 35, 25
- de Vaucouleurs G., 1955, AJ, 60, 126
- de Vaucouleurs G., 1959, Handbuch der Physik, 53, 275
- de Vaucouleurs G., Ables H. D., 1968, ApJ, 151, 105
- Dewdney P. E., Hall P. J., Schilizzi R. T., Lazio T. J. L. W., 2009, IEEE Proceedings, 97, 1482
- Disney M., Phillipps S., 1983, MNRAS, 205, 1253
- Disney M. J., 1976, Nature, 263, 573
- Driver S. P., Davies L. J., Meyer M., Power C., Robotham A. S. G., Baldry I. K., Liske J., Norberg P., 2015, ArXiv e-prints
- Driver S. P. et al., 2009a, in IAU Symposium, Vol. 254, IAU Symposium, Andersen J., Nordströara B., Bland-Hawthorn J., eds., pp. 469–474
- Driver S. P. et al., 2011, MNRAS, 413, 971
- Driver S. P., Liske J., Cross N. J. G., De Propriis R., Allen P. D., 2005, MNRAS, 360, 81

-
- Driver S. P. et al., 2009b, *Astronomy and Geophysics*, 50, 5.12
- Driver S. P. et al., 2012, *MNRAS*, 427, 3244
- Driver S. P. et al., 2016, *MNRAS*, 455, 3911
- Du W., Wu H., Lam M. I., Zhu Y., Lei F., Zhou Z., 2015, *AJ*, 149, 199
- Dunn J. M., 2010, *MNRAS*, 408, 392
- Edge A., Sutherland W., Kuijken K., Driver S., McMahon R., Eales S., Emerson J. P., 2013, *The Messenger*, 154, 32
- Efstathiou G., 1992, *MNRAS*, 256, 43P
- Efstathiou G., Ellis R. S., Peterson B. A., 1988, *MNRAS*, 232, 431
- Emerson J., Sutherland W., 2010, *The Messenger*, 139, 2
- Fan X., Carilli C. L., Keating B., 2006, *ARA&A*, 44, 415
- Fan X. et al., 2000, *AJ*, 120, 1167
- Felten J. E., 1977, *AJ*, 82, 861
- Ferguson H. C., Binggeli B., 1994, *A&ARv*, 6, 67
- Ferrara A., Tolstoy E., 2000, *MNRAS*, 313, 291
- Ferrarese L. et al., 2012, *ApJS*, 200, 4
- Freeman K. C., 1970, *ApJ*, 160, 811
- Frenk C. S., White S. D. M., Efstathiou G., Davis M., 1985, *Nature*, 317, 595
- Fukugita M., Ichikawa T., Gunn J. E., Doi M., Shimasaku K., Schneider D. P., 1996, *AJ*, 111, 1748
- Gallagher, III J. S., Hunter D. A., 1986, *AJ*, 92, 557
- Gallazzi A., Bell E. F., 2009, *ApJS*, 185, 253

-
- Geha M., Blanton M. R., Yan R., Tinker J. L., 2012, *ApJ*, 757, 85
- Gilmore G., Wilkinson M. I., Wyse R. F. G., Kleyna J. T., Koch A., Evans N. W., Grebel E. K., 2007, *ApJ*, 663, 948
- Giovanelli R. et al., 2005, *AJ*, 130, 2598
- Grebel E. K., 2001, *Astrophysics and Space Science Supplement*, 277, 231
- Grebel E. K., Gallagher, III J. S., 2004, *ApJ*, 610, L89
- Gunn J. E., Peterson B. A., 1965, *ApJ*, 142, 1633
- Guo Q., 2011, in *EAS Publications Series*, Vol. 48, *EAS Publications Series*, Koleva M., Prugniel P., Vauglin I., eds., pp. 447–453
- Hodge P. W., 1971, *ARA&A*, 9, 35
- Hoefl M., Yepes G., Gottlöber S., Springel V., 2006, *MNRAS*, 371, 401
- Høg E. et al., 2000, *A&A*, 355, L27
- Hogg D. W., 1999, *ArXiv Astrophysics e-prints*
- Hopkins A. M. et al., 2013, *MNRAS*, 430, 2047
- Hubble E. P., 1926, *ApJ*, 64, 321
- Humason M. L., Mayall N. U., Sandage A. R., 1956, *AJ*, 61, 97
- Ibata R., Martin N. F., Irwin M., Chapman S., Ferguson A. M. N., Lewis G. F., McConnachie A. W., 2007, *ApJ*, 671, 1591
- Impey C., Bothun G., 1997, *ARA&A*, 35, 267
- Impey C., Burkholder V., Sprayberry D., 2001, *AJ*, 122, 2341
- Irwin M. J. et al., 2007, *ApJ*, 656, L13

-
- Ivezić Ž. et al., 2002, in *Astronomical Society of the Pacific Conference Series*, Vol. 284, IAU Colloq. 184: AGN Surveys, Green R. F., Khachikian E. Y., Sanders D. B., eds., p. 137
- James B. L., Koposov S., Stark D. P., Belokurov V., Pettini M., Olszewski E. W., 2015, *MNRAS*, 448, 2687
- Janz J. et al., 2015, *ArXiv e-prints*
- Javanmardi B. et al., 2016, *A&A*, 588, A89
- Jennings Z. G. et al., 2015, *ApJ*, 812, L10
- Johnston K. V., Bullock J. S., Sharma S., Font A., Robertson B. E., Leitner S. N., 2008a, *ApJ*, 689, 936
- Johnston S. et al., 2007, *PASA*, 24, 174
- Johnston S. et al., 2008b, *Experimental Astronomy*, 22, 151
- Kang X., Macciò A. V., Dutton A. A., 2013, *ApJ*, 767, 22
- Karachentsev I. D., Karachentseva V. E., Huchtmeier W. K., Makarov D. I., 2004, *AJ*, 127, 2031
- Kauffmann G. et al., 2003, *MNRAS*, 341, 54
- Kelvin L. S. et al., 2014a, *MNRAS*, 439, 1245
- Kelvin L. S. et al., 2014b, *MNRAS*, 444, 1647
- Kim H.-S., Wyithe J. S. B., Power C., Park J., Lagos C. d. P., Baugh C. M., 2015, *ArXiv e-prints*
- Kirby E. N., Cohen J. G., Guhathakurta P., Cheng L., Bullock J. S., Gallazzi A., 2013, *ApJ*, 779, 102
- Kissler-Patig M., 2004, in *Astronomical Society of the Pacific Conference Series*, Vol. 322, *The Formation and Evolution of Massive Young Star Clusters*, Lamers H. J. G. L. M., Smith L. J., Nota A., eds., p. 535

-
- Klypin A., Kravtsov A. V., Valenzuela O., Prada F., 1999, *ApJ*, 522, 82
- Kniazev A. Y., Grebel E. K., Pustilnik S. A., Pramskij A. G., Kniazeva T. F., Prada F., Harbeck D., 2004, *AJ*, 127, 704
- Knox R. A., Hambly N. C., Hawkins M. R. S., MacGillivray H. T., 1998, *MNRAS*, 297, 839
- Kochanek C. S. et al., 2001, *ApJ*, 560, 566
- Koda J., Yagi M., Yamanoi H., Komiyama Y., 2015, *ApJ*, 807, L2
- Koposov S. et al., 2008, *ApJ*, 686, 279
- Koposov S. E., Belokurov V., Torrealba G., Evans N. W., 2015, *ApJ*, 805, 130
- Kormendy J., 1982, in *Saas-Fee Advanced Course 12: Morphology and Dynamics of Galaxies*, Martinet L., Mayor M., eds., pp. 113–288
- Kormendy J., 1985, *ApJ*, 295, 73
- Kron R. G., 1980, *ApJS*, 43, 305
- Kuijken K., 2011, *The Messenger*, 146, 8
- Lacey C., Guiderdoni B., Rocca-Volmerange B., Silk J., 1993, *ApJ*, 402, 15
- Lapi A., Danese L., 2015, *JCAP*, 9, 3
- Laureijs R. et al., 2011, *ArXiv e-prints*
- Liske J., Baldry I. K., Driver S. P., Tuffs R. J., 2015, *ArXiv e-prints*
- Lotz J. M., Jonsson P., Cox T. J., Croton D., Primack J. R., Somerville R. S., Stewart K., 2011, *ApJ*, 742, 103
- Loveday J. et al., 2015, *MNRAS*, 451, 1540
- Loveday J. et al., 2012, *MNRAS*, 420, 1239
- Loveday J., Peterson B. A., Efstathiou G., Maddox S. J., 1992, *ApJ*, 390, 338

-
- Mahajan S. et al., 2015, MNRAS, 446, 2967
- Mahtessian A. P., 2011, Astrophysics, 54, 162
- Martin N. F., Ibata R. A., McConnachie A. W., Mackey A. D., Ferguson A. M. N., Irwin M. J., Lewis G. F., Fardal M. A., 2013a, ApJ, 776, 80
- Martin N. F. et al., 2009, ApJ, 705, 758
- Martin N. F., Slater C. T., Schlafly E. F., Morganson E., Rix H.-W., 2013b, ApJ, 772, 15
- Martínez-Delgado D. et al., 2010, AJ, 140, 962
- McConnachie A. W., 2012, AJ, 144, 4
- McGreer I. D., Mesinger A., D'Odorico V., 2015, MNRAS, 447, 499
- Merritt A., van Dokkum P., Abraham R., 2014, ApJ, 787, L37
- Meyer M., 2009, in Panoramic Radio Astronomy: Wide-field 1-2 GHz Research on Galaxy Evolution, p. 15
- Miralda-Escudé J., Rees M. J., 1998, ApJ, 497, 21
- Moore B., Ghigna S., Governato F., Lake G., Quinn T., Stadel J., Tozzi P., 1999, ApJ, 524, L19
- Morrison C. B., Hildebrandt H., Schmidt S. J., Baldry I. K., Bilicki M., Choi A., Erben T., Schneider P., 2016, ArXiv e-prints
- Mortlock D. J. et al., 2011, Nature, 474, 616
- Naab T., Johansson P. H., Ostriker J. P., Efstathiou G., 2007, ApJ, 658, 710
- Peebles P. J. E., 2001, ApJ, 557, 495
- Peek J. E. G. et al., 2011, ApJS, 194, 20
- Peng Y.-j. et al., 2010, ApJ, 721, 193

-
- Phillipps S., Disney M., 1986, MNRAS, 221, 1039
- Phillipps S., Drinkwater M. J., Gregg M. D., Jones J. B., 2001, ApJ, 560, 201
- Planck Collaboration et al., 2014, A&A, 571, A1
- Planck Collaboration et al., 2015, ArXiv e-prints
- Planck Collaboration et al., 2016, A&A, 594, A13
- Popesso P., Biviano A., Böhringer H., Romaniello M., 2006, A&A, 445, 29
- Power C. et al., 2015, Advancing Astrophysics with the Square Kilometre Array (AASKA14), 133
- Pozzetti L. et al., 2010, A&A, 523, A13
- Prescott M., Baldry I. K., James P. A., 2009, MNRAS, 397, 90
- Press W. H., Schechter P., 1974, ApJ, 187, 425
- Prusti T., 2011, in EAS Publications Series, Vol. 45, EAS Publications Series, pp. 9–14
- Randich S., Gilmore G., Gaia-ESO Consortium, 2013, The Messenger, 154, 47
- Rees M. J., 1986, MNRAS, 222, 27P
- Richardson J. C. et al., 2011, ApJ, 732, 76
- Rines K., Geller M. J., 2008, AJ, 135, 1837
- Roberts M. S., Haynes M. P., 1994, ARA&A, 32, 115
- Robertson B. E., Ellis R. S., Furlanetto S. R., Dunlop J. S., 2015, ApJ, 802, L19
- Rosenbaum S. D., Krusch E., Bomans D. J., Dettmar R.-J., 2009, A&A, 504, 807
- Rubin V. C., Ford W. K. J., Thonnard N., 1980, ApJ, 238, 471
- Sand D. J. et al., 2015, ApJ, 806, 95

-
- Sandage A., 1975, *Classification and Stellar Content of Galaxies Obtained from Direct Photography*, Sandage A., Sandage M., Kristian J., eds., the University of Chicago Press, p. 1
- Sandage A., Binggeli B., 1984, *AJ*, 89, 919
- Sandage A., Binggeli B., Tammann G. A., 1985a, *AJ*, 90, 1759
- Sandage A., Binggeli B., Tammann G. A., 1985b, *AJ*, 90, 395
- Scaramella R., Sabatini S., 2009, *Memorie della Societa Astronomica Italiana Supplementi*, 13, 142
- Schaye J. et al., 2015, *MNRAS*, 446, 521
- Schechter P., 1976, *ApJ*, 203, 297
- Schlegel D. J., Finkbeiner D. P., Davis M., 1998, *ApJ*, 500, 525
- Schmidt M., 1968, *ApJ*, 151, 393
- Schneider S. E., Thuan T. X., Mangum J. G., Miller J., 1992, *ApJS*, 81, 5
- Schombert J., McGaugh S., 2015, *ArXiv e-prints*
- Shapley H., 1938, *Nature*, 142, 715
- Shapley H., Paraskevopoulos J. S., 1940, *Proceedings of the National Academy of Science*, 26, 31
- Sharp R. et al., 2006, in *Society of Photo-Optical Instrumentation Engineers (SPIE) Conference Series*, Vol. 6269, Society of Photo-Optical Instrumentation Engineers (SPIE) Conference Series
- Skillman E. D. et al., 2013, *AJ*, 146, 3
- Smoot G. F. et al., 1992, *ApJ*, 396, L1
- Springel V. et al., 2005, *Nature*, 435, 629

-
- Stoughton C. et al., 2002, AJ, 123, 485
- Strauss M. A. et al., 2002, AJ, 124, 1810
- Tal T., van Dokkum P. G., Nelan J., Bezanson R., 2009, AJ, 138, 1417
- Taylor E. N., Franx M., Glazebrook K., Brinchmann J., van der Wel A., van Dokkum P. G., 2010, ApJ, 720, 723
- Taylor E. N. et al., 2011, MNRAS, 418, 1587
- Tegmark M. et al., 2004, ApJ, 606, 702
- Tollerud E. J., Geha M. C., Greevich J., Putman M. E., Stern D., 2015, ApJ, 798, L21
- Toomre A., Toomre J., 1972, ApJ, 178, 623
- Trachternach C., Bomans D. J., Habertzettl L., Dettmar R.-J., 2006, A&A, 458, 341
- Tully R. B., Fisher J. R., 1977, A&A, 54, 661
- van den Bergh S., 1960, ApJ, 131, 215
- van Dokkum P., Conroy C., Villaume A., Brodie J., Romanowsky A., 2016, ArXiv e-prints
- van Dokkum P. G., 2005, AJ, 130, 2647
- van Dokkum P. G., Abraham R., Merritt A., 2014, ApJ, 782, L24
- van Dokkum P. G., Abraham R., Merritt A., Zhang J., Geha M., Conroy C., 2015, ApJ, 798, L45
- van Dokkum P. G., Conroy C., 2012, ApJ, 760, 70
- van Haarlem M. P. et al., 2013, A&A, 556, A2
- van Zee L., 2000, AJ, 119, 2757

- Verheijen M. A. W., Oosterloo T. A., van Cappellen W. A., Bakker L., Ivashina M. V., van der Hulst J. M., 2008, in American Institute of Physics Conference Series, Vol. 1035, The Evolution of Galaxies Through the Neutral Hydrogen Window, Minchin R., Momjian E., eds., pp. 265–271
- Walsh S. M., Jerjen H., Willman B., 2007, *ApJ*, 662, L83
- Walsh S. M., Willman B., Jerjen H., 2009, *AJ*, 137, 450
- Wester W., Dark Energy Survey Collaboration, 2005, in Astronomical Society of the Pacific Conference Series, Vol. 339, Observing Dark Energy, Wolff S. C., Lauer T. R., eds., p. 152
- White S. D. M., Rees M. J., 1978, *MNRAS*, 183, 341
- Williams R. P. et al., 2016, *MNRAS*, 463, 2746
- York D. G., Adelman J., Anderson, Jr. J. E., Anderson S. F., Annis J. e. a., 2000, *AJ*, 120, 1579
- Zeldovich Y. B., Kurt V. G., Syunyaev R. A., 1968, *Zhurnal Eksperimentalnoi i Teoreticheskoi Fiziki*, 55, 278
- Zibetti S., Charlot S., Rix H.-W., 2009, *MNRAS*, 400, 1181
- Zwicky F., Zwicky M. A., 1971, Catalogue of selected compact galaxies and of post-eruptive galaxies

“I’m coming back in ... and it’s the saddest moment of my life”

-Astronaut Ed White, Gemini 4